

See discussions, stats, and author profiles for this publication at: <https://www.researchgate.net/publication/378035467>

Characterisation and understanding of viscoelastic leading edge protection solutions used on offshore wind turbines

Thesis · February 2024

DOI: [10.13140/RG.2.2.15998.15684](https://doi.org/10.13140/RG.2.2.15998.15684)

CITATIONS

0

READS

52

4 authors:



Imad Ouachan

National Composite Centre

3 PUBLICATIONS 59 CITATIONS

[SEE PROFILE](#)



Carwyn Ward

University of Bristol

64 PUBLICATIONS 1,612 CITATIONS

[SEE PROFILE](#)



Kirsten Dyer

ORE Catapult, United Kingdom, Glasgow

17 PUBLICATIONS 272 CITATIONS

[SEE PROFILE](#)



Ian Hamerton

University of Bristol

279 PUBLICATIONS 6,820 CITATIONS

[SEE PROFILE](#)



**This electronic thesis or dissertation has been downloaded from Explore Bristol Research,
<http://research-information.bristol.ac.uk>**

Author:
Ouachan, Imad

Title:
Characterisation and understanding of viscoelastic leading edge protection solutions used on offshore wind turbines

General rights

Access to the thesis is subject to the Creative Commons Attribution - NonCommercial-No Derivatives 4.0 International Public License. A copy of this may be found at <https://creativecommons.org/licenses/by-nc-nd/4.0/legalcode>. This license sets out your rights and the restrictions that apply to your access to the thesis so it is important you read this before proceeding.

Take down policy

Some pages of this thesis may have been removed for copyright restrictions prior to having it been deposited in Explore Bristol Research. However, if you have discovered material within the thesis that you consider to be unlawful e.g. breaches of copyright (either yours or that of a third party) or any other law, including but not limited to those relating to patent, trademark, confidentiality, data protection, obscenity, defamation, libel, then please contact collections-metadata@bristol.ac.uk and include the following information in your message:

- Your contact details
- Bibliographic details for the item, including a URL
- An outline nature of the complaint

Your claim will be investigated and, where appropriate, the item in question will be removed from public view as soon as possible.

Characterisation and Understanding of Viscoelastic Leading Edge Protection Solutions Used on Offshore Wind Turbines



Imad Ouachan

A dissertation submitted to the University of Bristol in accordance with the requirements of the degree of Doctor of Philosophy in the Faculty of Engineering, Department of Aerospace Engineering, under the Bristol Composites Institute Centre for Doctoral Training (ACCIS CDT)

July 2022

Word count: 79,000 (approx.)

REDACTION STATEMENT

This is a redacted version of the full dissertation, as agreed by the candidate, the supervisors and Offshore Renewable Energy Catapult, the industrial sponsor of this PhD studentship in the Faculty of Engineering. The redactions cover key information that was deemed too sensitive to be published. The redactions have been kept to the minimum level necessary, so that the dissertation still shows the research excellence of the candidate.

ABSTRACT

Offshore wind turbine blades are expected to remain in operation with minimal maintenance for 35 years. However, it is now estimated that up to £1.3 million is spent on each turbine during its lifetime due to leading edge erosion from the impact of rain droplets. Erosion can be reduced by limiting blade tip speeds, but with reduced restrictions offshore, the current trend is to increase the blade length and tip speeds to maximise the potential of wind turbine technology as a source of clean and renewable energy helping to tackle climate change.

Current polyurethane/polyurea based coating solutions for offshore wind turbines typically fail prematurely, reducing the aerodynamic efficiency of blades and significantly decreasing energy capture. While lifetime prediction models are available, they are commonly only suitable for homogeneous materials that undergo brittle failure. However, state-of-the-art models cannot accurately predict the effect of rain erosion on the lifetime of highly viscoelastic materials that are currently being developed at industrial levels. This limitation is thought to be due to a lack of understanding of the failure mechanisms and an inability to measure key material properties using standard methods that have been shown to vary due to loading and environmental conditions.

This project aimed to address the challenge of capturing the viscoelastic behaviour of several commercial coating systems relating the results with measured rain erosion performance. This was achieved through the down selection and adaptation of a set of quasi-static and dynamic physiomechanical tests which were used to study the effect of strain rates, load, and temperature, on key material properties. In parallel, accelerated rain erosion testing was used to determine each materials' erosion performance, allowing for correlations to be made to the measured material parameters. The work included utilising a design of experiment approach, which allowed for the influence of individual and combinations of test parameters to be quantified and detailed the preliminary results of a bespoke thin film testing approach.

The main findings indicate that modern viscoelastic coating systems show considerable strain rate and temperature-dependent behaviour that affects both the quasi-static and dynamic material properties. As a result, modern prediction models need to be adapted to account for variations resulting from different loading and environmental conditions.

Overall this thesis combines several techniques into an overarching methodology to characterise modern coating materials and compare their viscoelastic characteristics. This allows for rapid, relevant, and cost-effective laboratory test methods for early erosion performance screening, reducing overall development time.

Acknowledgements

This PhD was the toughest challenge I have undertaken to date, a journey that included ups, downs and even a global pandemic. I am proud of the work produced and need thank the people that made it possible.

First and foremost I would like to thank my supervisory group whose expertise and support made it possible to turn an idea into a fascinating project. Dr Carwyn Ward for his patience, round the clock guidance and endless hours of proof reading for which I am very grateful. Professor Ian Hamerton who has supported me from my first materials lecture during my undergraduate studies through to the end of PhD providing invaluable advice and ideas. Dr Kirsten Dyer whose knowledge in the area of LEE was key in not only the initial conception of the project but ensuring that the work was impactful and remained industrially relevant through creating the BLEER JIP and providing support throughout the project.

I would also like to express my sincere thanks to Professor Paul Weaver for his valuable guidance and giving me the opportunity to join the CDT opening my eyes to the world of engineering and composite materials. This time has given me the skills to not only develop as a researcher but also opened my eyes to a wide range opportunities that now within reach.

I am extremely grateful to my fellow researcher and friend Dr Robbie Herring for his assistance and enduring my constant questions. I would also like to thank my extended PhD family who not only helped a chemist make sense of endless engineering concepts but became some of my closest friends. I have no doubt you will all be successful and hope that we will all remain friends wherever the next step in life takes you.

I would also like to thank the Wind Blade Research Hub and industrial partners that I have engaged with during the research. It has been a pleasure to work with them all.

I cannot begin to express my thanks to Emily Harvey who provided her unwavering support and belief throughout this five year PhD. Without you, I would not be the person I am today.

I would also like thank Dr Ashley Clack at OREC for the considerable amount of testing support and practical advice. Ian Chorley for not only his technical support within the BCI labs but also cheerfulness. Professor Peter Ziopoulos for the helpful advice and discussions while hosting me at Cranfield University.

Finally I would like to thank my family for their continual support and encouragement throughout my studies. My parents Rachid and Zahiat without whom I would never have enjoyed so many opportunities. My sister Nadia, and my brother Belal, who both from now on will address me as doctor. I joke, but I do wish you both great success in your own studies and careers and I hope I can provide the same support you gave me.

Author Declaration

I declare that the work in this dissertation was carried out in accordance with the requirements of the University's *Regulations and Code of Practice for Research Degree Programmes* and that it has not been submitted for any other academic award. Except where indicated by specific reference in the text, the work is the candidate's own work. Work done in collaboration with, or with the assistance of, others, is indicated as such. Any views expressed in the dissertation are those of the author.

SIGNED: *Imad Ouachan* DATE: 28/01/2023

List of Publications

Imad Ouachan, Kirsten Dyer, Ian Hamerton, Carwyn Ward (2021) **Engineering Viscoelastic Properties in Polyurethane Coatings to Reduce Erosion Risks in Wind Turbine Blades.** *SAMPE J* 57, 16-24.

Imad Ouachan, Martin Kuball, Dong Liu, Kirsten Dyer, Carwyn Ward, Ian Hamerton (2019) **Understanding of Leading Edge Protection Performance Using Nano-Silicates for Modification.** *J Phys Conf Ser* 1222, 012016.

List Of Conference Presentations

Work from this thesis has been presented at the following conferences:

Imad Ouachan, Kirsten Dyer, Ian Hamerton, Carwyn Ward. **The Impact of Viscoelasticity on Wind Turbine Blade Leading Edge Protection.** At *2nd International Symposium on Leading Edge Erosion of Wind Turbine Blades, Online, DTU Risø Campus, Denmark* – 2021.

Cameron Mackie, Robbie Herring, Grant Leishman, Imad Ouachan, Kirsten Dyer. **Rain erosion testing, weathering, and lifetime prediction.** At *EERA JP WIND R&I, Online* – 2021

Imad Ouachan, Kirsten Dyer, Ian Hamerton, Carwyn Ward. **The Impact of Viscoelasticity on Wind Turbine Blade Leading Edge Protection.** At *SAMPE Europe Conference and Exhibition, Online, Amsterdam, Netherlands* – 2020

Imad Ouachan, Kirsten Dyer, Carwyn Ward, Ian Hamerton. **Exploring Mechanisms of Rain Erosion on Wind Turbine Blades.** At *Blade O&M Europe 2019, Amsterdam, Netherlands* – 2019.

Imad Ouachan, Kirsten Dyer, Carwyn Ward, Ian Hamerton. **Understanding Leading Edge Protection Erosion Performance Using Nanosilicates for Modification.** At *8th Annual Conference of the CDT in Advanced Composites for Innovation and Science, Bristol, UK* – 2019.

Imad Ouachan, Kirsten Dyer, Carwyn Ward, Ian Hamerton. **Understanding of Leading Edge Protection Erosion Performance Using Nano-Silicates for Modification.** At *WindEurope, Bilbao, Spain* – 2019.

Table of Contents

Table of Contents	viii
List of Figures.....	xii
List of Tables	xix
List of Acronyms.....	xxi
List of Symbols	xxiii
Introduction.....	1
1.1 Research Context	2
1.1.1 Renewable Energy Trends.....	4
1.1.2 Current Wind Energy Market.....	7
1.1.3 Brief History and Current State of Wind energy.....	9
1.1.4 Wind Turbine Design and Composition	10
1.1.5 Wind Turbine Operating Environment	12
1.2 Problem Statement.....	14
1.3 Research Question	17
1.4 Thesis Outline.....	18
Literature Review.....	20
2.1 The Problem of Leading-Edge Erosion	21
2.2 Blade Coatings.....	24
2.2.1 Polyurethane and Polyurea Chemistry	27
2.3 Failure Modes	30
2.4 Rain Droplet Impact	32
2.5 Coating Lifetime Prediction.....	35
2.6 Implication on Material Selection.....	37
2.7 Review of Impact Springer Parameters	41
2.7.1 Modulus of Elasticity.....	41
2.7.2 Thickness.....	43
2.7.3 Poisson's Ratio	43
2.7.4 Tensile Properties	44
2.7.5 Implications of Viscoelasticity.....	44
2.7.6 Other Considerations	49
2.7.6.1 Environmental conditions.....	49
2.7.6.2 Industry Standardisation.....	50

2.8	Summary	51
Materials and Methods		54
3.1	Materials	55
3.2	Sample Preparation	55
3.2.1	Material Mixing and Cure	55
3.2.2	Block Casting	56
3.2.3	Thin Films	56
3.2.4	Coated Panels.....	57
3.3	Thermogravimetric Analysis	58
3.4	Dynamic Mechanical Thermal Analysis.....	59
3.5	Nanoindentation	60
3.6	Quasi-Static Tensile Testing	63
3.7	Accelerated Rain Erosion Testing.....	65
3.8	Ultrasonic Acoustic Testing.....	68
3.9	Summary	69
Tensile Testing		70
4.1	Introduction	71
4.2	Results.....	71
4.2.1	Strain at Break.....	72
4.2.2	Toughness	74
4.2.3	Tangent Modulus	75
4.2.4	Secant Modulus	77
4.2.5	Ultimate Tensile Strength	78
4.3	Discussion.....	80
4.4	Summary	82
Nanoindentation.....		84
5.1	Introduction	85
5.2	Method Development.....	85
5.2.1	Instrument Resolution	85
5.2.2	Thermal Drift.....	86
5.2.3	Adhesion	87
5.2.4	Choice of Reference Material	87
5.2.5	Material Behaviour	87
5.2.6	Viscoelastic effects.....	88
5.3	Results.....	90
5.3.1	Test 1 – Varying Loading Rate.....	90

5.3.2	Test 2 – Varying Maximum Load.....	97
5.3.3	Test 3 – Repeated Indentation and Varying Recovery Period	103
5.4	Discussion.....	107
5.4.1	Loading Rate.....	107
5.4.2	Maximum Load	110
5.4.3	Repeated Indentation and Recovery	113
5.5	Summary	115
	Dynamic Mechanical Thermal Analysis	117
6.1	Introduction	118
6.2	Dual Cantilever Testing	119
6.2.1	Study of Strain Dependence	119
6.2.2	Study of Temperature Dependence.....	122
6.2.3	Study of Frequency Dependence.....	125
6.2.3.1	Testing.....	128
6.2.3.2	Validation	133
6.3	Thin-Film Testing.....	138
6.3.1	Determination of Linear Viscoelastic Region	138
6.3.2	Study of Temperature Dependence.....	139
6.3.3	Study of Frequency Dependence	140
6.3.3.1	Validation	144
6.4	Discussion.....	146
6.4.1	Strain Dependence.....	146
6.4.2	Temperature Dependence.....	147
6.4.3	Frequency Dependence	147
6.4.4	Comparison of Damping Characteristics.....	149
6.4.5	Comparison to Ultrasonic Acoustic Data	152
6.5	Summary	157
	Accelerated Rain Erosion Testing	159
7.1	Introduction	160
7.2	Standard Approach	160
7.2.1	Method	160
7.2.2	Results.....	161
7.3	Design of Experiments Approach.....	172
7.3.1	Method	173
7.3.1.1	Factor Selection	174
7.3.1.2	Designed Test Plan.....	174

7.3.2	Results.....	176
7.3.2.1	Multivariate analysis.....	177
7.4	Thin Film Testing	180
7.5	Discussion.....	183
7.6	Summary	188
Discussion.....		190
8.1	Single Parameter Correlations To Erosion Performance	191
8.1.1	Tensile Testing	191
8.1.2	Nanoindentation.....	193
8.1.3	Dynamic Thermal Mechanical Analysis.....	194
8.2	System-Level Correlations to Erosion Performance	196
8.2.1	Average Impact Pressure	196
8.2.2	Effective Strength.....	199
8.3	Summary	200
Conclusions and Future Work.....		202
9.1	Research Question	203
9.2	Key Findings	205
9.3	Research Impact.....	206
9.4	Future Work.....	207
References.....		210

List of Figures

Figure 1.1 – Historical global renewable energy consumption adapted from B.P. statistical review of world energy 2021 [33]. Three regions are highlighted, identifying key events that influenced the historical landscape. i) 1973 Oil crisis, ii) Mid-2000 oil Spike, and iii) Fukushima Daiichi nuclear disaster.	6
Figure 1.2 – Annual offshore wind installations (left axis) and cumulative capacity (right axis). The figure is taken directly from Offshore wind in Europe key trends and statistics [38].	7
Figure 1.3 – a: Savonius rotor (left), b) Darrius vertical axis rotor (centre) c) horizontal axis rotor (right). Part a and b were directly reprinted with permission from Springer Nature [46]. Image are not to scale.	9
Figure 1.4 – Simplified diagram of a wind turbine detailing the main components. Reprinted from the literature with permission from Elsevier [51].	11
Figure 1.5 – Average failure rate of each turbine component showing the control system has the highest value followed by blades/pitch. Reprinted directly from literature with permission from Elsevier [58].	13
Figure 1.6 – Drone photography photo of an eroded leading edge seen on wind turbine blades in China. These images were kindly provided by Dennis Lin from Jotun.	15
Figure 2.1 – Drone photography photos of eroded leading edges seen on wind turbine blades in various locations in China. These images were kindly provided by Dennis Lin from Jotun.	22
Figure 2.2 – Diagram of a simplified leading-edge coating system cross-section. The leading-edge protection layer (LEP) and Topcoat are commonly feathered to minimise abrupt changes from one coating to another. The thicknesses of the coatings layers are not to scale.	25
Figure 2.3 – General polyurea and polyurethane reaction schemes used to form modern elastomeric coatings.	28
Figure 2.4 – Generalised polyurethane segment structure showing the formation of hard and soft segments and the presence of hydrogen bonding between chains. Adapted from the literature [107].	29
Figure 2.5 – Hexamethylene diisocyanate (HDI), methylene diphenyl diisocyanate (MDI) and toluene diisocyanate (TDI). TDI is commonly used as a mixture of isomers, but only one is shown for brevity.	29
Figure 2.6 – Common long-chain diols used to form modern elastomeric coatings. Left: poly(ethylene adipate glycol) (PEA) Right: polytetrahydrofuran (PTHF).	30
Figure 2.7 – Common low M_w chain extenders designed to react with isocyanates form part of the HS. Left: 2,5-bis(4-amino-phenylene)-1,3,4-oxadiazole (DAPO), a diamine chain extender. Right: butylene glycol (BDO), a diol chain extender.	30
Figure 2.8 – Schematic summarising the impacts of a spherical water droplet on a rigid surface. This figure depicts the three distinct waves originating from the point of impact. This figure was reprinted with permission from Elsevier [69].	32
Figure 2.9 – Schematic detailing of a wave propagating through a multi-layer system composed of a coating and substrate layer. Left: Visual representation of wave propagation and reflection. Right: Resulting stress propagation during two consecutive time instants. Where h represents coating thickness, C_c and C_L denote the speed of sound in the coating and liquid, respectively, and σ represents the magnitude of the stress wave. Both figures were adapted directly from the literature [86].	34
Figure 2.10 – A graph illustrating stages of erosion as defined by Springer et al. [111]. The figure is adapted from work by Eisenberg et al. [111].	36

Figure 3.1 – A baker film applicator with application thicknesses of 100 µm, 200 µm, 300 µm and 400 µm used to manufacture thin specimens used for quasi-static and dynamic tensile testing. Image not to scale. Image adapted from literature [151].....	56
Figure 3.2 – An image showing the bagged glass fibre under vacuum before the resin infusion process is undertaken. Image not to scale.	57
Figure 3.3 – Demonstrator sample of sequential application steps. Top left: GFRP composite. Top right: sanded composite. Bottom left: Filler layer application. Bottom Right: Topcoat and LEP layer. Image not to scale.	58
Figure 3.4 – A representation of indentation-load displacement data showing key parameters: P_{max} the peak indentation load, h_{max} the indenter displacement at peak load, h_f the final depth of the contact impression after unloading and S_u the contact stiffness of the unloading curve calculated from the unloading gradient. The area highlighted blue illustrates $W_{elastic}$ the elastic work, the area highlighted red illustrates $W_{plastic}$ the plastic work, the sum of these values, give W_{total} the total work during the indentation test. Figure adapted from the literature [155].....	61
Figure 3.5 – An image of the sectioned composite panels cast into a resin. The surfaces were polished using a lapping wheel prior to nanoindentation testing. Image not to scale.	61
Figure 3.6 –The schematic represents the thin film specimen bonded to the paper template using epoxy adhesive (yellow) before tensile testing. A gauge length of 10 mm was used for each test. The red dotted lines indicate the area to be cut once the sample is loaded into the test rig. Figure adapted from the literature [159].Image not to scale.	63
Figure 3.7 – Thin-film undergoing tensile testing in a Deben Microtest MT200 tensile tester. The instrument is approximately 15 cm x 8 cm x 5 cm for reference. Image not to scale.....	64
Figure 3.8 – Example material stress-strain curve detailing key points of interest. A: linear elastic region where stress is proportional to strain and generally obeys Hooke's law. B: The area toe corrections are applied as detailed in ASTM D882-00. C: The tangent modulus (E_{tan}) is calculated from the tangent of the Linear region. D: The secant modulus (E_{sec}) calculated from the secant from the toe corrected origin and the value at 0.4 strain. E: The ultimate tensile stress (UTS) is calculated from the maximum stress. F: The strain at break (ϵ_{break}) is calculated from the point of failure where load drops to zero. G: The toughness is calculated as the area under the stress-strain curve. Figure adapted from ASTM D882-00 [112].....	65
Figure 3.9 – Image of the whirling arm rain erosion tester at the Offshore Renewable Energy Catapult (OREC) in Blyth, UK.	66
Figure 3.10 – A schematic detailing the naming conventions used to identify the rain aerofoil shaped rain erosion test specimens.	67
Figure 3.11 – A Schematic is shown detailing the pulse-echo acoustic measurement technique of a homogeneous material. Left: A diagram showing a transducer placed on the material using a coupling gel between the interface. A signal is passed through the thickness of the material reflecting off the back wall resulting in a signal. Right: A representation of the expected signals. The first to occur is a reflection from the material's front wall, followed by a lower magnitude echo from the back-wall reflection. Figure adapted from the literature [160].	68
Figure 4.1 – Representative stress-strain curves for each coating material obtained at a 2mm/min displacement rate.	72
Figure 4.2 – A box plot is presented comparing the tensile strain break (STB) of materials used in leading-edge protection systems at 0.5 and 2 mm/min displacement rates. The † symbol denotes a significant difference ($P < 0.05$) between the two different displacement rate conditions, indicating that the material properties are dependent on the strain rate.....	73

Figure 4.3 – A box plot is presented comparing the tensile toughness of materials used in leading-edge protection systems at 0.5 and 2 mm/min displacement rates. Table A is a comparison of LEP materials, and Table B is a comparison of topcoat and.....	75
Figure 4.4 – A box plot is presented comparing the tensile tangent modulus of materials used in leading-edge protection systems at 0.5 and 2 mm/min displacement rates. Table A is a comparison of LEP materials, Table B is a comparison of topcoat and Table C is a comparison of filler materials. The † symbol denotes a significant difference ($P < 0.05$) between the two different displacement rate conditions, indicating that the material properties are dependent on the strain-rate.	77
Figure 4.5 – A box plot is presented comparing the tensile secant modulus (0.4 strain) of materials used in leading-edge protection systems at 0.5 and 2 mm/min displacement rates. The † symbol denotes a significant difference ($P < 0.05$) between the two different displacement rate conditions, indicating that the material properties are dependent on the strain-rate.....	78
Figure 4.6 – A box plot is presented comparing the ultimate tensile strength (<i>UTS</i>) of materials used in leading-edge protection systems at 0.5 and 2 mm/min displacement rates. Table A is a comparison of LEP materials, Table B is a comparison of topcoat and Table C is a comparison of filler materials. The † symbol denotes a significant difference ($P < 0.05$) between the two different displacement rate conditions, indicating that the material properties are dependent on the strain-rate.....	80
Figure 5.1 – Examples of pile-up and-in behaviour. A) Side view of an indenter demonstrating the maximum depth (<i>hmax</i>), and contact depth (<i>hc</i>). B) The resulting contact area from each behaviour. Figure directly reprinted with permission from literature [174].	88
Figure 5.2 – Classical elements are used to represent material behaviours over time. From left to right: elastic solids, viscous fluids, viscoelastic-fluid behaviour (including stress relaxation and permanent deformation) and viscoelastic-solid behaviour showing retarded but reversible deformation. Figure adapted from literature [164].....	89
Figure 5.3 – Generalised schematic of depth-load responses for two example cases undergoing a load-hold-unload method. <i>Pmax</i> , peak indentation load, <i>hmax</i> , indenter displacement at peak load, <i>hf</i> , final depth of the contact impression after unloading and <i>Su</i> , the contact stiffness of the unloading curve calculated from the unloading gradient. A: The response of an elastic material that shows negligible creep behaviour and permanent deformation. B: The response of a viscoelastic material displaying complete strain recovery and creep during the hold phase resulting in a characteristic nose shape. The red line demonstrates how the nose can cause an overestimation of the contact stiffness (<i>Su</i> *), and the green line represents how a lower contact stiffness can be obtained for fitting away from the nose. Figure adapted from the literature [155].	90
Figure 5.4 – A schematic detailing the two load-hold-unload nanoindentation methods used in Test 1. Loading time: 5 seconds / 60 seconds, maximum load: 100 μ N, hold time: 60 seconds, unload time: 2 seconds and N=5.....	91
Figure 5.5 – A bar chart is presented comparing the maximum depths measured during a load-hold-unload nanoindentation method (loading time: 5 seconds / 60 seconds, maximum load: 100 μ N, hold time: 60 seconds, unload time: 2 seconds and N=5). The asterisk (*) symbol indicates a significant difference between test loading rates ($P < 0.05$).	92
Figure 5.6 – A bar chart is presented comparing the reduced modulus values calculated using the Oliver Pharr method measured during a load-hold-unload nanoindentation method (loading time: 5 seconds / 60 seconds, maximum load: 100 μ N, hold time: 60 seconds, unload time: 2 seconds and N=5). Asterisk (*) symbol indicates a significant difference between test loading rates ($P < 0.05$).	93
Figure 5.7 – A bar chart is presented comparing the short term recovery values measured during a load-hold-unload nanoindentation (loading time: 5 seconds / 60 seconds, maximum load: 100 μ N, hold time: 60 seconds, unload time: 2 seconds and N=5). Asterisk (*) symbol indicates a significant difference between test loading rates ($P < 0.05$).....	94

Figure 5.8 – A bar chart is presented comparing the hardness values calculated using the Oliver Pharr method measured during a load-hold-unload nanoindentation (loading time: 5 seconds / 60 seconds, maximum load: 100 μ N, hold time: 60 seconds, unload time: 2 seconds and N=5). Asterisk (*) symbol indicates a significant difference between test loading rates ($P<0.05$).....	95
Figure 5.9 – A bar chart is presented comparing the indentation work measured during a load-hold-unload nanoindentation method (loading time: 5 seconds / 60 seconds, maximum load: 100 μ N, hold time: 60 seconds, unload time: 2 seconds and N=5). The complete bar represents the total work, the orange represents the plastic work, and the green represents the elastic work.....	96
Figure 5.10 – A schematic detailing the three load-hold-unload nanoindentation methods used in Test 2. Maximum loads: 100 μ N (blue), 200 μ N (purple) and 500 μ N (orange) loading time: 5 seconds / 10 seconds / 25 seconds (to maintain a constant loading rate), hold time: 30 seconds, unload time: 2 seconds and N=5.....	97
Figure 5.11 – A bar chart is presented comparing the maximum depths measured during a load-hold-unload nanoindentation method. Maximum loads: 100 μ N, 200 μ N, and 500 μ N, loading time: 5 seconds / 10 seconds / 25 seconds (to maintain a constant loading rate), hold time: 60 seconds, unload time: 2 seconds and N=5. The LEP B3 500 μ N was unable to be captured and is not displayed. The asterisk (*) symbol indicates a significant difference between maximum loads ($P<0.05$).	99
Figure 5.12 – A bar chart is presented comparing the reduced modulus values obtained using the Oliver Pharr method from a load-hold-unload nanoindentation method. Maximum loads: 100 μ N, 200 μ N, and 500 μ N, loading time: 5 seconds / 10 seconds / 25 seconds (to maintain a constant loading rate), hold time: 60 seconds, unload time: 2 seconds and N=5. The LEP B3 500 μ N was unable to be captured and is not displayed. The asterisk (*) symbol indicates a significant difference between maximum loads ($P<0.05$).	100
Figure 5.13 – A bar chart is presented comparing the short term recovery values measured during a load-hold-unload nanoindentation method. Maximum loads: 100 μ N, 200 μ N, and 500 μ N, loading time: 5 seconds / 10 seconds / 25 seconds (to maintain a constant loading rate), hold time: 60 seconds, unload time: 2 seconds and N=5. Asterisk (*) symbol indicates a significant difference between test loading rates ($P<0.05$).....	101
Figure 5.14 – A bar chart is presented comparing the indentation work values measured during a load-hold-unload nanoindentation method. Maximum loads: 100 μ N, 200 μ N, and 500 μ N, loading time: 5 seconds / 10 seconds / 25 seconds (to maintain a constant loading rate), hold time: 60 seconds, unload time: 2 seconds and N=5.....	102
Figure 5.15 – A schematic detailing the three load-hold-unload nanoindentation methods used in Test 3. Maximum load: 100 μ N, loading time: 2 seconds, hold time: 30 seconds, unload time: 2 seconds and N=1. For condition, A (blue), a 60 second recovery period (where the load was set at zero) was utilised, and no recovery period was used for condition B (purple). The subsequent indent was started immediately after the unload.	103
Figure 5.16 – A bar chart is presented comparing the repeated indentation work values at the same location of LEP A3 measured during a load-hold-unload nanoindentation method. The S value denotes the indentation sequence. Maximum load: 100 μ N, loading time: 2 seconds, hold time: 30 seconds, unload time: 2 seconds and N=1. For condition, A, a 60 second recovery period (where the load was set at zero) was utilised, and no recovery period was used for condition B. The subsequent indent was started immediately after the unload.....	104
Figure 5.17 – A bar chart is presented comparing the repeated indentation work values of topcoat A2 measured during a load-hold-unload nanoindentation method. The S value denotes the indentation sequence. Maximum load: 100 μ N, loading time: 2 seconds, hold time: 30 seconds, unload time: 2 seconds and N=1. For condition, A, a 60 second recovery period (where the load was set at zero) was	

utilised, and no recovery period was used for condition B. The subsequent indent was started immediately after the unload.....	105
Figure 5.18 – A bar chart is presented comparing the repeated indentation work values of LEP B3 measured during a load-hold-unload nanoindentation method. The S value denotes the indentation sequence. Maximum load: 100 μ N, loading time: 2 seconds, hold time: 30 seconds, unload time: 2 seconds and N=1. For condition, A, a 60 second recovery period (where the load was set at zero) was utilised, and no recovery period was used for condition B. The subsequent indent was started immediately after the unload.....	106
Figure 5.19 – A bar chart is presented comparing the repeated indentation work values of LEP B4 measured during a load-hold-unload nanoindentation method. The S value denotes the indentation sequence. Maximum load: 100 μ N, loading time: 2 seconds, hold time: 30 seconds, unload time: 2 seconds and N=1. For condition, A, a 60 second recovery period (where the load was set at zero) was utilised, and no recovery period was used for condition B. The subsequent indent was started immediately after the unload.....	107
Figure 5.20 – A line chart is presented comparing the short term recovery values (filled symbols and solid lines) and elastic work percentage (hollow symbols and dashed lines) measured during a load-hold-unload nanoindentation method. Maximum loads: 100 μ N, 200 μ N, and 500 μ N, loading time: 5 seconds / 10 seconds / 25 seconds (to maintain a constant loading rate), hold time: 60 seconds, unload time: 2 seconds and N=5. The LEP B3 500 μ N was unable to be captured and is not displayed. Error bars are omitted for clarity but are available in previous Figure 5.13.	112
Figure 5.21 - A line chart is presented comparing the total work values with 0-second recovery (filled symbols) and 60-second recovery (hollow symbols) measured during a load-hold-unload nanoindentation method (loading time: 2.5 seconds, maximum load: 100, hold time: 60 seconds, unload time 2 seconds, repeated indents: 4 and N=1).....	114
Figure 6.1 – Example of a dynamic strain sweep where the response of a material to increasing oscillatory deformation is recorded at a constant frequency and temperature. The red line is the storage modulus (E'), the blue line is the stress (σ), the dashed line indicates the end of the linear viscoelastic region (LVER). Within the LVER, E' is independent of strain and σ displays a constant slope.	119
Figure 6.2 – Results from a dual cantilever dynamic strain sweep where the response of a material to increasing deformation (up to 400 μ m) is recorded at a constant frequency (1 Hz) and temperature (0 °C). The blue line indicates the general linear viscoelastic region strain limit used in the subsequent testing.	120
Figure 6.3 – Comparison of measured yield stresses obtained from a dual cantilever dynamic strain sweep where the response of a material to increasing deformation (up to 400 μ m) is recorded at a constant frequency (1 Hz) and temperature (0 °C).	122
Figure 6.4 – A comparison of T_g values obtained from dual cantilever temperature sweeps (-50 °C to 80 °C) at a constant frequency (1 Hz) and amplitude (within the LVER).	124
Figure 6.5 – A schematic detailing the construction of the storage modulus (E') master curve using the time-temperature superposition principle. The left part of the graph shows frequency sweep data at varying temperatures. The right shows each sweep combined around a selected reference temperature (T_{ref}). The magnitude of the shift is represented by the various shift factors (a_{TX}). Figure adapted from the literature [186].	126
Figure 6.6 – Comparison of filler master curves generated from dual cantilever frequency sweeps. filler A1 (A) was between -40 °C to 40 °C and 0.01% strain, and filler B1 (B) was between -40 °C to 30 °C and 0.1% strain. Periodic variations are visible in the master curve due to the variability in the combination of multiple sweeps.....	129
Figure 6.7 – Comparison of topcoat master curves generated from dual cantilever frequency sweeps. Topcoat A2 (A) was between -40 °C to 30 °C and 0.01% strain, and topcoat B2 (B) was between -30°C to	

30°C and 0.1% strain. Periodic variations are visible in the master curve due to the variability in the combination of multiple sweeps.....	130
Figure 6.8 – Comparison of LEP master curves generated from dual cantilever frequency sweeps. LEP A3 (A) was at -40 °C to 30 °C and 0.01% strain, LEP B3 (B) is -30°C to 20 °C and 0.1% strain, and LEP B4 is -30°C to 20 °C and 0.1% strain. Periodic variations are visible in the master curve due to the variability in the combination of multiple sweeps.	132
Figure 6.9 – Cole-Cole plots for validation of filler and topcoat material master curves. A: filler A1, B: filler B1, C: topcoat A2, and D: topcoat B2.	136
Figure 6.10 – Cole-Cole plots for validation of LEP material master curves. A: LEP A3, B: LEP B3 and C: LEP B4.....	137
Figure 6.11 – Results from a thin film tension dynamic strain sweep where the response of a material to increasing deformation (up to 400 µm) is recorded at a constant frequency (1 Hz) and temperature (16 °C). The blue line indicates the general linear viscoelastic region strain limit used in the subsequent testing.	138
Figure 6.12 – Comparison of measured yield stresses obtained from a thin film tension dynamic strain sweep where the response of a material to increasing deformation (up to 400 µm) is recorded at a constant frequency (1 Hz) and temperature (16 °C).	139
Figure 6.13 – A comparison of T_g values obtained from thin-film tensile temperature sweeps (-40 °C to 80 °C) at a constant frequency (1 Hz) and amplitude (0.1 %).....	140
Figure 6.14 – Filler B1 master curve generated from thin-film tensile frequency sweeps at 0.1% strain and between -20 °C to 50 °C. Periodic variations are visible in the master curve due to the variability in the combination of multiple sweeps.	141
Figure 6.15 – Comparison of topcoat master curves generated from thin-film tensile frequency sweeps at 0.1% strain. Topcoat A2 (A) was between -30 °C to 30 °C, and topcoat B2 (B) was between -40°C to 30°C. Periodic variations are visible in the master curve due to the variability in the combination of multiple sweeps.	142
Figure 6.16 – Comparison of LEP master curves generated from thin-film tensile frequency sweeps at 0.1% strain. LEP A3 (A) was at -30 °C to 20 °C, LEP B3 (B) is -40°C to 30 °C and LEP B4 is -40°C to 20 °C. Periodic variations are visible in the master curve due to the variability in the combination of multiple sweeps.	143
Figure 6.17 – Cole-Cole plots for validation of filler and topcoat material master curves. A: filler B1, B: topcoat A2, and C: topcoat B2.....	145
Figure 6.18 – Cole-Cole plots for validation of LEP material master curves. A: LEP A3, B: LEP B3 and C: LEP B4.....	146
Figure 6.19 – Linear relationship between DMTA oscillation frequency (Hz) and strain rate (s) are presented. As two oscillation strains, 0.01 % (black) and 0.1% (red), were used, the graph shows each relationship and straight-line equations.....	149
Figure 6.20 – A comparison of specific damping capacities of coating materials from dual cantilever master curves.....	151
Figure 6.21 – A comparison of specific damping capacities of coating materials from thin-film tensile master curves. The data was smoothed using the adjacent averaging (25 pts) to aid visual comparison.	152
Figure 6.22 – A graph summarising the measured speed of sound values and calculated Young's modulus values obtained using a pitch-catch method and 5 MHz ultrasonic acoustic transducer (N=4).	154
Figure 6.23 – A comparison of the measured (5 MHz) speed of sound values (squares) and predicted speed of sound values obtained from the storage modulus of dual cantilever master curves (solid lines). The data was smoothed using the adjacent averaging (10 pts) to aid visual comparison.	155

Figure 6.24 – A comparison of the measured (5 MHz) speed of sound values (squares) and predicted speed of sound values obtained from the storage modulus of thin-film tension master curves (solid lines). The data was smoothed using the adjacent averaging (10 pts) to aid visual comparison.	156
Figure 7.1 – An example of surface voids present in an accelerated leading edge erosion test specimen that did not progress into active erosion over the duration of the test. Image not to scale.	163
Figure 7.2 – Eroded rain erosion test specimens tested in the OREC WARET. The high-speed tip is on the right Top: LEP A3 system tested at 1000 RPM and 55 l/h (T1) at 66 hours. Only two specimens are shown as the third specimen needed to be removed due to early failure of the composite substrate. Bottom: LEP A3 system tested at 1200 RPM and 25 l/h (T2) at 16 hours.	168
Figure 7.3 – VN graph displaying the impacts to the end of incubation at different local impact velocities. A power-law fit is presented to allow for a comparison of each test.....	171
Figure 7.4 – Visualisation of full factorial (left) and $\frac{1}{2}$ factorial (right) designs utilising two levels.	173
Figure 7.5 – Images of test specimens from Test 6 that underwent 5 hours of erosion time at 1100 RPM and a flow rate of 25 l/h. This image shows the delamination issues observed in many of the test specimens used in the campaign.....	176
Figure 7.6 – Pareto chart comparing the standardised effects in response to time to incubation for three factors. A: Rotational velocity, B: Flow rate and C: Material. The red line indicates a threshold value, responses exceeding threshold are considered statistically significant ($P < 0.05$).....	177
Figure 7.7 – A main effects plot for the time to incubation. The dashed line indicates the average time to the end of incubation.	178
Figure 7.8 – Interaction plots displaying the relationship between each chosen factor A: rotational velocity, B: Flow rate and C: Material.....	179
Figure 7.9 – A contour plot of time to end of incubation against flow rate and rotational velocity is presented. The model has a $R^2_{\text{predicted}}$ value of 87.63 %, indicating a good fit of the experimental data.	180

Figure 7.11 – Comparison of storage and loss moduli from dual cantilever master curves generated frequency sweeps calculated for a reference temperature of 20 °C using an amplitude of 0.1% strain. Medium was at -40 °C to 30 °C, Hard (B) is -40°C to 30 °C and strain, and Soft is -40°C to 30 °C. Each curve is smoothed using a 25 point adjacent averaging method.....	186
Figure 7.12 – Comparison of $\tan(\delta)$ from dual cantilever master curves generated frequency sweeps calculated for a reference temperature of 20 °C using an amplitude of 0.1% strain. Medium was at -40 °C to 30 °C, Hard (B) is -40°C to 30 °C and strain, and Soft is -40°C to 30 °C. Each curve is smoothed using a 25 point adjacent averaging method.....	187
Figure 8.1 – A parametric analysis of the effect of varying the speed of sound on the predicted average impact pressure using the Springer approach [111, 114]. The solid lines that overlap indicate the predicted values for LEP A3 (black), LEP B3 (blue) and LEP B4 (green). The coloured squares indicate the calculated value using each respective speed of sound measurement obtained using ultrasonic acoustic testing (Chapter 6). The purple dashed lines indicate the range of speed of sound values predicted from DMTA (Chapter 6).	198
Figure 8.2 – A parametric analysis of the effect of varying the speed of sound on the predicted effective material strength using the Springer approach [111, 114]. The solid lines indicate the predicted values for LEP A3 (black), LEP B3 (blue) and LEP B4 (green). The coloured squares indicate the calculated value using each respective single speed of sound measurement obtained using ultrasonic acoustic testing. The purple dashed lines indicate the range of speed of sound values predicted from DMTA (Chapter 6).	199

List of Tables

Table 1.1 – Worldwide and E.U. electricity generation fuel source distribution displayed in exajoules (E.J.) created using the B.P. statistical review of world energy 2021 [33].....	5
Table 1.2 – Levelised Cost Estimates for projects commissioned in the U.K. reproduced using data from the literature [43].	8
Table 1.3 – Historical trend in larger wind turbines from 1995 to 2015. Adapted from literature [18, 54].	12
Table 2.1 – A tabulated list of the naming conventions used for polyurethane and polyurea systems. These are composed of resin and a chain extender.....	28
Table 2.2 – Summary of key inputs into the lifetime prediction model presented by Springer et al. [86].	37
Table 2.3 – A selection of available material properties of several classes of materials for comparison. The abbreviated polymer system tabulated are low-density polyethylene (LDPE), ultra-high-molecular-weight polyethylene (UHMWPE), polymethyl methacrylate (PMMA), polyetheretherketone (PEEK) and polycarbonate (PC). Acoustic impedances were calculated using Equation 2.3, water hammer pressure using Equation 2.2 and relative impact pressure using Equation 2.6 (Impact velocity of 100 m/s). The table explains the trend towards softer, low acoustic impedance materials due to reduced impact pressures. Data adapted from Slot et al. and Johansen et al. [109, 124].	39
Table 3.1 – Naming conventions for coating systems used in the thesis.	55
Table 3.2 – Operational limits of whirling arm rain erosion tester. The rotational speed of 500-1386 rpm results in a rotation speed range of $42.2 - 173.4 \text{ ms}^{-1}$, dependent on the location of the specimen.	66
Table 4.1 – Comparison of the tensile strain break (<i>STB</i>) of materials used in leading-edge protection systems at 0.5 and 2 mm/min displacement rates.....	72
Table 4.2 – Comparison of the toughness values of materials used in leading-edge protection systems at 0.5 and 2 mm/min displacement rates.....	74
Table 4.3 – Comparison of the tangent modulus (<i>Etan</i>) values of materials used in leading-edge protection systems at 0.5 and 2 mm/min displacement rates.....	76
Table 4.4 – Comparison of the secant modulus (<i>Esec</i>) values of the LEP materials at 0.5 and 2 mm/min displacement rates.....	78
Table 4.5 – Comparison of the ultimate tensile strength (<i>UTS</i>) values of materials used in leading-edge protection systems at 0.5 and 2 mm/min displacement rates.....	79
Table 4.6 – A table summarising which materials demonstrated significantly different properties between 0.5 and 2 mm/min displacement rates. A ✓ indicates a p-value of < 0.05 and was considered statistically significant, and – indicates a p-value > 0.05 and is considered not statistically significant.	81
Table 5.1 – A table detailing the parameters used in Test 1 in a hold-load-unload test method to determine the influence of loading rate.....	91
Table 5.2 – A table detailing the parameters used in Test 2 in a hold-load-unload test method to determine the influence of maximum load while utilising a constant loading rate.....	98
Table 5.3 – A table detailing the parameters used in Test 3 in a hold-load-unload test method to determine the influence of repeated indentation and recovery periods.....	104
Table 5.4 – A table summarising which materials demonstrated significantly different properties between the two loading rates tested in Test 1. A ✓ indicates a P value of < 0.05 and was considered statistically significant, and – indicates a P value > 0.05 and is considered not statistically significant.	108
Table 5.5 – A table summarising which materials demonstrated significantly different properties between the maximum loads in Test 2. A ✓ indicates a P value of < 0.05 and was considered statistically significant, and – indicates a P value > 0.05 and is considered not statistically significant.	110

Table 5.6 – Tabulated average short term recovery (STR) percentage and elastic work percentage measured during a load-hold-unload nanoindentation method (loading time: 5/10/25 seconds, maximum load: 100/200/500 μ N, hold time: 60 seconds, unload time 2 seconds and N=5).	113
Table 6.1 – Tabulated onsets of degradation and mass loss percentages obtained for thermogravimetric analysis under air.	123
Table 6.2 – Summary of the shift factors analysis using the Williams-Landel-Ferry and Arrhenius equations for dual cantilever testing.	134
Table 6.3 – Summary of the shift factors analysis using the Williams-Landel-Ferry and Arrhenius equations for thin-film tensile testing.	144
Table 6.4 – Density of each coating material used in testing.	153
Table 7.1 – Accelerated rain erosion test plan used to compare the erosion performance of each coating system.	161
Table 7.2 – A selection of images taken of rain erosion test specimens displaying the process of erosion at a chosen time. Testing was conducted at 1000 RPM and 55 l/h. Images not to scale.	165
Table 7.3 – A selection of images taken of rain erosion test specimens displaying the process of erosion at a chosen incubation point. T2 and T4 testing was conducted at 1200 RPM and 25 l/h. T6 testing was conducted at 1200 RPM and 70 l/h. Images not to scale.	167
Table 7.4 – Summaries of time to incubation and failure of each coating system under various test conditions.	169
Table 7.5 – A summary of calculated VN curve constants and the respective coefficient of determination (R^2) values for each tested material.	172
Table 7.6 – A summary of the rain erosion test plan following a full factorial design of experiments with three levels and three factors.	175
Table 7.7 – Conversion of the rotational velocities used in the design of experiments test to rain droplet impact velocities.	180
.....	
.....	
Table 7.9 – Tensile test data provided by coating manufacturer for comparison. Tests were conducted at a displacement rate of 100 mm/min, under a pretension of 0.1 N using cast samples of 36 mm x 6 mm x 2 mm (N=2).	185
Table 8.1 – Material input parameters used in average impact pressure and effective material strength calculations.	197
Table 8.2 – Droplet impact input parameters used in average impact pressure and effective material strength calculations.	197
Table 8.3 – A summary of the material parameters and their individual correlation to measured erosion performance. Reliability is reported from calculated R^2 values where values > 0.95 are considered excellent, values below 0.95 and above 0.85 are considered good, and values below 0.85 are considered poor.	200

List of Acronyms

AEP	Annual Energy Production
BLEER	Blade Leading Edge Erosion Research
CDT	Centre For Doctoral Training
OAPEC	Organization Of Arab Petroleum Exporting Countries
G.E.	General Electric
JIP	Joint Industry Project
LCOE	Levelised Cost Of Energy
LEP	Leading Edge Protection
CO ₂	Carbon Dioxide
CCC	Committee On Climate Change
LEE	Leading Edge Erosion
U.K.	United Kingdom
UV	Ultraviolet Radiation
OREC	Offshore Renewable Energy Catapult
WBRH	Wind Blade Research Hub
RET	Rain Erosion Testing
O&M	Operation And Maintenance
AEP	Annual Energy Production
DTV	Damage Threshold Velocity
CFD	Computational Fluid Dynamic
CT	Computerised Tomography
BLEEP	Blade Leading Edge Erosion Programme
GFRP	Glass Fibre Reinforced Polymer
PU	Polyurethane
PUR	Polyurea
HDI	Hexamethylene Diisocyanate
HDA	Hexa-1,6-Diamine
SS	Soft Segment
HS	Hard Segment
TDI	Toluene Diisocyanate
MDI	Methylene Diphenyl Diisocyanate
RP	Recommended Practice
COBRA	Comprehensive Methodology For Blade Rain Erosion Analysis
PEEK	Polyetheretherketone
WARET	Whirling Arm Rain Erosion Tests
UTS	Ultimate Tensile Strength
FEA	Finite Element Analysis
DMTA	Dynamic Mechanical Thermal Analysis
FEM	Finite Element Method
TPU	Thermoplastic Polyurethanes
DETA	Dielectric Thermal Analysis
O&M	Operation And Maintenance
CF	Carbon Fibre
PEA	Poly(Ethylene Adipate Glycol)

PTHF	Polytetrahydrofuran
BDO	Butylene Glycol
DAPO	2,5-Bis(4-Amino-Phenylene)-1,3,4-Oxadiazole
PMMA	Poly Methyl Methacrylate
LDPE	Low-Density Polyethylene
UHMWPE	Ultra-High-Molecular-Weight Polyethylene
PC	Polycarbonate
CNC	Computer Numerical Controlled
DFT	Dry Film Thickness
WFT	Wet Film Thickness
RT	Room Temperature
TGA	Thermogravimetric Analysis
LVER	Linear Viscoelastic Region
STR	Short Term Recovery
RPM	Revolutions Per Minute
DOE	Design Of Experiments
FS	Fused Silica
OP	Oliver Pharr
QS	Quasi Static
DC	Dual Cantilever
TF	Thin Film
LVER	Linear Viscoelastic Region
TTS	Time Temperature Superposition
WLF	Williams-Landel-Ferry
UNDT	Ultrasonic Non-Destructive Acoustic Testing

List of Symbols

T_g	Glass Transition Temperature
M_w	Molecular Weight
P_T	Amount Of Energy Captured
ρ	Density
A	Swept Turbine Area
U	Volume Flux
C_p	Power Coefficient
P	Water Hammer Pressure
C	Speed Of Sound
V	Velocity
Z	Acoustic Impedance
θ	Impingement Angle
E	Young's Modulus
σ	Stress
S	Material Strength
d	Droplet Diameter
ν	Poisson's' Ratio
σ_{uts}	Ultimate Tensile Strength
b	Fatigue Constant
h	Thickness
ε	Strain
t	Time
E'	Storage Modulus
E''	Loss Modulus
$\tan \delta$	Damping Factor
δ	Phase Angle
H	Hardness
P_{max}	Maximum Indentation Load
A_c	Projected Contact Area Of Indentation
S_u	Unloading Stiffness
P_{Indent}	Applied Indentation Load
h_{indent}	Indenter Penetration Depth
E_r	Reduced Elastic Modulus
β	Berkovich Indenter Head Constant
W	Apparent Work
ε_c	Critical Strain
σ_c	Yield Stress
α	Frequency-Temperature Shift Factor
f	Frequency
T	Temperature
E_A	Activation Energy
R^2	Coefficient Of Determination
φ	Specific Damping Capacity
C_l	Longitudinal Speed Of Sound
C_{DMTA}	Speed of Sound Predicted Through DMTA

1

Introduction

This thesis is the culmination of work completed by the author over four years at the University of Bristol. This introductory chapter provides background, motivations, and an overview of the work presented in the following chapters, which serves to help the reader frame the work presented in later chapters.

1.1 Research Context

The now widely accepted problem of climate change refers to long-term shifts in temperatures and weather conditions in an area over an extended period. It is critical in influencing ecosystems and the groups of people who live in or depend on them. Historical fluctuations in global temperatures are well documented and show that the Earth's climate has repeatedly experienced periods of extreme temperatures [1–5]. However, the current trend shows a rapid and continued increase in the Earth's average temperature, unlike any past warming event. This change is attributed to the rapid expansion in human industrial activity, resulting in severe consequences [6]. These include the declining arctic sea ice, a rise in sea level, and an increase in the number of extreme weather events [7–9]. The scale and urgency of the issue was highlighted by Barack Obama in a poignant statement in 2014 at the United Nation Headquarters, in which he said [10]:

"We are the first generation to feel the effect of climate change and the last generation who can do something about it."

Atmospheric carbon dioxide (CO₂) is a significant contributor to the greenhouse effect, a process where gases accumulate in the atmosphere. This phenomenon increases the amount of heat radiated back to the surface, raising the average temperature of the planet [11]. Historically, levels in the atmosphere have increased by 50 % from 278 ppm (in the pre-industrial era *circa* 1800) to 417 ppm (in 2021) and are currently predicted to further increase by 2 ppm each year [12]. As atmospheric CO₂ is a critical factor in global warming, numerous regulations have been implemented; with additional revisions and regulations planned for the future aiming to minimise emissions and to slow the rapid increase [13].

In response to the climate crisis, *The Paris Agreement* was proposed and adopted by almost every nation. Many deemed it the most critical and defining moment in the global pursuit of preventing irreparable damage being inflicted on our planet [14]. This agreement set out a global framework intending to decrease global greenhouse gas emissions and reduce the global temperature increase to well below 2 °C when compared to pre-industrial levels. The Committee on Climate Change (CCC), the U.K.'s independent advisor on tackling climate change, identifies several effects of limiting global warming to 2 °C [14]:

- The risk of extreme weather events is significantly reduced. An example is the reduction of average global drought lengths from 18 months to 11 months compared to a global temperature increase of 3 °C.

- Significant changes to ecosystems will still occur with an increase of 2 °C, but this impact will be lessened. The global extinction risk level will be reduced from 'high' to 'moderate' compared to a 4 °C increase. However, many species will still not adapt or migrate to suitable regions within the timeframe.
- The detrimental impact of floods and reduced crop yields will be reduced but not completely prevented.
- More specifically, benefits will be seen in the U.K. through reductions in water stress, flooding, coastal erosions, and summer-time heat.
- The probability of an ice-free arctic summer, where no sea-ice would be in the Arctic, would be reduced from 50 % to 10 %. The presence of sea ice is critical for arctic ecosystems and is linked to the weather patterns worldwide. However, even with limiting warming to 1.5 °C, irreversible changes to marine ice stability in Antarctica and Greenland are still possible.

In order to combat rising temperatures, the *Climate Change Act 2008* is an act of the U.K. parliament, which identified six major greenhouse gases, of which CO₂ was the most significant contributor [15]. It is primarily produced from burning fossil fuels in power production such as coal and gas, with other contributors including industrial processes and waste management [16]. Together these two groups accounted for 19 % of the U.K.'s emissions in 2018 and are recognised as critical areas for improvement.

In June 2019, the U.K. parliament passed further legislation requiring the government to reduce the net emissions of greenhouse gases to levels 100 % lower relative to 1990 by 2050 [17]. By achieving this goal, the U.K. would become a net-zero emitter, meaning the amount of greenhouse gas emissions produced would balance the amount removed from the atmosphere. A net-zero target was selected as it is not feasible in such a short timeframe to achieve a gross-zero target where no emissions are produced. Instead, emissions will be reduced and offset through carbon sinks such as oceans and forests, with potential for nascent technologies such as carbon capture and storage to directly remove carbon dioxide before it reaches the atmosphere [18].

The U.K. has made progress, as greenhouse gas emissions have consistently fallen for the past 30 years in contrast to the increasing global levels [14]. However, current reports suggest that the U.K. is not on track to meet its target by 2050 and, as a result, requires rapid and long-term policy changes across multiple sectors [15]. The passing of legislation imposes a legal obligation on the U.K. government to achieve these targets. This approach has come under criticism as it is unclear how it will be enforced on such a wide-reaching and complex problem. However, this legislation has been

influential in subsequent policy decisions, with a high-profile example being the ruling that the government's stance on the Heathrow airport expansion was unlawful [19]. The decision was attributable to a lack of consideration of its impact on climate change and the absence of mitigation strategies to offset its effects. An example of a mitigation strategy that can be implemented is carbon offsetting [20]. Although it is best to remove all harmful greenhouse gases, it is not viable in many cases to do so with current technology [21]. Carbon offsetting provides businesses with a method of transitioning by neutralising any emissions generated from their activities by purchasing carbons credits generated by projects cleaning the atmosphere to compensate for the emissions. However, the effectiveness of this scheme has come into question as it could allow for more CO₂ to be produced as companies can offset their emissions, albeit at a cost [22]. Additionally, there are concerns around how long the projects funded by this scheme will operate, meaning that instead of mitigating emissions, they are just being delayed.

In October 2014, the European Council agreed targets relating to greenhouse gas reduction, focusing on developments in renewable energy. These targets legally bind the member states to reduce greenhouse emissions by 40 % (compared to 1990 levels), achieve 27 % energy consumption from renewable sources and improve energy efficiency to at least 27 % (from 17 % in 2018) by 2030 [23–25]. More recently (December 2018), the *Renewables Energy Directive (2018/2001)* has been introduced, increasing the renewable energy target for the E.U. by at least 32 % with a clause for a possible upward revision in 2023 [26]. This EU legislation has been retained in UK law as a form of domestic legislation known as retained EU legislation [27]. Several exemplar countries, such as Sweden, already meet over 50 % of energy demand with renewables [28]. Conversely, countries such as the Netherlands have one of the lowest proportions of renewable energy at approximately 7 %.

1.1.1 Renewable Energy Trends

Renewable energy sources play a vital part in the global and domestic efforts in combating climate change and remaining below emission targets [29]. This fact is of particular importance as it is predicted that the total electricity demand will increase at an unprecedented rate because of the electrification of heating and methods of transport [30]. During this same period, additional electricity supply will also be required to replace decommissioned coal and nuclear power stations [31, 32]. Current published data summarised in Table 1.1 show that non-renewable fuel sources are still the most prevalent energy source globally [33]. However, the E.U. and U.K. show a much lower percentage of non-renewable derived electricity compared to worldwide data where the uptake of renewable energy sources is not as fast.

Table 1.1 – Worldwide and E.U. electricity generation fuel source distribution displayed in exajoules (E.J.) created using the B.P. statistical review of world energy 2021 [33].

Energy Type	World (EJ)	World (%)	Europe (EJ)	Europe (%)	UK (EJ)	UK (%)
Oil	173.7	31.2	26.1	33.8	2.4	34.6
Natural gas	137.6	24.7	19.5	25.2	2.6	37.9
Coal	151.4	27.2	9.4	12.2	0.2	2.8
Nuclear	24.0	4.3	7.4	9.6	0.4	6.5
Hydro	38.2	6.9	5.8	7.5	0.1	0.8
Renewables	31.7	5.7	8.9	11.6	1.2	17.4
Annual Total	556.6		77.1		6.9	

The combined change in legislation and focus on renewable energy development can be seen in the growth of renewable sources such as wind energy. The area has seen rapid and significant development in the past ten years, resulting in 17 % of the U.K.'s energy being generated directly from wind in 2018 [29]. This growth can be attributed to technological improvements in key areas of wind turbine design, manufacturing, and operation [18, 29, 34]. Examples are increases in turbine size, lower costs for financing (due to the sector maturity and government support), and the use of more efficient construction and maintenance operations that have resulted in reduced costs. These developments, coupled with government subsidies, have facilitated the area's growth, resulting in the U.K. possessing the largest offshore wind capacity in the world [29].

A historic graph displaying the global renewable energy consumption over time is shown in Figure 1.1. It compares the uptake of each renewable energy source and demonstrates an increasing trend over the last twenty years in most sources apart from nuclear. In particular, wind energy has shown the most rapid growth due to increased global wind capacity. This trend is expected to continue to rise as not only does the shift towards renewables have clear environmental benefits, but it also allows nations to mitigate the volatility of the energy market, providing long term economic security [33].

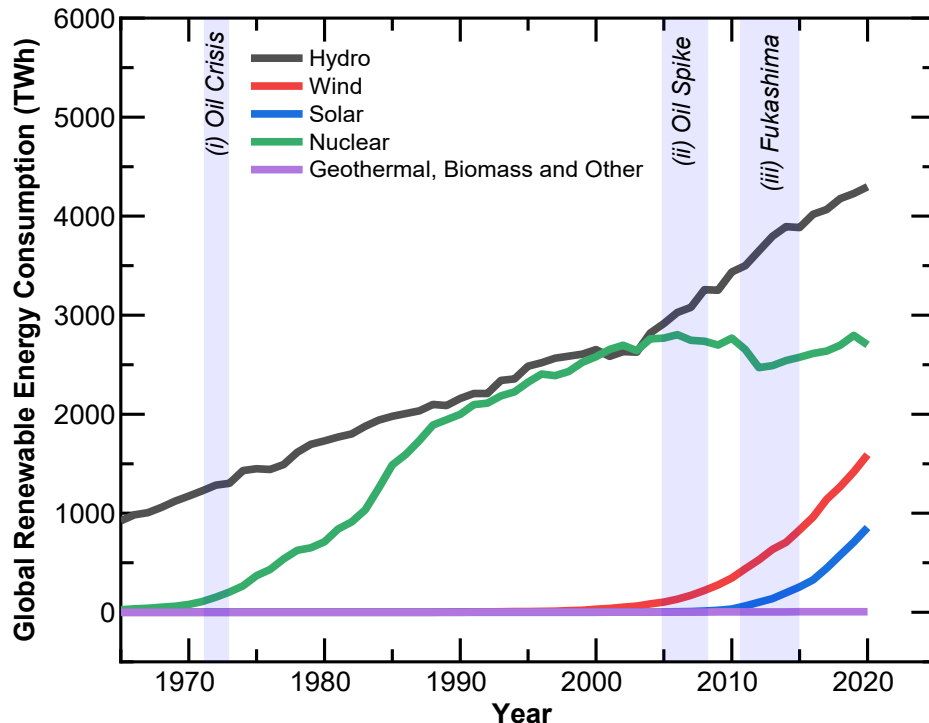


Figure 1.1 – Historical global renewable energy consumption adapted from B.P. statistical review of world energy 2021 [33]. Three regions are highlighted, identifying key events that influenced the historical landscape. i) 1973 Oil crisis, ii) Mid-2000 oil Spike, and iii) Fukushima Daiichi nuclear disaster.

Figure 1.1 highlights three critical events that influenced the energy landscape, which include:

- i) In 1973 the Organization of Arab Petroleum Exporting Countries (OAPEC) declared an oil embargo targeted at nations supporting Israel [35]. The embargo, which ended in 1974, resulted in oil prices rising 300 % in just one year. The effects of this on the global economy were felt throughout the 1970s. This volatility led to greater interest in renewable energy sources such as nuclear power and domestic fossil fuels resulting in policy changes and increased development over the following years.
- ii) In the mid-2000s, the oil price varied significantly, causing significant economic uncertainty [36]. Oil prices rapidly rose during this time due to a combination of geopolitical events and natural disasters (such as Hurricane Katrina); however, by 2008, a global recession resulted in decreased demand for energy causing oil prices to drop by 80 % within 6 months.
- iii) In 2011 the Fukushima Daiichi nuclear disaster resulted in the closure of most nuclear power plants in Japan [37]. This event damaged public confidence in nuclear power, and as a result, policy changes were implemented to phase out the majority of nuclear power stations. These changes led to a loss of 30 % of the country's energy-generating capacity and led to much greater reliance on liquefied gas and coal.

1.1.2 Current Wind Energy Market

Generating power from renewable sources, particularly wind energy, is critical in the U.K.'s plan to achieve net-zero. Figure 1.2 shows the historic growth of wind energy in Europe, demonstrating a clear upward trend in cumulative installed capacity [38]. The U.K. has vast potential to develop its offshore wind capacity, reflected in the consistent increases in the number of installations. This cumulative installed capacity is further increased due to replacing older turbines with higher capacity turbines or retrofitting them with more efficient components, significantly increasing wind farm production and extending wind farm life.

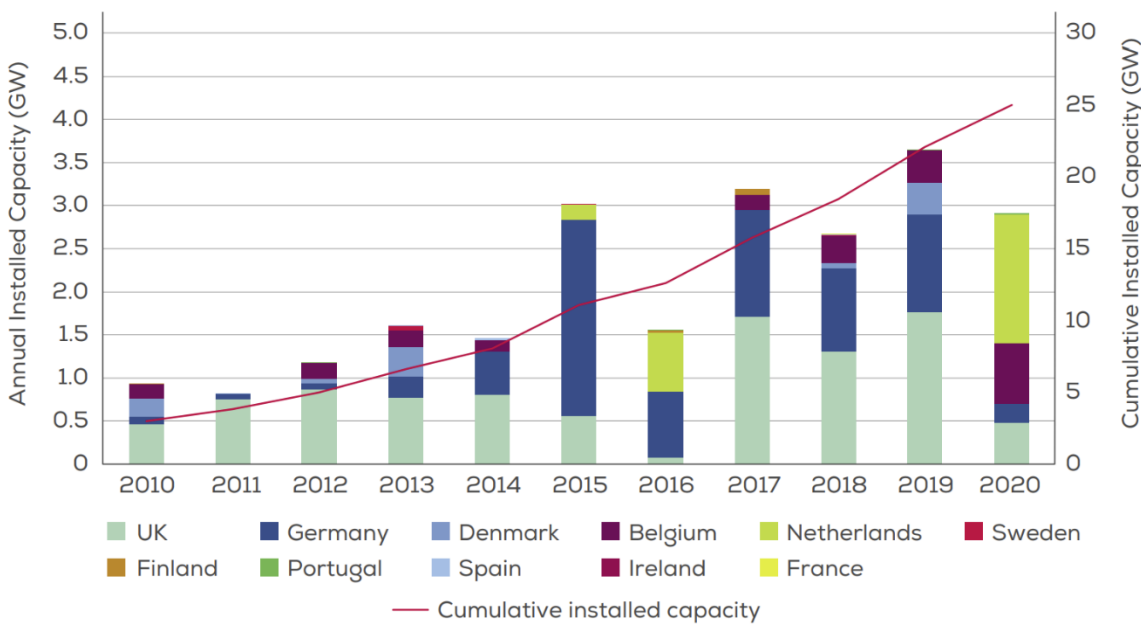


Figure 1.2 – Annual offshore wind installations (left axis) and cumulative capacity (right axis). The figure is taken directly from Offshore wind in Europe key trends and statistics [38].

The U.K. is in the process of building the world's largest offshore wind farm Dogger Bank, located more than 130 km off the northeast coast of England [39]. General Electric (G.E.) is confirmed to be supplying the 13 MW Haliade X and, for the final phase, upscaled 14 M.W. versions. These turbines feature 220-meter rotor diameters comprising 107-metre-long blades and are expected to have lifetimes of 35 years. It is expected that when installed, a single revolution of the 13 M.W. turbine rotor will produce enough electricity to power a home for two days. Upon completion of all the phases in 2026, it will produce 3.6 GW of electricity, enough for 5 million U.K. homes, or about 5 % of the U.K.'s predicted energy demand [40].

There are clear benefits to the uptake of renewable energy; however, the most significant barrier to the use of renewables has always been cost [41]. Energy is often compared solely on its cost per unit, and demand will always gravitate towards the cheapest option regardless of any other

benefits such as CO₂ reduction. The initial capital costs required for some renewable energy sources are considerably higher than other non-renewable methods, *e.g.*, installing a wind farm compared to mining coal. On the other hand, the operation and maintenance costs (O&M) are comparably minimal, with no need for fuel. As a result of these higher initial costs, financial institutions perceive renewables as riskier leading to higher rates and discouraging investors [18]. To overcome this, governments put subsidies to minimise the disparity between prices and allow for improvement in the technology and reduction in costs that occur upon scale-up of energy production. In the UK, this is the *Contracts for Difference Scheme* and is the government's primary mechanism for supporting low-carbon energy electricity generation [42]. Ideally, this would continue for a fixed time until the technology is mature enough to be competitive with other sources when the subsidy is removed.

Different sources can be compared in electrical energy production using the Levelised Cost Of Energy (LCOE). This metric considers a plant's economic life, including construction, operation, maintenance, and fuel costs. The cost of generating electricity from large wind farms dropped by more than 50 % between 2015 and 2017 due to technological advances and price reductions due to the increasing scale of wind farms [29]. Table 1.2 shows predictions for LCOEs for projects starting in 2025. It shows a consistent predicted decrease in the cost of offshore wind with a possibility of it becoming cheaper than onshore wind by as early as 2025. However, it should be noted that these are simplified estimations that are conservative for some technologies, especially renewable sources. The calculations do not consider any technological advances or cost reductions that may change the predictions. Conversely, the estimations assume the increased repair costs associated with increasing tip speed and blade diameters.

Table 1.2 – Levelised Cost Estimates for projects commissioned in the U.K. reproduced using data from the literature [43].

		Year of Commissioning			
		2025	2030	2035	2040
Offshore Wind (£/MWh)	High	63	53	48	44
	Central	57	47	43	40
	Low	51	43	39	36
Onshore (£/MWh)	High	52	51	50	50
	Central	46	45	44	44
	Low	39	39	38	38

1.1.3 Brief History and Current State of Wind energy

Windmills have been utilised to extract energy from natural sources as far back as 2000 years ago by the Persians and Chinese for primarily agricultural purposes, e.g., moving water or grinding corn [18]. In the early 19th century, little research was conducted in the field and machines were developed to produce small (32 V) direct currents in rural America to power small appliances. The first large wind machine used to generate electricity was installed in Cleveland, Ohio, in 1888 by Charles F. Brush [44]. The abundance of non-renewable fuels and lack of emission controls meant that there were no economic or societal drivers to develop alternative technologies for electricity generation present at the time. However, the spike in oil prices in 1973 spurred interest in the field of wind energy in addition to increased funding from government bodies [44, 45].

Further work on wind generators was conducted in the USA, reinforced by the knowledge gained in the aerospace field designing aeroplane propellers and monoplanes. The oldest designs of wind rotors utilised a vertical axis of rotation and initially only utilised pure drag-type rotors, examples of which are shown in Figure 1.3 [46]. An example of this is the Savonius rotor found in ventilators on rail carriages, on top of delivery vehicles and as cup anemometers used to measure wind velocity. In the last century, vertical axis designs utilised aerodynamic lift, with designs such as the Darrius rotor being trialled. The benefits of the vertical axis rotors are their simplicity, ability to capture wind without considering wind direction and the possibility of housing all the turbine components at ground level [18, 46]. On the other hand, vertical axis rotors have low tip speed ratios, cannot self-start, and cannot control speed/power output by pitching its blades.

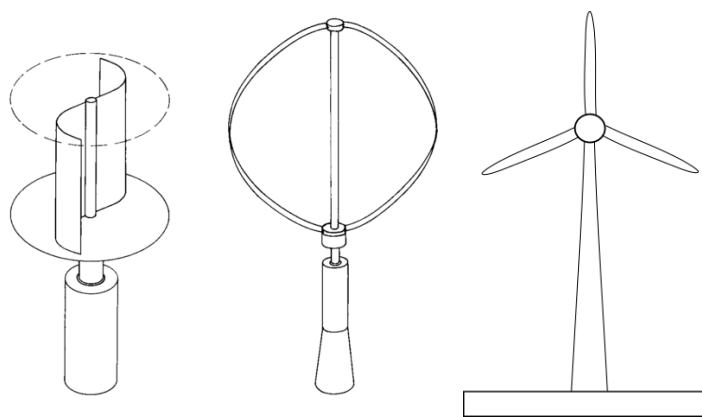


Figure 1.3 – a: Savonius rotor (left), b) Darrius vertical axis rotor (centre) c) horizontal axis rotor (right). Part a and b were directly reprinted with permission from Springer Nature [46]. Images are not to scale.

Horizontal axis rotors are based upon the concept of propellers used in maritime transport. They have the inherent benefits of controlling power/speed output by pitching blades about their longitudinal axis allowing for protection against extreme wind speed where the speed can be limited or stopped altogether. Additionally, the remarkable advances made in aviation during the previous

world wars have shown that the rotor blades can be optimised to achieve high efficiencies, and because of these factors, most turbines to date have been the horizontal axis rotors type [18, 47].

More recently, certain countries have begun to face a shortage of suitable inland locations due to financially viable sites becoming less abundant [48]. This issue has presented opportunities for large offshore wind farms made up of many turbines. This move towards offshore locations allows them to have access to faster and steadier windspeeds, overcome the size/noise constraints that limit their use inland, and justify the extra costs required to construct and connect these farms to the grid. Currently, wind-powered generators operate in numerous size ranges used in small battery charging up to gigawatt offshore wind farms supply energy directly to the national grid. More recently, developments in floating turbine technology have allowed for trials of 'floating' turbines to exploit previously untapped locations in deeper waters [49].

1.1.4 Wind Turbine Design and Composition

The technology of wind turbines draws from multiple disciplines ranging from aerodynamics and mechanics used in blade design to the chemistry involved in material selection and coating design [18]. Turbines themselves have progressed from fixed speed to actively controlled types, which require additional technologies such as electrical design and control systems. Horizontal wind turbines, an example of which is given in Figure 1.4, generally consist of three main parts [50]:

- A rotor with wing-shaped blades attached to a central hub captures power from the wind and converts it to kinetic mechanical power.
- The nacelle houses the drivetrain, a group of components that transmits mechanical power from rotors to the generator. This element comprises a gearbox that converts the rotor's slow-moving and high torque to the generator's fast rotation. In addition to this, a generator is installed to convert mechanical power to electrical power and other machinery involved in controlling the turbine (*e.g.*, those used in active control mechanisms).
- The tower contains any related ground-mounted equipment, such as connections to the external electrical grid.

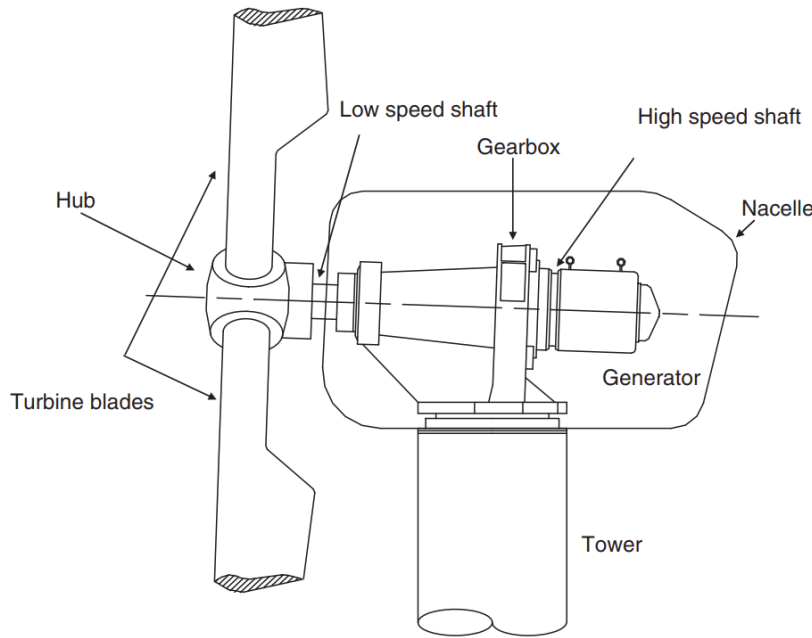


Figure 1.4 – Simplified diagram of a wind turbine detailing the main components. Reprinted from the literature with permission from Elsevier [51].

Key design parameters such as a turbine height and rotor diameter determine how much power an individual turbine can produce [18]. This relationship is demonstrated by

$$P_T = \frac{1}{2} \cdot \rho \cdot A \cdot U^3 \cdot C_p \quad 1.1$$

where P_T is the amount of energy captured, ρ is the air density, A is the swept turbine area, U is the volume flux and C_p is the power coefficient (efficiency of power extract from the total power of wind resource).

Wind turbine efficiency is theoretically limited to a maximum extractable power fraction known as the Betz limit (59.3 %) [18]. Higher efficiency is not possible due to the fluid mechanical nature of wind power and the requirement of the sustained flow of wind through the mechanism. Additionally, although its power capacity increases to the square of the rotor diameter, its volume and mass (using traditional metrics) also scale to the third power of rotor diameter, which historically limited the size of the blades [52]. However, innovations in design and manufacturing, such as the use of composite materials, have enabled manufacturers to create more efficient turbines with less material. Moreover, the increase in capital costs of producing larger turbines is not proportional due to the benefits of economies of scale. Fewer turbines of higher capacity should result in lower costs of foundations, electrical infrastructure, and installation. This approach has resulted in an upward trend in turbine size, especially in the offshore environment where fewer restrictions are present. Historical examples of this are presented in Table 1.3, with the current largest being the 14 MW

Haliade-X [53, 54]. The size of turbines is still predicted to increase in the future; however, priorities may change from maximising energy production to ensuring blades are recyclable. This may result in turbine blade growth plateauing and driving into developing improvements in wind farm site selection and optimisation.

Table 1.3 – Historical trend in larger wind turbines from 1995 to 2015. Adapted from literature [18, 54].

	Year						
	1985	1990	1995	2000	2005	2015	2019 (Haliade-X 12 MW)
Rated Power (kW)	80	250	6000	1500	3000	7000	12000
Rotor Diameter (m)	20	30	46	70	90	130	220
Rotor Sweep (m ²)	314	707	1662	3848	6362	13273	38000
Hub Height (m)	40	50	78	100	105	150	150
Annual Energy production (MW h)	95	400	1250	3500	6900	15000	67000

1.1.5 Wind Turbine Operating Environment

Wind turbines blades experience numerous environmental conditions during their service life, and these can vary significantly due to location [18, 55]. Offshore turbines are inherently more exposed to hostile conditions due to being at sea and experiencing much greater rotational speeds and loads when compared to those installed inland [56]. Figure 1.5 summarises the most commonly reported component damage for offshore wind turbines and identifies the gearbox, blades, and electrical system are vulnerable areas susceptible to failures.

Several of the most significant contributors to blade damage are summarised below [18]:

- Extreme gusts and turbulence – due to the nature of wind turbines, they are usually deployed in exposed areas and, as a result, are exposed to strong winds that can cause damage to the turbine.
- Sunlight and temperature extremes – turbines in all locations will be exposed to Ultraviolet Radiation (UV) in sunlight and can accelerate degradation. Additionally, temperature variations differ from site to site in terms of duration and intensity.
- Ice – climates exposed to freezing temperatures commonly experience icing and is problematic to the safe and efficient operation of wind turbine blades resulting in reduced performance.
- Particulates – a consideration for most turbines are particulates that can cause severe erosion and or accumulation on the blade. The severity is highly dependent on where the turbine is situated. In desert or coastal environments, sand impingement may be an issue, whereas

onshore locations, wildlife and insects can contact the blades, causing damage or accumulation of debris.

- Sea-spray – for offshore turbines, blades contact with sea spray can cause impingement damage akin to rain erosion in addition to the formation of salt crystals on the blade surface.
- Lightning – due to turbines' height and composition, they are susceptible to lightning strike damage. Incidents such as these can impair the control/electronic systems and destroy the blades due to increased temperature due to explosive expansion.
- Rain and hail – turbines experience varying levels of rain/hail impingement dependent on the location and weather conditions in which they operate. The prevalence of these events causing damage has been highlighted in a white paper published by the Electric Power Research Institute [57]. The paper reported findings of a survey to capture the current industry practices related to damage and defect characterisation. The work identified that the categorisation of defects and the resulting maintenance programs vary significantly between operators. The majority deemed characterisation and repair of erosion a significant challenge to turbine management.

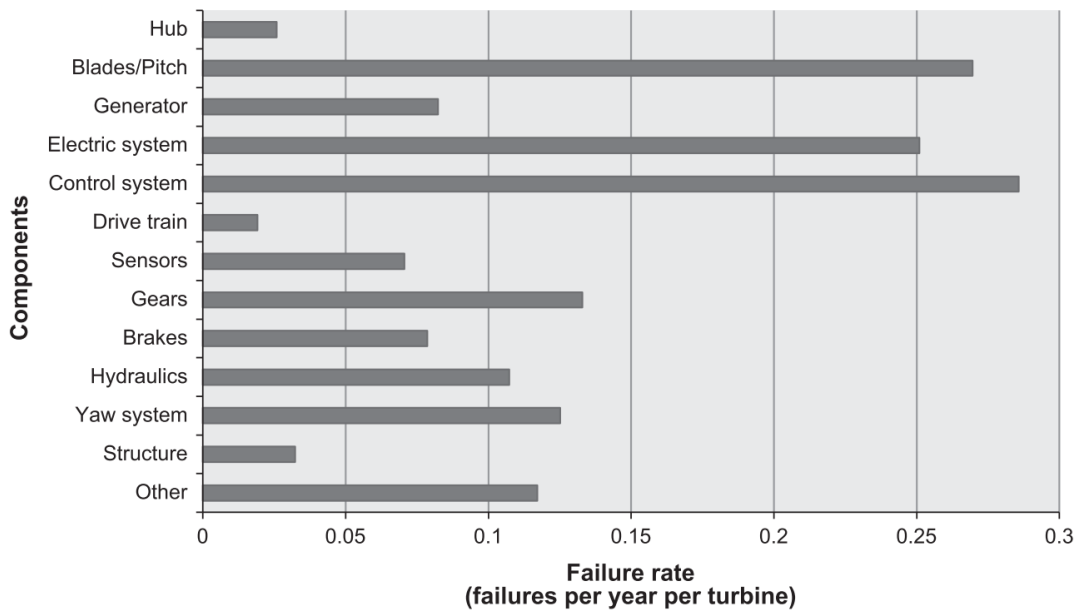


Figure 1.5 – Average failure rate of each turbine component showing the control system has the highest value followed by blades/pitch. Reprinted directly from literature with permission from Elsevier [58].

1.2 Problem Statement

Offshore wind turbine blades are expected to remain in operation with minimal maintenance for a service life of 35-years in the field (the target for maintenance-free operation) but are currently requiring significant repairs within just a few years into their service [34, 59, 60]. Currently, up to £1.3 million is estimated to be presently spent on each turbine during its lifetime, with the majority of this cost coming from additional unexpected repairs and lost power production due to Leading Edge Erosion (LEE) [34, 61, 62].

One of the current industrial solutions implemented by wind farm operators to minimise blade damage is to limit blade tip speeds to approximately 100 m/s from the start of service [34, 63, 64]. However, this is contrary to current design and application trends, where greater blade lengths or tip speeds can be more favourable for energy production. The use of a reduced tip speed is reported to require heavier and more expensive gearboxes, increasing the LCOE of the turbine [18, 34]. This increase of the LCOE is seen as detrimental to the potential uptake of wind turbine technology as a source of clean and renewable energy, and therefore this approach is undesirable [18].

In combination with limiting the speed of turbine blades, Leading Edge Protection (LEP) solutions, such as coatings and tapes, are routinely implemented to minimise LEE effects. However, current commercially available solutions for offshore wind turbines typically require repair or replacement prematurely into the desired lifetime of the blade [34, 65]. LEE presents itself as a progressive and destructive loss of material caused by the impact of rain, hail, dust, and other airborne particulates. Offshore turbines are particularly affected by rain droplet impacts, which, when coupled with high tip speeds, result in complex and damaging interactions that are further discussed Chapter 2. When combined with the probable harsh environmental conditions seen offshore, which include exposure to UV radiation and high salinity levels, it leads to a rough outer profile, an example of which is shown in Figure 1.6. Damage appears to mainly initiate near the blade's tip on the leading edge, where the rotational speed is at the highest. After initiation, the damage rapidly progresses through the thickness of the coating, and in extreme cases, can eventually cause structural damage to the composite substrate. Over time these areas of damage also progress down the length of the blade towards the root. These areas can combine with other damaged sites, further accelerating the damage propagation due to areas left unprotected by the loss of LEP coating.



Figure 1.6 – Drone photography photo of an eroded leading edge seen on wind turbine blades in China. These images were kindly provided by Dennis Lin from Jotun.

Even though the current LEPs do not last the entire expected lifetime, they still can protect for several years depending on their location (offshore/onshore) and the environmental conditions the turbine experiences [60]. As a result, it is not feasible to always use *in-situ* testing to evaluate the material's performance, especially in the case of offshore turbines, due to the time and costs required. Instead, accelerated testing methods, such as whirling arm testing rigs, are used to evaluate and compare the performance of LEPs in development. While this method can show differences in performance under controlled test conditions, these results do not always accurately match *in-situ* performance, an issue that has become more prevalent in modern LEPs. These observations agree with Dyer *et al.*, who point out that good test performance does not always correlate to good in-service performance [66]. This difference in LEP performance has been attributed to a lack of understanding of the environmental conditions blades experience and the ability to measure the correct material properties required to predict lifetime. In particular, literature has identified that modern LEPs are inherently more viscoelastic than those used historically [34, 53, 60, 67, 68]. As a result, they can elastically dissipate impact energy and recover deformations over time. Whilst these materials show improved performance, their viscoelastic nature makes characterising them more difficult due to the dependence on temperature and strain rate caused by rain droplet impacts reported in the region of $10^6 - 10^9 \text{ s}^{-1}$ [67]. These phenomena are not captured by current lifetime prediction models and are not generally used as design criteria for the development of coatings due to a lack of understanding of their importance.

The Offshore Renewable Energy Catapult (OREC), the UK's leading innovation and research centre for offshore renewable energy, were challenged by industry to tackle the question of how

viscoelastic materials properties of modern coatings were influencing erosion performance. Through the Wind Blade Research Hub (WBRH) at the University of Bristol, in which I was situated, OREC consequently tasked this PhD project with developing a more fundamental understanding of modern LEP systems. State-of-the-art commercial rain erosion test facilities at OREC were utilised for material characterisation, whilst up-to-date coating materials were made available from material suppliers through their participation on the Blade Leading Edge Erosion Research (BLEER) Joint Industry Project (JIP). BLEER aimed to correlate coating properties to rain erosion degradation, facilitating the use of commercial LEP coating systems and industry expertise throughout the project.

Thus, this project evaluated modern leading edge materials and their influence on accelerated testing and lifetime prediction, particularly considering their relevance and limitations when applied to viscoelastic materials. It provided a more fundamental understanding of current materials used in LEP systems, providing a framework for future testing that can capture the temperature and time-scale dependent properties of materials used in LEP solutions. The work spanned multiple levels of the conventional testing pyramid, ranging from coupon level to component level. This building-block approach provides a systematic methodology in determining the effects at each level. At the lower coupon level, fundamental material properties can be identified and be used to define the requirements and design allowables necessary at higher length scales and component complexity. It is possible at this scale because materials can be tested using robust methods to control and systematically change variables of interest. The knowledge gained at the coupon level can inform component-level testing, which in this case, is accelerated Rain Erosion Testing (RET). As at this scale, it is not possible to control and measure all parameters therefore it is difficult to understand complex erosion behaviour. From these lower levels, conclusions can be made to explain why and how the full structure level, in this case, an in-service blade erosion performance, is influenced by viscoelastic coatings.

As a result, the knowledge gained can be rapidly correlated and deployed, offering a greater understanding of the implications of viscoelasticity on LEE and so:

- A step towards developing standardised test methodologies that can be used to compare and quantify relevant viscoelastic effects coatings erosion behaviour irrespective of material composition.
- Current lifetime prediction models can be improved to account for these phenomena resulting in improved accuracy. With this development, lifetime prediction can directly improve Operation and Maintenance (O&M) strategies reducing the need for in-situ inspection.

- Contributing to eliminating the issue of LEE and making wind energy a more feasible option to phase out non-renewable energy sources.

1.3 Research Question

As a result of the problem statement discussed in Section 1.2, which desires an improved understanding of modern viscoelastic coatings used for LEPs to resist LEE in the offshore environment, the fundamental research question this thesis seeks to answer is:

The following aims and objectives have been defined:

What are the key physicochemical properties of modern viscoelastic materials that are affecting their performance as leading edge protection systems, and how can their characterisation be improved?

To answer this research question, the following aims and objectives have been defined:

Aim 1 – Detailing the state of the art in the understanding of LEE

- Objective 1.1 – Conduct a review of academic literature surrounding material characterisation.
- Objective 1.2 – Conduct a review of the industrial literature surrounding modern coatings.
- Objective 1.3 – Summarise the literature and identify gaps and directions for further research.

Aim 2 – Material and Method Development

- Objective 2.1 – Determine the relevant commercial materials for use in the project.
- Objective 2.2 – Understand current testing methods used for modern viscoelastic coatings.
- Objective 2.3 – Development of a multi-method/step characterisation methodology.

Aim 3 – Coupon Level Testing

- Objective 3.1 – Individually characterise the different materials used in coating solutions.
- Objective 3.2 – Capture the strain-rate dependent behaviour of each coating material.
- Objective 3.3 – Capture the temperature-dependent behaviour of each coating material.
- Objective 3.4 – Utilise non-destructive ultrasonic testing to characterise each coating material.
- Objective 3.5 – Determine the implications for the coupon level testing on erosion performance.

Aim 4 – Component Level Understanding

- Objective 4.1 – Characterise the coating systems under larger-scale test conditions.
- Objective 4.2 – Optimise rain erosion test methodology to improve the amount of data gathered for testing.
- Objective 4.3 – Determine coupon level testing effect on VE and rain erosion performance.

Aim 5 – Modelling and New Design Understanding

- Objective 5.1 - Use knowledge gained from component level studies to comment on full structure in-service erosion performance.
- Objective 5.2 – Identify and discuss how knowledge gained from this work can be applied to in-service conditions.

1.4 Thesis Outline

The work presented in the thesis is divided into nine distinct chapters:

Chapter 2 provides an up-to-date review of the literature surrounding leading-edge erosion of offshore wind turbine blades, focusing on material characterisation. As a result of this review, it can be concluded that while it is now accepted that modern viscoelastic materials provide improved protection, there is a lack of fundamental understanding as to how different impacts and environmental conditions influence performance.

Chapter 3 summarises the materials testing approaches used throughout the work. Each method used in the work is discussed, identifying the significance, a brief overview of the theory, details of the instrument used, and the test parameters used.

Chapter 4 presents the tensile testing results of thin-film specimens at two different displacement rates to identify the presence of strain rate dependent behaviour. While not all materials showed strain-rate dependency, fundamental material properties such as strain to break, toughness, Young's modulus and ultimate tensile strength were captured and compared.

Chapter 5 presents the nanoindentation results of several coating materials analysed using the Oliver-Pharr method. The effects of loading rate, maximum load, repeated indentation, and recovery periods were captured and compared for each material.

Chapter 6 presents the results from the characterisation of each coating material using DMTA with strain rate and temperature dependent behaviour observed in all materials. The time-temperature superposition principle was also used to predict material behaviour at strain rates outside the working range of the instrument.

Chapter 7 presents the accelerated rain erosion testing results of each coating system using a commercial rain erosion test rig situated at the Offshore Renewable Energy Catapult. A standard and novel design of experiments approach were utilised to quantify and compare each system's erosion performance. Further trials of a novel thin film testing methodology are also presented that captures the change in material properties by using accelerated thin film testing combined with dynamic mechanical thermal analysis.

Chapter 8 compares the measured material properties from Chapters 4, 5 and 6 to the accelerated rain erosion testing results from Chapter 7. Correlations between individual parameters were observed, and the multilayer system-level implications were discussed.

Chapter 9 details the key findings from this thesis and relates them proposed research question defined in Chapter 1. The research contributions to academia and industry are highlighted by identifying key areas of future work that the author suggests should be conducted to close final research gaps and further advance the understanding of LEE.

2

Literature Review

This chapter provides an up-to-date review of the literature surrounding leading-edge erosion of offshore wind turbine blades, focusing on material characterisation. As a result of this review, it can be concluded that while it is now accepted that modern viscoelastic materials provide improved protection, there is a lack of fundamental understanding as to how different impact and environmental conditions influence performance.

2.1 The Problem of Leading-Edge Erosion

Erosion of materials due to impact has been a research topic in the aerospace industry for many years, with Gohardani publishing a comprehensive review of the history in the area [69]. As a result, advancements have affected many aircraft, missiles, and unmanned aerial vehicles material selection and design. However, the same erosion issues caused by the solid and liquid impact is still prevalent in the wind industry despite being considered predictable and preventable in modern commercial and military aircraft lifetimes [69]. Work by Katsaprakakis *et al.* recognises that wind turbines are susceptible to a wide range of damage mechanisms which include: LEE, lightning strikes, fatigue loads and ice accumulation. The author also reviews the impact of each of these damage types identifying the current techniques proposed to prevent these failures [70]. However, LEE remains one of the most common and problematic issues in modern turbines. This finding is supported by Mishnaevsky Jr. *et al.*, who state that in terms of minor failures, surface erosion of blades is the most significant contributor to unplanned repair, being reported twelve times more often than structural failure [71]. The ongoing issues with LEE raise the question of why current aerospace solutions are not utilised on wind turbine blades and why current lifetime prediction methods cannot accurately predict *in-situ* performance.

The LEE of wind turbine blades, which can be seen in Figure 2.1, can be caused by rain, hail, sea spray, and other particulate debris such as sand, depending on the operating environment of the turbine [72]. While each issue can pose a significant hazard to the structure's lifetime, interactions between them have been identified to accelerate damage further [2]. As the focus of this work is related to offshore wind turbines erosion caused by rain was selected as the focus of this project to limit the scope of the study. Erosion of leading edges is typically qualitatively assessed using photos to capture and categorise the damage [18, 34, 57, 67, 73–76]. This inspection method depends on the individual's experience performing the inspection or analysis of erosion. As a result, tracking progression and comparing erosion of different blades or turbines is challenging. Carroll *et al.* state there are no standardised ways of defining failure, and as a result, reported failure rates and costs associated with repair vary significantly across the literature [77].

Significant LEE has been reported in several large wind farm projects, highlighting the criticality of the issue. An example is the offshore Horns Rev 2 wind farm composed of 273 blades that required refurbishment in 2015, with some requiring transport to an onshore facility for more substantial repair, due to LEE [78, 79]. A more recent example in 2018 is the 630 MW London Array in the UK, which required an emergency blade repair campaign to 140 of the projects 175 Siemens Gamesa 3.6-120 turbines [80]. In the same year, a similar repair campaign has also begun at Ørsted's

400 MW Anholt wind farm in Denmark, where 87 out 111 of the same turbine models are being retrofitted with rubber-like shells to mitigate the LEE issues [81]. These examples present a cause of concern for newer developments, such as the 2022 'ScotWind' seabed tender, which will host 25 GW of offshore wind on the Scottish seabed [82]. While it is difficult to predict if LEE will impact this project, repair costs from other installations indicate that it could require significant repair early into the designed lifetime.

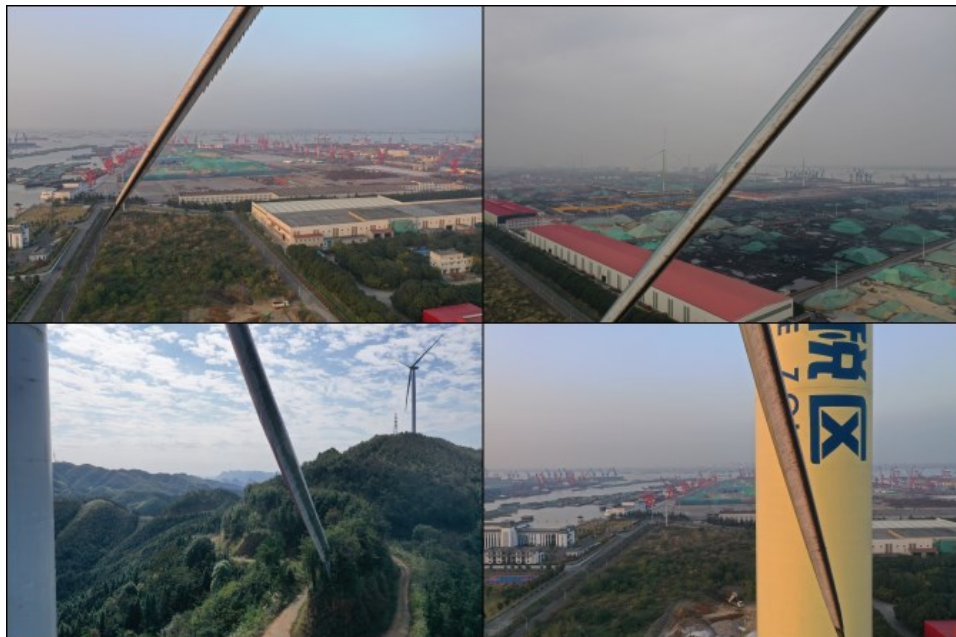


Figure 2.1 – Drone photography photos of eroded leading edges seen on wind turbine blades in various locations in China. These images were kindly provided by Dennis Lin from Jotun.

While the reduced Annual Energy Production (AEP) caused by LEE is a significant expense over the turbine's lifetime, the repair and subsequent preventative maintenance also contribute considerably [67, 79]. In 2015, Carroll *et al.* estimate¹ the material cost of a single blade repair ranges from £170 to £2300 depending on the severity [77]. In some instances, a major replacement² is required resulting in a material cost of £90,000. These costs can become alarming, especially when multiple blades or turbines within a single farm require repair. Furthermore, turbine blades, especially offshore, are inherently difficult to access due to their size and requirement for safe working conditions. Keegan and, more recently, Mishnaevsky Jr. summarise the challenges surrounding access and repair of modern offshore turbines identifying issues such as weather and tidal variations that can limit access to turbines for extended periods of time [67, 83]. As a result, removal of blades is costly,

¹ The analysis was based on ≈350 offshore wind turbines in 2015 that were; between 3 to 10 years old. Each turbine had an 80 m to 120 m rotor diameter and nominal power between 2 MW and 4 MW.

² Costs greater than €10,000 are considered a major replacement in the study.

carries significant risk and is used only as a last resort making *in-situ* inspection and repair the most economically viable [77].

For turbines currently in service, prevention and avoidance of LEE are considered by many to be the most easily implemented solutions [65, 79]. A notable example of this is presented by Bech *et al.*, who hypothesise that a significant amount of damage can be mitigated by controlling turbine rotational speed during high-intensity rain events with minimal losses to AEP [79]. While this provides a good framework for understanding the issues, several assumptions make predictions possible. This work is based on Damage Threshold Velocity (DTV), a fatigue-based approach derived for brittle materials [18, 63, 65, 67, 84]. This approach defines which droplets are below the DTV and can essentially be ignored as they are thought not to cause damage. However, it is known that modern material properties vary significantly due to impact and environmental conditions due to their viscoelastic nature, meaning that the predicted DTV could be inaccurate [53, 68]. The weather conditions are also simplified, utilising homogenous droplet sizes rather than a realistic distribution found *in situ* [34]. The work also assumes LEE damage progression is linear; however, it is commonly accepted that material undergoes an incubation period with minimal damage or mass loss before showing signs of erosion [85, 86]. Similarly, the effect of droplet size on damage is also extrapolated from the Wöhler curve. Finally, the correlation between LEE damage and the decrease in aerodynamic performance is still not fully understood [87, 88]. Despite these assumptions, the method presented by Bech *et al.* could be implemented in current and future turbine installations to minimise the effects of LEE until a material or design based solution has been developed.

A common criticism of studies into erosion are the discrepancies between predictions of the impact of LEE in current literature models [67, 87, 89–92]. Work presented shows agreement that the presence and severity of erosion results in a decrease in the lift coefficient, an increase in drag and a decrease in AEP. Sareen *et al.* showed that leading-edge erosion lowered the lift coefficient by up to 17 % and increased drag from between 6 % to 500 %, depending on the severity [88]. This prediction estimates minimal erosion to result in AEP loss of 3 % to 5 % and up to 25 % in cases that present severe erosion with pits, gouges and delamination. However, Schramm *et al.* utilised Computational Fluid Dynamic (CFD) modelling techniques and demonstrated significantly lower changes in predicted lift and drag values resulting in a lower AEP loss of 9 % [93]. Schramm *et al.* address this difference by highlighting that the work by Sareen *et al.* simulated the same level of erosion along the length of the blade, which is not the case *in-situ* as erosion is mainly concentrated on the tip section of the blade and gradually progresses towards the root. This opinion is supported by work from Han *et al.*, who showed a similar reduction in AEP by 2 % to 3.7 %, close to those predicted using CFD [94]. While the studies presented attempts to quantify the impact of erosion, there are common points of critique

between them. Zidane *et al.* highlight that many studies present data from specific Reynolds numbers between 1×10^3 and 1×10^6 and use specific aerofoil designs, which can cause differences in results [92]. Furthermore, there are differences in the distribution of erosion in lab-made or simulated test specimens as erosion is seen not only progressing along the leading edge but through the thickness. This issue could be overcome with high fidelity models created using state of the art imaging such as X-ray Computerised Tomography (CT) scanning but would be computationally expensive.

A recent campaign by *Offshore Renewable Energy Catapult*, called the *Blade Leading Edge Erosion Programme* (BLEEP), aimed to provide more representative results by measuring the effect of erosion on the annual energy production of in-service offshore wind turbines [62]. It was found that an uplift in annual energy production between 1.5 % to 2 % can be achieved following the repair of moderate erosion. These findings were more aligned with values reported by Han *et al.* and Schramm *et al.* [93, 94]. These reductions in AEP increase the LCOE, and as a result, protective LEP solutions are implemented to mitigate this. However, both Herring *et al.* and Schramm *et al.* also identify that LEP tapes or coating systems can be detrimental to AEP [34, 93]. The change in the profile is shown to result in < 1 % AEP reduction, which is deemed acceptable compared to the damage and resultant in AEP loss of an uncoated leading edge.

2.2 Blade Coatings

The most common method for mitigating the effect of LEE is by using protective coatings. Typically, a blade comprises a Glass Fibre Reinforced Polymer (GFRP) substrate with a coating system applied in-mould during manufacture. In-mould solutions generally use a single layer of gelcoat with similar properties as the composite matrix for the outermost layer. Fibres are layered on top, and upon infusion, a chemical bond is formed between the outer gelcoat and the composite surface.

Conversely, if coating is applied as a post-mould solution, the composite is sanded before filler application [60]. This process is used to ensure geometric conformance, remove manufacturing defects, and ensure a smoother surface, as these can be initiation sites for LEE. Post mould solutions, illustrated in Figure 2.2, are coated in multi-layer systems after the part is cured using brushing or spraying or roller techniques. In some instances, the filler is followed by a primer or a tie-coat. This preliminary layer ensures the following LEP layer has adequate adhesion, enhances the durability of the LEP and, in general, extends the life of the coating and improves the aesthetic finish. A topcoat layer is used to cover the blade's surface, providing general protection from the environmental conditions experienced offshore and is usually applied on all areas of the blade except the leading -- edge where a layer commonly referred to as the LEP is applied. [34, 72, 79, 95].

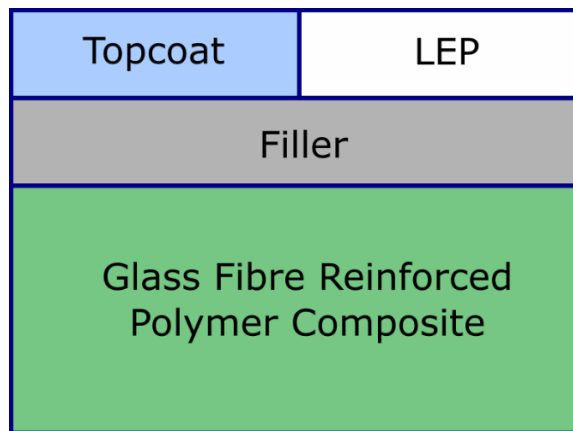


Figure 2.2 – Diagram of a simplified leading-edge coating system cross-section. The leading-edge protection layer (LEP) and Topcoat are commonly feathered to minimise abrupt changes from one coating to another. The thicknesses of the coatings layers are not to scale.

These coating systems are supplied by several companies that include PPG, Mankiewicz, Hempel, Teknos, AkzoNobel and Jotun [96–101]. The majority of the modern systems are based upon Polyurethane (PU) and Polyurea (PUR) chemistries. These are versatile polymers with many readily available components that can be substituted during synthesis. This flexibility allows tuning both chemical and mechanical properties for desired applications. [102, 103]. While this material class has demonstrated good erosion performance, a fundamental understanding of how variations in material properties affect the performance is not fully understood [60].

For these coating systems to be effective, they must be applied proficiently, minimising defects that can act as initiation points for damage or lead to delamination [34]. All coatings systems need to consider the practical issues around application when designing a coating. The ease of use must consider the initial coating post-manufacture and the more complex in-field application usually conducted by rope access. While conducting testing at the OREC facility in Blyth, the author had the opportunity to discuss offshore application procedures with AccessTec, a rope-access repair and maintenance provider. Below key points from a conversation are summarised (personal communication, August 2021) :

- Coating systems should possess wide humidity and temperature application windows. This range is important as while it can be possible to control these parameters in an onshore manufacturing facility, working on an offshore turbine, these conditions are constantly changing and hard to predict. Consequently, coatings that have narrow application windows require longer out service periods or can fail early due to working outside this range.
- The number of different material layers and required recoats should be minimised. This factor considerably reduces the time to coat the blade, which significantly reduces the time out of service due to repair.

- The number of components needing to be mixed should be kept to a minimum. Systems that require more than two components require more weight to be carried by applicators during rope access.
- Coating systems should be easy to mix and not require heavy equipment. Systems that utilised manual or motorised applicator guns were deemed the most suitable by the applicators. This method removed issues around ensuring the correct mixing ratio.
- The coatings used must have good sag resistance, which is the ability to resist bending or drooping of the coating during cure. It was stated that materials with low sag resistance resulted in areas of poor application. A high sag resistance also allows for work on different blades simultaneously as the turbine can be rotated while coatings are curing.
- Applicators prefer fast cure systems as rope access requires both suction cups to manoeuvre around the blade and ropes to contact the blade, which can cause damage to wet paints.

While multi-layer post mould coatings present many of the same issues as discussed above, several solutions are available to improve the application process. An alternative protection method to coatings is the use of highly flexible PU tape products, an example of which is the 3M™ W8607 Wind Protection Tape [104]. This type of product aims to address the issues with coating application by minimising the number of defects present. The reduction is achieved by manufacturing the tapes autonomously in a controlled environment which minimises batch variability and defects [34]. Owing to these factors, the tapes possess an excellent surface finish and consistent thickness, which are thought to be causes of initiation of erosion in LEP solutions. A further benefit of the tape products also includes a wider application window. Unlike multi-layer coating that required a chemical reaction to cure on to the blade, the tapes are reported not to be affected by weather conditions simplifying application. However, Herring *et al.* have shown that whilst certain tapes (3M™ W8607) show good erosion performance, this solution can be highly susceptible to water ingress beneath the coating layer and disbonding from the composite substrate [34]. Further improvement of the adhesion between the tape and the blade are required before leading-edge tapes can be considered the best solution to combating LEE.

Another promising alternative system is the Teknoblade Repair 9000-20, an elastomeric coating composed of 100 % solids and no volatile organic compounds, designed to tackle most issues faced by rope applicators when repairing in-service blades [99]. This system is applied using a dispenser gun that removes human errors such as incorrect ratios of components and insufficient mixing. The system is also designed for use in unpredictable offshore environments as it possesses the ability to cure at temperatures as low as 5 °C rapidly. Unlike other coating systems, which rely upon chemical adhesion to the surface, this product relies on mechanical adhesion. This process fills voids

or pores in the surface and holds the coatings onto the surface together through interlocking. This alternative mechanism is beneficial as it is reported to be insensitive to the underlying coating layers making it a versatile solution that can be used as a repair material for any underlying coating system. However, owing to the adhesion being mechanical, it is heavily reliant on the surface preparation of the area, which can itself be difficult in offshore conditions and can introduce human error.

2.2.1 Polyurethane and Polyurea Chemistry

PUs are a widely used polymer that possesses urethane linkages. Otto Bayer first introduced these in 1937 at the laboratories of IG Farben in Leverkusen, Germany [105–107]. The basic idea was related to spinnable products made of Hexamethylene Diisocyanate (HDI) and Hexa-1,6-diamine (HDA), followed by the publication of German Patent *DRP 728981* in November 1937: "*A process for the production of polyurethanes and polyureas*" [107]. During this time, PURs were also explored as they were found to possess far superior thermal properties and extremely high melting points. However, these proved challenging to implement in commercial manufacturing settings until the development of reaction injection moulding in the early 1980s.

Research into PUs accelerated during World War II to search for an alternative to rubber as it was expensive and hard to obtain. By 1950 Bayer had made significant advancements by systematically studying this material class, leading to the discovery of Vulkollan® rubbers. These PU elastomers had many benefits over natural rubber, such as higher abrasion resistance, higher tear strength, and improved resistance to oxygen ageing while maintaining the required flexibility and elasticity. In the following years, production capacity and demand for the products increased rapidly, with large chemical companies such as The Dow Chemical Company and Imperial Chemical Industries entering the market to supply the large volumes required.

Today PUs and PURs are used in countless applications due to their availability, tailorability and wide range of desirable properties. Examples of its use in modern times are coatings, adhesives, sealants, foams, absorbents, flame retardants, biomedical implants [103, 107]. As the range of PU and PUR systems that can be produced is so vast, only a brief overview of the general composition of these materials is provided here to give context for later works. A more thorough review of the chemistry is available in the literature [105–107].

PUs are typically formed by a polyaddition reaction of a di/polyisocyanate and a hydroxyl-terminated resin. PURs, on the other hand, are formed by the step-growth reaction of a di/polyisocyanate and generally an amine-terminated polymer resin. These general combinations are summarised in Table 2.1.

Table 2.1 – A tabulated list of the naming conventions used for polyurethane and polyurea systems. These are composed of resin and a chain extender.

Resin	Chain Extender	System Type
Polyetheramine	Amine Terminated	Polyurea
Polyether Polyol	Amine Terminated	Polyurea/Polyurethane
Polyetheramine	Glycol	Polyurethane/Polyurea
Polyether Polyol	Glycol	Polyurethane/Polyurea

The general reaction schemes of PU and PUR is presented in Figure 2.3 and describe how the monomer forms the long-chain polymer systems for modern coating systems.

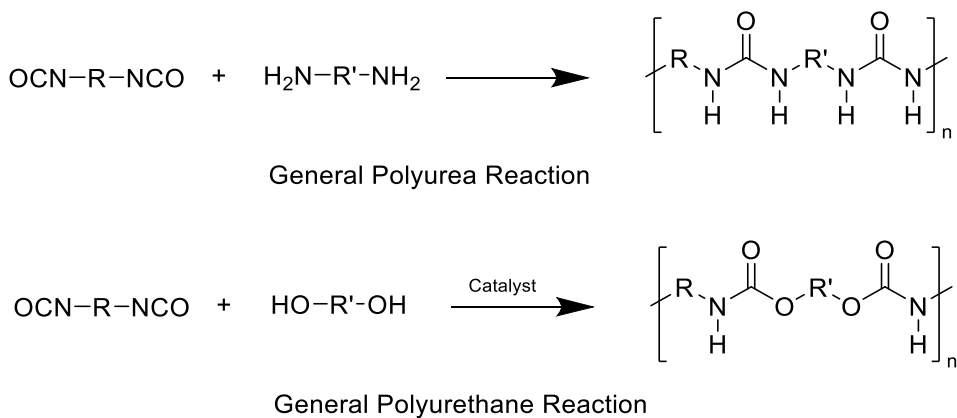


Figure 2.3 – General polyurea and polyurethane reaction schemes used to form modern elastomeric coatings.

When these reactions are combined, repeating urethane/urea groups are formed, generally including a chain extender, catalyst, and other additives to improve performance and aesthetics [107]. Common bonds include ester, ether, urea, and aromatic rings, along with urethane linkages in the PU/PUR backbone. As these constituents can include essentially any structure, the number of structures produced can be considered almost unlimited [105].

Polyurethane elastomers are materials formed by reacting three components: a diisocyanate (aromatic or aliphatic), a long chain diol and a small molecule chain-extender diol or diamine. As illustrated in Figure 2.4, the resulting polymer can be considered a copolymer composed of the long-chain diols and the diisocyanate-chain extenders components termed Soft Segments (SS) and Hard Segments (HS).

The elastomeric properties are highly dependent on the flexible chains with a low degree of intermolecular interaction. As a result, cross-linking and Glass Transition Temperature (T_g) are essential in material design [107]. The SS generally has a T_g below ambient temperature, unlike the HS, which is typically composed of rigid aromatic molecules which possess glass transition temperatures above ambient temperature. These HS also act as physical cross-links due to hydrogen

bonding between HS groups and act as filler particles within a rubbery SS matrix. Chemical cross-links can also be formed using multi-functional constituents, and unlike hydrogen bonds, they are not as easily broken by thermal treatments.

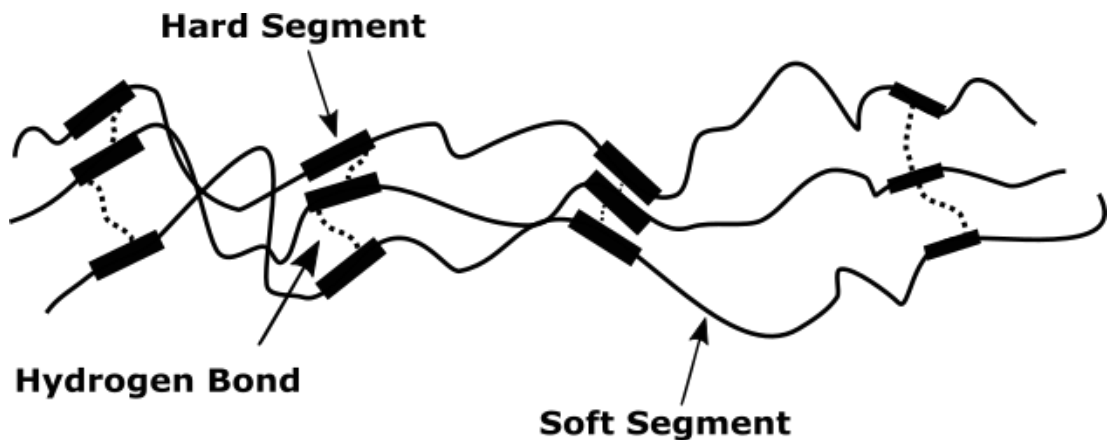


Figure 2.4 – Generalised polyurethane segment structure showing the formation of hard and soft segments and the presence of hydrogen bonding between chains. Adapted from the literature [107].

Examples of isocyanates are illustrated in Figure 2.5. These are di/polyfunctional, with two or more NCO groups per molecule. The most common are Hexamethylene Diisocyanate (HDI), Methylene Diphenyl Diisocyanate (MDI) and Toluene Diisocyanate (TDI). The isocyanate group possess two double bonds, where its reactivity is determined by the positive character of the carbon atom. As a result, it is susceptible to attack by nucleophiles or oxygen and nitrogen as electrophiles.

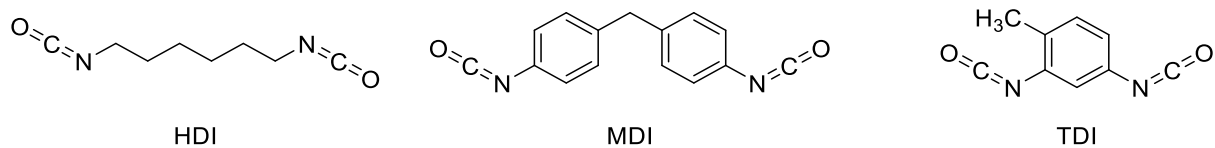


Figure 2.5 – Hexamethylene diisocyanate (HDI), methylene diphenyl diisocyanate (MDI) and toluene diisocyanate (TDI). TDI is commonly used as a mixture of isomers, but only one is shown for brevity.

Long-chain diols that form the SS are typically polyester or polyether diols of varying Molecular Weights (M_w) [107]. Examples of long-chain diols are illustrated in Figure 2.6. The choice of polyol significantly affects its physical state and the PUs elastomeric properties [103]. The important characteristics of polyols are reported to be the M_w , primary hydroxyl percentage, functionality and viscosity. The properties of PU also depend significantly on the degree of cross-linking. Highly branched polyols will result in rigid materials with good heat and chemical resistance [105, 107]. In contrast, a less branched material will produce good flexibility and low chemical resistance. Similarly, high M_w (long-chain) polyols yield a flexible PU, whereas low M_w (short-chain) polyols result in a more rigid material.

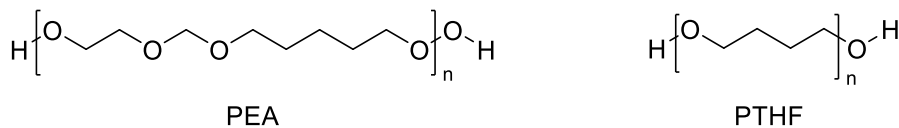


Figure 2.6 – Common long-chain diols used to form modern elastomeric coatings. Left: poly(ethylene adipate glycol) (PEA)
Right: polytetrahydrofuran (PTHF).

Chain extenders are typically low M_w and designed to react with isocyanates groups to form the HS [105, 107]. Examples of common chain extenders are illustrated in Figure 2.7. The inclusion of these materials is essential in forming a material with adequate mechanical properties for engineering applications. They influence the ability of the HS to create ordered structures and, in some instances, lead to microphase separation, resulting in increased modulus and increased HS T_g values. Generally, materials extended with polyols produce softer materials than when diamine extenders are used. This change is because the urea segments possess greater hydrogen bonding resulting in higher T_g and greater thermal stability.

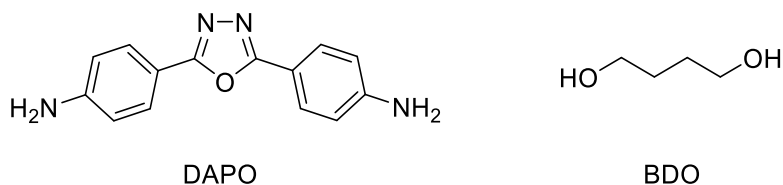


Figure 2.7 – Common low M_w chain extenders designed to react with isocyanates form part of the HS. Left: 2,5-bis(4-amino-phenylene)-1,3,4-oxadiazole (DAPO), a diamine chain extender. Right: butylene glycol (BDO), a diol chain extender.

In addition to the polyols and isocyanates, additives are generally required to improve processing and final properties. These are generally commercially sensitive with exact compositions not available in the open literature, but typically they can control the reaction, modify required reaction conditions, or modify the final properties [107]. Examples of these are crosslinkers, fillers, moisture scavengers and colourants. In some instances, catalysts are added to promote reaction via several different methods but generally, all allow for reaction to occur at lower temperatures and in shorter times which is generally an issue with PUs but less so for PURs.

2.3 Failure Modes

Modelling and predicting material performance has been attempted through various methods; however, it is generally accepted that coatings can fail through several distinctive modes [69, 108–111]. As a result, different characterisation and modelling approaches are required to capture these behaviours accurately.

At different levels of the testing pyramid, different failure modes can occur. At the coupon level, testing utilises standardised methodologies typically based on or adapted from those provided

by ASTM International or the International Organization for Standardization to capture material responses and guide material design. These tests are conducted to ensure specimens fail in a specific way to capture desired properties, with examples including tensile and adhesion testing [112, 113]. While several properties are considered influential in determining material performance, how these properties obtained at coupon level affect the component and system level is still an area of active research. At the component and full structure level, more complex failure modes are seen, especially during accelerated or *in-situ* testing. These include the issues from the initial manufacturing to commonly documented in-service failures. The DNV Recommended Practice (RP) provides a valuable way of dividing observed failure modes into three main categories [108].

The first is erosion, defined as a progressive failure caused by damage accumulation. This failure is attributed to rain and solid particulate (e.g., sand, hail, and insects) impacts. The latter has been studied in detail in the aerospace industry in relation to wing and helicopter leading edges, especially in desert environments [69]. However, this is considered outside the scope of the RP due to the significantly different mode of erosion seen when compared to erosion caused by rain droplets. In contrast, rain droplet impacts are generally the most significant contributor to LEE in offshore wind turbines. This difference is due to their location away from land and position in areas with high wind speeds and rainfall intensities [34]. The current method for lifetime materials that fail through rain erosion is based upon the Springer incubation model [108, 111, 114]. This model is a semi-empirical approach that links measured erosion performance to predict lifetime. This method is discussed in more detail in Section 2.5.

Delamination is the second category defined by the RP. Typically, this term refers to the failure of a laminated material such as glass fibre or carbon fibre reinforced plastic composites used in the blades. This failure results from fractures within the structure, either in the reinforcing fibre or the supporting epoxy resin that constitutes the composite structure. Alternatively, delamination or debonding can also refer to when a protective system applied to the blade (coating or protective shield) begins to separate from the substrate or between coating layer [95]. This failure is where the chemical adhesive interaction between the coating and the substrate fails due to excessive load or environmental attack. The RP categorises delamination into two groups; failures triggered by blade deformation, either by damage caused by fatigue loading or due to extreme loads that lead to large blade deflections. Another subcategory groups failures caused by external forces such as extreme impacts or damage from the transport and handling of the blade.

The final category captures other failure modes that do not fall under erosion or delamination. Examples of this are typically attributed to manufacturing defects where adhesive or protective

coatings were not applied for manufacturers guidelines or within acceptable conditions (*e.g.* humidity levels). These issues typically result in premature failures, such as peeling from areas of poor application.

2.4 Rain Droplet Impact

Understanding how liquid droplets impact a solid surface is of great importance in LEE and several other applications such as surface cleaning, spray coating, spray cooling, and ink-jet printing [115]. This knowledge is also used in larger applications such as erosion in steam and wind turbine blades, where water impacting a surface above a certain threshold velocity can eventually lead to erosion [67, 115, 116]. The impact of a rain droplet on a rigid surface initially appears to be a simple static case. However, research has shown that it is a complex and dynamic event that results in shockwaves, also called stress waves, propagating through the entire coating system and not just the LEP surface coating [72].

Figure 2.8 shows how an impact can be broken down into three behaviours: the initial longitudinal compressional stress wave, the transverse shear wave, and a third Rayleigh wave caused by droplet deformation from pressure rebounding from the coating [67, 72]. The resulting Rayleigh wave is reported to contain two-thirds of the collision energy, with the maximum pressure not being highest at the centre of the impact but the edges of the contact circle reached by the initial shockwave [117]. The compressed liquid front behaviour spreads towards and past the initial impact area on the target surface, leading to lateral jetting across the material surface. The reduction of oscillation amplitude, called damping, is related to the distance from the impact centre [109]. The bulk waves decay with $1/r$ into the solid and with $1/r^2$ at the surface. However the damping of Raleigh waves which occur with $1/\sqrt{r}$ and are less significant.

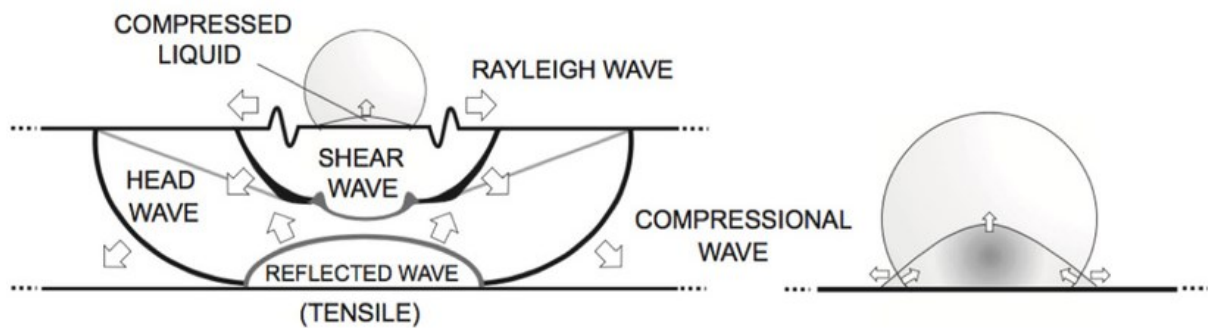


Figure 2.8 – Schematic summarising the impacts of a spherical water droplet on a rigid surface. This figure depicts the three distinct waves originating from the point of impact. This figure was reprinted with permission from Elsevier [69].

Historically, most of the erosion on metal surfaces in contact with water was attributed to corrosion and thought to be exacerbated due to water's movement over them. Cook proposed that this was not the key mechanism but instead was a water hammer phenomenon resulting in the momentary high pressures exceeding the materials yield strength of materials [67, 118]. This event is a pressure surge caused by the near incompressibility of water upon impacting a rigid surface resulting in the kinetic energy of the moving mass of liquid being converted into pressure energy [118]. Historically, the water hammer equation has been used in piping systems and could be predicted by

$$P = \rho_0 C_L V_L \quad 2.1$$

where P is the resulting water hammer pressure, ρ_L is the density of the undisturbed fluid, C_L is the speed of sound in the disturbed liquid and V_L is the impact velocity of the droplet [67].

Following this, the droplet begins to collapse, leading to lateral jetting (a key contributor to surface damage), causing water to be forced across the surface up to 40 times greater than the original impact speed. As a result, high pressures are generated at the wavefront exceeding the observed water hammer pressure by up to a factor of three [117]. The impact duration is in the order of 100 ns and is related to the material, diameter and speed of the impinging droplet [117]. This phenomenon is further complicated because less than 5 μ s separate interactions between subsequent stress waves under certain conditions. As a result, the impacts are considered a high strain rate yet comparably low strain impact event, making it challenging to analyse using conventional methods.

An improvement on this theory was proposed by Springer *et al.*, who applied the concept of water hammer pressure creating a damage model that took into account the propagation of pressure waves through the target material and the water droplet itself [115]. This advancement was possible as a sudden halt of liquid in a pipe can be considered equivalent to a liquid droplet impact on a solid surface. This concept was applied to rain droplet impacts and used to predict impact pressure by

$$P_c = \frac{V_L \rho_l C_l \cos \theta}{1 + \frac{Z_L}{Z_S}} \quad 2.2$$

where P_c is the water hammer pressure ρ is the density, C is the speed of sound, and V is the velocity [86]. X_l and X_s are subscripts that refer to the liquid and substrate, respectively. Z_X is the acoustic impedance, a measure of the ease of which sound propagate through a particular medium and is calculated by

$$Z_X = \rho_x C_x \approx \sqrt{\rho_x E_x} \quad 2.3$$

where E is Young's modulus, and the subscript x can denote the liquid or substrate. From this equation, it can be seen that by using a low modulus or density material, impact pressures can be reduced.

Stress wave propagation through a leading-edge is further complicated as coating systems are composed of multiple layers and lead to internal reflections. Springer *et al.* provide a framework for understanding its impact and state that a stress wave can be reflected when there is a change in acoustic impedance [86, 111]. This difference can result from layers possessing different material properties or defects such as voids and delaminations that vary the local impedance properties. Stress waves that reach an interface are partially reflected and transmitted. The two new resulting waves possess different amplitudes, which depend on the difference between the acoustic impedances of the two materials. This concept is analogous to the process used in ultrasonic non-destructive testing, where high-frequency sound is used to examine materials [72]. This method is commonly used in flaw detection/evaluation, dimensional measurements, material characterisation. A schematic detailing the process of internal reflections, as described by Springer *et al.*, is demonstrated in Figure 2.9 [86].

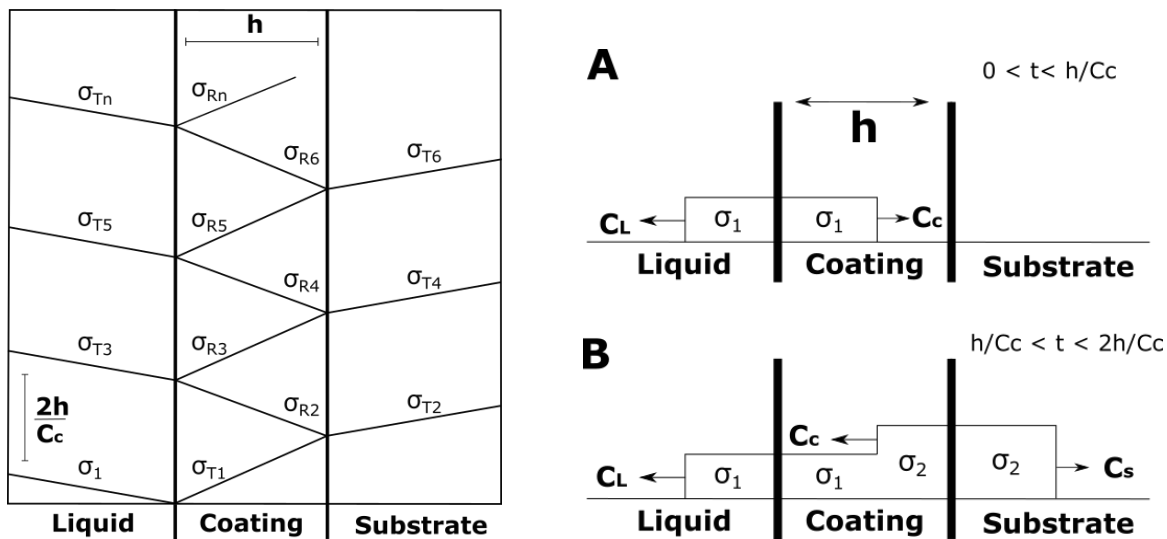


Figure 2.9 – Schematic detailing of a wave propagating through a multi-layer system composed of a coating and substrate layer. Left: Visual representation of wave propagation and reflection. Right: Resulting stress propagation during two consecutive time instants. Where h represents coating thickness, C_c and C_L denote the speed of sound in the coating and liquid, respectively, and σ represents the magnitude of the stress wave. Both figures were adapted directly from the literature [86].

The initial stress is a wave created by the impact of a water droplet, denoted by σ_1 . This value is equal to the initial hydrostatic impact pressure P , previously derived by Equation 2.1. Upon impact, two different wavefronts travel through the coating and liquid, the transmitted wave denoted by σ_{T1} and the wave reflected into the droplet, the latter is not displayed for clarity. The transmitted wavefront travels through the coating until reaching an area of differing impendence where part of the wave is reflected into the coating σ_{R2} , and the remainder σ_{T2} , is transmitted through the

substrate. The internal reflection process repeats, denoted by the increasing subscript number, until equilibrium stress is reached. The internal reflections can interact through constructive interference, resulting in increased stress and considered to contribute to more damage. Springer *et al.* demonstrate this by varying the impedances at the coating-substrate interface, highlighting the importance of selecting materials that are appropriately matched [86].

While the model presented by Springer *et al.* is the most widely accepted theory implemented for rain droplet impact in LEE, several assumptions must be considered :

- The problem is understood to be one-dimensional, accounting for only waves propagating normal to the surface, ignoring shear waves. While in reality, it is a three-dimensional problem where multiple impacts can interact.
- The substrate is considered to be semi-infinite.
- A perfect bond is assumed between layers meaning displacements between layers are equal.
- The attenuation effects are not included as stress is only reduced through transmission from the coating to the liquid or substrate. However, in reality, materials possess inherent damping characteristics that reduce stress wave amplitude as they travel through a system [72]. This assumption is particularly important as modern coating materials are more viscoelastic and inherently more attenuating.

2.5 Coating Lifetime Prediction

Springer *et al.* also used the understanding of water hammer pressures to create a damage model allowing for predicting the lifetime of a material [86]. This theory is based upon the fatigue characteristics of the material and considers the impact pressure of each droplet impinging the surface. The work simplified material failure into two main stages detailed in Figure 2.10. First is the incubation period, where there is no observable change or loss in material or mass. This period is followed by the ‘steady material loss’ period, where after a certain amount of fatigue damage has accumulated, a steady increase of mass loss is seen.

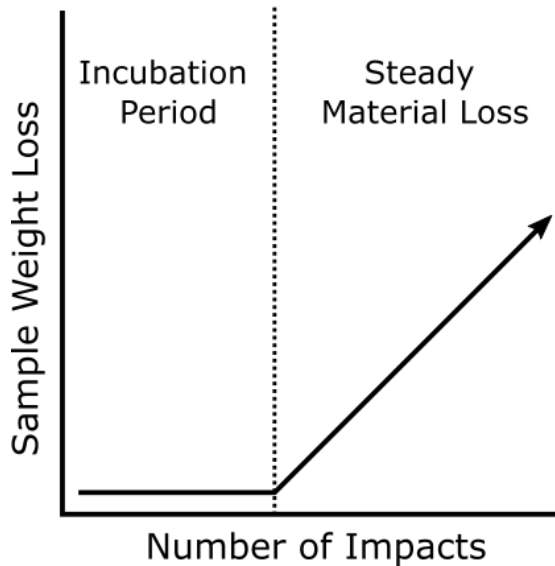


Figure 2.10 – A graph illustrating stages of erosion as defined by Springer *et al.* [111]. The figure is adapted from work by Eisenberg *et al.* [111].

The model aims to provide a specific number of impacts to the onset of erosion (N_i) and thus allows for predicting the performance of different materials under various conditions. The model can be found in various forms however is commonly simplified to

$$N_i = \frac{8.9}{d^2} \left(\frac{S}{P_c} \right)^{5.7} \quad 2.4$$

where d is the droplet diameter in mm, S is the material strength, and P_c is the impact water hammer pressure derived from Equation 2.1. The material strength S is based on the experimental fatigue properties and determined by

$$S = \frac{4\sigma_{uts}(b - 1)}{1 - 2\nu} \quad 2.5$$

where σ_{uts} is the ultimate tensile strength, ν is the Poisson's ratio, and b is the fatigue constant. The b value is determined from an SN-curve/Wöhler curve which plots the magnitude of alternating stress over many cycles for a given material [86, 119]. This value is obtained by subjecting a coupon of material to cyclic stress until a crack or failure occurs, resulting in SN/Wöhler curve. While the strength parameter, in theory, can be deduced from material properties, it is more commonly obtained through empirical rain erosion testing. The empirical method is used due to the difficulty of obtaining Wöhler curves for certain materials, especially the current lower modulus coatings [119].

This approach, put forward by Springer *et al.*, is the prevailing theory on erosion damage and is widely utilised by both academia and industry [72, 86, 111]. This approach provides a framework

for identifying the key parameters in determining material erosion performance over its lifetime and provides direction for the literature review tabulated in Table 2.2.

Table 2.2 – Summary of key inputs into the lifetime prediction model presented by Springer et al. [86].

Material Inputs	Symbol	Impact Inputs	Symbol
Speed of sound	c	Impact angle	θ
Density	ρ	Velocity	v
Thickness	h	Diameter	d
Fatigue 'b' value	b		
Poisson's ratio	ν		

While it is known that predictions made by using this model can be inaccurate, especially for the modern soft coating used as LEPs, some of these discrepancies have been linked to specific criticisms of the model itself. To address this DNV launched a Joint Industry Project with ten commercial partners to develop a Comprehensive Methodology For Blade Rain Erosion Analysis (COBRA) in 2019 [120]. This project resulted in the Recommended Practice, DNVGL-RP-0573, outlining this new procedure being published in 2020 [108]. An in-depth review and critique can be found in the thesis published by Herring conducted in parallel to this project but is considered outside the scope of this current project [121].

2.6 Implication on Material Selection

Many materials have been used in LEP solutions to mitigate LEE and prolong the lifetime of a turbine [34]. A common example are the rigid protective layers called gel-coats (similar to those used in the marine industry) that are applied in-mould at the start of the manufacturing process. More recently there has been an increase in the use of coatings that are applied post-mould that possess a low modulus, and are made from durable PU/PUR materials that are thought to reduce the impact energy of a droplet impact [122].

This trend towards low modulus/low impedance materials can be seen in Table 2.3, where several properties are tabulated. The magnitude of the impact pressure depends on the difference in acoustic properties between the droplet and the coating material.

The relative impact pressures Z_r are calculated by

$$Z_r = P_c V_d \quad 2.6$$

where P_c is the water hammer pressure (Equation 2.2) and V_d is the droplet velocity. It can be used to compare the reduction of impact pressures (according to the Springer approach) between different material classes, with the lower value being considered optimal.

However, it must be noted that this is a simplified approach that assumes that the only factor determining performance is the water hammer pressure, which has been commonly found not to correlate well to the erosion performance of materials. Nevertheless, as the Springer approach is the prevailing method for understanding erosion, it provides a straightforward way of conducting an initial comparison of different classes of materials and can be used as a point for discussion through the work.

A selection of material classes and their properties are listed in Table 2.3. Each of these is further discussed by linking the material properties to the reduction in impact pressure, which Springer *et al.* hypothesised was key to LEP performance [86].

The first group details properties related to composite systems and the high modulus gel coats historically (*circa* 2010) used to protect the leading edge [34]. As discussed in Section 2.2, modern blades are primarily composed of an E-glass and epoxy resin, typically costing around £26/kg [123]. While composite materials do show a reduction in impact pressures in comparison to other materials, they are much more susceptible to progressive erosion damage and, in extreme cases, can lead to structural failures [70]. As a result, protection of the leading edge is required, and polyester resins, which typically cost around £1.5/kg, have been used historically as gel coats for this purpose [123]. The use of this resin results in a reduction in impact pressures compared to directly impacting the composite substrate.

The second group, metals, are included as they have been used to protect leading edges in the aerospace industry and have been proposed as long term solutions by authors such as Herring *et al.* [95]. This class of materials possess high moduli and densities, resulting in high impact pressures compared to other materials, and should perform poorly under rain impact through this simplified understanding. However, it has been reported that these materials perform well under accelerated rain erosion testing [95]. This has been attributed to metals possessing considerably higher acoustic impedances than polymeric coatings. As a result, upon droplet impingement, metals reflect a large proportion of the droplet impact energy leading to high energy lateral jetting across the surface. As the surface of metals are generally hard and smooth this type of mechanism is considered to be less damaging to metallic coating materials. Despite this desirable behaviour, these materials are reported to be susceptible to debonding, which can be exacerbated by the difference in stiffness between the metal shield and the blade. A further disadvantage of using these materials is the high costs compared to gel coats, which range from approximately £0.5/kg for steel and up to £20/kg for high-performance alloys [123].

Table 2.3 – A selection of available material properties of several classes of materials for comparison. The abbreviated polymer system tabulated are low-density polyethylene (LDPE), ultra-high-molecular-weight polyethylene (UHMWPE), polymethyl methacrylate (PMMA), polyetheretherketone (PEEK) and polycarbonate (PC). Acoustic impedances were calculated using Equation 2.3, water hammer pressure using Equation 2.2 and relative impact pressure using Equation 2.6 (Impact velocity of 100 m/s). The table explains the trend towards softer, low acoustic impedance materials due to reduced impact pressures. Data adapted from Slot et al. and Johansen et al. [109, 124].

Material	Density (kg/m ³)	Young's Modulus (MPa)	Longitudinal Speed of Sound (m/s)	Acoustic Impedance (kg/m ² .s)	Water Hammer Pressure (MPa)	Relative Impact Pressure (MPa s/m)
Impact Medium						
Water	1000	-	1480	-	-	-
Fibres, Resin and Composite						
E-Glass Fibre	2540	70000	5250	13.34	133.2	1.33
Unsaturated Polyester Resin (Low E)	1150	2400	1445	1.66	78.3	0.78
Unsaturated Polyester Resin (High E)	1250	4600	1918	2.4	91.5	0.92
Epoxy Resin (Low Cure)	1175	3500	1726	2.03	85.6	0.86
Epoxy Resin (High Cure)	1250	3500	1673	2.09	86.7	0.87
E-Glass/Epoxy Composite (v _f = 60%)	2000	10000	2236	4.47	111.2	1.11
Metals						
Aluminium (Alloys)	2700	70000	5092	13.75	133.6	1.34
Titanium (Alloys)	4430	115000	5095	22.57	138.9	1.39
Steel	7850	205000	5110	40.11	142.7	1.43
Nickel	8890	204000	4790	42.58	143	1.43
Ceramics						
Aluminium Oxide	3800	360000	9733	36.99	142.3	1.42
Zirconium Dioxide	6000	200000	5774	34.64	141.9	1.42
Polymers						
LDPE	920	400	659	0.61	43	0.43
UHMWPE	945	800	920	0.87	54.8	0.55
PMMA	1185	3000	1591	1.89	82.9	0.83
PEEK	1320	4200	1784	2.35	90.9	0.91
PC	1200	2400	1414	1.7	79.1	0.79
Elastomers						
Natural Rubber	920	25	165	0.15	13.8	0.14
Styrene-Butadiene Rubber	910	300	574	0.52	38.6	0.39
Neoprene (Chloroprene)	1240	40	180	0.22	19.4	0.19
Polyurethane (Low E)	1150	10	93	0.11	10	0.1
Polyurethane (Mid E)	1150	75	255	0.29	24.5	0.24
Polyurethane (High E)	1150	300	511	0.59	42.1	0.42

The third group presents two ceramic materials as a comparison. While these have not been utilised as an LEP solution within the wind industry, they are advantageous in high load and temperature environments [125]. As with metals, this class of materials possesses high acoustic impedances and will result in significant energy reflection resulting in high energy lateral jetting. These materials, however, are more expensive, ranging from £14/kg to £53/kg and are also susceptible to similar failure through debonding, as seen in the metallic LEP solutions [123].

The fourth group details engineering polymers, as they possess lower modulus and density values than the other coatings discussed, resulting in decreased impact pressure [126]. These materials also benefit from being highly durable and flexible, which are deemed desirable properties for an LEP coating system [72]. Keegan found that flexible coatings exhibited considerable geometric deformation that allowed for a smoother impact response and resulted in reduced damage [67]. The cost of these materials is similar to that of a gelcoat, costing between £1.1/kg and £2/kg [123]. However, certain high-performance polymers such as Polyetheretherketone (PEEK) are significantly more expensive, priced at approximately £47/kg [123].

The final group of materials listed are elastomers, which possess low moduli and large elongations to break compared to other polymers [126]. These materials are reported to cost between £0.9/kg to £2.8/kg, similar to gel coat solutions [123]. While these materials also undergo considerable geometric deformation, they also demonstrate the most significant reduction in impact pressure and are predicted to be the most suitable for LEP solutions. This aligns with work by O'Carroll, who correlated lower modulus material with improved rain erosion performance [127].

While this trend does suggest that lower modulus materials are more suited as LEPs, it does not include the effects of multi-layer wave reflection as discussed in Section 2.4. It must also be noted that the material will still need to be suitable for the application. These materials are required to not only withstand the droplet impacts but must allow for the routine loading and deflections in the transport and operation of the blade while maintaining adhesion to underlying layers. In addition to these criteria, Jotun reports several general rules of thumb currently in use in their coating design (personal communication):

- Good resistance to weathering.
- Resistant to the accumulation of dirt.
- Long accelerated RET lifetime.

Elastomers present themselves as an ideal material as they possess a low Z_r , high ductility, flexibility, and strain to failure. This finding agrees with the literature as modern LEPs are commonly found in this class of materials. As a result, many commercially materials are based on polyurethane/polyureas, examples of highly tailorabile elastomers discussed in Section 2.2. However,

further work is still required to understand why these material properties do not always correlate with rain erosion performance.

2.7 Review of Impact Springer Parameters

This section presents a review of the literature surrounding the key parameters used in the Springer lifetime prediction method summarised in Table 2.2.

2.7.1 Modulus of Elasticity

Young's modulus (E) measures the stiffness of elastic material and is defined as the ratio of stress to strain. As discussed in Section 2.5, the erosion model proposed by Springer *et al.* identifies that a low modulus and density are critical in improving the erosion performance of LEP materials [86]. This material choice reduces the water hammer pressures by selecting materials with appropriate acoustic impedances. These findings are supported by more recent work by Eisenberg *et al.*, who revisited the model to improve the AEP losses over different wind turbine sites [111]. The work found that the best performing coatings generally have lower impedances than water and the substrate, effectively protecting the substrate while reducing damage to the coating. O'Carroll *et al.* also identified the potential issues with mismatches in modulus values between layers [127]. The work states that a coating layer with a lower modulus value than water would be ideal but accepts that this is hard to produce. During the work, it was also recognised that erosion performance depends on temperature, attributing it that the material being tested had a characteristic glass transition temperature (T_g), which can vary the material modulus. Accelerated RET testing showed that material above the T_g (*i.e.* within the elastic state) performed better than those tests below their T_g (within the glassy state). Work by Pugh *et al.* also supports these points, suggesting that the combination of different materials can have synergistic effects, potentially amplifying the magnitude of the stress wave if not matched appropriately [68].

Cortes *et al.* [72] state epoxy or polyester gel coats are appropriate in general protection due to their high modulus, rigidity, and brittleness. As a result of these properties, they can diminish the stresses transmitted to the coating surface and substrate. However, it is suggested that these materials are not suitable for the leading edge, especially in areas experiencing high tip speeds. In these areas, the work suggests using low modulus elastomeric materials. The work utilised accelerated rain erosion testing³ to show that lower modulus LEPs performed better than rigid LEPs. These

³ The performance of an LEP system is assessed in an accelerated rain erosion commonly following the DNV-RP-0171 [147]. In this, a specimen is rotated at a high speed through an artificial rain field until erosion occurs. It is an active research topic for both blade and coating manufacturers as there is no validated method that is able to relate accelerated test results to in-field erosion performance [119].

conclusions are further supported by work showing that materials with a lower degree of cure outperformed those with a higher one. This difference was attributed to changes at the interface but can also be linked to a lower modulus in partially cured materials. In addition to the low modulus, the work also identified that an ideal material would possess a high strain rate deformation capacity suitable for the expected impacts on the leading edge.

While these conclusions agree with Springer's findings, the methodology used to obtain rain erosion performance must be considered. The test speeds used in a Whirling Arm Rain Erosion Tests (WARET) are reported to be 135 m/s which is significantly higher than commonly seen *in-situ* [128]. The use of very high tip speeds has been shown to result in failures that typically did not follow the same mechanisms as seen at lower impact speeds [34]. The test setup also utilises a whirling arm erosion rig housed within a small enclosed chamber. It is unclear if the unit is temperature-controlled, as the operation of a motor can result in significant heat being generated, which affects the material properties and, ultimately, the material lifetime [53]. The use of flat specimens was reported to result in a very concentrated area of droplet impact around the 12 o'clock position [34]. This uneven droplet distribution has been identified to cause different failure mechanisms and reduce lifetimes [61]. While these observations do not invalidate the results, it should be noted that if tested in another test rig such as the whirling arm test rig based at the OREC, the results may differ significantly. This difference can be attributed to using a more distributed rain field, in combination with lower rotational speeds, resulting in a much longer lifetime and is thought to be a more representative accelerated erosion mechanism.

Slot *et al.* and Mishnaevsky Jr. *et al.* suggest that soft, lower modulus coatings are preferable to improve rain erosion performance [109, 129]. However, both papers highlight the importance of minimising defects as any heterogeneities such as particles and voids affect crack initiation and erosion performance. 3M™ Wind Protection Tape is a coating solution that minimises the number of defects present [43]. This reduction is achieved by manufacturing the tapes autonomously in a controlled environment which minimises batch variability and defects [5]. While it has shown improved erosion resistance, debonding of the tape system is still a common problem suggesting that modulus cannot be the only consideration when designing a coating system.

Further work by Mishnaevsky Jr. identifies conflicting reviews on the stiffness of coatings [60]. The paper highlights that while softer coatings show improved erosion behaviour in many cases, they can also undergo different failure mechanisms as a result. The review also references work by Sigamani, who showed that soft polyester based PU films demonstrated ductile deformation at initial stages of erosion, leading to the formation of fragments [130]. Conversely, brittle cracks formed in

stiffer films, resulting in spalling being observed on the material. In another study by Barkoula *et al.*, the improved performance of the softer materials was attributed to the dissipation of impact energy upon deformation of the material, which minimised the amount of material lost in soft and ductile materials [131]. Differences in erosion behaviour were also linked to the removal mechanisms seen for different material types. Rubbers showed signs of tearing and fatigue; ductile metals and polymers showed cutting and chip formation; ceramics, metals and brittle polymers showed cracking. These observations suggest that high modulus materials such as polyester gel coats undergo different failure mechanisms than softer coatings and may require a different approach to understanding their failure.

2.7.2 Thickness

The Springer model shows that greater thicknesses increase erosion performance [86]. Mishnaevsky Jr. *et al.* conducted modelling work that demonstrated that stress amplitudes are predicted to be significantly higher for thin coatings, indicating that thicker coatings could improve erosion performance and, in cases, delay the onset of damage [129]. On the contrary, the work also identifies that increasing the coating thickness also increases the likelihood of debonding failure, limiting the LEP system's lifetime [60]. Work by Pugh *et al.* also states that increasing coating thickness leads to increased prevalence of defects such as sagging and delamination and should be considered limiting factors [68]. The work also suggests that if layer thickness is incorrectly chosen, it can lead to further problems in that it generates stress wave reflections, accelerating fatigue failure.

A practical consideration that is not discussed is how increasing the thickness of current PU LEPs would affect application time. Typical LEP layers are applied to form a thickness of < 0.5 mm. Due to how these coating systems are designed, increasing the layer thickness would require many overcoats, significantly adding to the application time, increasing any downtime required during a repair and increasing the chance of defects due to the number of layers required. However, significantly thicker (3.4 mm) systems are commercially available such as the Poly Tech ELLE™, a precast shell that removes the need for multiple coatings [60, 132].

2.7.3 Poisson's Ratio

The Springer model predicts that an increase in Poisson's ratio results in increased material strength and thus leads to increased erosion performance [86]. Recent work by Doagou-Rad *et al.* agrees with the correlation between increasing Poisson's ratio and erosion performance [133]. The work demonstrates a decrease in stress magnitude by modelling the impact on a coated surface. This finding suggests that an ideal coating would possess a high Poisson's ratio in addition to a low density, in agreement with [86]. The author in [133] also presents Equation 2.7, a potential comparative indicator to screen for improved erosion behaviour.

$$\text{Erosion Performance} = \frac{\text{Strength. Damping}}{\sqrt{\text{Stiffness. Density}}} \quad 2.7$$

The work also identifies that while it is possible to have a variety of Poisson's ratios, this can also affect how stress waves propagate through the system [133]. Rayleigh waves (discussed in Section 2.4) dominate at low Poisson's ratios. However, at Poisson's ratio close to 0.5, the shear wave becomes almost an equal contributor to the Rayleigh wave, potentially resulting in different failure modes. This point is particularly important as one of the assumptions used by Springer *et al.* is that it is considered a one-dimensional problem that only accounts for longitudinal waves and ignores shear waves [86].

2.7.4 Tensile Properties

Tensile properties affect two main parts of the Springer equation, the Ultimate Tensile Strength (*UTS*) and fatigue slope parameter (*b*). The Springer methodology predicts that an increase in either of these parameters improves erosion performance.

Pugh *et al.* state that tensile testing utilised by Springer is meant for the characterisation of ductile coating materials [68]. However, many materials employed today are considered elastomeric and more difficult to test than common polymers. While they can fail due to elongation, specific polymers can withstand over 500 % strain before failing. These materials can also fail due to exceeding the maximum strain rate the material can accept; however, this is difficult to measure without specialist equipment in many cases. Instead, these materials are more commonly made to fail through fatigue to obtain the *UTS* and *b* values. The method for conducting these tests on polymers is detailed by Herring *et al.* [119]. The work also critiques the current methodology suggesting that the accepted material parameters and constants used in lifetime prediction are unlikely to be suitable for modern materials in use as LEPs. This method was improved by including confidence factors to account for the uncertainty of the true material properties. By using this approach, the uncertainty from different tests can be combined to provide a range of lifetimes rather than a single value. The work concludes that even with modern methods available today, there is still significant variability in results, making obtaining an accurate value difficult, resulting in added uncertainty to the predictions. Furthermore, the work highlights the need to develop methods that accurately capture modern viscoelastic material behaviour at high strain rates.

2.7.5 Implications of Viscoelasticity

Hooke's law of linear elasticity commonly describes many solid materials as they are considered elastic. This law states that stress (σ) is proportional to strain (ε) [134]. However, certain materials are viscoelastic, where the relationship between stress and strain also depends on time (t). Modern

Polymeric coatings, especially those based on polyurethane and polyurea chemistries, are examples of materials that are considered to be viscoelastic. This behaviour is due to the interaction between polymer chains dictating a material's viscoelastic characteristics. Viscoelastic materials demonstrate various phenomena such as strain-rate dependence, temperature dependence, the ability to dissipate energy and recover deformations over time.

Materials showing viscoelastic behaviour add complexity to characterising and predicting the performance of the coating materials as they are linked not only to rain droplet impacts but also to the environmental conditions that the material experiences over its lifetime. These droplet impacts are associated with high strain rates (10^6 - 10^9 Hz) predicted from Finite Element Analysis (FEA) models of rain droplet impacts [67]. These predicted strain rates bring into question the validity of using conventional mechanical tests to predict the lifetime of an LEP system which are typically quasi-static methods that are considered low strain-rate [53, 61, 68]. This point is critical in lifetime prediction as proposed by Springer, where key inputs include modulus, speed of sound, coating thickness, and tensile properties [86, 111]. As modern, flexible materials are considered viscoelastic, this will significantly influence lifetime prediction values.

In order to predict the impact pressure and lifetime of the material, as discussed in Section 2.5, acoustic impedance is required [86]. This calculation requires the material stiffness and density to provide an approximation. For materials considered elastic or lacking viscoelastic characteristics, a simple method such as tensile testing is suitable for acquiring stiffness. However, for more viscoelastic materials, the stiffness properties are more complex and dependent on temperature, strain rate, and loading regime [68]. Three parameters can represent the stiffness of viscoelastic materials: the storage modulus (E') *i.e.* the amount of elastic material stored by the material; the loss modulus (E''), the amount of energy dissipated through viscous losses and heating; and the $\tan \delta$ value, the ratio of E'' to E' , an indicator of the viscoelasticity of the material and its ability to dissipate energy.

A paper by Karger-Kocsis *et al.* is commonly referenced in the field as an early study that linked impacts to dynamic properties. The work utilised instrumented impact testing on notched Charpy impact specimens and dynamic mechanical thermal analysis (DMTA) to characterise polypropylene specimens [135]. Two correlations were found; Positive correlations were found between maximum impact force and E' ; and between the notched impact strength and the $\tan \delta$. These correlations were attributed to the increased stiffness and energy in energy dissipation found at higher $\tan \delta$ values. It was also identified that the failure mode depended on several factors; frequency, temperature and concentration of the elastomer present in the blend. While this work provides a link between viscoelastic material properties and forces, it should be noted that its measurement is conducted using

a Charpy test, which is considered not to be representative of a liquid impingement. Furthermore, the characterisation of materials using DMTA was only conducted at 10^1 Hz, significantly lower than predicted to occur in a rain droplet impact using the Finite Element Method (FEM) [67].

Arena *et al.* measured the wear resistance of several Thermoplastic Polyurethanes (TPU) by employing erosion and abrasion tests identifying that softer elastomers usually show a better solid particle erosion resistance because of less crack propagation and more elastic/plastic deformation [136]. Conversely, harder TPU systems typically exhibited higher wear resistance [130, 136, 137]. These results were linked to viscoelastic parameters through the use of high-frequency DMTA. The work identified a good linear correlation between the loss modulus and the mass lost during the erosion test, irrespective of the impingement angle. The authors state that loss modulus is a critical parameter in erosion resistance, especially in elastomeric materials. The findings of the work are also supported by Karger *et al.*, as both brittle and ductile failure modes are identified; however, this study attributed to variation in the impact time and impingement angle. Bowden *et al.* also showed that different failure modes were seen for low *vs.* high damping materials [138]. Liquid impacts at supersonic speeds showed that failure patterns differed between higher modulus polymers such as PMMA and low modulus natural rubbers like neoprene, which are considered highly damping. However, the study utilises significantly higher impact speeds (343 m/s) than experienced by wind turbine currently operation (100 m/s), which could lead to unrepresentative failure modes [34]. While the work by Arena *et al.* presents significant advancement in the understanding of the impact of viscoelastic moduli, it only considers the case of solid impact, which is different to that seen in liquid impingement. The work also characterises basic TPUs, which currently possess different material properties such as stiffness and viscoelastic properties compared to modern coating systems used on turbines.

Work by O'Carroll *et al.* correlated rain erosion performance with material properties obtained from nanoindentation [128]. A negative correlation between storage modulus and rain erosion performance was found, but the work could not replicate the same correlation with loss modulus as reported by Arena *et al.* [136]. A further link between high material recovery and improved erosion performance was also identified. While both short and long term recovery were studied, only the former correlated. This finding is supported by several other studies which found similar results [60, 61, 72, 139]. However, it should be noted that while the work did characterise several common polymeric materials, the ones chosen are known to demonstrate significantly less viscoelastic behaviour than the PU based coatings used in modern coatings.

While nanoindentation allows for the characterisation of the material, it only allows for the analysis at a single frequency or temperature, which could be overcome with further analysis with a technique such as DMTA. Godfrey *et al.* explored the effect of temperature on the erosion of polyurethane LEPs building on work by O'Carroll *et al.* [128, 140]. The work found that erosion performance was reduced at low temperatures resulting in an increased prevalence of abrasion and pitting. The work concludes that a coating should possess a minimal temperature dependence to improve rain erosion performance. While this work does show clear differences in erosion mechanisms highlighting the importance of temperature effects, the impacts studied were caused by solid particle erosion, which is known to induce significantly different failure mechanisms than seen in liquid impingement. These differences are commonly attributed to the differences in density between solid particulates and the absence of the water hammer phenomenon described in Section 2.4. As a comparison, it is reported that approximately double the damage was seen from water droplet impacts in comparison to solid ice spheres of comparable size and at a given speed [69]. However the current projects scope included only the effect of rain erosion as it thought to be more a more prominent issue in modern offshore wind farms.

Mishnaevsky Jr. identified key erosion predictors from published literature and also highlighted viscoelastic moduli's importance [60, 136]. A higher E' is correlated with higher erosion values caused by solid impact. The work also identifies that brittle and ductile materials can fail differently and play a significant role in erosion. Ductile materials are considered favourable due to their deformability, which results in less material being lost. The work also identifies the importance of phase-separated structures in modern PU and PUR coatings. The hard segment content is stated to directly impact the Youngs' modulus, yield strength, recovery, hysteresis and mode of failure of the coating. In contrast, the soft segment content determines the viscous behaviour of the material, which is linked to the $\tan \delta$.

A more recent study by Doagou-Rad *et al.* investigated the parameters controlling rain erosion performance through systematic finite element modelling [133]. This work was a new method that combined DMTA and finite element modelling to predict rain droplet impact behaviour. DMTA was used to obtain the viscoelastic properties and input as a Prony-parameters into the viscoelastic model created in ABAQUS FEA software in addition to uniaxial stress-strain data. The addition of the viscoelastic parameters to the model showed that the area of maximum stress moved to the area below the surface of the coating. This finding suggests that the presence of voids found within the coating from the evaporation of solvent/moisture during the curing process may be a more significant initiator for damage than previously thought.

The initial peak stress values were found to be similar; however, with the inclusion of damping behaviour, the stress in the droplet was reduced by half in addition to varying the strain rate experienced by the coating. The reduction of energy supports the currently accepted understanding that the ability of a material to dissipate energy is beneficial to the material's lifetime. The reduction in strain rate is important as while they are predicted to be in the order of 10^7 , this may only affect certain parts of the coating and not the entire thickness. Further analysis showed that defects such as voids increased the stress at those points and elevated the overall stress within the coating structure. Viscoelastic input parameters were shown to drastically alter material performance, highlighting the importance of capturing the viscoelastic effects. While experimental inputs of uniaxial stress-strain curves and DMTA temperature sweeps were used, the resulting prediction of the material responses has not been validated. As a result, the finding of this work can only be used as estimations providing a roadmap for future work identifying which material properties could play a significant role in erosion behaviour.

Domenech *et al.* identify that modern materials show a significant viscoelastic character, and as a result, the key parameters used in the Springer approach will be affected [141]. It has been identified that both frequency and temperature of the material will affect not only the viscoelastic properties but also the acoustic properties used in the Springer methodology. The work used DMTA and Dielectric Thermal Analysis⁴ (DETA) to measure the viscoelastic moduli and presents a method for linking the acoustic measurements to the storage and loss moduli. While the work does advance the field by identifying the variation in material properties due to viscoelastic characteristics, these are not implemented. The author uses constant values, irrespective of impact and environmental conditions, *e.g.* for the speed of sound. This issue is explained as the method remains consistent with Springer's approach, which is currently accepted but may not be correct. Furthermore, while the model does use material inputs the resulting stress evolutions are unvalidated and requires *in-situ* stresses to be measured but this has not been reported to date.

Further work by Domenech *et al.* built on the previous paper considering how the variations in material properties such as speed of sound would affect the predicted lifetime and add to the uncertainty in predictions [142]. The matching of layers was found to improve the predicted lifetime of LEP in specific cases significantly. However, the substrate used in prediction was found to have the

⁴ Analogous to DMTA, a specimen can be subjected to a constant or oscillating electric field rather than mechanical stress during measurements [206]. Dipoles in the material will attempt to orient with the electric field, whereas ions, often present as impurities, will move toward the electrode of opposite polarity. Even non-polar materials contain polar impurities which give sufficient response for the behaviour of the specimen to be analysed by these methods. The resulting flow of current is a measure of the freedom of charge carriers to respond to the applied field.

most significant influence. This was attributed to the substrate roles in transferring energy of impacts to the laminate, which in the case of Springer, is considered to be semi-infinite. However it was found that even with the inclusion of uncertainties results did not exactly match RET test data. Nevertheless is provides a overview of how variations in key material properties can affect the predicted lifetime.

Mishnaevsky Jr. also identifies that the thickness of the coating is critical in predicting material behaviour [60, 134]. As a stress wave travels through a medium, the intensity diminishes exponentially with the distance travelled. This phenomenon, known as attenuation, is due to several mechanisms which have been correlated to $\tan \delta$, with O'Carroll *et al.* suggesting that a material possessing a high $\tan \delta$ value is considered favourable as it ensures energy is dissipated rather than stored [128]. This correlation is further supported by Cortes *et al.*, whose findings also suggest that materials with high damping characteristics are favourable for erosion performance [72]. The work states that rapidly dissipating energy will reduce the stress at the impact surface, effectively damping the stress wave. Further work by Mishnaevsky Jr. *et al.*, that modelled segmented PU systems, also highlighted the importance of $\tan \delta$ [110]. The highlighted correlation showed that PUs with higher tan delta values showed less intensive erosion and increased coating lifetime under erosion conditions. While it is possible to design PU/PUR materials to possess good damping characteristics, these changes can also affect other properties. In the case of PU/PURs, changes to material composition can alter other mechanical properties and, in cases, make the material very sensitive to changes in temperature, neither of which are considered desirable.

2.7.6 Other Considerations

Whilst this review has covered the key areas surrounding material properties used by Springer, a further two topics which influence these are discussed. These include the potential of a material to degrade when exposed to environmental conditions and the issues surrounding standardisation in the industry.

2.7.6.1 Environmental conditions

Polymer systems are known to change over time due to harsh environmental conditions seen in the field, meaning that material properties can also vary over the lifetime of a blade [18, 67]. This change is particularly important as offshore turbines are commonly situated in challenging conditions that include elevated temperatures, UV exposure, and exposure to moisture.

PUs are considered a relatively thermostable polymer at inert atmospheres and moderate temperatures [107]. However, when held at elevated temperatures for extended periods, this class of materials have been shown to undergo chain scission of the urethane bond, causing a decrease in

crosslink density. Work by Tcharkhtchi *et al.* has shown that this phenomenon was found to decrease the T_g , Young's modulus, and strength of the PU materials, all of which are known to significantly influence erosion performance [143]. While the work does show a detrimental effect on mechanical properties, the temperatures used were 85 to 120 °C, which is not representative of offshore environments. Nevertheless, these reductions in mechanical properties may still occur at lower temperatures or over the extended period a turbine is expected to be in service.

Many studies document the impact of UV degradation on polymeric coating materials, with most showing that mechanical properties begin to deteriorate with extended exposure [122, 144]. An example is a work by Shokrieh *et al.*, which showed that through accelerated UV exposure, polyester resin exhibited a decrease of 15 % in average failure strain, a decrease of 30 % in ultimate strength and an 18 % decrease in the tensile modulus [145]. However, this effect heavily depends on the chemical nature of the matrix materials employed and highlights the possible sensitivities of any polymer system used in either the coating or composite substrate.

Exposure to moisture from rain, humidity or sea spray can also exacerbate damage to the blade [18, 70]. While the effect of moisture on the coating system is not well documented, it has been reported that through-thickness erosion can result in water and particulate (e.g. NaCl crystal) ingress to the internal blade structure [70]. This process has been identified to lead to delamination of the coating system or even compromise the blade's structural integrity due to the failure of the composite substrate [146].

2.7.6.2 Industry Standardisation

As highlighted by DNV [147], there is a lack of standardised material characterisation methodologies, which makes it difficult to know how best to analyse samples and compare results. The few available provide minimum performance characteristics but only utilise basic test methods [68, 148, 149]. While coating manufacturers have internal test methods and desired material properties, these are typically kept confidential. However, as in this work, more complex methods of characterising materials are being developed, providing a much greater understanding of material behaviour in a wide range of conditions. Nevertheless, there are still barriers to furthering the understanding.

The first is the lack of standardised test methods and parameters, resulting in large amounts of data. While more data are beneficial, the vast range of tested parameters can mean that measured results can sometimes be challenging to compare. These material parameters are now commonly used in intricate models to predict material behaviour. However, while these models produce promising results, there is a noticeable lack of widely accepted validation. This issue is due to difficulties in

capturing high strain rate responses experimentally, lack of access to test facilities and unavailability of offshore turbine data.

Furthermore, there is a lack of clear correlations when characterising different coating systems, which can be attributed to variations in chemical composition. In PU materials alone, the constituents can include essentially any structure, meaning that the number of structures produced, which can possess vastly different properties, can be considered almost unlimited [105]. This issue is commonly further compounded by the fact that work that utilises commercial coating systems do not have access to the exact chemical composition, meaning that material properties are commonly not linked directly to the molecular structure of the materials. While this is understandable as coating manufacturers are required to protect intellectual property, this hinders the ability to understand why certain correlations only hold for specific materials.

2.8 Summary

The erosion of materials by liquid impingement is an active area of research spanning multiple disciplines. As a result, a range of literature has attempted to advance the field and explain the phenomena of LEE. The scope of this review covered several areas, the prevalence and impact of LEE; modern protection strategies presently employed; the currently accepted understanding of rain droplet impact and its implications on coating design; and a summary of the material properties that influence erosion performance.

The review identifies that the issue of LEE is still significantly impacting the offshore wind industry with several recent high profile examples presented. Current solutions for mitigating LEE were summarised in addition to identifying the most commonly observed failure mode and focused upon one of the most prevalent solutions, post-mould multi-layer coating systems, which generally are low modulus and flexible. The identified coating systems were all based upon PU/PUR chemistry due to their inherent tailorability allowing for specific material properties to be obtained. The chemistry surrounding PU/PUR systems was examined, and the influence of each of the chemical constituents was defined.

It was observed that the erosion model presented by Springer *et al.* is still the most widely used and accepted method for understanding liquid droplet impingement and predicting erosion performance. Several authors have critiqued the model, identifying inaccuracies in the lifetime prediction of modern LEP solutions attributing it to shortfalls in the model and inaccuracies in the material input parameters used. Nevertheless, the model is shown to provide an adequate framework to address the problem of LEE. A concise review of the model was conducted, demonstrating the

reasoning for using low impedance materials and explaining the improved erosion properties compared to other material types. Additional parameters that influenced LEP materials' erosion performance were identified from the model and guided the subsequent section of the literature review. These were identified as Young's modulus, coating thickness, Poisson's ratio, tensile properties and the phenomena that arise from the use of viscoelastic materials. The latter included strain rate and temperature dependence, energy damping properties and the ability to recover strains after deformation.

While reviewing the literature surrounding LEE, several gaps were identified. Firstly, while the detrimental impact of LEE is widely accepted, discrepancies were found in the quantification of damage and its impact on the AEP of the turbine. This issue is attributed to the lack of a robust methodology for capturing the onset and progression of erosion damage, resulting in varying estimations by different studies. Additionally, lab-made or simulated test specimens were found to have unrepresentative erosion explaining the wide range of estimations of the impact of LEE.

Furthermore, the model proposed by Springer *et al.* makes several assumptions that need to be considered when using the method to understand and predict the impact of LEE. The first is it is considered a one-dimensional problem, where only longitudinal stress waves are considered. This issue becomes problematic as it has been shown that with certain materials with higher Poisson's ratios shear waves begin to dominate and could result in changes in the failure mode. Another issue surrounds the measurement of the *b* values used in lifetime prediction. Work shows that today's modern methods show significant variability in results, making obtaining an accurate value difficult and adding uncertainty to the prediction method.

Another gap in the literature is the lack of consideration of the implication of the viscoelasticity of modern soft coatings. With the trend towards modern LEPs that possess significant viscoelastic character, the validity of lifetime predictions for these materials has been questioned. This uncertainty has been attributed to the materials currently in use having variable material properties that depend on loading and environmental conditions. Furthermore, owing to the viscoelastic nature of the materials, the effects of attenuation and material recovery are more prominent. While these issues are identified in some literature, these factors vary significantly from material to material due to the inherent tailorability of PU/PUR chemistry.

These gaps in the literature, specifically related to the material characterisation of viscoelastic materials, must be addressed to improve the fundamental understanding of LEE of modern coating systems. Whilst literature has identified which parameters influence the erosion performance of materials, they are commonly either characterised using methods that are not comparable or not

implemented into erosion predictions. If a greater understanding is achieved, the current lifetime prediction models can be improved to account for these phenomena resulting in improved accuracy. With this development, lifetime prediction can directly improve Operation and Maintenance (O&M) strategies reducing the need for in-situ inspection. Further improvements in the fundamental understanding of viscoelasticity and LEE can also improve and develop new LEP solutions that could provide long term protection for the 25-year lifetime of the turbine.

As a consequence of the literature review findings, the research presented in this thesis addresses several issues highlighted as gaps in the literature, particularly the uncertainties around the characterisation of viscoelastic materials. Further work to develop robust test methods that can characterise viscoelastic in relation to other materials will be included in subsequent chapters.

3

Materials and Methods

This section provides a summary of the materials testing approaches used throughout the work. Each method used in work is discussed, identifying the significance, a brief overview of the theory, details of the instrument used, and the test parameters used.

3.1 Materials

The materials used in this work are commercially sensitive, and as a result, Table 3.1 assigns each material a code to allow for identification throughout the thesis.

Table 3.1 – Naming conventions for coating systems used in the thesis.

System	Material Code	Material Type
A	A1	Filler
	A2	Topcoat
	A3	LEP
	A4	LEP (Soft)
	A5	LEP (Hard)
B	B1	Filler
	B2	Topcoat
	B3	LEP
	B4	LEP Variant

System A is a commercial system comprising a filler, topcoat and three LEP materials. While A3 is the commercially available LEP material, A4 and A5 were modified versions of A3 with different soft and hard segment ratios (the exact ratio was not disclosed by the supplier).

System B is also a commercial system comprising a filler, topcoat, and two LEP materials. The difference between the two LEP has not been disclosed by the supplier.

While it is known that material properties can vary at the interfaces of multi-layer coating systems, for this work the author has chosen to focus on the characterisation of the bulk properties of the materials [72]. This is due to the currently accepted Springer model utilising bulk material properties and also allows for measured values to be more representative as it includes the effects of defects present in applied coating systems [86].

3.2 Sample Preparation

3.2.1 Material Mixing and Cure

Materials from Systems A and B were provided as two-part mixes that separated the reactive components. Mixing the components was conducted following the manufacturer's recommended guidelines with additional care taken to avoid entrapping air, produce the desired thickness, and minimise the number of voids visible in the specimen. The components for each material were mixed manually for a minimum of 30 seconds using a wooden stirrer in a disposable beaker with care taken to minimise the amount of air entrapped in the liquid.

3.2.2 Block Casting

Uncured materials were cast into custom silicone female moulds (designed by the author) made from AS40 Addition Cure Silicone Rubber supplied by Easy Composites (Stoke on Trent, UK). The uncured mixture was poured into the moulds (lowest height possible) and manually agitated to remove excess air. Two mould designs were used: cuboid specimens (60 mm x 10 mm x 2 mm) for use in dual cantilever DMTA testing; cuboids of varying depth (2 cm x 2 cm x 0.5-2 cm) for acoustic testing. Both are cured under atmospheric pressure and ambient temperature following the manufacturer's recommended procedure. Although manufacturers state that materials are suitable for service in several days, the author found that leaving the material under constant extraction for a further month ensured that all samples were hard to touch, indicating an adequate level of cure. At that point, samples with visible voids or surface curvature were discarded⁵.

3.2.3 Thin Films

Thin films were produced using a drawdown method commonly used in the paint industry to form films of specific thicknesses [150]. The uncured material is poured on to a metal plate covered with adhesive-backed plastic forming a thickness of ≈ 0.5 mm. The material is drawn down using a Baker film applicator that allows for a constant wet film thickness (WFT) between 100 μm and 400 μm to be achieved, as shown in Figure 3.1. As with the casting, the material was allowed to cure under constant extraction for one month to allow further cure.

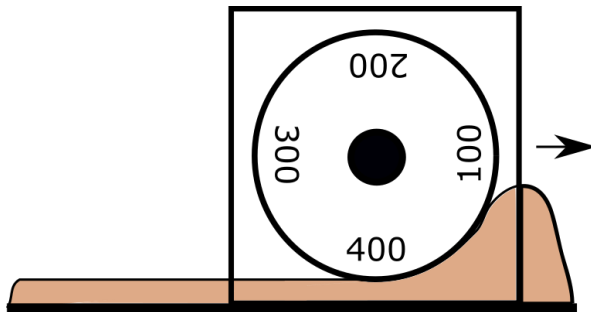


Figure 3.1 – A baker film applicator with application thicknesses of 100 μm , 200 μm , 300 μm and 400 μm used to manufacture thin specimens used for quasi-static and dynamic tensile testing. Image not to scale. Image adapted from literature [151].

⁵ While only visual inspections were used to discard unsuitable test specimens at this stage a study was conducted prior to this to optimise the manufacturing method reducing the number of through thickness voids. This included the use of different mixing methods (manual/powered) different curing surfaces and were quantified using cross sectioning, density measurements and variability in tensile properties.

3.2.4 Coated Panels

Six composite panels were also manufactured following standard techniques used in the Bristol Composites Institute (BCI). Unidirectional E-Glass (06-UE-591-1200) and E-Glass biaxial +/-45° (20-EX600-127) 600 g/m² fabrics supplied by Saertex (Saerbeck, Germany) were used in combination with the RS-M135 low-temperature cure epoxy and hardeners (RS-MH134 and RSMH-137) supplied by PRF Composites (Poole, UK). This resin system is re-branded from Hexion RIMR 135 & RIMH 134-137. Several composite panels ([+/-45, 0, +/-45, 0, +/-45]) were manufactured using resin infusion. The bagged fibres, seen in Figure 3.2, were infused following standard BCI procedure at room temperature. The plates were cured using the supplier's recommended parameters (16 hours at 60 °C) with no post-curing steps.

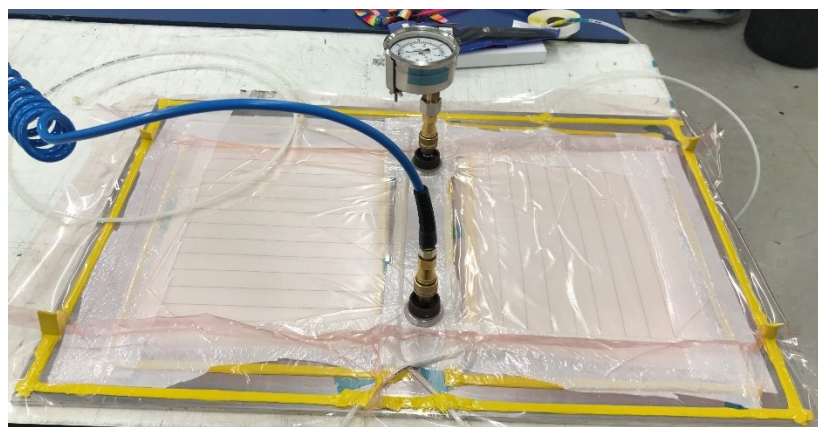


Figure 3.2 – An image showing the bagged glass fibre under vacuum before the resin infusion process is undertaken. Image not to scale.

Cured composite panels were inspected using a tap test method and visual inspection to ensure consistency and identify poorly infused areas. The panels were then trimmed using a composite diamond saw and sanded with P180 grit paper. This stage was followed by cleaning with ethanol, a microfibre cloth and pressurised air to remove any remaining particulates.

While each coating system has different recommended application procedures, e.g. overcoat times, wet film thicknesses (WFT) and the number of repeat coatings, a generalised methodology for coating a composite panel is provided.

- First, the filler material is applied using a smoothing tool with cork guides to maintain a constant thickness. This layer was allowed to cure at ambient temperature for the time specified by the coating manufacturers before being sanded (P240) and cleaned using ethanol and microfibre cloth. These surfaces were then dried using compressed air and left at ambient temperature for five minutes.

- The topcoat system is applied using a short nap roller as recommended by the coating manufacturers and cured at ambient temperature. After the recommended curing time, the topcoat layer is sanded (P240) and wiped clean.
- The LEP is applied using a new short nap roller to the recommended WFT, in cases, multiple layers are applied to reach the desired Dry Film Thickness (DFT), and again allowed to cure at RT under constant extraction for a minimum one month.

The cured panel is then trimmed using a Computer Numerical Controlled (CNC) diamond saw while utilising a low feed rate and high cutting speed to minimise the delamination of layers. An example completed system coated on a composite substrate is seen in Figure 3.3.

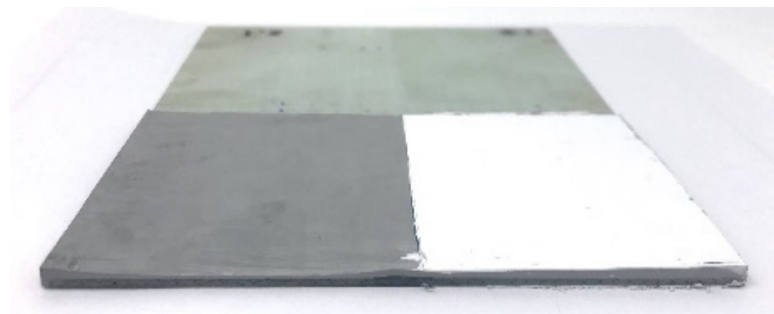


Figure 3.3 – Demonstrator sample of sequential application steps. Top left: GFRP composite. Top right: sanded composite. Bottom left: Filler layer application. Bottom Right: Topcoat and LEP layer. Image not to scale.

3.3 Thermogravimetric Analysis

Thermogravimetric Analysis (TGA) measures the thermal stability of materials such as polymers. This method was used in Chapter 6 to determine the onset of degradation, moisture content, and residual mass of coating materials to ensure subsequent testing was not causing significant thermal degradation. The weight change of the substance is monitored as a function of temperature or time while the specimen is subject to a controlled temperature program under a controlled (nitrogen or air) atmosphere.

A calibrated NETZSCH STA 449 F3 Jupiter® equipped with an autosampler was used. The sample cell was used under air, with a constant flow rate of $50 \text{ cm}^3 \text{ min}^{-1}$. Nitrogen was used as a protective gas with a constant $20 \text{ cm}^3 \text{ min}^{-1}$ flow rate. Open aluminium oxide crucibles containing 5 - 10 mg of the cured material (obtained from larger cast specimens) was used.

Samples were equilibrated at RT, followed by a temperature ramp to 800°C at a heating rate of 10 K min^{-1} under air and nitrogen, respectively. From these data, the onset of degradation can be deduced to inform further testing.

3.4 Dynamic Mechanical Thermal Analysis

Dynamic mechanical thermal analysis (DMTA), used predominantly in Chapter 6, is an instrument utilised to characterise the viscoelastic behaviour of solid materials under controlled conditions [134, 152]. It is achieved by applying a sinusoidal stress or strain to a sample and analysing the transient or dynamic response. This approach is very sensitive to the polymer chain motions and so allows for the interrogation of polymer transitions. A calibrated TA DMTA Q800 equipped with an ACS chiller system was used for testing. Dual cantilever and tensile fixtures, designed for use with the DMTA, were purchased from TA instruments and used to assess the properties of cuboid and thin film samples, respectively.

The most common DMTA approach utilised in literature is the dynamic oscillatory test, where a sinusoidal stress/strain is applied to the material, and a resultant stress/strain is measured. From these responses, the phase difference (δ) between the two sine waves can be deduced. For purely elastic materials, this lag will be 0° and 90° for a purely viscous material. However, viscoelastic materials exhibit elastic and viscous character to different extents resulting in an intermediate phase difference. From the measurement of δ and the stress/strain, the storage modulus (E') and loss modulus (E'') can be deduced. E' is the elastic component related to the material's stiffness and ability to store energy. E'' is the viscous component and is linked to the ability of the material to dissipate energy. The tangent of the phase angle ($\tan \delta$) is another important parameter that can also be deduced; this is a measure of material damping and implies a more significant potential for energy dissipation and lower elasticity. This parameter can also be calculated by dividing E'' by E' .

For dynamic oscillatory testing, three test types were utilised with the available dual cantilever and tensile fixtures:

- Strain sweeps were used to determine the linear viscoelastic region (LVER) of each material. In these experiments, the frequency (1 Hz) and temperature (RT) are held constant while the strain is increased (to a minimum of 400 μm). Subsequent tests used an amplitude/strain within this region, selected as 0.1 % to 0.01 % strain (see Chapter 6 for further details).
- Temperature sweeps were used to identify the transitions in the material, particularly the most significant change, the T_g . In these experiments, the frequency (1 Hz) and amplitude (within the LVER) were held constant while the temperature was increased. Samples were equilibrated at the start temperature of -50 °C for a minimum of 5 minutes, at which point a 10 °C min⁻¹ temperature ramp was applied to reach the desired final temperature. This final temperature was set below the onset of degradation determined through TGA. Three T_g values are presented, the E' onset, the E'' peak maximum and $\tan(\delta)$ peak maximum.

- Frequency sweeps were used to identify the effect of frequency on the viscoelastic properties of the material, in particular, the change in damping behaviour. In these experiments, the amplitude (within the LVER) and temperature (RT) were held constant while the frequency of oscillation was increased (1 – 100 Hz).

3.5 Nanoindentation

Nanoindentation was used in Chapter 5 to identify the hardness, Young's modulus, indentation work and short term recovery of coating materials. The general principle of indentation applies a predefined load or depth, which is then removed, returning to the unloaded state. Upon removing the load, the material begins to recover to its original shape, but it is reduced by any plastic deformation. During this process, the instrument records the depth of penetration of an indenter, of known geometry, into the specimen in addition to the measured load.

Nanoindentation was chosen over micro indentation as it utilised projected contact areas rather than the needing to measure the area using an optical microscope after indentation which is difficult to obtain due to the rapid recovery of the materials. It also provided greater instrument resolution essential for the analysis of soft polymers and allowed for the effects of local defects, interfaces and changes within micron thick layers.

Conventional indentation tests measure the residual impression left due to plastic deformation to calculate material properties; however, the contact area used in nanoindentation is too small to measure accurately using optical methods. Instead, the contact area is calculated from the measured depth of penetration and the known geometry of the indenter. From the instrument output, as shown in Figure 3.4, and the indenter properties, the mechanical properties of the materials can be extracted based on the Hertz elastic contact equations [153, 154].

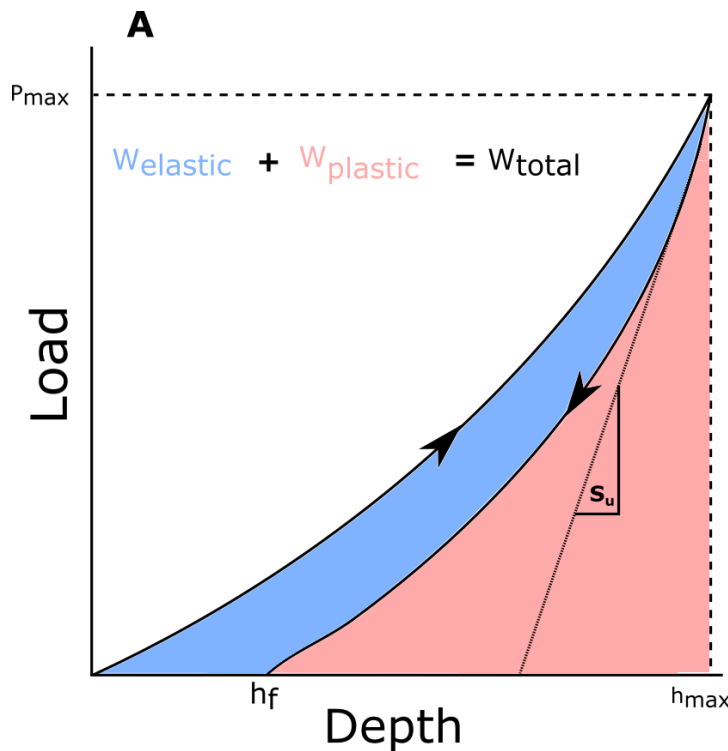


Figure 3.4 – A representation of indentation-load displacement data showing key parameters: P_{max} the peak indentation load, h_{max} the indenter displacement at peak load, h_f the final depth of the contact impression after unloading and S_u the contact stiffness of the unloading curve calculated from the unloading gradient. The area highlighted blue illustrates $W_{elastic}$ the elastic work, the area highlighted red illustrates $W_{plastic}$ the plastic work, the sum of these values, give W_{total} the total work during the indentation test. Figure adapted from the literature [155].

Cross-sections of the coated composite panels (detailed in Section 3.2.4) were used to characterise individual layers using nanoindentation. The coated panels were sectioned into several 1 cm² samples using a CNC diamond saw while utilising a low feed rate and high cutting speed to minimise the delamination of layers. These materials were cast in EL2 Laminating resin (Easy Composites, U.K) forming cylindrical specimens, as seen in Figure 3.5. These were polished to avoid measurement errors from surface uncertainties using a lapping wheel and progressively finer SiC papers (12 to 1200 grit). Care was taken to ensure no resin was left on the surface and that the face was flat, a key requirement for nanoindentation testing.



Figure 3.5 – An image of the sectioned composite panels cast into a resin. The surfaces were polished using a lapping wheel prior to nanoindentation testing. Image not to scale.

The load-hold-unload indentation cycles were conducted using a Hysitron TI Premier equipped with a Berkovich shaped⁶ diamond indenter. A fused silica reference sample was used for calibration before conducting the nanoindentation. Both load P_{Indent} and displacement h_{indent} were continuously recorded during the experiment, and with responses obtained with a minimum distance of 20 nm between indents. Various loading programs were used and are defined later in Chapter 5. However, each test followed a variation of the load-hold-unload cycle to identify the effect of varying indentation depth, load and loading rate.

In this work, Oliver-Pharr⁷ analysis was used to determine the hardness and reduced elastic modulus from the unloading curve [156]. Hardness (H) is a ratio calculated by

$$H = \frac{P_{max}}{A_c} \quad 3.1$$

where P_{max} is the maximum load and A_c is the projected area of indentation.

Unloading contact stiffness (S_u) is determined from the initial unloading slope at P_{max} by

$$S_u = \frac{dP_{Indent}}{dh_{indent}} \quad 3.2$$

where P_{Indent} and h_{indent} denote the applied load and penetration depth, respectively.

The reduced elastic modulus (E_r) is calculated with the contact stiffness by

$$E_r = \frac{S_u \sqrt{\pi}}{2\beta \sqrt{A_c}} \quad 3.3$$

where β is a factor related to the specific geometry of the Berkovich indenter.

The Young's Modulus (E) is calculated by

$$E = \frac{1 - \nu_s^2}{E_r} \sqrt{\frac{1}{E_r} - \left(\frac{1 - \nu_i^2}{E_i} \right)} \quad 3.4$$

where E_i and ν_i (quoted as 1140 GPa and 0.07 respectively by Bruker) represent the elastic modulus and Poisson's ratio of the indenter whereas E_s and ν_s correspond to specimen values.

Further analysis of the data yields two more parameters of interest:

⁶ The Berkovich tip is a three-sided pyramid. The angle between the centerline and the three faces is 65.3°.

⁷ The most frequently adopted method in instrumented indentation is to calculate the elastic modulus of materials [173].

Short Term Recovery (*STR*) is a measure of elastic recovery and is thought to be a key variable in raindrop impact. This parameter was calculated by

$$STR = \frac{(h_{max} - h_f)}{(h_{max})} \quad 3.5$$

where h_{max} and h_f denotes maximum indenter depth and final indenter depth, respectively.

The work done during the indentation which relates to deformation, movement and reorientation of different structural elements can also be calculated by integrating the area under the loading and unloading curve [157, 158]. The total apparent work (W_{total}) is calculated by

$$W_{total} = W_{elastic} + W_{plastic} \quad 3.6$$

where $W_{elastic}$ is the recoverable apparent elastic work and $W_{plastic}$ is the non-recoverable apparent plastic work.

3.6 Quasi-Static Tensile Testing

The mechanical properties of polymer films (detailed in Section 3.2.3) were determined using tensile testing to determine whether rate-dependent behaviour was observable during quasi-static testing. These properties are particularly important as lifetime prediction models utilise tensile properties, such as ultimate tensile strength (*UTS*), as an input.

Thin-film samples were cut into 15 x 5 mm strips and bonded onto paper templates with epoxy adhesive at each end, as shown in Figure 3.6. The paper was used to hold the sample, preventing misalignment and minimising slack, both of which would affect results. Once the sample was loaded into the instrument, the paper template was carefully cut to allow film properties to be measured.

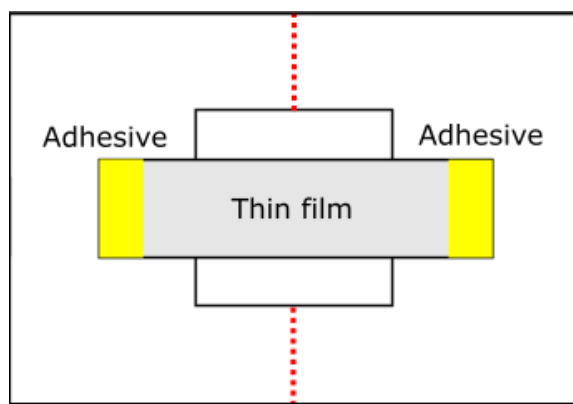


Figure 3.6 –The schematic represents the thin film specimen bonded to the paper template using epoxy adhesive (yellow) before tensile testing. A gauge length of 10 mm was used for each test. The red dotted lines indicate the area to be cut once the sample is loaded into the test rig. Figure adapted from the literature [159].Image not to scale.

The mechanical properties were tested using a Deben rig (Deben Microtest MT200 Tensile Tester) shown in Figure 3.7, under displacement control with 5 and 20 N load cells. Two crosshead displacement rates (0.5 mm min^{-1} and 2 mm min^{-1}) were used to obtain the material properties and observe any strain rate dependent behaviour.



Figure 3.7 – Thin-film undergoing tensile testing in a Deben Microtest MT200 tensile tester. The instrument is approximately $15 \text{ cm} \times 8 \text{ cm} \times 5 \text{ cm}$ for reference. Image not to scale

Stress-strain curves were produced based on the acquired load-displacement data, as shown in Figure 3.8. Following ASTM D882-00, toe compensation was carried out to correct for artefacts caused by the take up of slack or incorrect seating of the samples [112]. Two variants of Young's modulus (E) were determined. First, the tangent modulus (E_{tan}) was calculated using linear regression within the linear elastic region. Additionally, the secant modulus (E_{sec}) was calculated by performing a linear regression between the corrected origin and the value at 0.4 strain corresponding to the maximum expected strain in a droplet impact [67]. The Ultimate Tensile Strength (UTS) was determined as the maximum stress value on the stress-strain curve. Strain-at-break (ϵ_{break}) was the strain value at the point of failure where the load drops to zero. The toughness was determined from the area under the stress-strain curve.

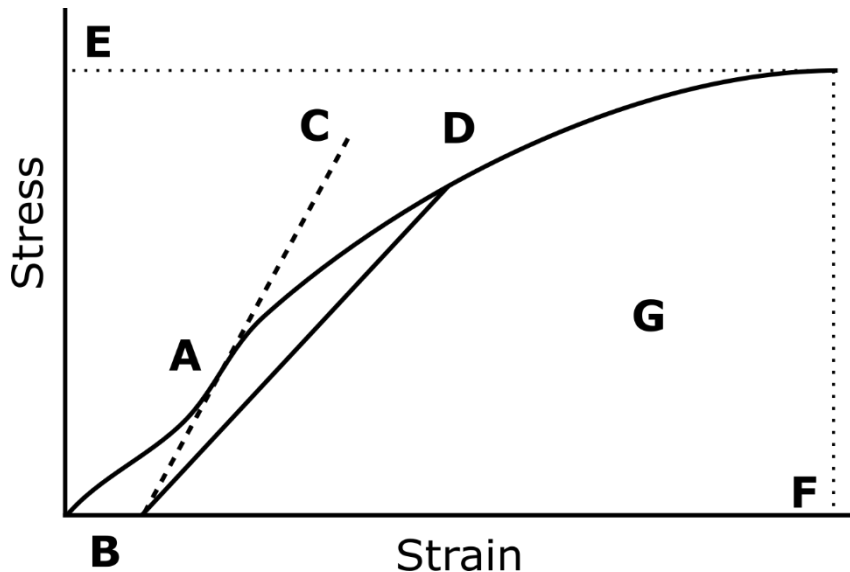


Figure 3.8 – Example material stress-strain curve detailing key points of interest. A: linear elastic region where stress is proportional to strain and generally obeys Hooke's law. B: The area toe corrections are applied as detailed in ASTM D882-00. C: The tangent modulus (E_{tan}) is calculated from the tangent of the Linear region. D: The secant modulus (E_{sec}) calculated from the secant from the toe corrected origin and the value at 0.4 strain. E: The ultimate tensile stress (UTS) is calculated from the maximum stress. F: The strain at break (ϵ_{break}) is calculated from the point of failure where load drops to zero. G: The toughness is calculated as the area under the stress-strain curve. Figure adapted from ASTM D882-00 [112].

3.7 Accelerated Rain Erosion Testing

An accelerated⁸ rain erosion test is used to assess the performance of LEP systems against the impingement of water. The standard testing procedure⁹ developed by the Offshore Renewable Energy Catapult (OREC) aims to quantify rain erosion resistance of LEP systems, in terms of time, through extended exposure of test specimens. This allows for simple comparisons between systems to be made. As this is an accelerated test, results cannot currently be related with any degree of certainty to the performance of the system when applied to a turbine blade offshore.

GFRP composite test specimens (NACA634-021 aerofoil geometry) supplied by Olsen Wings were used as a standardised substrate. These were then sent to each coating manufacturer to apply the complete coating system to minimise defects and variability. Before testing, each coated specimen was photographed and visually inspected to identify defects that could act as initiation sites.

Rain erosion tests are carried out using the OREC whirling arm rain erosion tester (WARET), supplied by R&D AS. Access to the WARET was made possible through the collaboration with OREC, who trained the author to operate the system independently during a secondment to the test facility in Blyth, UK. The test rig, shown in Figure 3.9, is a standard design analogous to those used in the

⁸ The test is considered accelerated as the rotational velocities, droplet sizes and impact frequencies the test specimens are exposed to can exceed those observed in operation.

⁹ Developed by OREC to comply with both ASTM G73 and DNVGL-RP-0171 [147, 207].

DNVGL-RP-0171 guideline. The rig comprises a whirling arm configuration with three arms, testing three samples simultaneously whilst exposed to the same distributed rain field produced from 600 needles, freely dropping water at a 90° angle to the leading-edge under gravity. The test rig is semi-autonomous with an in-built camera system that is used to photograph the specimens at various intervals, called slices, during testing. At the end of each slice, specimens are removed, weighed, manually photographed, and any changes documented. As the test progresses material loss is observed and stopped upon the exposure of the composite substrate.



Figure 3.9 – Image of the whirling arm rain erosion tester at the Offshore Renewable Energy Catapult (OREC) in Blyth, UK.

A wide number of parameters can be controlled and are recorded throughout the test program. The operational limits of the WARET are detailed in Table 3.2.

Table 3.2 – Operational limits of whirling arm rain erosion tester. The rotational speed of 500-1386 rpm results in a rotation speed range of 42.2 – 173.4 ms⁻¹, dependent on the location of the specimen.

Parameter	Unit	Operating Range
Droplet diameter	mm	2.0-3.5
Rotational speed	rpm	500-1386
Water flow-rate	l/hr	20-120
Water temperature	°C	0-30
Chamber temperature	°C	0-30

The naming conventions used to identify specimens and test parameters are detailed Figure 3.10. The first letter defines the substrate material used where A and B denote aluminium and GFRP, respectively. The following segments represent the test parameters used: rotational speed (RPM), flow rate (l/h), needle gauge, tested material, and the test number.

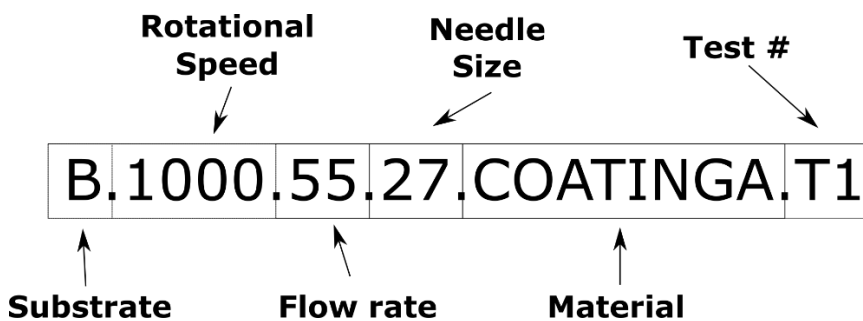


Figure 3.10 – A schematic detailing the naming conventions used to identify the rain aerofoil shaped rain erosion test specimens.

As several parameters can be varied, numerous test programmes can be conducted. Currently, different standard tests are defined between different facilities and organisations¹⁰. Tests for this project used a wide range of parameters that included the use of the statistical Design of Experiments (DOE) and are detailed in Section 7.

The work utilises two methods for assessing the rain erosion performance of LEP:

- Qualitative analysis is conducted through visual inspection. Before testing, samples are photographed, documenting the size and location of any observable defects along the specimen's length. During testing, the specimens are inspected at the end of each slice, recording any changes to the material surface. Comparisons of the time to end of incubation (onset of surface damage) and failure (exposure of composite substrate) are used to compare LEP system performance tested under the same conditions.
- Quantitative analysis is used to generate incubation and breakthrough curves following the DNVGL RP-0171. After each test slice, the number of impacts per unit area is plotted against the calculated impact velocity at the damage location. As damage progresses toward the specimen root, curves for the end of incubation and breakthrough are produced. These curves can be transformed into the log-log scale and fit using a power-law equation resulting in a curve resembling the SN curves discussed in Section 2.5. The power laws and subsequent parameters are reported and can be used to compare different LEP systems under the same test conditions.

¹⁰ The standard testing parameters used by the ORE-C is defined as 55 l/h and 1000 rpm. In comparison, the DNV guidelines are defined as 800 rpm and approximately 2 mm droplet diameter [147].

3.8 Ultrasonic Acoustic Testing

Ultrasonic testing is utilised in Chapter 6, it uses high-frequency sound to examine materials as described in DNVGL-RP-0573. This is particularly important as the lifetime prediction of LEP systems utilises the material speed of sound (C) as a key input.

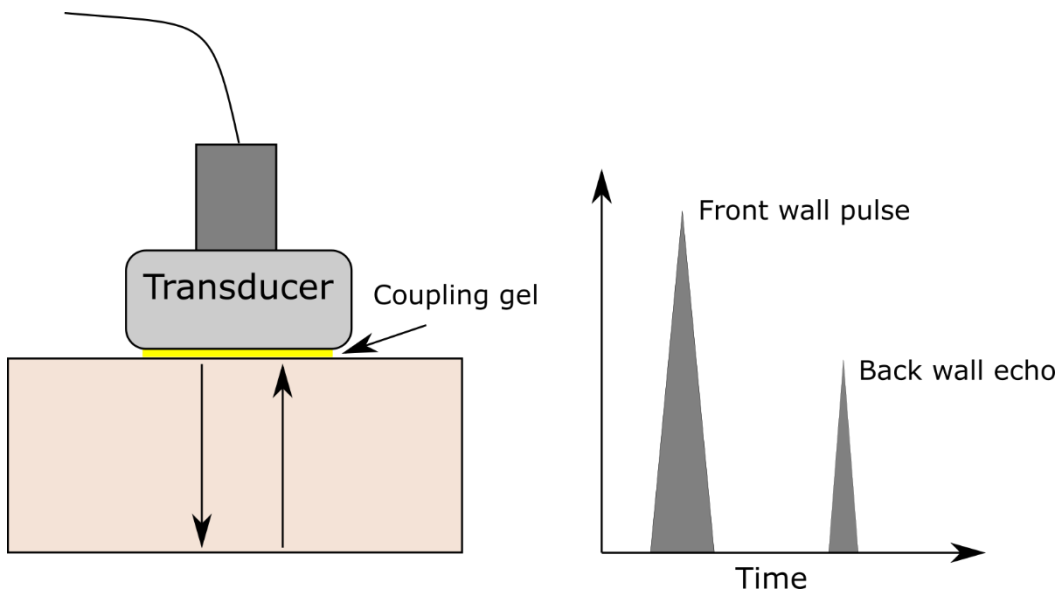


Figure 3.11 – A Schematic is shown detailing the pulse-echo acoustic measurement technique of a homogeneous material. Left: A diagram showing a transducer placed on the material using a coupling gel between the interface. A signal is passed through the thickness of the material reflecting off the back wall resulting in a signal. Right: A representation of the expected signals. The first to occur is a reflection from the material's front wall, followed by a lower magnitude echo from the back-wall reflection. Figure adapted from the literature [160].

This measurement utilised the pulse-echo technique, as shown in Figure 3.11, which is based on analysing the propagation of ultrasonic waves through homogenous coating materials. For this work, cast cuboids of each material with varying depths (2 cm x 2 cm x 0.5-2 cm) were used for acoustic testing, as detailed in Section 3.2.2. The method is used to determine the time for the signal to travel between the front and back wall of the test specimen of known thickness. This reflection is possible as, at each interface, some signal is reflected towards the transducer. By identifying the time between these signals, the speed of sound (C) can be calculated by

$$C = \frac{2h}{t_{Echo}} \quad 3.7$$

where h is the thickness of the specimen and t_{Echo} is the time between the front and back wall echo.

An OLYMPUS 5072PR pulser/receiver was used to generate the pulse signal in combination with a Keysight InfiniiVision DSOX2024A digital storage oscilloscope which visualised and recorded the responses. A 5 MHz (Olympus Panametrics-NDT V310- 5MHZ/0.25") transducer was used to characterise materials. Videoscan transducer variants were used which were identified as the best

option for highly attenuating materials as they provide a good signal-to-noise ratio while possessing a slightly broader frequency response.

To analyse the responses, raw data were filtered using a MATLAB® bandpass filter, removing signals outside the 1 – 10 MHz range [161]. The Hilbert transform was then used through MATLAB® to create an analytic signal and the response envelope [162]. The peaks of each envelope were then used as markers to calculate the material speed of sound.

3.9 Summary

As many samples were manufactured and tested, not all the data can be included in the thesis. The samples prepared and the tests used are summarised below.

The thermal analysis techniques utilised material extracted from cast specimens or an uncured mixture of the precursor materials. TGA was used to determine the thermal stability of all materials tested to inform subsequent testing.

Several composite panels were manufactured and coated with Systems A and B for subsequent testing. These panels were sectioned and made into six potted specimens used for the nanoindentation tests. The three specimens made were; system A with A3 LEP, System B with B3 LEP, System B with B4 LEP. Nanoindentation was used to characterise the six different potted coating cross-sections, including system A with A3 LEP, System B with B3 LEP, and System B with B4 LEP. Three different tests methods were used to characterise each material layer (18 tests).

All materials were cast into specimens used for dual cantilever DMTA (60 mm x 10 mm x 2 mm), ultrasonic acoustic testing (2 cm x 2 cm x 0.5-2 cm), thin films (200 µm and 400 µm thickness) for dynamic and quasi-static tensile testing. DMTA was used to characterise both the dual cantilever and thin-film specimens. Dynamic testing included: strain sweeps, temperature sweeps, and frequency sweeps (at temperatures between -40 °C and 50 °C). Transient testing included: strain sweeps, creep tests, and stress relaxation studies (ambient temperature). Quasi-static tensile testing of the cast thin films was conducted on A1, A2, A3 and B1, B2, B3, B4 (14 total tests). Ultrasonic Acoustic Testing of all materials was conducted using 5 MHz and 10 MHz transducers and at multiple thicknesses (48 samples).

Coating of leading-edge RET specimens was conducted externally by each manufacturer for each of the 15 RET tests (45 samples total). RET testing was used to determine the rain erosion performance of the five LEP systems utilised in the work. This was achieved through standard testing methods and a novel systematic design of experiments approach, totalling 15 RET tests in triplicate.

4

Tensile Testing

This chapter presents the results of the tensile testing of thin-film specimens at two different displacement rates. While not all materials showed strain-rate dependent behaviour, fundamental material properties such as strain to break, toughness, Young's modulus and ultimate tensile strength were captured and compared.

4.1 Introduction

The Springer lifetime prediction model, detailed previously in Section 2.5, identifies a set of material properties that influence a coating material's erosion performance and consequent lifetime [86]. These include several properties obtained using either quasi-static or cyclic tensile testing, such as the ultimate tensile strength (*UTS*), the fatigue *b* value and the Young's modulus (*E*). As the tested polymeric systems are considered viscoelastic, they demonstrate both elastic and viscous behaviour when deformed [163]. As a result, viscous behaviour dominates when a slow deformation is applied, whereas, at a higher deformation rate, the elastic behaviour dominates [134]. This phenomenon results in material properties varying at different strain rates and is termed strain-dependent behaviour. The impact of this variability of material properties is typically not considered or approximated as constant in current material lifetime prediction [86, 147].

Thin-film tensile testing was employed, as detailed in Section 3.6, as a starting point to characterise the different materials used in this work. The aim was to determine whether any statistically significant differences could be observed when testing at two different displacement rates (0.5 and 2 mm/min), adapting the methodology from ASTM D638-14 [113]. Each test was replicated ($N=7$); however, specimens that failed outside of the gauge length (e.g. within the grips) or failed due to a defect were omitted as suggested by the standard. These incorrect failures resulted in varying numbers of replicates in each test condition; a minimum of three successful tests were conducted for each condition; the results extracted from the stress-strain data are summarised into box and whisker plots for brevity. A p-value of 0.05 was selected as the threshold of significance for this work. Therefore t test results with a p-value less than 0.05 are considered statistically significant. Conversely, if the calculated p-value is higher than 0.05, it is considered not to be statistically significant.

4.2 Results

The planned tensile test campaign was completed and captured the stress-strain curves of all the coating materials apart from A4 and A5 as they were introduced into the testing at the end of the project. Examples of these curves are presented in Figure 4.1 and demonstrate the clear differences in response between material types. The following sections examine the material responses, explore the differences in key properties derived from these curves, and identify any statistical differences.

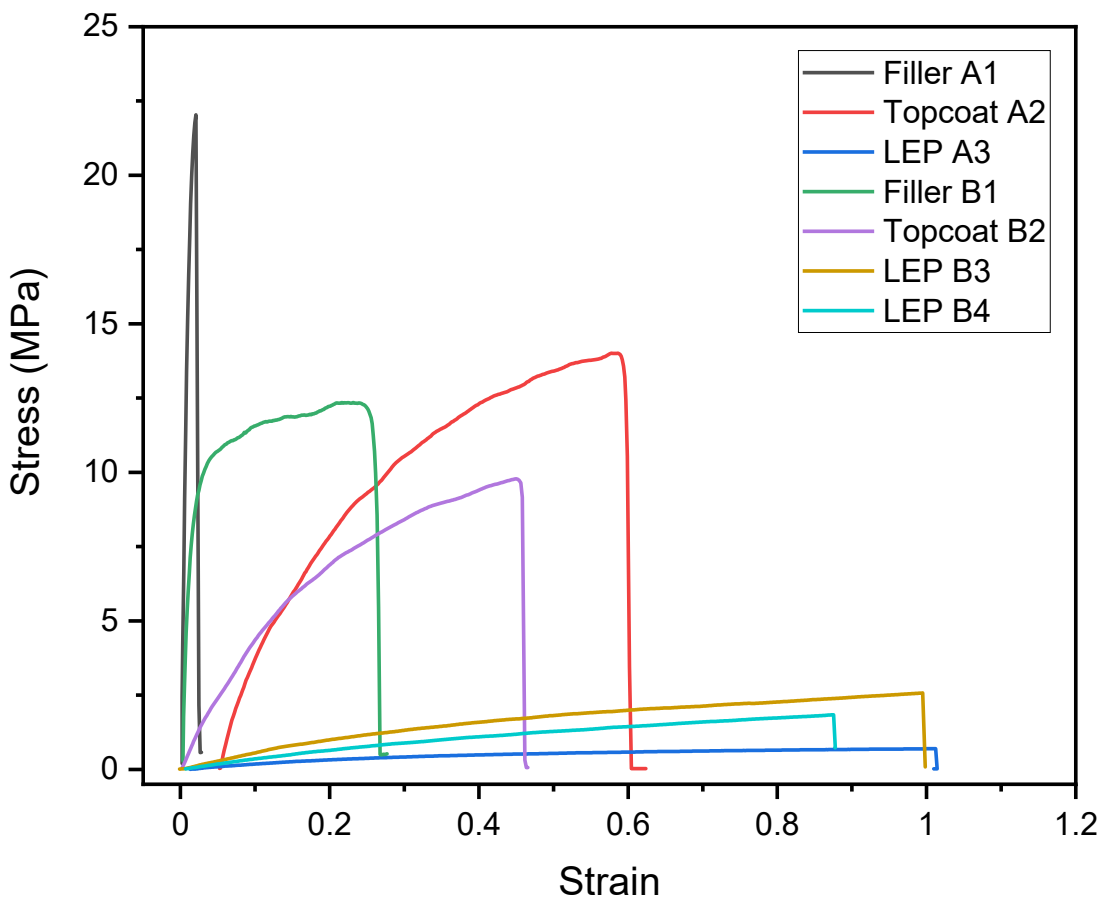


Figure 4.1 – Representative stress-strain curves for each coating material obtained at a 2mm/min displacement rate.

4.2.1 Strain at Break

Strain at break (*STB*) is a measure of material ductility, indicating how much a material can be elongated before breaking. Table 4.1 and Figure 4.2 provide comparisons of the measured *STB* values.

Table 4.1 – Comparison of the tensile strain break (*STB*) of materials used in leading-edge protection systems at 0.5 and 2 mm/min displacement rates.

Material	Displacement Rate (mm/min)	
	0.5	2
LEP B4	0.832 ± 0.090	0.861 ± 0.014
LEP B3	0.868 ± 0.040	0.829 ± 0.184
LEP A3	0.987 ± 0.016	0.967 ± 0.065
Topcoat B2	0.325 ± 0.007	0.414 ± 0.111
Topcoat A2	0.489 ± 0.097	0.608 ± 0.081
Filler B1	0.298 ± 0.029	0.281 ± 0.062
Filler A1	0.054 ± 0.055	0.027 ± 0.006

As expected, the LEP materials showed the largest *STB* values of the material types tested, with an average of 0.89 strain. No significant differences were seen between displacement rates, indicating no strain-rate dependency. At the 0.5 mm/min rate, the LEP A3 material displayed significantly greater *STB* than the LEP B3 and LEP B4 materials. However, at the 2 mm/min rate, the LEP A3 *STB* was only significantly greater than the LEP B4 material.

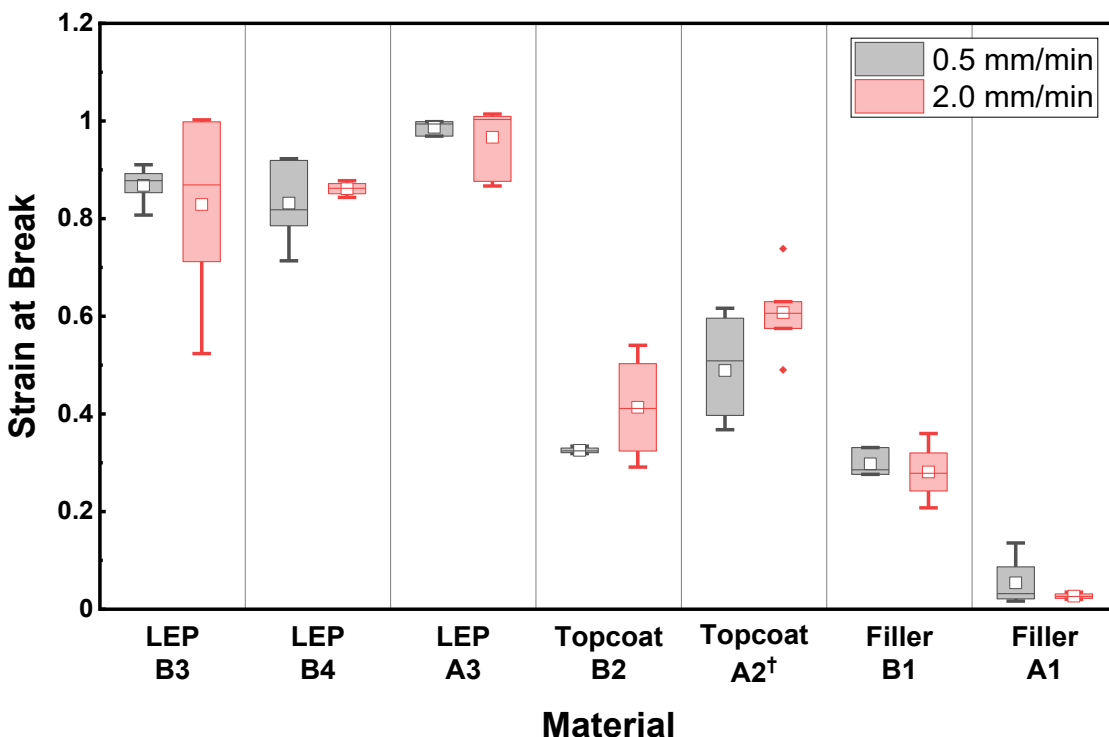


Figure 4.2 – A box plot is presented comparing the tensile strain break (*STB*) of materials used in leading-edge protection systems at 0.5 and 2 mm/min displacement rates. The [†] symbol denotes a significant difference ($P < 0.05$) between the two different displacement rate conditions, indicating that the material properties are dependent on the strain rate.

The average topcoat *STB* values were 0.46 strain, considerably lower than the LEP materials. This difference is an interesting observation as it shows that the materials used as the outmost coatings of the blade can withstand different magnitudes of deformation before failure. The topcoat A2 material was found to have significantly different *STB* values at each displacement rate, demonstrating strain-dependent behaviour. The topcoat A2 materials also showed significantly greater *STB* values at both displacement rates when compared with topcoat B2.

The filler materials, which were observed to be the most brittle, showed the lowest *STB* values of material types tested, with an average of 0.16 strain. While no significant differences were found between displacement rates, the filler B1 material showed significantly higher *STB* when compared to filler A1 values at both displacement rates.

4.2.2 Toughness

Toughness is the ability of a material to absorb energy without fracture. In a tensile stress-strain plot, the area under the curve is used to quantify this parameter. Table 4.2 and Figure 4.3 provide comparisons of the measured toughness values.

Table 4.2 – Comparison of the toughness values of materials used in leading-edge protection systems at 0.5 and 2 mm/min displacement rates.

Material	Displacement Rate (mm/min)	
	0.5	2
LEP B4	0.827 ± 0.126	0.881 ± 0.075
LEP B3	1.338 ± 0.119	1.173 ± 0.364
LEP A3	0.326 ± 0.026	0.394 ± 0.062
Topcoat B2	1.580 ± 0.144	2.649 ± 0.990
Topcoat A2	3.716 ± 0.964	5.343 ± 1.218
Filler B1	2.716 ± 0.258	3.028 ± 0.706
Filler A1	0.500 ± 0.337	0.279 ± 0.116

The LEP materials showed the lowest toughness values of the tested material types, with an average of 0.83 MJ/m^3 . They generally were observed to be the most ductile and resulted in the lowest stresses of the materials tested. While no LEP showed a significant difference under different displacement rates, a trend in toughness can be seen when comparing the different materials. At 0.5 mm/min, significant differences can be seen between the materials where LEP B3 > LEP B4 > LEP A3. At 2 mm/min, no significant difference was found between LEP B3 and LEP B4; however, the former showed a wider range of results than other materials. Furthermore, it can be seen that LEP A3 is significantly different, measuring lower toughness values than both LEP B3 and LEP B4 materials.

The topcoat materials were found to have the highest average toughness value of 3.30 MJ/m^3 . These higher toughness values resulted from a combination of the strength and ductility of the material. This higher toughness could be beneficial as topcoat materials are used to coat the majority of the blade providing all-around protection. The topcoat A2 material displayed a significant difference in toughness, showing a higher value at the increased displacement rate, indicating strain-rate dependency. The topcoat A2 material also possessed significantly higher toughness values than topcoat B2 at both displacement rates.

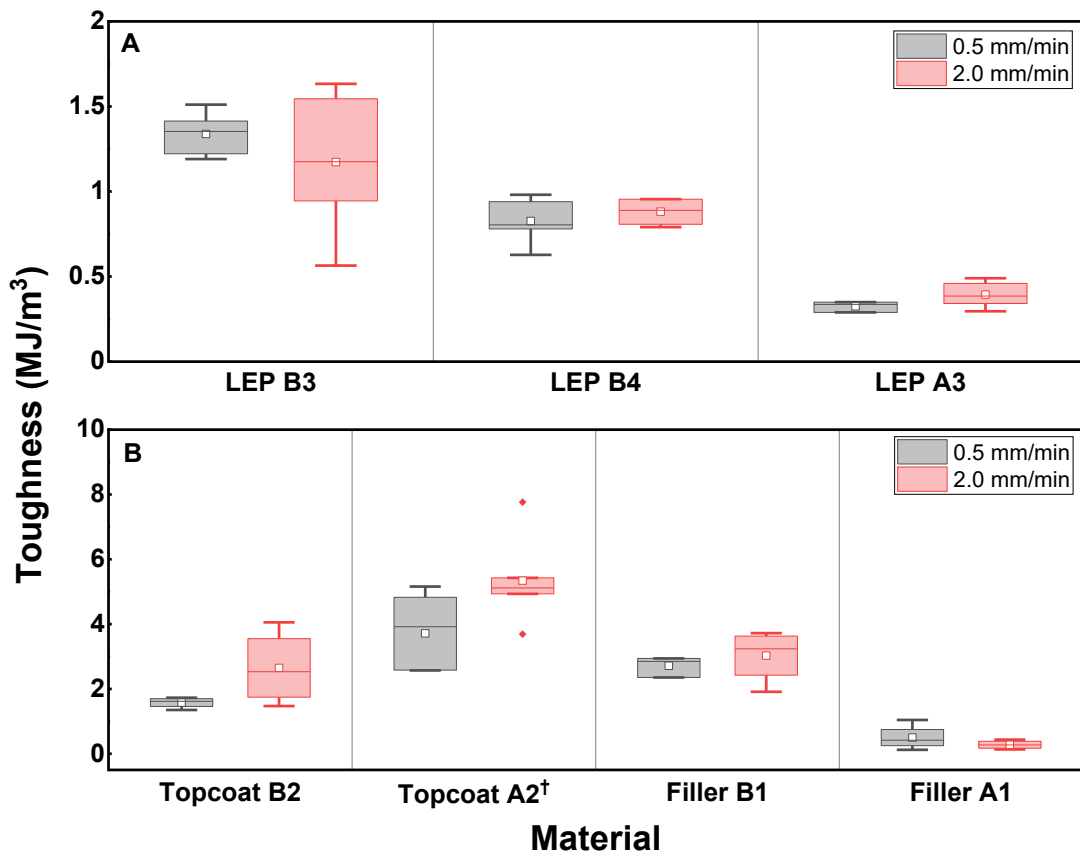


Figure 4.3 – A box plot is presented comparing the tensile toughness of materials used in leading-edge protection systems at 0.5 and 2 mm/min displacement rates. Table A is a comparison of LEP materials, and Table B is a comparison of topcoat and filler materials.

The filler materials were found to have an average toughness value of 1.60 MJ/m³. The highest stresses were observed when testing these materials, but considerably lower toughnesses were observed due to the low ductility of this material type. While neither of the materials showed a significant difference under different displacement rates, filler B1 was found to have significantly greater toughness values in both conditions when compared to filler A1.

4.2.3 Tangent Modulus

The Tangent modulus (E_{tan}) describes the material's stiffness obtained from the linear region of the material response. Table 4.3 and Figure 4.4 provide summaries of the measured E_{tan} values.

Table 4.3 – Comparison of the tangent modulus (E_{tan}) values of materials used in leading-edge protection systems at 0.5 and 2 mm/min displacement rates.

Material	Displacement Rate (mm/min)	
	0.5	2
LEP B4	3.276 ± 0.250	3.686 ± 0.520
LEP B3	4.894 ± 0.374	4.988 ± 0.436
LEP A3	1.137 ± 0.287	1.642 ± 0.269
Topcoat B2	34.421 ± 3.714	39.060 ± 1.710
Topcoat A2	43.391 ± 7.580	62.054 ± 17.146
Filler B1	477.391 ± 89.758	690.318 ± 101.071
Filler A1	1405.195 ± 365.210	1332.429 ± 218.619

The LEP materials showed the lowest E_{tan} values of the tested material types, with an average of 3.27 MPa when including all displacement rates. This finding supports trends in literature that state that lower modulus materials are being used, which typically have improved erosion performance thought to be due to reduced impact pressures, as discussed in Section 2.6 [60, 128]. The LEP A3 material displayed a significant difference in E_{tan} , showing a higher value at the increased displacement rate, indicating strain-rate dependency. Furthermore, a clear, statistically significant trend in E_{tan} can be seen at both displacement rates, LEP B3 > LEP B4 > LEP A3.

The topcoat materials were found to have an average E_{tan} value of 44.70 MPa when including all displacement rates, significantly higher than the LEP materials. The topcoat A2 material displayed a significant difference in E_{tan} , with a higher value observed at the increased displacement rate, indicating strain-rate dependency. At 0.5 mm/min, no statistically significant difference was observed between materials E_{tan} ; however, at the higher 2 mm/min rate, topcoat A2 was found to be higher than topcoat B2.

The filler materials showed the highest E_{tan} values of the tested material types, with an average of 976.25 MPa when including all displacement rates. While neither of the materials showed a significant difference under different displacement rates, filler A1 was found to have significantly greater E_{tan} values in both conditions when compared to filler B1.

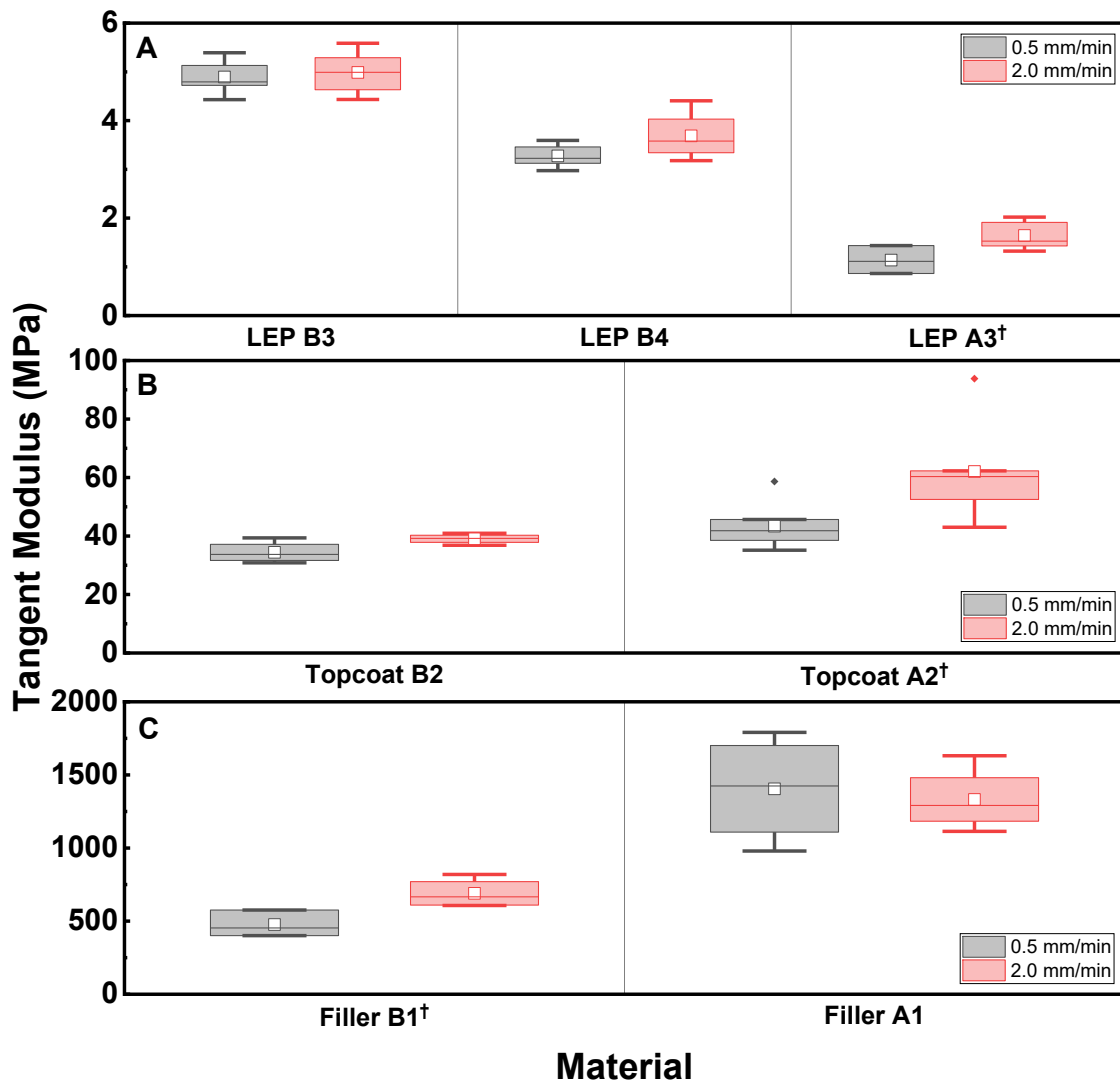


Figure 4.4 – A box plot is presented comparing the tensile tangent modulus of materials used in leading-edge protection systems at 0.5 and 2 mm/min displacement rates. Table A is a comparison of LEP materials, Table B is a comparison of topcoat and Table C is a comparison of filler materials. The † symbol denotes a significant difference ($P < 0.05$) between the two different displacement rate conditions, indicating that the material properties are dependent on the strain-rate.

4.2.4 Secant Modulus

Similar to the E_{tan} , the secant modulus (E_{sec}) provides a different method of comparison that is commonly used for non-Hookean responses and provides a robust and straightforward way of comparing of materials outside the linear region. As described in 3.6, a strain of 0.4 was selected and used to calculate the modulus. This strain value was chosen as Keegan defines 0.379 as the maximum strain that occurs during a rain droplet impact (60° impact angle, 100 m/s and 3 mm droplet diameter) [67]. Therefore, a slightly higher value was chosen as the secant modulus strain for comparison. This comparison was only conducted for the LEP materials as the STB values of topcoat and filler materials were too low to capture the E_{sec} at 0.4 strain. Table 4.4 and Figure 4.5 provides summaries of the measured E_{sec} Values for the LEP materials.

Table 4.4 – Comparison of the secant modulus (E_{sec}) values of the LEP materials at 0.5 and 2 mm/min displacement rates.

Material	Displacement Rate (mm/min)	
	0.5	2
LEP B4	2.895 ± 0.115	2.885 ± 0.292
LEP B3	4.120 ± 0.399	4.248 ± 0.189
LEP A3	0.946 ± 0.083	1.164 ± 0.190

The LEP materials were found to have an average E_{sec} value of 2.71 MPa and as expected were lower than the corresponding E_{tan} values due to the inclusion of some plastic deformation. While none of these materials showed a significant difference under different displacement rates, a trend in the E_{sec} can be seen when comparing the different materials. Significant differences can be seen between the materials at both displacement rates where LEP B3 > LEP B4 > LEP A3.

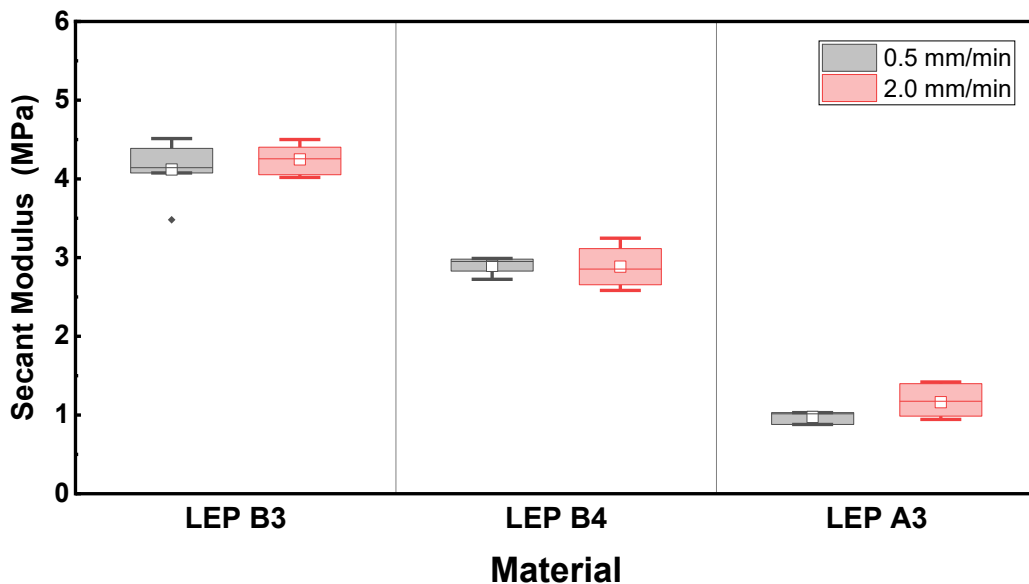


Figure 4.5 – A box plot is presented comparing the tensile secant modulus (0.4 strain) of materials used in leading-edge protection systems at 0.5 and 2 mm/min displacement rates. The † symbol denotes a significant difference ($P < 0.05$) between the two different displacement rate conditions, indicating that the material properties are dependent on the strain-rate.

4.2.5 Ultimate Tensile Strength

The ultimate tensile strength (UTS) is defined as the maximum stress a specimen can sustain under tension. Table 4.5 and Figure 4.6 provide summaries of the measured UTS values.

Table 4.5 – Comparison of the ultimate tensile strength (*UTS*) values of materials used in leading-edge protection systems at 0.5 and 2 mm/min displacement rates.

Material	Displacement Rate (mm/min)	
	0.5	2
LEP B4	1.680 ± 0.089	1.711 ± 0.173
LEP B3	2.543 ± 0.169	2.273 ± 0.320
LEP A3	0.463 ± 0.055	0.533 ± 0.112
Topcoat B2	7.659 ± 0.689	9.432 ± 1.232
Topcoat A2	11.991 ± 0.749	13.468 ± 1.201
Filler B1	11.099 ± 1.299	13.241 ± 1.168
Filler A1	16.671 ± 4.277	18.046 ± 4.478

The LEP materials showed the lowest *UTS* values of the tested material types, with an average of 1.53 MPa. The measured stress continually increased in the LEP materials tested past the yield point, failing at the *UTS* value. While none of the LEP materials showed a significant difference under different displacement rates, a trend in the *UTS* can be seen when comparing the different materials. At 0.5 mm/min significant and clear trend in *UTS* values with LEP B3 > LEP B4 > LEP A3. At 2 mm/min, t-test results show no significant difference between LEP B3 and LEP B4; however, these materials *UTS* values were significantly higher than LEP A3.

The topcoat materials were found to have an average *UTS* value of 10.63 MPa. The measured stress continually increased in the topcoat materials tested past the yield point, failing at the *UTS* value. Both materials showed a significant difference under the different displacement rates indicating a strain-rate dependence. Furthermore, at both displacement rates, a significant difference was seen between materials with topcoat A2 showing higher *UTS* values than topcoat B2.

The filler materials were found to have an average *UTS* value of 14.78 MPa. The filler A1 material demonstrated significantly higher *UTS* values at both displacement rates, which can be attributed to higher stiffness when compared to filler B1. The filler B1 material was observed to be more ductile, resulting in a lower *UTS* but could withstand much greater strains (as seen in the STB comparison) at this load comparison. Neither material showed a significant difference under different displacement rates.

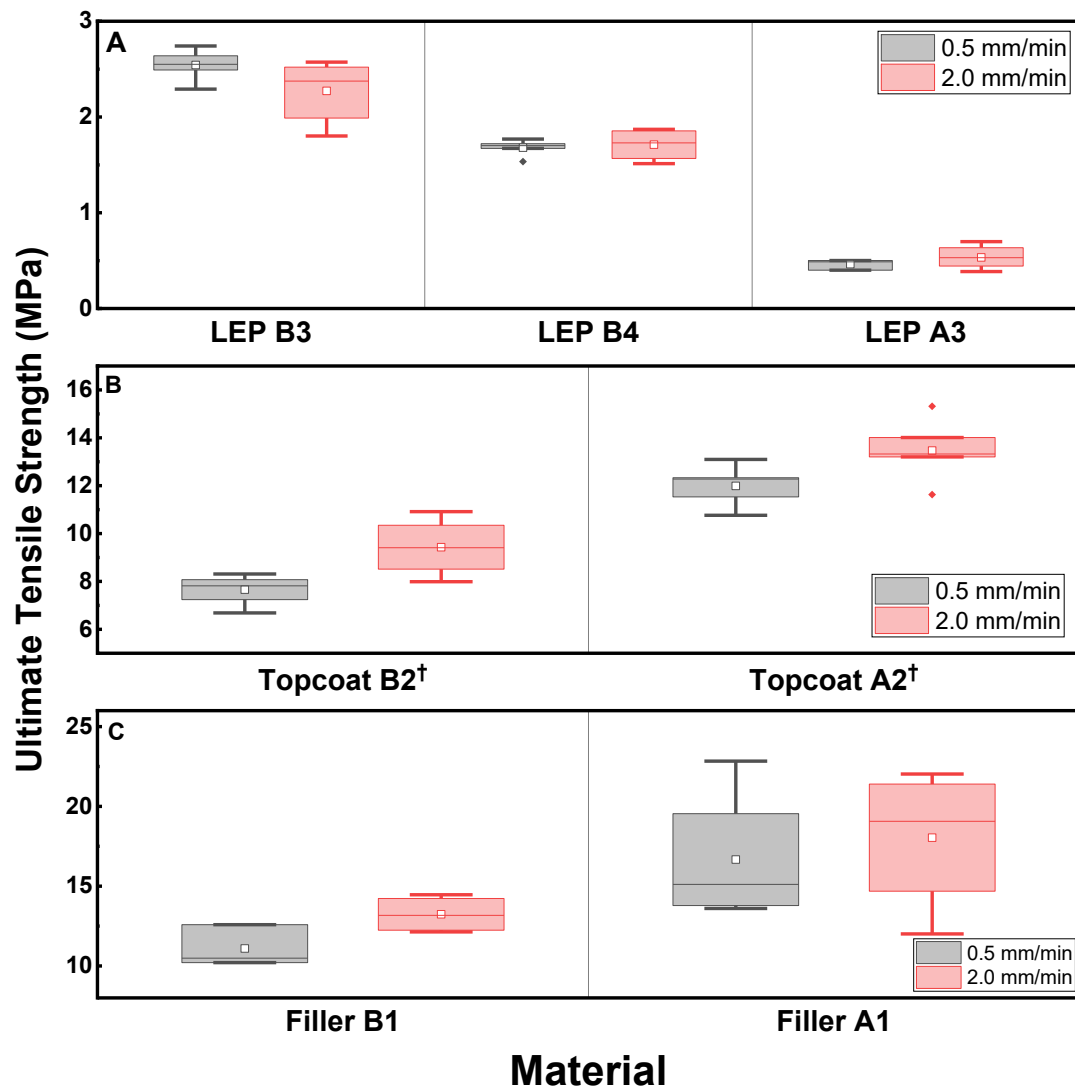


Figure 4.6 – A box plot is presented comparing the ultimate tensile strength (UTS) of materials used in leading-edge protection systems at 0.5 and 2 mm/min displacement rates. Table A is a comparison of LEP materials, Table B is a comparison of topcoat and Table C is a comparison of filler materials. The † symbol denotes a significant difference ($P < 0.05$) between the two different displacement rate conditions, indicating that the material properties are dependent on the strain-rate.

4.3 Discussion

The main aim of these tests was to determine whether any of the materials used in this work showed strain-dependent behaviour under tension. Table 4.6 identifies which materials and measured parameters were found to be significantly different, indicating a strain-rate dependence.

The measured STB values were found to follow the order of LEP > topcoat > filler. Materials with a high STB value are generally considered desirable for coating materials [60, 72, 111]. High values indicate that a material is more likely to deform, whereas low values indicate the material is brittle and can fracture easily under tensile load. These findings align with the literature review in Section 2.7, which highlighted the current prevalence of elastomeric materials that possess high STB

values. As a result, materials are reported to undergo different failure modes, which have been linked to improved rain erosion performance [34, 129, 130, 138].

Table 4.6 – A table summarising which materials demonstrated significantly different properties between 0.5 and 2 mm/min displacement rates. A ✓ indicates a p-value of < 0.05 and was considered statistically significant, and – indicates a p-value >0.05 and is considered not statistically significant.

	LEP B3	LEP B4	LEP A3	Topcoat B2	Topcoat A2	Filler B1	Filler A1
Strain at Break	-	-	-	-	✓	-	-
Toughness	-	-	-	-	✓	-	-
Tangent Modulus	-	-	✓	-	✓	✓	-
Secant Modulus	-	-	-	-	-	-	-
Ultimate Tensile Stress	-	-	-	✓	✓	-	-

The measured toughness values were found to follow the order of topcoat ≈ filler > LEP. Materials possessing high toughness values are generally considered desirable for use as advanced engineering polymers. A higher value indicates that a material can absorb greater amounts of energy before failing. Generally, a balance of strength and ductility is required to achieve this, increasing the area under the stress-strain curve. However, this metric is mainly influenced by the energy absorption mechanisms that occur due to plastic deformations. These cause permanent changes to the dimensions and properties of the material. While large deformation to the coating systems can occur, these are typically associated with issues such as handling during transport and blade flexure during operation. Rain droplet impacts, however, are reported to result only in low strains considered to be elastic rather than plastic [67]. The results show that the LEP systems typically had lower toughness values than the topcoat and filler materials, both of which have worse rain erosion performance. A potential explanation for this is that while LEP materials possess lower toughness values, they typically do not undergo plastic deformations and are designed to withstand repeated rain droplet impacts that stay within the elastic region. The literature supports this finding, suggesting that the extent to which a coating material dissipates energy is more important than absorbing it through plastic deformation [60, 72, 128]. As a result, using toughness as an indicator for rain erosion performance may not be suitable, but it can be used to quantify the suitability of a material as an engineering polymer.

Clear trends were observed between material types for E_{tan} and E_{sec} with filler > topcoat > LEP. However, the values reported for E_{sec} were found to be lower as this method includes the plastic deformation of the material, reducing the gradient and, therefore, the resulting value. These modulus values are of particular importance as, according to the Springer lifetime prediction model and the literature review in Section 2, a lower modulus value improves rain erosion performance [114]. This

reduction is related to the reduction of water hammer impact pressures, as detailed in Section 2.4. This trend toward low modulus material can be seen in the results presented, with the LEPs showing significantly lower moduli than the other coating materials. While this method does provide Young's modulus values that can be compared, obtaining these values has been reported to be inaccurate, often by a factor of two or more [126]. This inaccuracy is due to contributions from the material creep or the deflection of the testing machine. To more accurately measure the material moduli, they should be captured dynamically either through measuring the frequency of natural vibrations or a beam or wire or, as is conducted in work in Chapter 6, by measuring the velocity of a sound wave through a material.

The measured *UTS* values were found to follow the order of LEP > topcoat > filler. The *UTS* of a material is another key material input into the Springer model [72, 86]. This approach states that the rebounding tensile stresses from a droplet impact are the primary cause of material failure. A higher *UTS* value increases the material strength, calculated from Equation 2.5, improving rain erosion performance. While the LEP materials showed the lowest *UTS* values, they also possess the best rain erosion performance of the material types tested. This difference is attributed to how the materials fail under tension. More compliant LEP materials generally have a larger *STB*, which reduces stresses as the material elongates. Conversely, brittle materials with lower *STB* values tend to show much higher maximum stresses, at which point the material fails rather than elongating.

While many materials did not display strain-rate dependent behaviour, this could be attributed to the small difference between the 2 mm/min and the 0.5 mm/min conditions, which correspond to strain-rate of $3.3 \times 10^{-3} \text{ s}^{-1}$ and $8 \times 10^{-4} \text{ s}^{-1}$, respectively. It is possible that exploring high strain-rates closer to the predicted strain rates of 10^7 s^{-1} may result in materials displaying behaviour not captured at these low strain-rates [67]. This highlights a potential limitation of the springer model which typically uses material properties such as UTS obtained from low strain rate testing and not from the high strain rates discussed prior. Other methods such as dynamic mechanical thermal analysis (DMTA) can be used to explore higher strain-rate behaviour while also exploring the effects of temperatures under controlled conditions.

4.4 Summary

In this chapter, tensile testing of thin films was successfully used to characterise individual materials used in coating systems. Novel data were generated that were used to compare material in effort to correlate behaviour to rain erosion performance. The aim of this set of testing was to identify if significant strain-rate dependent behaviour was observed and quantify its influence on material properties commonly obtain from the method. The only LEP material to show any significant

differences was LEP A3, which displayed an increased E_{tan} value at the higher displacement rate. The topcoat A2 material demonstrated significant differences in all measured parameters. The other topcoat, topcoat B2, only showed a significant difference in UTS . The only filler to show any significant difference was filler B1 which displayed a higher E_{tan} value at the higher displacement rate.

In summary, tensile testing does indicate how a material will behave under loading but at a much lower strain rate than expected during a high-speed rain droplet impact. To measure the material moduli more accurately, they should be captured dynamically by measuring the velocity of a sound wave through a material. While it is useful to compare each property individually, a combination of these is required for good erosion performance. These findings are supported by the Springer prediction model and coating manufacturers' design criteria (detailed in Section 2.6), which favour the use of materials that possess a high STB , high UTS , and low Young's modulus [86]. These material properties are dependent on the chemical composition and morphology of each coating system. By varying the constituents and curing conditions, these important properties can be tailored to improve rain erosion performance.

5

Nanoindentation

This chapter presents the nanoindentation results of several coating materials analysed using the Oliver-Pharr method. The effect of loading rate, maximum load, repeated indentation, and recovery periods were captured and compared for each material.

5.1 Introduction

Nanoindentation is a powerful tool in measuring the mechanical properties of materials on the nanoscale. The ability to carry out indentation on this scale allows for the characterisation of local mechanical properties of thin films and coatings to be measured without any influence of the substrate. Additionally, this method can apply a controlled loading regime to examine possible failure modes because of contact-induced stresses.

This method was selected due to its ability to measure the properties of coated composite specimens, as seen in Figure 3.5, with layer thicknesses in the micron range using a similar deformation mode that would be applied in a rain droplet impact. As many current coating systems are thin multi-layer systems, nanoindentation provides a technique that allows for the characterisation of individual layers as a function of depth and load with negligible influence of the other layers or the substrate. The technique also allows for the effect of local defects and the variation of material properties at the interface to be quantified. The validity of the results produced depends greatly on the analysis procedures used to process the experimental data. The most common method, named after the authors ‘W. C. Oliver and G. M. Pharr’, is detailed in Section 3.5 and used in the subsequent work [156].

5.2 Method Development

It should be noted that the use of nanoindentation as a characterisation method was initially designed to measure the hardness and modulus of materials such as metals and ceramics, which are generally very hard and stiff. However, In recent years, there has been a trend toward testing softer materials that possess moduli of under 1 GPa, such as polymeric materials [164–168]. These materials can be characterised using the same methodology; however, several issues have been identified in the literature as causes of systematic error that complicate understanding and modelling of these behaviours [164, 165, 168–170]. A review of all aspects of nanoindentation is beyond the scope of this work; however, it is essential to discuss the potential limitations of the method and the attempts used to mitigate them, resulting in the test methodologies used in the work.

5.2.1 Instrument Resolution

Lack of instrument resolution is a commonly reported issue in literature and is due to the high compliance of polymers when compared to metals and ceramics. This difference results in significantly lower forces and depths requiring test equipment to possess adequate resolution during the experiment. Measurements conducted on polymers samples are typically in the order of 100 μN and the nano Newton range for the determination of the initial contact force [164, 165]. In a

nanoindentation test, the indentation depth should be measured from the level of the specimens' surface; however, achieving this in practice can prove challenging. For an instrument to detect a surface, a preload, the smallest force the instrument can output, is used to detect the initial contact point. At the depth where a force is registered, the indentation depth and contact area are set to zero. When applying a preload to low compliance material such as metals or ceramics, the resultant displacement from the actual surface depth can be considered minimal. Conversely, the application of even a small preload to highly compliant materials, such as polymers, can result in significant displacement resulting in an uncertain initial contact depth and area. Generally, softer materials show larger underestimations of contact area resulting in larger modulus and hardness as they are directly used in their calculation [164]. For example, studies on polydimethylsiloxane (with a tensile modulus of 1 MPa) show variations of up to 400 % in measured modulus due to underestimations in the predicted contact depth and, therefore, area [164]. These overestimations in material properties have also been supported by comparing measurements using alternative techniques such as DMTA (see Chapter 6) [154].

To minimise the issues of instrument resolution, a specialist indenter with adequate accuracy was utilised. The instrument used in this work states the working load range to be between 75 nN to 10 mN and the working displacement range to be between 0.2 nm to 5 µm. However, in practice, literature states that its actual achievable resolution is closer to 100 nN because of various external influences such as vibrations and thermal drift [164, 171]. Furthermore, while the assumption is that the material surface is flat, as a result of polishing, it was observed that there were areas of varying heights as they appeared out of focus during optical surface inspection. As a result of these considerations each indentation was conducted in flat areas (areas in focus during optical inspection) that were free of observable defects. Each resulting indentation curve was inspected to ensure for an adequate contact point and acceptable load displacement curve. The depth resolution was not found to be an issue during the testing of the materials in this work. Due to the compliance of the tested materials, measured depths were within the normal working displacement range even at the lower loads.

5.2.2 Thermal Drift

Thermal drift is another commonly reported source of error in nanoindentation. It refers to the variation in the dimensions of the indenter head in response to a change in ambient temperature or from heat generated from the act of indenting a surface [165, 172]. To minimise these effects, the instrument and the surrounding environment are temperature controlled. However even in a temperature-controlled environment, variations were still observed during the test. These variations

were measured and accounted for using thermal drift correction conducted prior to testing. A hold segment is conducted at a constant load producing a displacement-time curve. Using linear regression allows for the thermal drift rate to be calculated, and these values are then considered in the test correcting for thermal drift.

5.2.3 Adhesion

When two surfaces interact, there are always competing forces of attraction and repulsion between the atoms that make up the surfaces. Literature states that attractive forces experienced between the material and the indenter tip are significant and should be considered if possible [154]. Studies have demonstrated this by comparing indenter tips made of diamond and tungsten when characterising polymeric samples [164]. The resulting measurements showed significantly higher results for the diamond tip when compared with the tungsten tip. This difference was attributed to the stronger adhesion between diamond and polymeric materials changing the contact area calculations. It was not possible to change the tip material during this work, and a diamond tip was used throughout. Furthermore, it was observed that partially cured materials caused significant adhesion between the material and the tip. To mitigate this, all samples were allowed to cure for extended periods to ensure a suitable degree of cure.

5.2.4 Choice of Reference Material

As part of the OP method, fused silica (FS) is used to calibrate the tip area function [156]. This process allows for conversion between measured indentation depth to the projected contact area accounting for any imperfections or misalignments of the indenter tip. As FS is a relatively high stiffness material compared to many polymers, the maximum load of the indenter results in indentation depths no greater than several hundred nanometres. On the contrary, when indenting a softer polymer-based material, the maximum depth can exceed this depth [153, 164, 165, 168, 172, 173]. While it could be possible to utilise a more compliant material as a reference, no alternative calibration standards were available at the time of testing. As a result, high depth indents used in this work may not have been corrected for during the indenter tip calibration stage due to the differences in depths.

5.2.5 Material Behaviour

The OP analysis is that the method assumes that the material displays 'sink-in' behaviour, where the material 'sinks' inwards toward the indentation. However, it does not consider the effect of 'pile-up' where the material moves upwards away from the indentation [170]. These two examples are compared in Figure 5.1. In this work, due to the ductility of some of the materials being tested it was

assumed pile up would occur meaning larger contact areas are estimated by the method resulting in overestimations of hardness and modulus which should be considered.

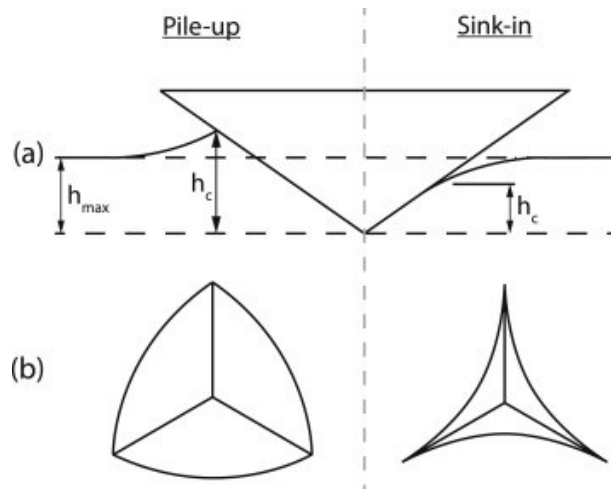


Figure 5.1 – Examples of pile-up and-in behaviour. A) Side view of an indenter demonstrating the maximum depth (h_{max}), and contact depth (h_c). B) The resulting contact area from each behaviour. Figure directly reprinted with permission from literature [174].

Sink in behaviour was observed in the less compliant filler materials; however, it was not possible to identify if pile-up behaviour was observed in the topcoats and LEP. This was due to the difficulty in imaging the surface and the rapid recovery of each material.

5.2.6 Viscoelastic effects

Preliminary testing identified that the impact of time-dependent viscoelastic behaviours, which resulted in the poor fitting of the depth-load curve, was the most significant issue when characterising coating materials. This problem was most apparent in the compliant LEP materials, which are found to be more viscoelastic. As a result, a change in methodology was needed before further testing could be undertaken.

This poor fitting of the load curve was due to the irregular material response observed when a load was applied. The more viscoelastic materials show a delayed response, unlike purely elastic materials, which are considered instantaneous. Simplistic ways of demonstrating this behaviour can be achieved using combinations of springs and dashpots summarised in Figure 5.2.

The Hooke model is comprised of a single spring and demonstrates a perfectly elastic system with instantaneous deformation and recovery with no plastic deformation. Conversely, the Kelvin model is comprised of a single dashpot and demonstrates a viscous fluid with retarded deformation and no strain recovery. By combining these two, the Maxwell and Kelvin-Voight systems provide better representations of material behaviour, in particular the increase in deformation at a constant

load which is defined as creep. This behaviour strongly impacts the results of indentation tests, and as a result, care must be taken to identify if any of these behaviours are influencing results.

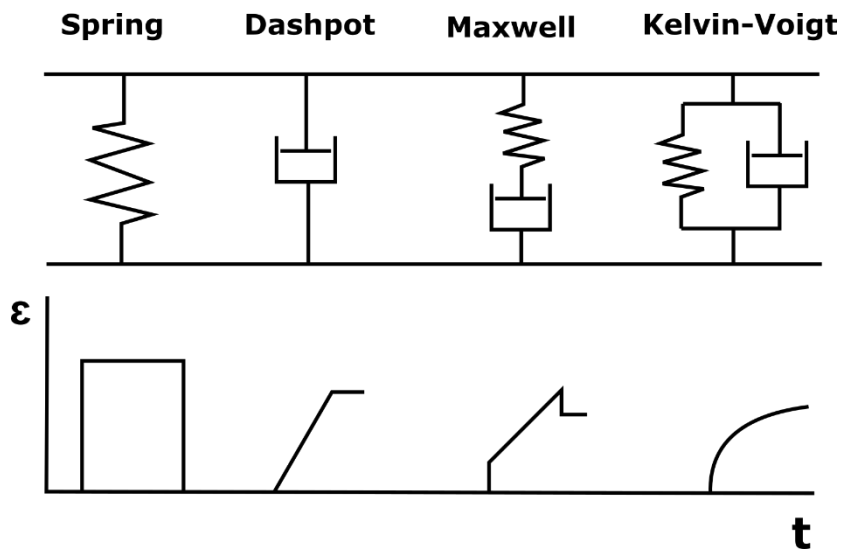


Figure 5.2 – Classical elements are used to represent material behaviours over time. From left to right: elastic solids, viscous fluids, viscoelastic-fluid behaviour (including stress relaxation and permanent deformation) and viscoelastic-solid behaviour showing retarded but reversible deformation. Figure adapted from literature [164].

These material behaviours can significantly affect the characterisation of the coating systems used in this work. In conventional OP analysis of data, the unloading curve is related to the elastic recovery of the material and used to determine the S_u and subsequently the modulus E [156, 175]. In an elastic material, this upper portion of the unloading curve can be assumed to be approximated to a linear response (Figure 5.3). However, a characteristic 'nose' is seen during the unloading step for a viscoelastic material.

This feature is present because of delayed creep deformation that continues at constant peak load and, in cases, continues to increase during the unloading step. As a result, the approximation of linearity does not hold, resulting in the gradient of the unloading curve appearing much steeper than it would without the 'nose', resulting in an overestimation of modulus and errors with curve fitting. However as properties such as recovery have been reported to correlate well to erosion performance this method was chosen to explore if similar relationships could be seen in the materials selected for this work while also trying to minimise the variability caused by viscoelastic effects [127].

A review of the literature shows that it is possible to overcome these effects by adjusting the testing methodology in two ways [164, 165, 175–178]. Firstly, increasing the amount of time the method is held at peak load allows for the viscoelastic creep effects to 'complete' (equilibrate), allowing for an elastic unloading phase *via* the standard OP method. Alternatively, increasing the rate at which the material is unloaded is reported to lead to a more consistent elastic response.

As a result, extended hold times (30 seconds/1 minute) and short unloading times of 2 seconds were used in all methods to minimise the number of variables and ensure consistent results. While these may not have been needed for the harder and stiffer materials being tested, the same principles were used to allow for comparison between materials.

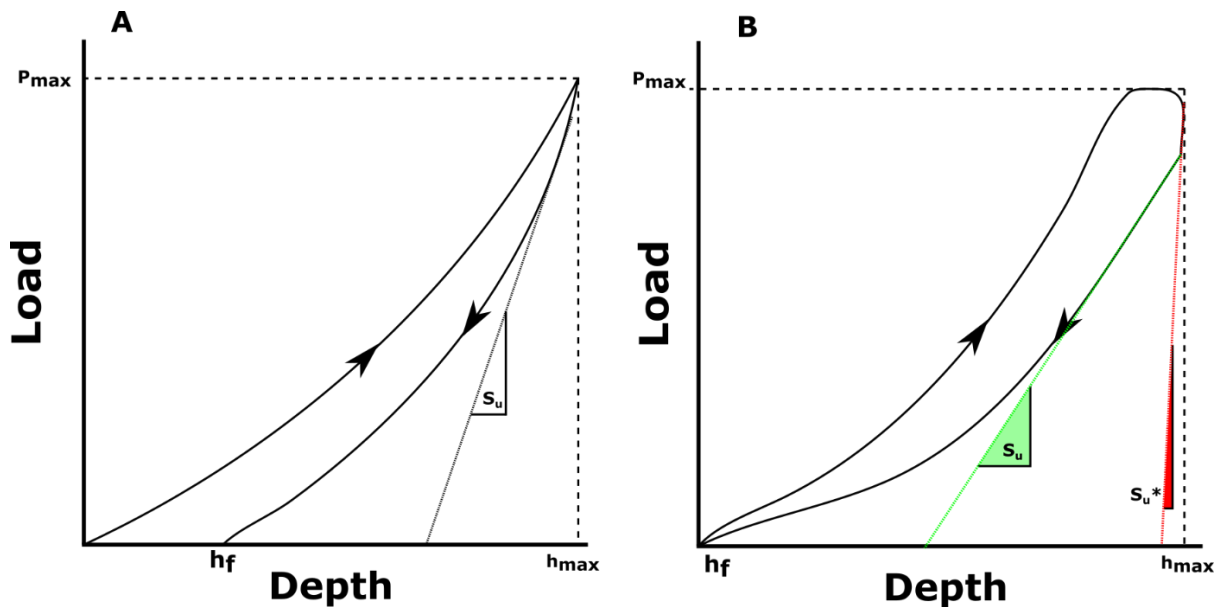


Figure 5.3 – Generalised schematic of depth-load responses for two example cases undergoing a load-hold-unload method. P_{max} , peak indentation load, h_{max} , indenter displacement at peak load, h_f , final depth of the contact impression after unloading and S_u , the contact stiffness of the unloading curve calculated from the unloading gradient. A: The response of an elastic material that shows negligible creep behaviour and permanent deformation. B: The response of a viscoelastic material displaying complete strain recovery and creep during the hold phase resulting in a characteristic nose shape. The red line demonstrates how the nose can cause an overestimation of the contact stiffness (S_u^), and the green line represents how a lower contact stiffness can be obtained for fitting away from the nose. Figure adapted from the literature [155].*

5.3 Results

During this work, a novel set of tests were designed to capture the material responses of viscoelastic coating materials. The use of these test programmes on materials of this kind are not commonly available in the open literature. Using nanoindentation makes it possible to characterise materials through a loading cycle typically consisting of load-hold-unload segments. While these parameters provide a wide range of variables to study, the work presented here aims to minimise the number of variables being changed to investigate how the change in methodology affects the material response and resulting properties. Test 1 varied the loading rate, Test 2 the maximum load, and Test 3 investigated the effect of repeated indentations and recovery periods.

5.3.1 Test 1 – Varying Loading Rate

The first test explored the impact of varying the loading rate using a load-hold-unload method, as presented in Figure 5.4 and summarised in Table 5.1.

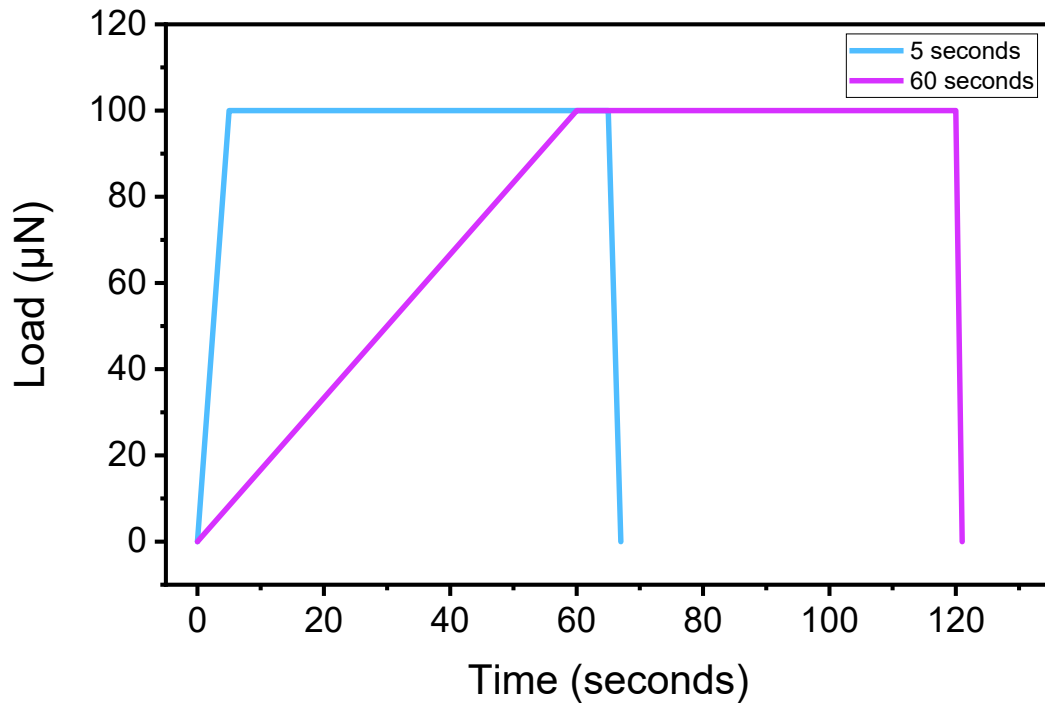


Figure 5.4 – A schematic detailing the two load-hold-unload nanoindentation methods used in Test 1. Loading time: 5 seconds / 60 seconds, maximum load: 100 μN , hold time: 60 seconds, unload time: 2 seconds and N=5.

The maximum depth of indentation for each material is compared in Figure 5.5. The increase in indentation depth can occur during any of the method steps (load/hold/unload). While the maximum depth value does not show the changes in depth over the entire loading period, it is still a useful value as the indentation depth can significantly influence the calculation of other parameters.

Table 5.1 – A table detailing the parameters used in Test 1 in a hold-load-unload test method to determine the influence of loading rate.

Test Parameters	
Loading time (s)	5 and 60
Maximum load (μN)	100
Hold time (s)	60
Unload time (s)	2
Repeats (N)	5

As expected, due to their relatively high stiffness compared to the other materials used in this work, the filler systems showed the lowest indentation depths. The topcoat A2 material showed no significant difference in maximum depth compared to the filler materials. However, the topcoat B2 material displayed significantly greater maximum depth when compared to the topcoat A2 material. The topcoat B2 material was also observed to have a significantly lower depth at the slower loading

rate indicating a dependence on the loading rate¹¹. The LEP materials consistently showed much greater indentation depths than the filler and topcoat materials, in the order of LEP B3 > LEP A3 > LEP B4. LEP B3 and LEP B4 showed significantly higher depths at slower loading, resulting in an increased indentation depth, unlike the behaviour of the topcoat B2 material. This difference could be attributed to the LEP materials possessing more viscoelastic characteristics resulting in the depth increasing over the longer test duration due to creep phenomena.

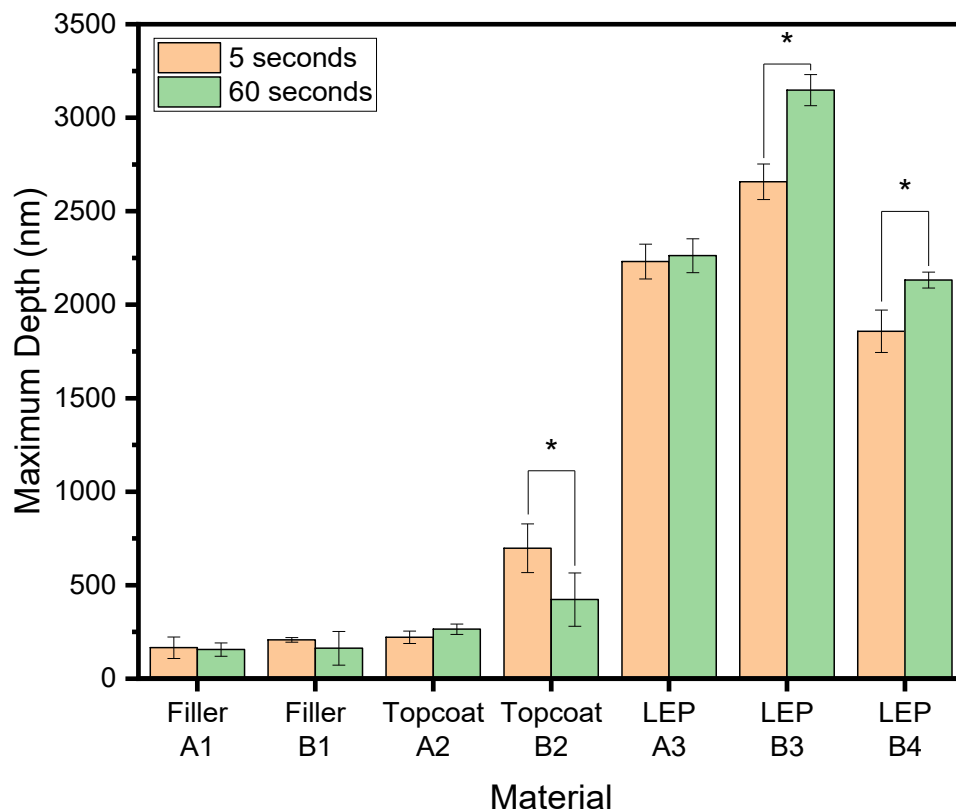


Figure 5.5 – A bar chart is presented comparing the maximum depths measured during a load-hold-unload nanoindentation method (loading time: 5 seconds / 60 seconds, maximum load: 100 μ N, hold time: 60 seconds, unload time: 2 seconds and N=5). The asterisk (*) symbol indicates a significant difference between test loading rates ($P<0.05$).

The reduced modulus (E_R) was calculated from the load-depth curve using Equation 3.3 and presented in Figure 5.6. This value is indicative of the materials Young's modulus that can be obtained by substituting in the Poisson's ratio for the material being tested using Equation 3.4. However, in this work, measured Poisson's ratios showed high standard deviations and were deemed unsuitable to be included. Instead of presenting it in this form, the influence of Poisson's ratio is removed but still allows for comparison between materials.

¹¹ This result was unexpected as viscoelastic materials are commonly expected to display an increase in displacement over a longer period. Instead, the material shows repeated occurrences of this opposite behaviour which cannot be explained in this dataset. This could be due to the material displaying less creep behaviour making the difference between the two test conditions more prominent however this requires further study.

The filler materials consistently showed the largest standard deviations of any material tested. This observation was attributed to the cellular-like structure that these types of material form, which result in significant local property variations as documented by the author in other work [61]. No significant difference was observed between filler A1 or filler B1 materials or because of loading rate variation. topcoat A2 was found to have similar E_R values to the filler materials, whereas topcoat B2 showed significantly lower E_R values and showed a significant difference between loading rates, displaying a higher E_R at the slower loading rate. The LEP materials were all found to possess a considerably lower E_R than the other material types. The LEP A3 material was observed to have the highest E_R however, this was found to not be statistically different to the E_R at the slower loading rate. LEP B3 displayed a significantly lower E_R than LEP B4, with both materials showing significantly lower E_R values at the slower loading rate indicating a dependence on loading rate.

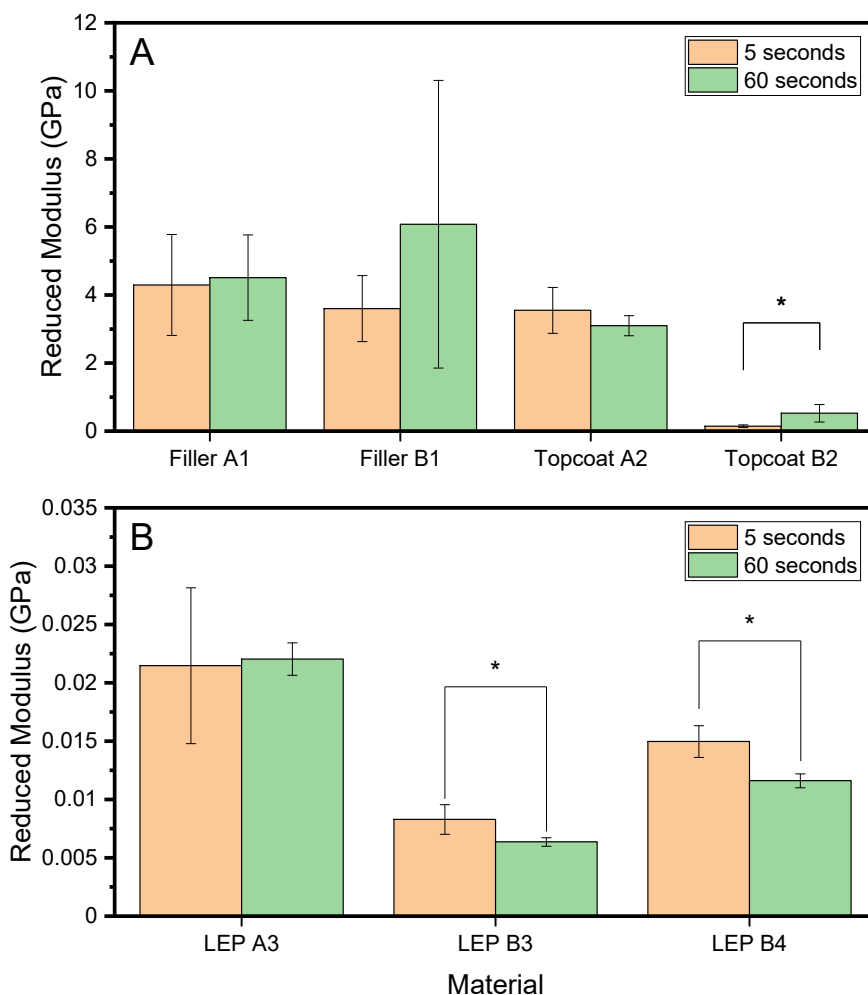


Figure 5.6 – A bar chart is presented comparing the reduced modulus values calculated using the Oliver Pharr method measured during a load-hold-unload nanoindentation method (loading time: 5 seconds / 60 seconds, maximum load: 100 μ N, hold time: 60 seconds, unload time: 2 seconds and N=5). Asterisk (*) symbol indicates a significant difference between test loading rates ($P<0.05$).

The Short Term Recovery (*STR*) was calculated from the load-depth curve using Equation 3.5 and presented in Figure 5.7. This value indicates the extent a material can recover from deformation once the load is removed but is only reported as a change. As a result, any comparisons should also refer to the maximum indentation depth. Overall, no significant differences in *STR* values were found between the loading rates for any material, indicating that there was no dependence on the loading rate of the material. No significant difference was observed between filler materials. For the topcoat materials, topcoat A2 was observed to possess significantly lower *STR* values than topcoat B2. For the LEP materials, LEP A3 was found to possess a significantly lower *STR* in comparison to the LEP B3 and LEP B4 materials, which were found not to be significantly different.

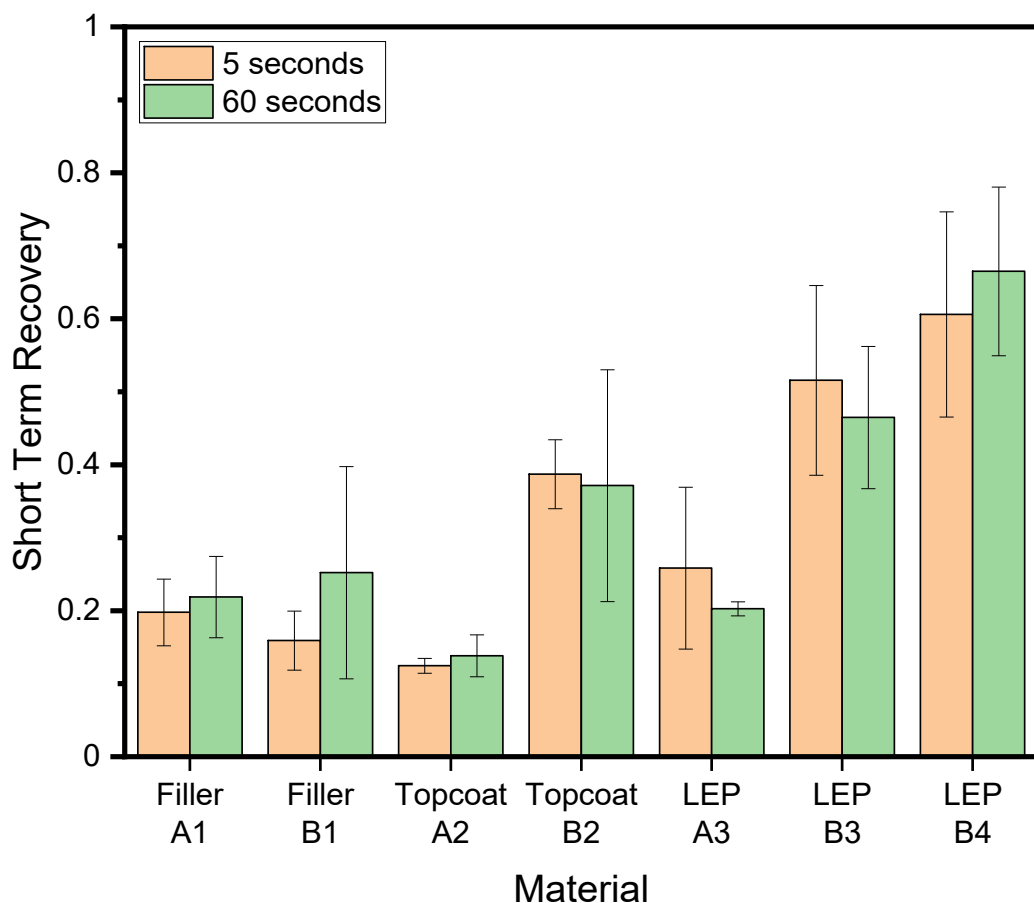


Figure 5.7 – A bar chart is presented comparing the short term recovery values measured during a load-hold-unload nanoindentation (loading time: 5 seconds / 60 seconds, maximum load: 100 μ N, hold time: 60 seconds, unload time: 2 seconds and N=5). Asterisk (*) symbol indicates a significant difference between test loading rates ($P<0.05$).

The hardness (H) was calculated from the load-depth curve using Equation 3.1 and presented in Figure 5.8. This value indicates a material's ability to resist the penetration of an indenter head, which is assumed to be non-deformable.

As with the E_R , the H measurements demonstrated considerable standard deviations, and as a result, no significant differences were found between the materials or loading conditions. Both

topcoat materials were found to possess lower H values than the filler materials, with the topcoat B2 material displaying significantly lower values at the faster loading rate. Owing to their compliant behaviour, the LEP materials were observed to possess a much lower hardness than the other material types. The H values of LEP A3 and LEP B3 were not statistically different at the faster loading rate; however, at the slower loading rate, LEP B3 was found to be significantly lower. LEP B4 was also observed to have a significantly higher H than the other LEPs in both loading conditions. LEP A3 showed no significant difference between loading conditions, whereas, for LEP B3 and LEP B4, a significant decrease in hardness was observed at the lower loading rate indicating a dependence on loading rate.

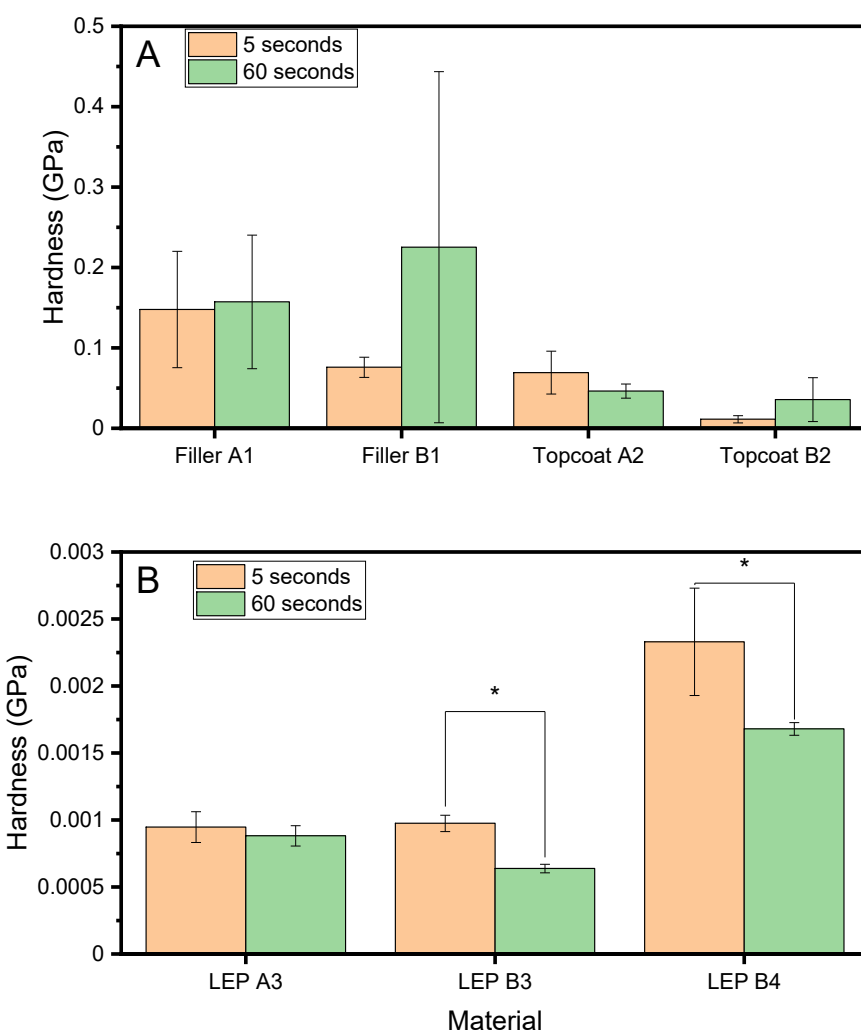


Figure 5.8 – A bar chart is presented comparing the hardness values calculated using the Oliver Pharr method measured during a load-hold-unload nanoindentation (loading time: 5 seconds / 60 seconds, maximum load: 100 μ N, hold time: 60 seconds, unload time: 2 seconds and $N=5$). Asterisk (*) symbol indicates a significant difference between test loading rates ($P<0.05$).

The indentation work was calculated from the load-depth curve by integrating the area under the curve and using Equation 3.6 and presented in Figure 5.9.

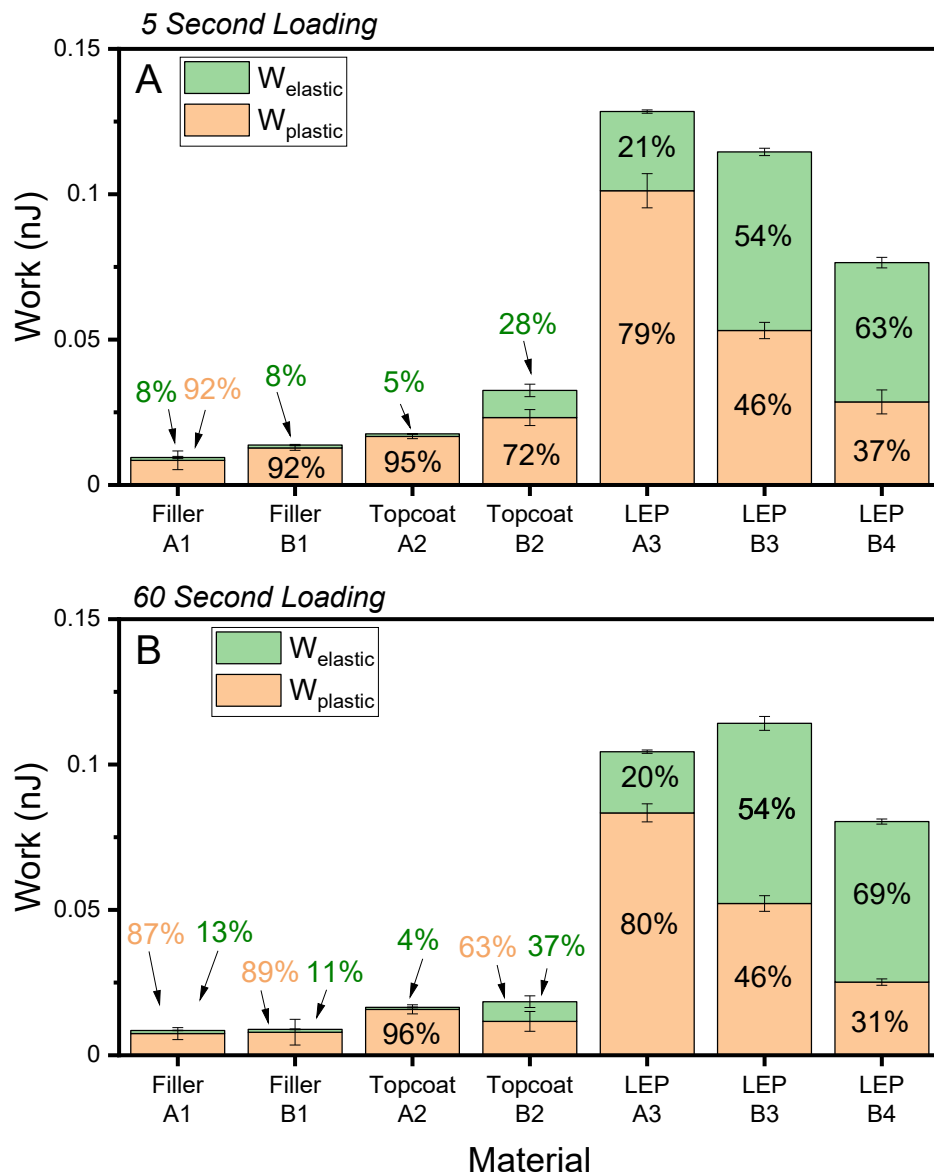


Figure 5.9 – A bar chart is presented comparing the indentation work measured during a load-hold-unload nanoindentation method (loading time: 5 seconds / 60 seconds, maximum load: 100 μ N, hold time: 60 seconds, unload time: 2 seconds and $N=5$). The complete bar represents the total work, the orange represents the plastic work, and the green represents the elastic work.

The filler materials were observed to undergo the lowest total work (W_{total}), with 92 % being plastic work ($W_{plastic}$). Both filler materials displayed similar W_{total} at each loading rate; however, at the lower loading rate, the percentage of elastic work ($W_{elastic}$) increased in both materials. The topcoat materials were observed to undergo greater W_{total} than the filler materials. It was also found that the topcoat A2 showed significantly lower W_{total} while also demonstrating a considerably lower $W_{elastic}$ than the topcoat B2 at the lower loading rate. All the LEP materials showed considerably greater W_{total} values than other material types; however, marked differences in the distribution of elastic and plastic responses were observed. LEP B4 showed the lowest work in both conditions, demonstrating a 5 % increase in $W_{elastic}$ at the lower rate. LEP B3 had the second highest W_{total} at

the faster loading rate but highest at a slower rate; no considerable difference was seen between the loading conditions. LEP A3 showed the highest W_{total} at the slower rate, which was found to be 80 % plastic. At a higher loading rate, a reduction in W_{total} was observed with minimal changes in the elastic-plastic distribution.

Overall strain rate dependency was seen only in LEPs (B3 and B4) and topcoat B2. These findings could indicate that at different impact velocities material properties can vary significantly especially for the more viscoelastic materials. However as the difference between loading rates was limited by the equipment other significant difference may be observable using a different loading methodology.

5.3.2 Test 2 – Varying Maximum Load

The second test explored the impact of different maximum loads using a load-hold-unload method, as shown in Figure 5.10 and are summarised in Table 5.2.

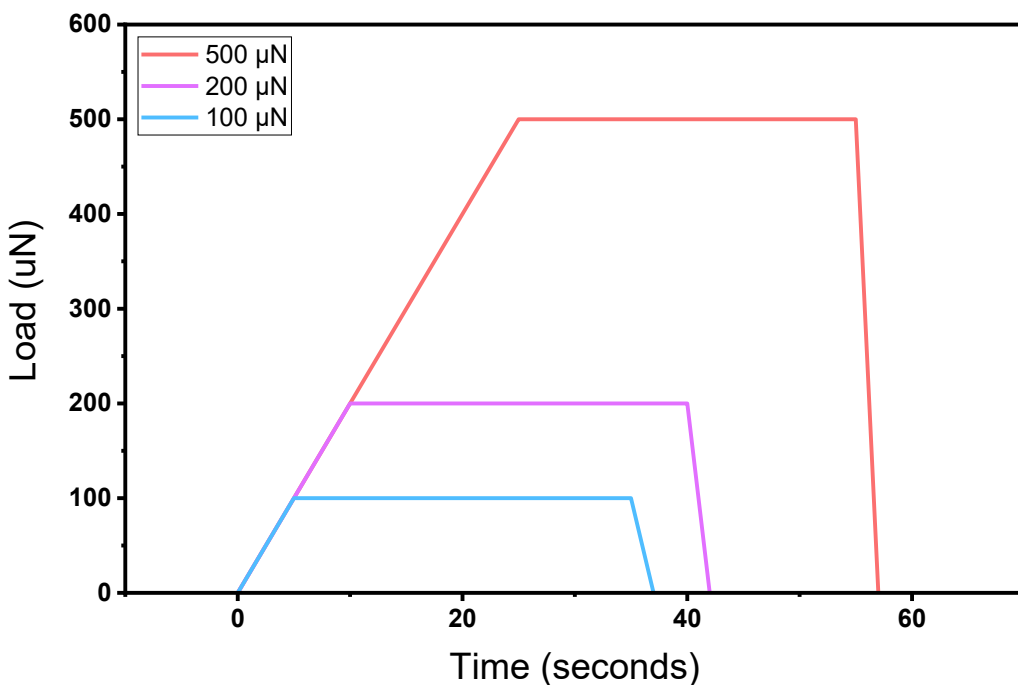


Figure 5.10 – A schematic detailing the three load-hold-unload nanoindentation methods used in Test 2. Maximum loads: 100 μN (blue), 200 μN (purple) and 500 μN (orange) loading time: 5 seconds / 10 seconds / 25 seconds (to maintain a constant loading rate), hold time: 30 seconds, unload time: 2 seconds and N=5.

The maximum depth of indentation for each material is compared in Figure 5.11. For most materials, an increase in load resulted in an increased maximum depth being recorded during the indentation. As expected, owing to their high modulus, the filler materials displayed the lowest maximum depths; however, it was observed that for the filler A1 material, the increase of load from 200 μN to 500 μN resulted in a decrease in maximum depth. This result was the only one not to follow

the trend of increased maximum depth when maximum load is increased. For the topcoat materials, when compared to the filler materials, the topcoat A2 was observed to have a similar depth at the lowest load; however, at 200 µN and 500 µN, the topcoat B2 showed considerably greater depths.

Table 5.2 – A table detailing the parameters used in Test 2 in a hold-load-unload test method to determine the influence of maximum load while utilising a constant loading rate.

Test Parameters	
Loading time (s)	5, 10 and 25
Maximum load (µN)	100, 200 and 500
Hold time (s)	30
Unload time (s)	2
Repeats (N)	5

The LEP materials showed significantly higher maximum depths in all conditions with clearly observable increases upon increasing maximum load. This can be attributed to their low modulus and ability to undergo creep over time. The LEP B3 500 µN measurement is missing as the instrument deemed the material response to be inaccurate for the OP method, and as a result, these results were not used.

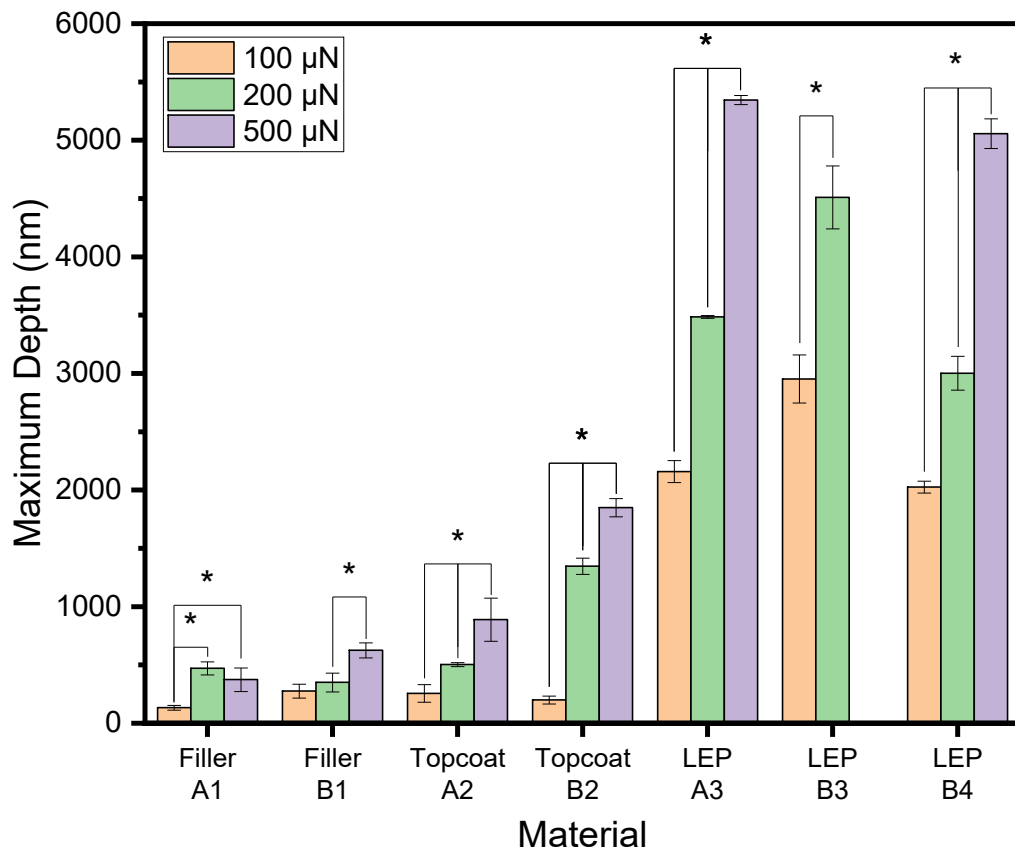


Figure 5.11 – A bar chart is presented comparing the maximum depths measured during a load-hold-unload nanoindentation method. Maximum loads: 100 μN , 200 μN , and 500 μN , loading time: 5 seconds / 10 seconds / 25 seconds (to maintain a constant loading rate), hold time: 60 seconds, unload time: 2 seconds and N=5. The LEP B3 500 μN was unable to be captured and is not displayed. The asterisk (*) symbol indicates a significant difference between maximum loads ($P<0.05$).

The effect of maximum load on E_R is presented in Figure 5.12. The filler materials demonstrated large standard deviations in certain conditions, making identifying a trend in cases challenging. No significant difference in E_R was observed between the 100 μN and 500 μN loads for the filler A1 material; however, the E_R in the 200 μN condition was found to be significantly lower. The filler B1 material appears to show a decreasing trend, but no significant differences were found between the conditions. Of the topcoat materials tested, topcoat A2 was observed to have the highest E_R which decreased significantly from the 100 μN to the 500 μN conditions. The topcoat B2 material displayed significantly different results for each loading rate; however, a decrease in E_R was observed from 100 μN to 200 μN but also increased between 200 μN to 500 μN . No clear trend could be observed for the LEP A3 and LEP B3 materials when varying the maximum load. The LEP A3 E_R values were statistically different at each maximum load in the order of 100 μN > 500 μN > 200 μN . The LEP B4 did show a significant decrease in E_R from the 100 μN to the 500 μN maximum load conditions.

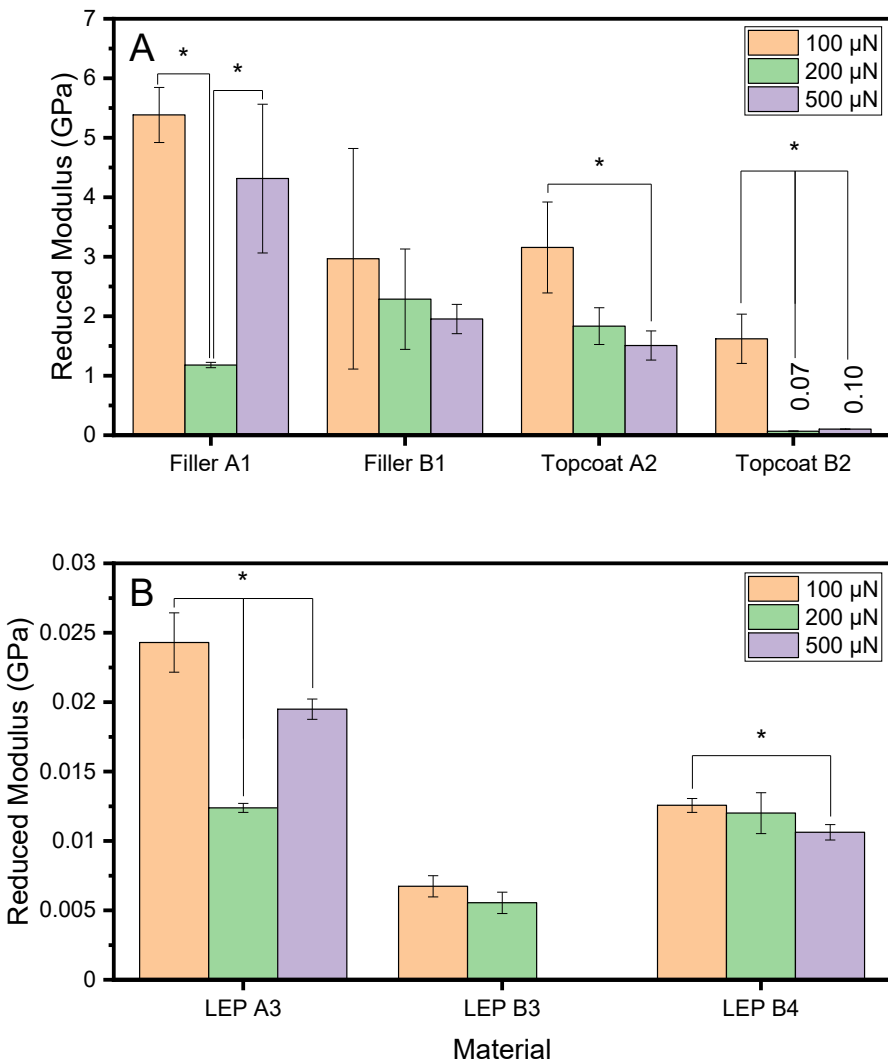


Figure 5.12 – A bar chart is presented comparing the reduced modulus values obtained using the Oliver Pharr method from a load-hold-unload nanoindentation method. Maximum loads: 100 μN , 200 μN , and 500 μN , loading time: 5 seconds / 10 seconds / 25 seconds (to maintain a constant loading rate), hold time: 60 seconds, unload time: 2 seconds and N=5. The LEP B3 500 μN was unable to be captured and is not displayed. The asterisk (*) symbol indicates a significant difference between maximum loads ($P<0.05$).

The effect of maximum load on *STR* is presented in Figure 5.13. No significant difference is seen between the filler *STR* values at the 100 μN max load where filler A1 > filler B1. A clear and significant difference was observed between the two topcoat materials at all loads, with topcoat B2 displaying the higher *STR* values. However, there was no significant difference observed in *STR* values due to variation in the maximum load. For the LEP materials, LEP B4 showed no significant differences due to variation of the maximum load, resulting in the highest values in all three loading conditions. The LEP A3 results showed significantly different *STR* values in each loading condition in the order of 200 μN > 100 μN > 500 μN . The LEP B3 result also varied significantly, increasing *STR* between 100 μN and 200 μN conditions. The differences between results at different loads could be attributed to high plastic deformations at higher loads and increased variability at lower indentation depths that are

linked with potential difference in properties closer to the surface potentially due to abrasion during sample preparation.

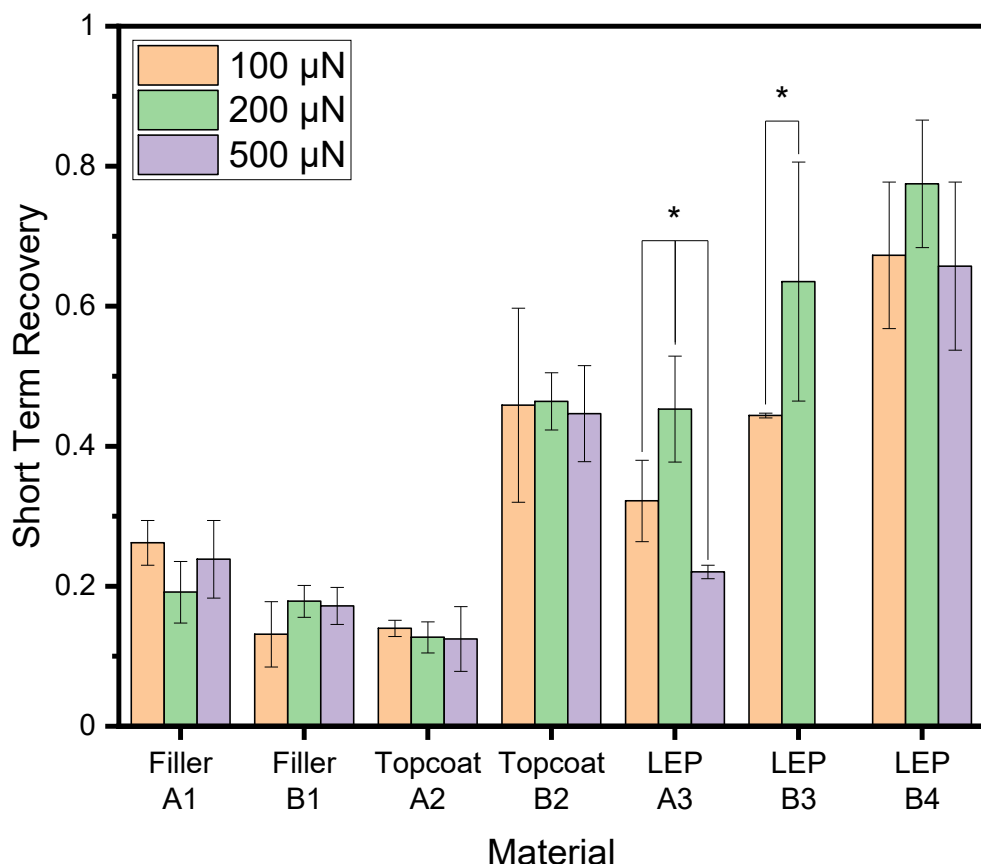


Figure 5.13 – A bar chart is presented comparing the short term recovery values measured during a load-hold-unload nanoindentation method. Maximum loads: 100 μN , 200 μN , and 500 μN , loading time: 5 seconds / 10 seconds / 25 seconds (to maintain a constant loading rate), hold time: 60 seconds, unload time: 2 seconds and $N=5$. Asterisk (*) symbol indicates a significant difference between test loading rates ($P<0.05$).

The effect of maximum load on indentation work is presented in Figure 5.14. For all materials tested, the increase in maximum load increased the observed work values. The filler materials showed the lowest W_{total} in all load conditions, with the filler A1 material being the lowest of the two. The filler A1 material demonstrated a predominately plastic response, which became more elastic at the 200 μN then returned to approximately the same value at the 500 μN condition. The filler B1 material showed a more considerable plastic response with increased load resulting in a greater $W_{elastic}$ percentage. At the 100 μN load condition, topcoat A2 displays a greater W_{total} than topcoat B2; however, for the higher loading conditions, topcoat B2 is observed to be higher. For the topcoat A2 material, there is a minimal change in the distribution of elastic/plastic work. Conversely, topcoat B2 shows a clear change, initially displaying primarily plastic response at 100 μN , reaching approximately equal distribution at the 200 μN and 500 μN conditions.

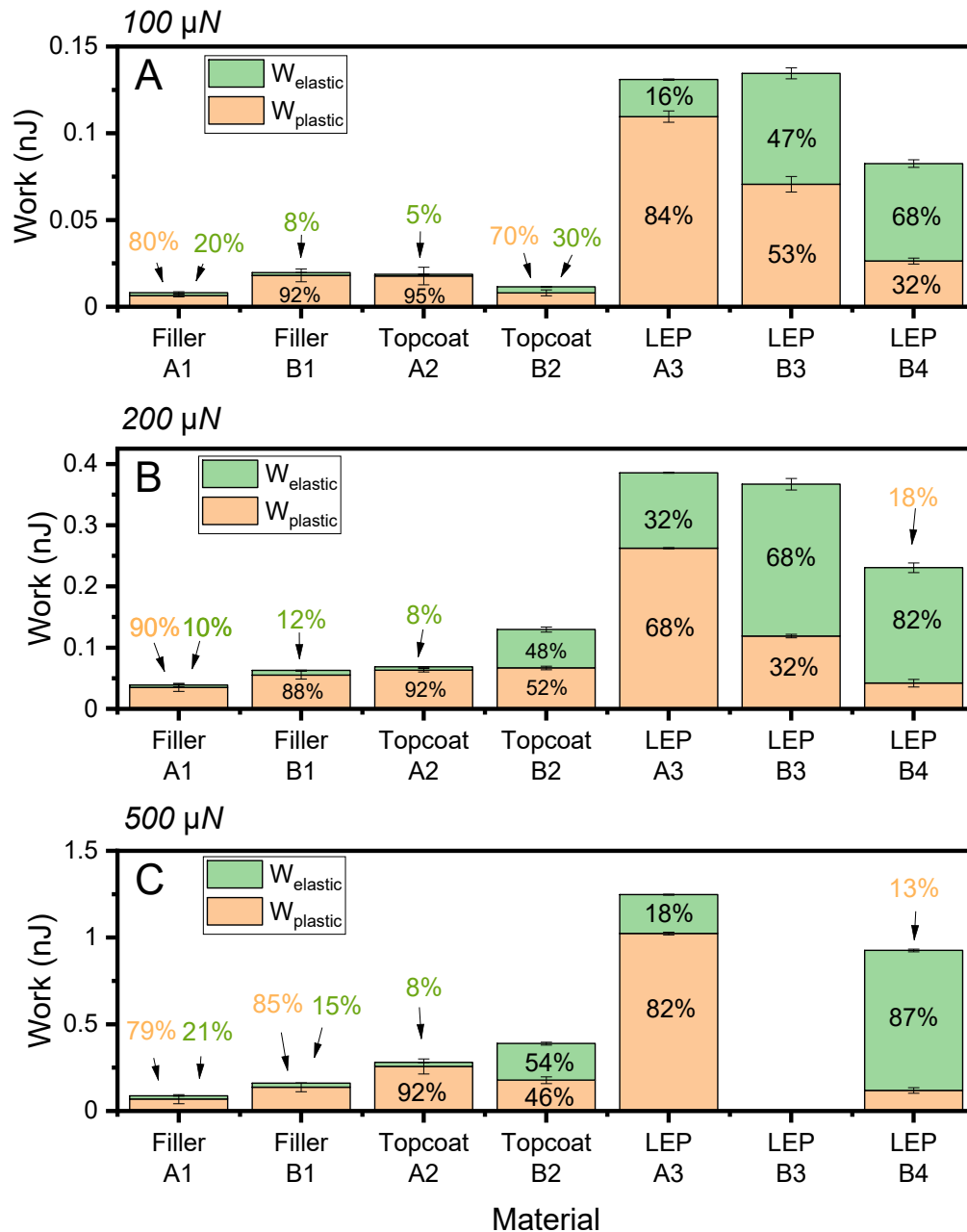


Figure 5.14 – A bar chart is presented comparing the indentation work values measured during a load-hold-unload nanoindentation method. Maximum loads: 100 μN , 200 μN , and 500 μN , loading time: 5 seconds / 10 seconds / 25 seconds (to maintain a constant loading rate), hold time: 60 seconds, unload time: 2 seconds and N=5.

The LEP materials displayed the highest W_{total} in each of the load conditions. LEP B4 was found to display the lowest work value of the LEPs at each condition, with its response becoming more elastic at the 200 μN and 500 μN conditions. The LEP A3 and LEP B3 showed similar W_{total} values at each load; however, the elastic/plastic distribution was considerably different. LEP A3 displayed a predominately plastic response at 100 μN , whereas the LEP B3 is approximately an equal distribution. At the 200 μN conditions, both LEP A3 and LEP B3 display an increased W_{elastic} percentage, with the latter material being considerably more elastic. At the 500 μN condition, the LEP A3 material response

becomes more plastic, returning to approximately the 100 μN distribution, unlike the LEP B4 response which becomes more elastic.

5.3.3 Test 3 – Repeated Indentation and Varying Recovery Period

The final test explored the impact of repeated indentations and recovery times using a load-hold-unload method, as shown in Figure 5.15 and summarised Table 5.3.

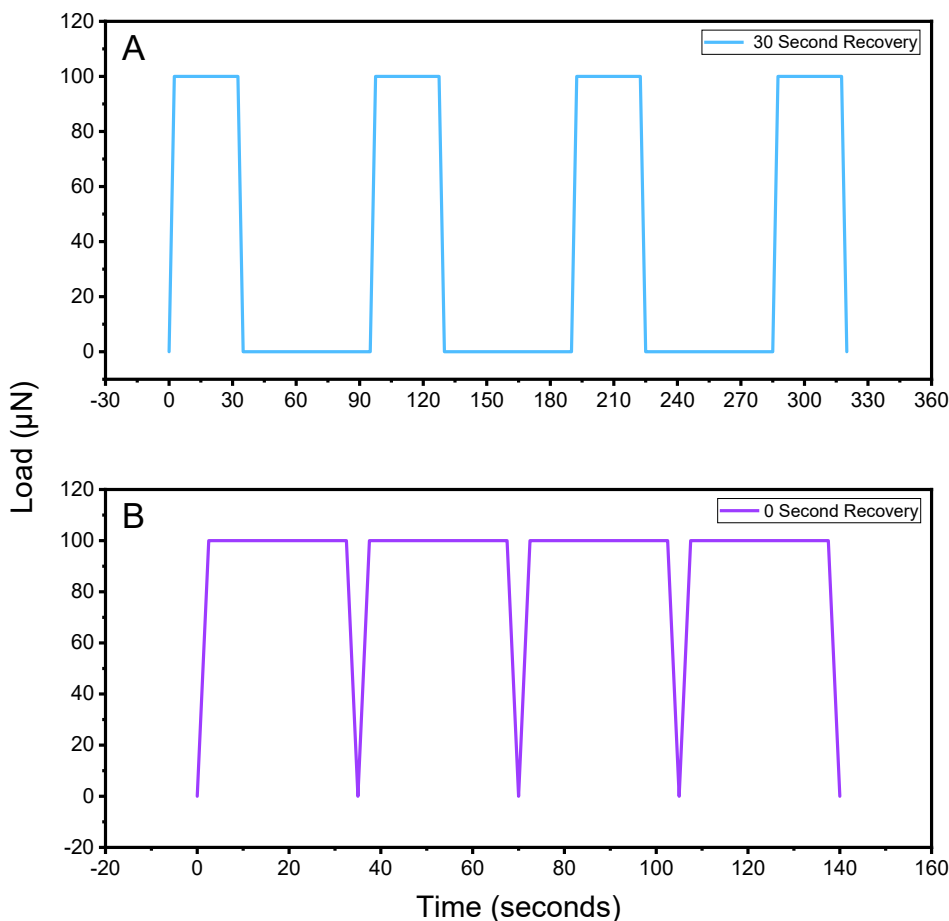


Figure 5.15 – A schematic detailing the three load-hold-unload nanoindentation methods used in Test 3. Maximum load: 100 μN , loading time: 2 seconds, hold time: 30 seconds, unload time: 2 seconds and $N=1$. For condition A (blue), a 60 second recovery period (where the load was set at zero) was utilised, and no recovery period was used for condition B (purple). The subsequent indent was started immediately after the unload.

For the LEP A3 material shown in Figure 5.16, a clear difference was seen in the material response between both conditions. The initial indent in both conditions resulted in similar W_{total} values and elastic/plastic work distribution. The observations for each of the test conditions were:

- For the condition with the 0-second recovery period, a considerable decrease of $\approx 50\%$ in the W_{total} was observed after the first indentation. This change can be seen to reduce the $W_{plastic}$ as the $W_{elastic}$ value remains consistent through subsequent indentations. The

third and fourth indentations also display a slight decrease in W_{total} and are due to the decrease in $W_{plastic}$.

- For the 60-second recovery period, a smaller $\approx 20\%$ decrease in the W_{total} was observed due to a reduction in the $W_{plastic}$ in the second indentation. The third and fourth indentations showed no considerable change in W_{total} or plastic-elastic work distribution.

Table 5.3 – A table detailing the parameters used in Test 3 in a hold-load-unload test method to determine the influence of repeated indentation and recovery periods.

Test Parameters	
Loading time (s)	2.5
Maximum load (μ N)	100
Hold time (s)	30
Unload time (s)	2.5
Recovery time (s)	60 and 0
Repeated indents	4
Repeats (N)	1

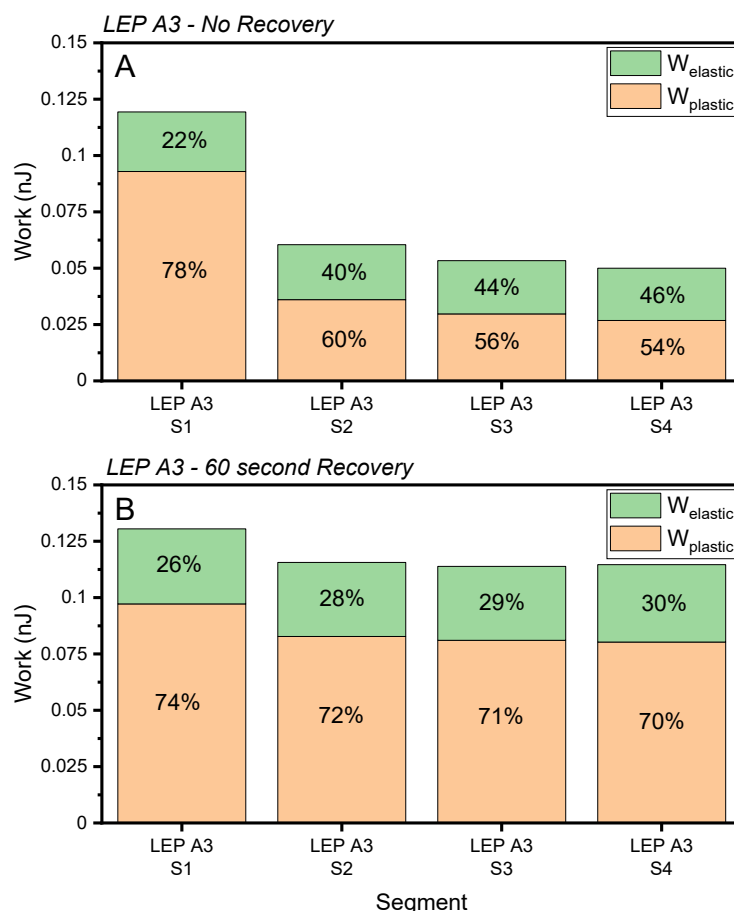


Figure 5.16 – A bar chart is presented comparing the repeated indentation work values at the same location of LEP A3 measured during a load-hold-unload nanoindentation method. The S value denotes the indentation sequence. Maximum load: 100 μ N, loading time: 2 seconds, hold time: 30 seconds, unload time: 2 seconds and N=1. For condition A, a 60 second recovery period (where the load was set at zero) was utilised, and no recovery period was used for condition B. The subsequent indent was started immediately after the unload.

For the topcoat A2 material shown in Figure 5.17, the distribution of work was predominately plastic in all indents. A clear difference was seen in the material response between both conditions. The initial indent in the 0-second recovery condition was 0.05 nJ higher than the 60-second recovery period; however, the elastic-plastic distribution was similar. The second indentation resulted in a decrease of $\approx 60\%$, showing a considerable decrease in $W_{plastic}$ and a slight increase in $W_{elastic}$. The third and fourth indent both showed a considerably lower decrease to the W_{total} because of the reduction in the $W_{plastic}$ with no minimal changes to the $W_{elastic}$. For the condition with the 60-second recovery period, a smaller reduction in total work of $\approx 40\%$ was observed. This decrease was due to the reduction of $W_{plastic}$, with $W_{elastic}$ not showing any considerable change. The third and fourth indentations showed decreases in W_{total} of 15% and 10%, respectively, both due to the reduction in $W_{plastic}$.

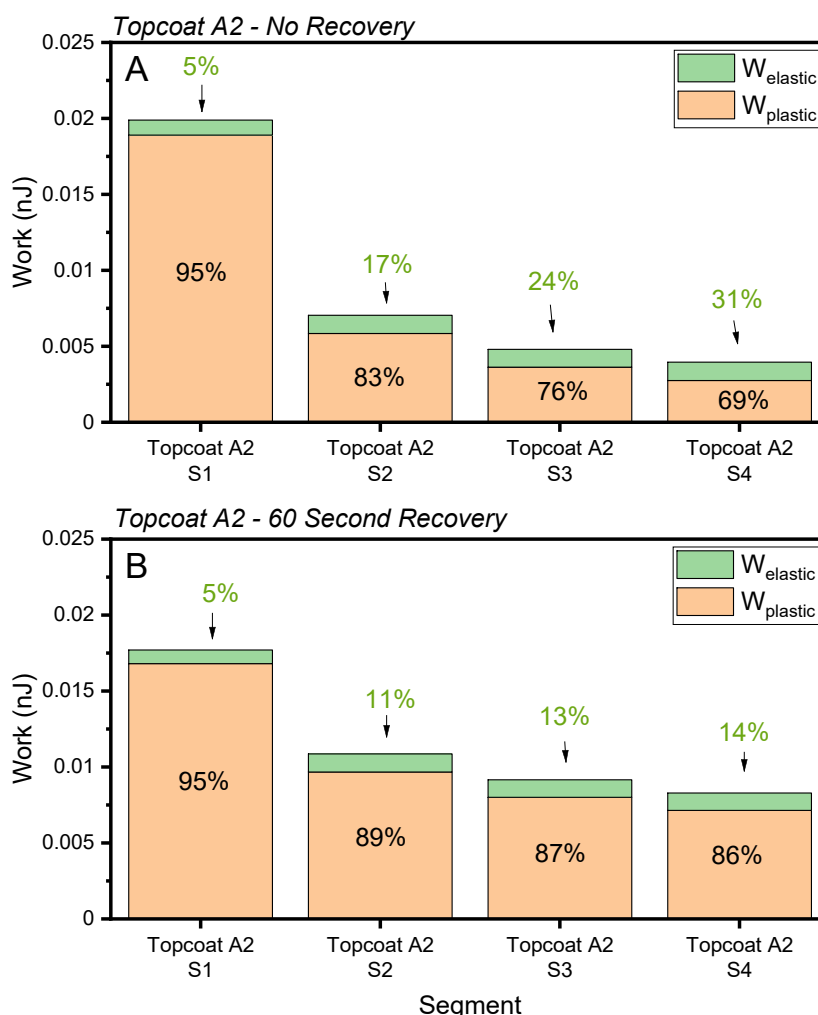


Figure 5.17 – A bar chart is presented comparing the repeated indentation work values of topcoat A2 measured during a load-hold-unload nanoindentation method. The S value denotes the indentation sequence. Maximum load: 100 μ N, loading time: 2 seconds, hold time: 30 seconds, unload time: 2 seconds and N=1. For condition A, a 60 second recovery period (where the load was set at zero) was utilised, and no recovery period was used for condition B. The subsequent indent was started immediately after the unload.

The LEP B3 material shown in Figure 5.18 demonstrated a considerably larger amount of $W_{elastic}$ than the previous topcoat A2 and LEP A3 materials. For the 0-second recovery condition, a $\approx 25\%$ decrease in the W_{total} was observed due to the decrease in the $W_{plastic}$. The subsequent indentations resulted in minor decreases in the W_{total} of $\approx 3\%$ after each indent, again due to reduced $W_{plastic}$. For the 60-second recovery period, no considerable change was seen due to repeated indentation, with the elastic-plastic distribution remaining similar throughout.

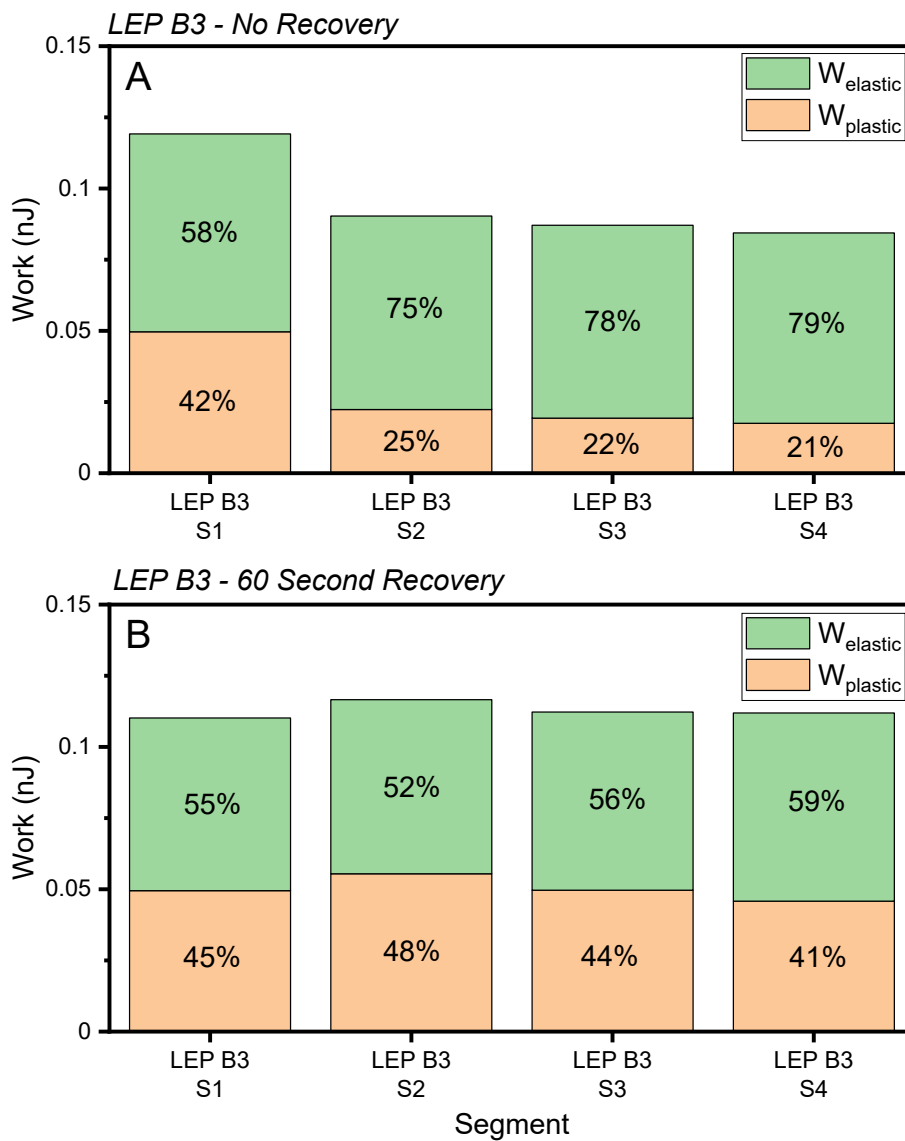


Figure 5.18 – A bar chart is presented comparing the repeated indentation work values of LEP B3 measured during a load-hold-unload nanoindentation method. The S value denotes the indentation sequence. Maximum load: 100 μ N, loading time: 2 seconds, hold time: 30 seconds, unload time: 2 seconds and N=1. For condition A, a 60 second recovery period (where the load was set at zero) was utilised, and no recovery period was used for condition B. The subsequent indent was started immediately after the unload.

For the LEP B4 material shown in Figure 5.19, a similar material response was observed between both conditions. The initial indent in both conditions resulted in similar W_{total} and elastic-plastic work distribution. For the second indentation of the 0-second recovery condition, a $\approx 10\%$

decrease in the W_{total} was observed due to the decrease in the $W_{elastic}$. The subsequent indentations were observed to have approximately the same W_{total} and elastic-plastic distribution. For the second indentation of the 60-second recovery period, the total work decreased by $\approx 5\%$, with subsequent indentations resulting in minor increases in $W_{plastic}$ and reductions in $W_{elastic}$.

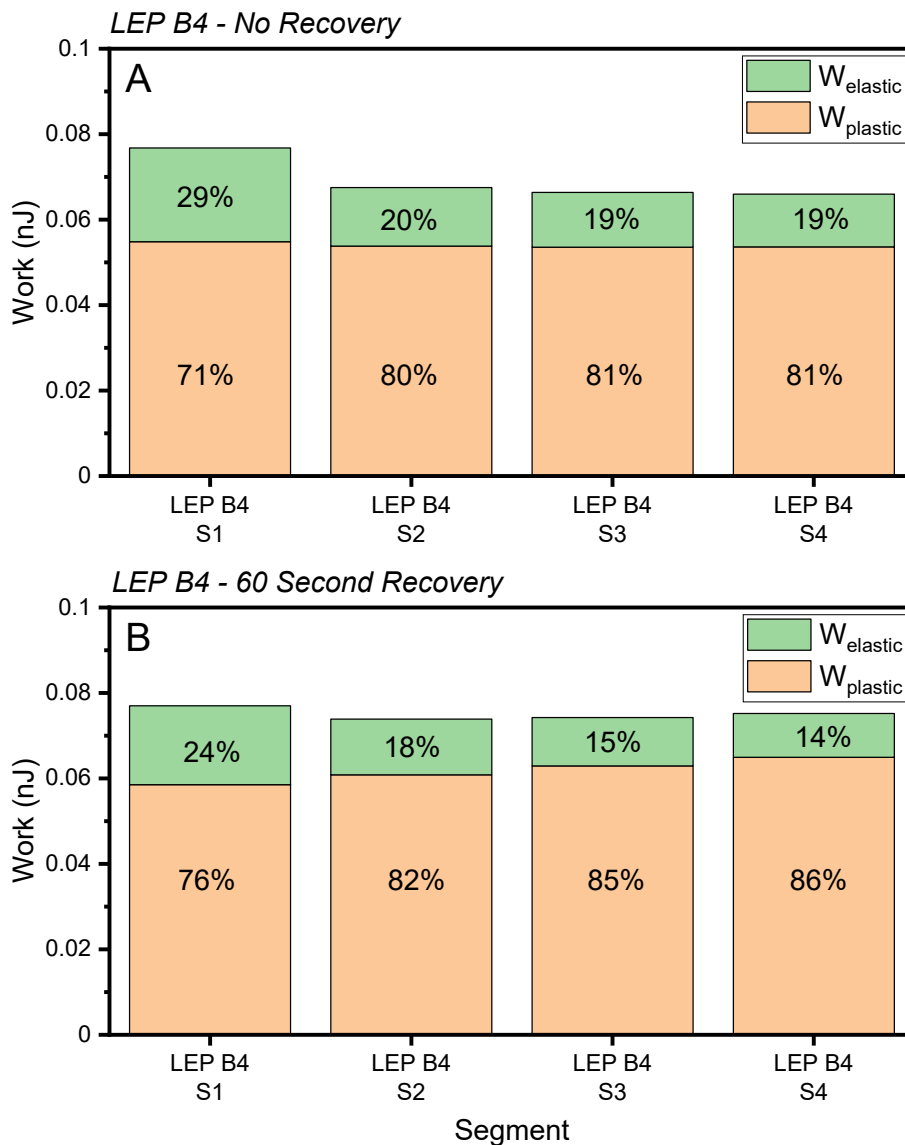


Figure 5.19 – A bar chart is presented comparing the repeated indentation work values of LEP B4 measured during a load-hold-unload nanoindentation method. The S value denotes the indentation sequence. Maximum load: 100 μ N, loading time: 2 seconds, hold time: 30 seconds, unload time: 2 seconds and N=1. For condition A, a 60 second recovery period (where the load was set at zero) was utilised, and no recovery period was used for condition B. The subsequent indent was started immediately after the unload.

5.4 Discussion

5.4.1 Loading Rate

Test 1 aimed to vary the loading rate in a hold-load-unload cycle to identify if any significant strain-rate dependent behaviour (with the data provided it was not possible to calculate the strain rate but is

assumed to be quasi-static) could be observed in the tested materials. These differences, summarised in Table 5.4, can be used to compare how a material behaves under different strain rates that can occur as a result of different impact conditions. The differences between materials are thought to be attributed varying molecular structures and their associated relaxation times. At lower strain rates, there is sufficient time to plastically flow or relax the induced stress making the appears as a more ductile polymer. At higher rates, the material cannot plastically respond rapidly enough and so it appears as more brittle material. As the molecular structure of each material is not known it is not possible to directly link them to changes in material properties.

Table 5.4 – A table summarising which materials demonstrated significantly different properties between the two loading rates tested in Test 1. A ✓ indicates a P value of <0.05 and was considered statistically significant, and – indicates a P value >0.05 and is considered not statistically significant.

	LEP B3	LEP B4	LEP A3	Topcoat B2	Topcoat A2	Filler B1	Filler A1
Maximum Depth	✓	✓	-	✓	-	-	-
Reduced Modulus	✓	✓	-	✓	-	-	-
Short Term Recovery	-	-	-	-	-	-	-
Hardness	✓	✓	-	-	-	-	-
Indentation Work	-	-	-	-	-	-	-

In this test, an extended hold time and a rapid unload time was used to allow for the use of the OP analysis method. However, this may have made identifying any significant difference between loading rates challenging to obtain as the material properties are calculated from the unloading curve rather than the loading curve. Owing to the extended hold period that allows for the creep effects to equilibrate, it may have masked some of the effects that could have occurred if a shorter loading time had been utilised. Future tests could be designed to initially identify the minimal amount of time required for the creep effects to equilibrate in each material. These material-specific values could then be used in subsequent tests as the hold period duration makes identifying any difference between loading conditions less challenging. However, creep testing requires considerable time and requires a dedicated programme focused on the topic to improve understanding. In addition to the time required for this testing, the use of nanoindentation is expensive. In many cases, the cost is prohibitive for use outside of an academic environment.

It was observed that the materials reached different maximum indentation depths when the same method was applied. As expected, the more compliant materials were found to have the largest depths in the order of LEPs > topcoats > fillers with the LEP B3, LEP B4, and topcoat B2 materials displaying significant differences between loading rates. Nevertheless, this data highlights considerable differences in how materials behave under the same loading conditions, contributing to

mismatches at interfaces between materials. These variations are also crucial as they can influence the other calculated material properties and increase uncertainty at high depths. The latter issue was discussed in Section 5.2, where increased testing depth can result in greater uncertainty in the predicted contact area.

The E_R values of each material were obtained and found to be in the order of fillers > topcoats > LEPs. While the values differ (actual modulus values require Poisson's ratios for each material), the order of materials matches the tensile testing order detailed in Section 4.2.3 and Section 4.2.4. This observation implies that the use of nanoindentation could be a suitable alternative for measuring the modulus of coating materials adding the ability to investigate local variations of E_R through the thickness or around defects. The LEP B3, LEP B4, and topcoat B2 materials were observed to have significant differences between loading rates implying that the chemistry used in these materials is more sensitive to loading rate variations in the time-scale of these tests. However, as with tensile testing, this approach is considered quasi-static and cannot capture the higher Young's moduli at higher strain rates.

The STR measurements were observed to possess considerable standard deviations, potentially preventing any significant relationships from being observed. Nevertheless, STR values for all materials were obtained with clear differences between some of the topcoat and LEP materials. topcoat A2 was found to have significantly lower STR than topcoat B2, and the LEP A3 material was significantly lower than both the LEP B3 and LEP B4 materials. From these results, it appears that the System B materials are better able to elastically recover deformations, a property that has been correlated to improved erosion performance [128]. This recovery behaviour is reported to be linked to the crosslinking density/groups in each material [134, 179]. This parameter could be modified by varying the coating constituents to increase the crosslinking density or by utilising stronger bonds that are less likely to dissociate under expected deformations.

The hardness of each material was obtained generally following the order of filler (which possessed considerable standard deviations) > topcoats > LEPs. Owing, to the proportional relationship between H and Young's modulus, the order of these H values correlates to the measured E_r values [180]. However, H is the resistance to indentation and can be used as an alternative metric of comparison of how materials responded to a surface deformation (at the system level taking into account size effects) rather than by comparing E_r values, which are intrinsic material properties that generally define several material behaviours, e.g. materials under tension/compression. It was observed that the LEP B3 and LEP B4 both were significantly different at the two loading rates indicating a strain-rate dependence. This decrease in H at higher strain rates indicated that materials

could undergo more significant surface deformation upon impact, correlating with the aforementioned decrease in E_r .

It was observed that filler materials underwent the lowest W_{total} and could be attributed to the low indentation depths, due to the higher modulus values compared with the other material types. 92 % of the work was plastic implying that the filler materials have the least recoverable work of all the material types. The topcoat materials were observed to undergo marginally more work than the fillers, which could be attributed to the increased depths; however, the elastic-plastic distribution differed considerably. topcoat A2 was found to be 95 % plastic and topcoat B2 63 % plastic, again correlating with the STR values. The LEPs were found to have the highest W_{total} , which is linked to the increased indentation depths. The more interesting observation is the elastic-plastic distribution for each material. The LEP A3 response was 80 % plastic, LEP B3 was 46 % plastic, and LEP B4 was 31 % plastic. The higher elastic work percentages correlate to increases in STR . Overall, no significant differences were found in the total work or elastic-plastic distribution between the two loading conditions, indicating an insensitivity to the loading rate. Nevertheless, the data demonstrated the repeatability of a novel method (not seen by the author in this field of LEE) to extract further information about the elastic and plastic deformations occurring during an indentation that are used again in Test 2 and Test 3 obtaining more significant findings.

5.4.2 Maximum Load

Test 2 aimed to vary the maximum in a hold-load-unload cycle to determine whether any significant difference in material behaviour could be observed in the tested materials. These differences, summarised in Table 5.5, can be used to compare how a material behaves under different loads, which coating materials can experience due to impacts or handling. Generally higher loads are able to overcome additional molecular interactions resulting in greater strains. These can exceed the elastic limit of the material and lead to non-recoverable plastic deformation that can influence measured parameters which are further discussed below.

Table 5.5 – A table summarising which materials demonstrated significantly different properties between the maximum loads in Test 2. A ✓ indicates a P value of <0.05 and was considered statistically significant, and – indicates a P value >0.05 and is considered not statistically significant.

	LEP B3	LEP B4	LEP A3	Topcoat B2	Topcoat A2	Filler B1	Filler A1
Maximum Depth	✓	✓	✓	✓	✓	✓	✓
Reduced Modulus	-	✓	✓	✓	✓	-	✓
Short Term Recovery	✓	-	✓	-	-	-	-
Indentation Work	✓	✓	✓	✓	✓	✓	✓

It was observed that the materials reached different maximum indentation depths when the same method was applied. As expected, the most compliant materials were found to have the largest depths in the order of LEPs > topcoats > filler, with significant increases observed upon increasing load for all materials.

It was generally observed that as the load was increased, the E_R was found to decrease with filler A1, topcoat A2, topcoat B2, LEP A3, and LEP B4 materials displaying significant differences between maximum loads. This observation indicates that the property at the surface may be different further into the thickness of the material. However, filler A1, topcoat B2, and LEP A3 all showed highest value at 100 μN , decreasing at 200 μN but then displaying an increase at 500 μN load. This observation implies that it may not be a simple gradient of material properties but discrete sections of coating with different material properties possibly caused by how the material cures under different conditions, *e.g.* levels of light, temperature and moisture levels. The response of the topcoat B2 material should also be highlighted as it displayed the largest difference between indents. From the 100 μN to the other indents, a $\approx 94\%$ decrease in E_R observed, which could indicate that the material was partially cured below the surface. However, it should be noted that owing to the high loads and depth used, there is potential for this difference to be attributed to either pile-up or poor calibration for the tip, as discussed in Section 5.2.

The STR measurements possessed considerable standard deviations in cases, potentially preventing any significant relationships from being observed. The order of material STR was generally the same as Test 1 in each condition however, significant differences in STR were observed in the LEP A3 and LEP B3 materials. Between the 100 μN and 200 μN conditions, the increase in load resulted in an increased STR , and in the case of the LEP A3, the highest 500 μN condition resulted in a significant decrease in STR . This implies that the material undergoes greater plastic deformation at the greater loads/displacements, which is unrecoverable. This observation highlight that the test parameters used to measure the STR are important and can lead to different results.

An increase in W_{total} was observed for all materials as the load was increased. While no trend could be observed in the filler and topcoat materials, the LEP materials showed considerable changes in the elastic-plastic distribution. Data presented in Figure 5.13 and Figure 5.14 are combined and presented in Figure 5.20 to illustrate a correlation between the STR and $W_{elastic}$. When compared, both methods rank the materials in the same order indicating that they are both a measure of the material's elasticity. However, there are differences of up 21 % between the two methods, with the average difference calculated to be 8 %. These differences are reported in Table 5.6.

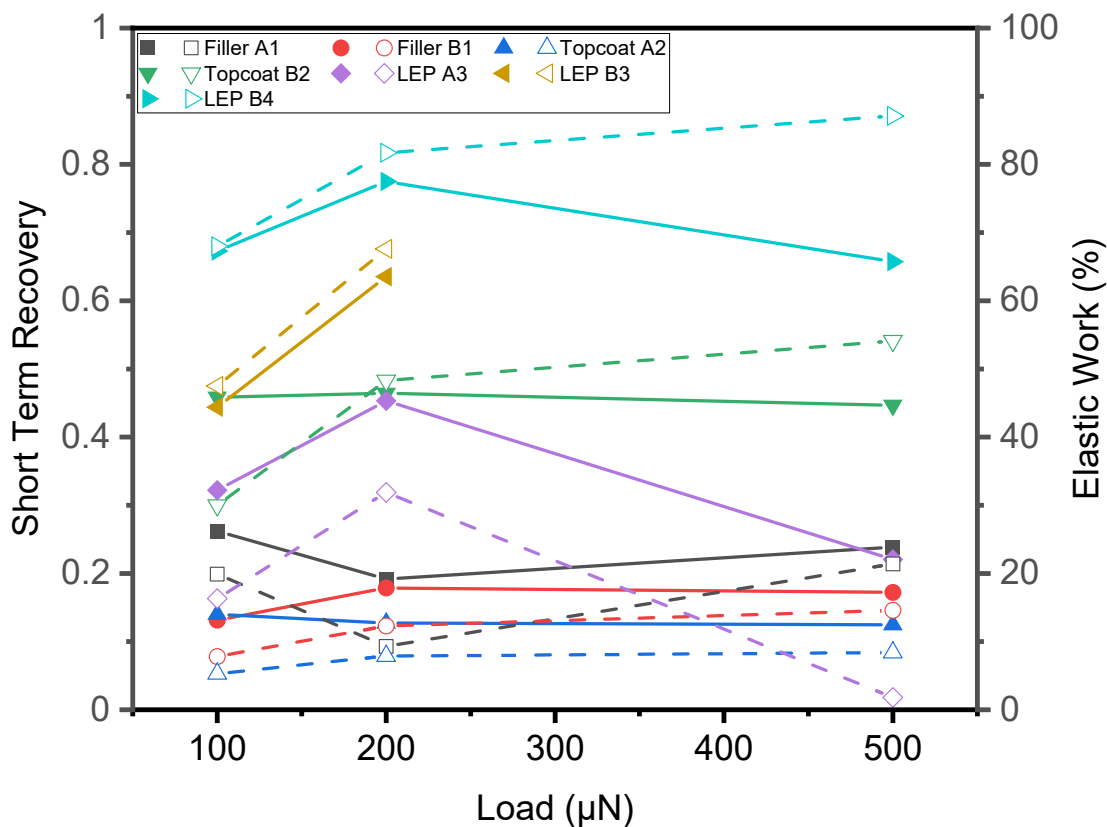


Figure 5.20 – A line chart is presented comparing the short term recovery values (filled symbols and solid lines) and elastic work percentage (hollow symbols and dashed lines) measured during a load-hold-unload nanoindentation method. Maximum loads: $100 \mu\text{N}$, $200 \mu\text{N}$, and $500 \mu\text{N}$, loading time: 5 seconds / 10 seconds / 25 seconds (to maintain a constant loading rate), hold time: 60 seconds, unload time: 2 seconds and $N=5$. The LEP B3 $500 \mu\text{N}$ was unable to be captured and is not displayed. Error bars are omitted for clarity but are available in previous Figure 5.13.

This comparison indicates that both STR and $W_{elastic}$ could be used as a metric to assess the material's elastic properties through nanoindentation. The differences observed between the two methods can be attributed to how the value is calculated. STR is influenced by the maximum and final depth during the loading cycle whereas $W_{elastic}$ uses integration to obtain the reported value. As a result, the latter method is affected by the maximum depth, final depth and any changes in loading, hold, or unloading curve; consequently, this suggests that the use of $W_{elastic}$ as a metric of comparison is more sensitive to any changes in the material's elasticity. While further testing is still required to determine the uncertainty of the results, this provides an additional tool to support materials development by coating manufacturers by providing more information at different loads and depths rather than single values.

Table 5.6 – Tabulated average short term recovery (STR) percentage and elastic work percentage measured during a load-hold-unload nanoindentation method (loading time: 5/10/25 seconds, maximum load: 100/200/500 μN , hold time: 60 seconds, unload time 2 seconds and $N=5$).

Max Load (μN)	Material	Average STR (%)	Average $W_{\text{elastic}} (\%)$	Difference (%)
100	Filler A1	26	20	6
	Filler B1	13	8	5
	Topcoat A2	14	5	9
	Topcoat B2	46	30	16
	LEP A3	32	16	16
	LEP B3	44	48	-4
200	LEP B4	67	82	-15
	Filler A1	19	9	10
	Filler B1	18	12	6
	Topcoat A2	13	8	5
	Topcoat B2	46	48	-2
	LEP A3	45	32	13
500	LEP B3	63	68	-5
	LEP B4	77	82	-5
	Filler A1	24	21	3
	Filler B1	17	15	2
	Topcoat A2	12	8	4
	Topcoat B2	45	54	-9
	LEP A3	22	2	20
	LEP B3	-	-	-
	LEP B4	66	87	-21

5.4.3 Repeated Indentation and Recovery

The majority of materials were observed to display a decrease in W_{total} due to repeated indentation, with considerable differences seen when the recovery time was varied. The normalised change in W_{total} is presented in Figure 5.21 to provide a comparison between the materials tested. These differences are attributed to the ability of a material to recover during the time between indents and the amount of plastic deformation that the material undergoes during each indent. These factors are determined by the molecular structure of each material which can be varied to change the elastic limit and the rate/extents a material can recover.

The topcoat A2 material was the only material to possess predominantly plastic work in all responses reduced upon repeated indentation. While the material did display the most considerable decrease in W_{total} the addition of a recovery period resulted in a lesser decrease than from subsequent indentations.

The LEP A3 material displayed a predominately plastic response for the initial indents. However, subsequent indents were observed to be more elastic with a recovery period and remained predominately plastic when allowed to recover. A considerable difference in W_{total} was seen between the two conditions. The no-recovery condition was observed to undergo a considerable decrease on the second indentation, whereas the 60-second recovery was found to undergo a lesser decrease.

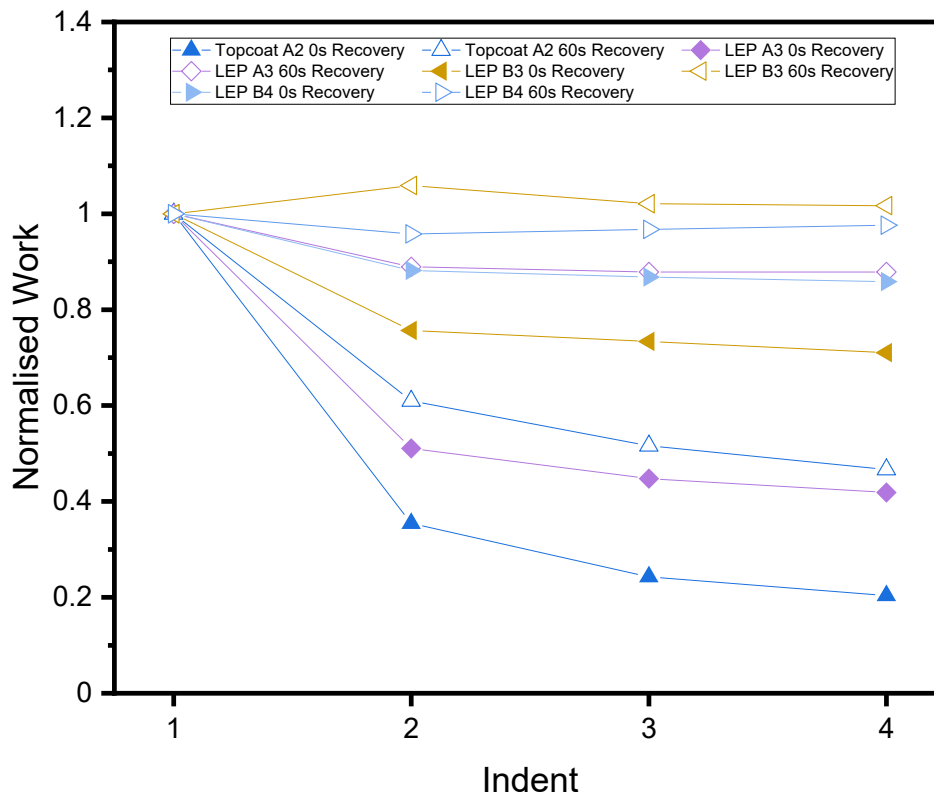


Figure 5.21 - A line chart is presented comparing the total work values with 0-second recovery (filled symbols) and 60-second recovery (hollow symbols) measured during a load-hold-unload nanoindentation method (loading time: 2.5 seconds, maximum load: 100, hold time: 60 seconds, unload time 2 seconds, repeated indents: 4 and N=1)

The LEP B3 material displayed an approximately equal distribution of plastic-elastic work during the first indent. The no-recovery condition displayed a decrease in W_{total} with an increase in elastic work percentage, whereas the 60-second recovery condition displayed minimal change with no considerable change in elastic-plastic distribution.

The LEP B4 material was observed to have a predominantly plastic response in both conditions. A decrease in total work was observed after the first indent but subsequent indents saw no further change regardless of recovery time.

These observations identified during this test could be linked to the *STR* of a material, a parameter reported to be correlated with improved rain erosion performance [128, 136]. A material

that can recover deformations in a shorter period may appear to show no change in subsequent indents as it is able to recover most of the deformation. Therefore, it implies that a material that has a consistent response with minimal changes would be advantageous in a LEP material as it could be assumed there would be less change in the materials dimensions and properties that can occur during the recovery phase. This behaviour is governed by the 3D polymer network and can be varied by changing the constituents discussed in Section 2.2.1.

Furthermore, the elastic-plastic work distribution has also been quantified allowing for more of an understanding of the material response to be captured. By using this method, it found that not only did material possess different elastic-plastic distributions, but these were found to vary because of recovery time and repeated indentation. Intuitively, a material that is predominately elastic would be more favourable for coating material as the deformation is recoverable. However, when comparing the LEP materials we see that the LEP B3, which is found to display predominately elastic work, has been found to perform more poorly under accelerated RET testing (Section 7) than LEP B4 and LEP A3, which displayed more plastic work. Therefore, the rain erosion performance of a material is not directly correlated to the elastic-plastic work distribution and suggests that there are other key parameters, such as those currently utilised in the Springer approach, that need to be considered.

When interpreting these results, it is important to consider the time scale of the methodology being used. In this test, each indent takes 65 seconds and then a further 60 seconds is added for recovery. It is possible that if the test was conducted over a different duration the results observed may be different. If the test was conducted over a longer period, materials recover to a greater degree resulting in fewer differences being observed between materials. Conversely, if it was possible to conduct the test in a shorter duration, it may be possible to observe further differences as not all materials could recover during the time.

The final point that must be considered is that the method used is not a standard test currently used to characterise these types of coating material. Due to time and cost constraints, repeats of each condition were not possible, meaning that statistical analysis to identify whether differences were significant was not possible. However, from Test 2 it is possible to state that the breakdown of the elastic-plastic response is repeatable and results in small standard deviations, which can allow for comparisons to be made between materials.

5.5 Summary

In this chapter, nanoindentation was successfully used to characterise individual materials used in coating systems. Novel data was generated to allow for comparisons between materials in an effort

to correlate behaviour to rain erosion performance. It is the authors opinion that of the tests used the variation of load and the use of repeated indentations are the most relevant for rain erosion. The former can be related to different stresses imparted on the coating under different impact conditions and the latter is valuable in understanding how a material responds when repeatedly loaded as it would be when in heavy rain conditions on a rotating leading edge.

Strain-rate dependent behaviour was observed in some topcoat and LEP materials; however, some behaviour may not have been identified due to the chosen methodology, which included long hold times.

The use of different maximum loads resulted in significant differences in the properties of all of the materials tested. Within this work, a correlation between the elastic-plastic work and *STR* was identified. This finding presents an alternate method of extracting additional information from an indentation load-depth curve not seen in current LEP characterisation literature. Unlike *STR*, which considers two data points, the new method includes information from all parts of the load-hold-unload curve, making it more sensitive to material differences.

Clear differences were observed when materials underwent repeated indentation with LEP materials demonstrating the greatest amount of recovery between indents. The topcoat A2 showed the most considerable decrease in work, potentially due to the lower recovery values presented in this chapter. Most of the LEP materials demonstrated reductions in subsequent indents when there was no recovery period. However, when allowed to recover, all LEP materials demonstrated increased work values suggesting that the material had recovered and required additional work again to cause the indent. This finding is of particular interest as it is currently thought that materials with good recovery levels are expected to have good rain erosion performance.

In reality droplets can cause impacts that result in much higher strain rates and occur in much shorter periods. These effects could be captured using dynamic nanoindentation in future studies. However, this chapter focused on characterising the quasi-static material behaviour of each material by allowing for viscoelastic creep effects to equilibrate to minimise variation. The work demonstrated novel methodologies that can be used by coating manufacturers to aid in coating characterisation and design. Further work in Chapter 6 explores the use of DMTA, which allows for the characterisation of materials under controlled conditions that include temperature and higher strain rates closer to those reported to occur in-situ.

6

Dynamic Mechanical Thermal Analysis

This chapter presents the results from the characterisation of each coating material using DMTA with strain rate and temperature dependent behaviour observed in all materials. The time-temperature superposition principle was also used to predict material behaviour at strain rates outside the working range of the instrument.

6.1 Introduction

Characterisation of viscoelastic engineering polymers commonly involves determining the deformation behaviour and material strength under different loads, displacements and stresses (e.g. tension, compression, shear and torsion). These are commonly conducted under quasi-static (QS) conditions, meaning that time and inertial forces are considered to be negligible. These tests are commonly used as a baseline for most material characterisation. Both Section 4 and Section 5 utilised methods that are considered QS due to the relatively low strain rates used; even so, rate-dependent behaviour was observed in certain materials. The limitation of QS static testing is it is limited to low strain-rates which are considerably lower than those that are predicted to occur as a result of rain droplet impacts on modern blades. Dynamic mechanical thermal analysis (DMTA) is a method that allows for the characterisation of material behaviour under controlled conditions. These include considerably higher frequencies/strain rates¹² than conventional QS tests and at different temperatures allowing for a greater understanding of how a material can behave over a wide range of conditions, including those seen offshore.

A DMTA, described in Section 3.4, is an instrument that should be commonly available in many coating manufacturers' material characterisation labs in addition to conventional thermal analysis and QS test instruments. However, DMTA is expected to only be used for basic testing to determine the T_g of a material. As a result of this, the wealth of information around frequency dependence, which is particularly important for viscoelastic materials, is not captured. This chapter demonstrates improved methodologies that can be used to characterise individual materials used in coating systems linking these findings to rain erosion performance.

Two test fixtures were used during the testing:

The first was the dual-cantilever (DC) flexural bending fixture. Flexural testing using this fixture results in the material experiencing a combination of stresses through the thickness of the sample. The top (concave) face of the sample will be in compression, whereas the bottom (convex) face will be under tension. This was chosen initially for two reasons; it is expected to be a de facto fixture supplied with the many DMTA instruments meaning coating manufacturers were more likely to own it and be able to compare results produced in this work; it also utilised thicker specimens which would be more insensitive to defects within the sample meaning it could withstand a wider range of frequencies and temperatures.

¹² These terms are used interchangeably throughout the work and are related in Figure 6.19.

The second was the thin film tensile (TF) fixture. A form of uniaxial testing that subjects a specimen to a controlled tension. This was chosen as it was identified as the best evaluation mode for thin-film materials which are of similar thickness to those used in-situ, allowed for testing of single deformation tensile stress, as it is reported that peak stresses are tensile due to rebounding pressure from the surface of the material. By using the second test it could be possible to decouple behaviours and identify if the testing mode influences materials properties. However, unlike DC samples these are more susceptible to defects meaning they could be less likely to be able to withstand the desired wide frequency and temperature ranges.

6.2 Dual Cantilever Testing

This section details the characterisation of each coating material utilising the DC test fixture thought to be the most commonly available fixture supplied with DMTA instruments.

6.2.1 Study of Strain Dependence

The Linear Viscoelastic Region (LVER), of a material is important in the dynamic analysis of materials as within this range the viscoelastic parameters are considered to be strain independent as there are no permanent changes to the microstructure [181]. The upper limit of the LVER, shown in Figure 6.1, is called the Critical Strain (ϵ_c) and is used to determine the maximum oscillation strains that can be used in a test.

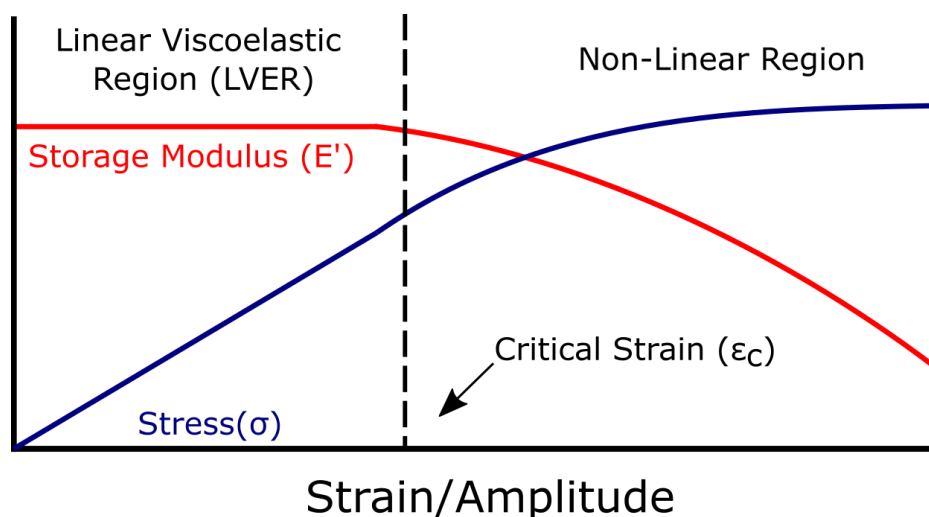


Figure 6.1 – Example of a dynamic strain sweep where the response of a material to increasing oscillatory deformation is recorded at a constant frequency and temperature. The red line is the storage modulus (E'), the blue line is the stress (σ), the dashed line indicates the end of the linear viscoelastic region (LVER). Within the LVER, E' is independent of strain and σ displays a constant slope.

The supplier of the DMTA used in this work (TA Instruments, UK) recommends strain values around 15 μm to 25 μm or 0.02 % to 1 % strain for polymeric coating materials [181]. While it would be possible to arbitrarily choose a value within this range the choice was made to analyse the strain

response of a material to confirm the values chosen were suitable. A temperature of 0 °C was chosen, as the ε_c for materials is reported to decrease at lower temperatures. This LVER and ε_c can be identified by a decrease in the storage modulus (E') or where the oscillatory stress-strain relationship becomes non-linear. While these indicators can be identified visually, a mathematical approach is used to remove bias for comparison results.

The method of calculating these points¹³ is similar to those used in literature and is as follows [134, 181]:

- From a plot of oscillatory strain vs E' , the onset¹⁴ of the curve and strain at a 5 % decrease in E' are reported as the ε_c .
- From a plot of the oscillatory stress-strain curve, the derivative is calculated. A perfectly linear response has a value of one and shifts upon becoming non-linear. In this approach, the first strain value to deviate by > 0.05 from the maximum is reported as the ε_c .

The determination of the ε_c for each material is summarised in Figure 6.2 using the previously mentioned methods from strain sweep tests.

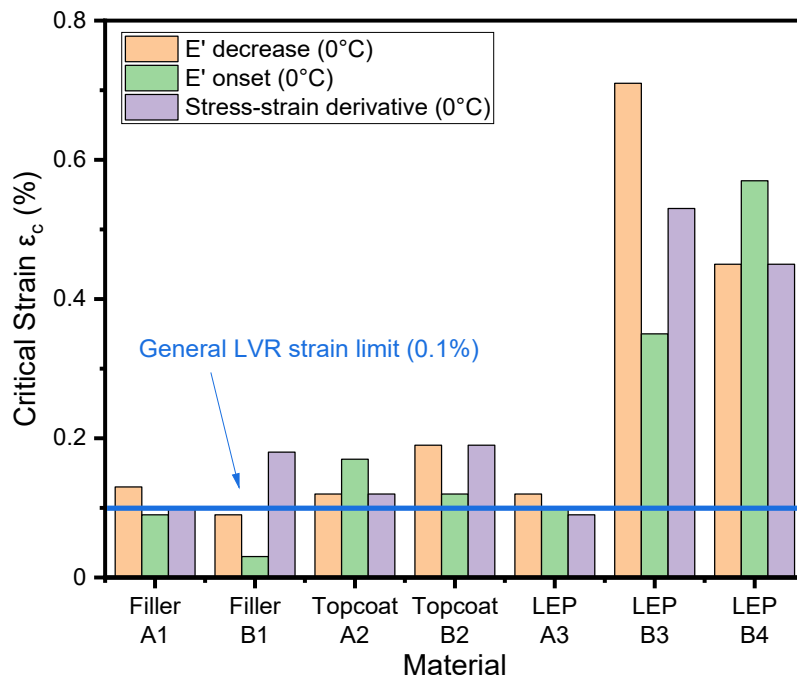


Figure 6.2 – Results from a dual cantilever dynamic strain sweep where the response of a material to increasing deformation (up to 400 μm) is recorded at a constant frequency (1 Hz) and temperature (0 °C). The blue line indicates the general linear viscoelastic region strain limit used in the subsequent testing.

¹³ The limits e.g. the 5 % decrease or change in derivative are essentially academic and are only selected to provide an indication of the LVER and is not expected to be completely accurate. Other studies may use different values and result in different ε_c values and therefore different LVERs.

¹⁴ The onset point is defined as the intersection of an initial tangent line with a final tangent line [181].

From these results, it can be seen that there is variation between the ε_c calculated by using each method. As expected, due to their considerably higher modulus when compared to other coating materials, the filler materials were found to have the lowest average ε_c values of 0.11 % for filler A1 and 0.10 % for filler B1. The topcoats, a more elastomeric material, were calculated to have marginally higher average ε_c values than the fillers, with 0.14 % for topcoat A2 and 0.14% for topcoat B2. The LEP materials displayed the highest average ε_c , which was expected as they can possess high STB values. The average ε_c for LEP B3 was 0.53 % and 0.49 % for LEP B4. However, LEP A3 showed considerably lower values of 0.1 %, meaning that non-linear behaviour begins at much lower strains when compared to LEP materials and was more similar to the filler materials in this regard.

While in theory testing at strain below the lowest measured ε_c would be suitable, extremely low strains can result in poor quality data due to the instrument's lack of torque or sensitivity. The selected strain also has to produce acceptable responses over the range of frequencies and temperatures used in the test. In this work, the DMTA waveform¹⁵ was checked to ensure waveforms were sinusoidal and smooth in each test, with ε_c values of 0.01 % to 0.1 % strain found to be suitable as constant parameters for further testing.

From the selected ε_c value, the corresponding stresses of the materials are compared Figure 6.3. This value is the Yield Stress (σ_c), the stress at which an object changes from undergoing elastic to plastic deformation.

As expected, due to their considerably higher modulus, the filler materials displayed the highest average yield stresses, 4.01 MPa for filler A1 and 2.31 MPa for filler B1. For the topcoat materials, average yields stresses of 1.59 MPa for topcoat A2 and 0.60 MPa for topcoat B2 were observed. For the LEPs, which are the lowest modulus materials, values of 0.11 MPa for LEP A3, 0.09 MPa for LEP B4 and 0.46 MPa for LEP B3. It can be observed that between materials, there are considerable differences in both ε_c and σ_c . This finding implies that materials could behave differently under the same loading conditions undergoing varying amounts of elastic and plastic strains.

¹⁵ Data not recorded by the instrument and therefore not reportable.

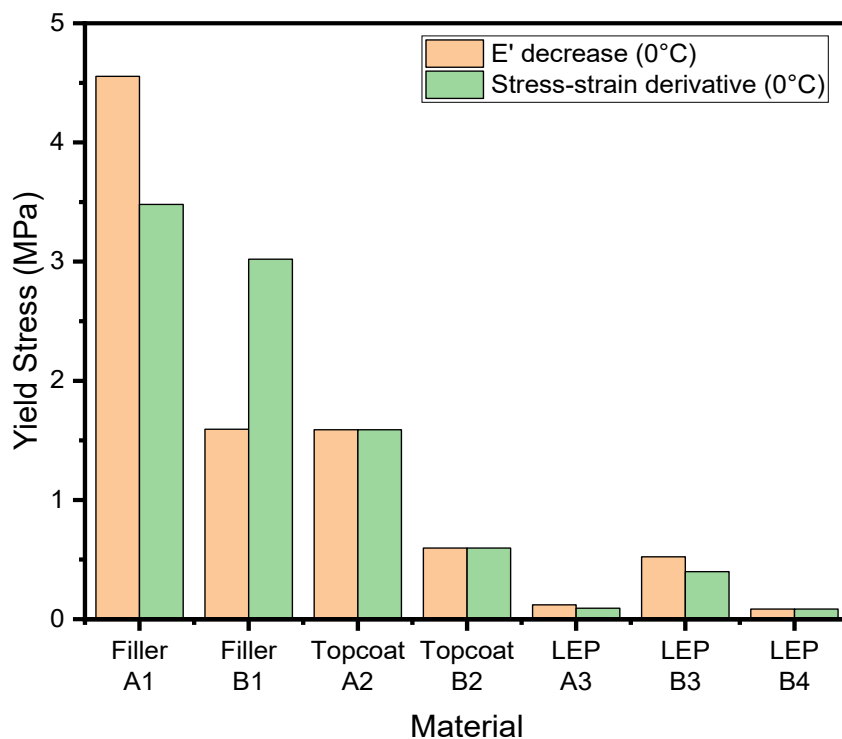


Figure 6.3 – Comparison of measured yield stresses obtained from a dual cantilever dynamic strain sweep where the response of a material to increasing deformation (up to 400 μm) is recorded at a constant frequency (1 Hz) and temperature (0°C).

6.2.2 Study of Temperature Dependence

The viscoelastic behaviour of polymeric materials is also highly sensitive to changes in temperature, which can influence material properties such as stiffness. These temperature variations can alter the viscoelastic behaviour and the resulting material performance.

Thermogravimetric analysis was initially used, following the methodology detailed in Section 3.3, to identify a suitable working temperature range that could be used in further testing. This step was required to ensure that no observable degradation would occur during elevated testing, which can add complexities to testing and minimise the amount of exhaust fumes produced.

The onset of degradation and total mass loss of each material are summarised in Table 6.1. The onset is used to identify the upper-temperature limit where it is assumed that minimal thermal degradation occurs. Air was chosen as the degradation gas as it is more suitable for the expected operating conditions. However, the use of air can complicate the degradation curves obtained as the effects of combustion are present. If more information is required using an inert gas such as nitrogen can give an improved understanding of the aromatic and aliphatic content.

Table 6.1 – Tabulated onsets of degradation and mass loss percentages obtained for thermogravimetric analysis under air.

Material	Onset of degradation (°C)	Mass loss (%)
Filler A1	234	63
Filler B1	318	56
Topcoat A2	290	46
Topcoat B2	308	48
LEP A3	292	81
LEP B3	314	96
LEP B4	309	96

An upper limit of 200 °C was selected from these data as the maximum working temperature used in work. However, in this work, temperatures did not exceed 80 °C.

The onset values reported were calculated for the first degradation step. While this information is useful for comparing materials at a basic level, it was observed that certain materials underwent multiple degradation steps. These further degradation mechanisms could be explored in further studies but were not considered relevant to this work due to being at temperatures considerably exceeding those seen in the field.

The measured mass loss value provides a comparison that includes all the degradation steps that occur up to 800 °C in air. However, only speculative comparisons can be made as the exact chemical structures, and stoichiometric ratios are unknown. The order of mass loss was LEPs > filler > topcoats, with the LEP materials observed to have considerably higher mass losses than the other two material types. LEP B4 was expected to have a lower mass loss percentage when compared to LEP B3 due to the increased aromaticity. However, this was not observed, and minimal differences were seen between the two.

With the LVER and working temperatures identified, DMTA can be used to undergo temperature sweeps to characterise the behaviour of each material as a function of temperature, as described in Section 3.4.

While it is possible to compare the magnitude of moduli values, identifying each material's T_g is critical in understanding at what temperature material properties can change considerably. In literature three T_g values are commonly reported and are associated with different phenomena [134, 182]. The first is the E' onset, which generally is the lowest of the reported T_g values and relates to mechanical failure of the material. The second is the E'' peak maximum, which is linked to molecular processes and considered the temperature at which segmental motion begins. This commonly occurs at a slightly higher temperature than the E' onset. The final is the tan (δ) peak maximum, typically the highest of the three measurements and is the most commonly reported in the literature. This

value provides a measure of the leathery midpoint between the glassy and rubbery states of the polymer. Figure 6.4 displays each of the T_g variants for each material obtained from dynamic temperature sweeps.

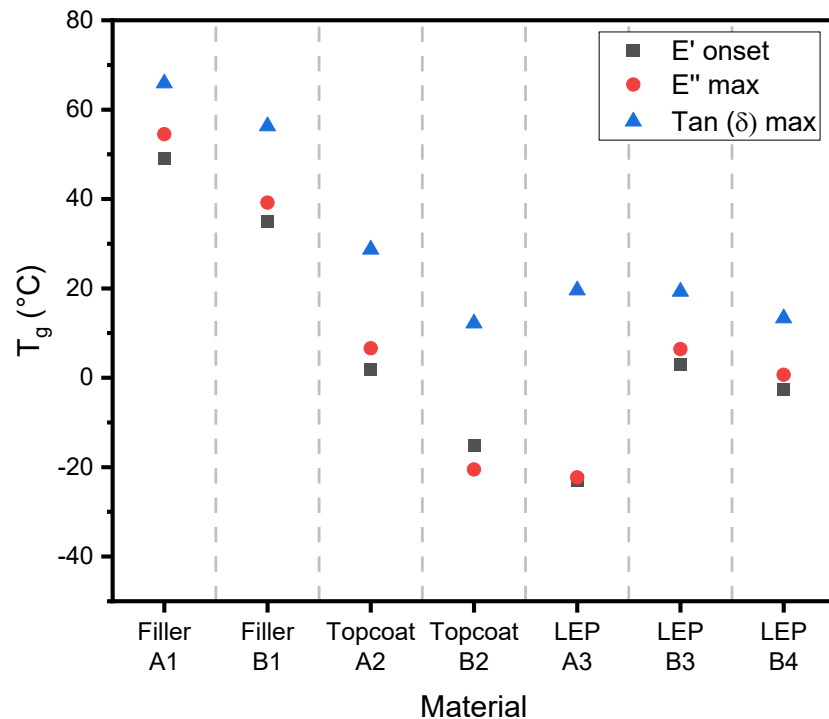


Figure 6.4 – A comparison of T_g values obtained from dual cantilever temperature sweeps (-50 °C to 80 °C) at a constant frequency (1 Hz) and amplitude (within the LVER).

For the filler materials, relatively small changes were observed in material behaviour before reaching the E' onset, where both materials were observed to undergo deterioration in mechanical performance. This change occurred at ≈ 35 °C for filler B1 and 50 °C for filler A1. After these points, both the E' and E'' rapidly decrease, resulting in a rapid increase in $\tan(\delta)$. A slight difference was observed in $\tan(\delta)$ peaks, with filler A1 being 0.7 and filler B1 being 0.6, indicating that the filler A1 material had greater material damping within the measured temperature range.

The topcoat materials displayed similar responses to one another; however, the topcoat B2 material displayed considerably lower T_g values in all methods. Unexpectedly the E'' max was observed to be lower than the E' onset which is uncommon in measurements of this kind and could be attributed to the variations in E'' plateau below the E'' max. Similar $\tan(\delta)$ peak values of ≈ 0.4 were observed for both materials, indicating similar material damping.

For the LEP materials, LEP B3 and LEP B4 showed similar responses, with the former being approximately ≈ 5 °C higher in all T_g measurements. As the difference between these materials is a variation in the blend of isocyanates used (detailed in Section 3.1), this suggests that it influences the

temperature at which the material behaviour changes from glassy to rubbery. While the temperature of the $\tan(\delta)$ peaks was similar, the peak values differed with ≈ 0.8 for LEP B4 and ≈ 0.7 for LEP B3.

The LEP A3 material $\tan(\delta)$ peak was observed at ≈ 20 °C, similar to the LEP B3 and LEP B4 materials. However, the $\tan(\delta)$ peak value was ≈ 0.5 , the lowest of all the LEP materials. The LEP A3 material also was observed to have considerably lower E' onset and E''_{\max} T_g values. This indicates that the material loses mechanical performance from ≈ -30 °C and implies that segmental motion begins at considerably lower temperatures than the LEP B3 and LEP B4 materials.

6.2.3 Study of Frequency Dependence

In Chapters 4 and 5, strain-rate dependence was observed during QS testing programs, which is common in viscoelastic materials. At higher strain rates, which are possible by varying the frequency of oscillation parameter in DMTA, more considerable changes can be observed, such as the transition from rubbery to brittle. While DMTA allows the use of considerably higher frequencies (up to 200 Hz using the Q800 instrument), it still does not capture the different behaviours that occur at the higher frequencies. Instead, time-temperature superposition (TTS) was used to overcome these limitations and characterise coating materials over a wide range of frequencies and temperatures.

TTS is a method of studying the viscoelastic behaviour of linear viscoelastic materials. This process allows for characterisation over a broader range of temperatures and frequencies than obtainable directly from experimental results. The TTS principle states a mutual correspondence between the frequency and temperature effects. As a result, the change in mechanical properties induced by a temperature variation can be identical to that produced by a frequency variation [183, 184]. This relationship is based on the theory that these parameters depend on molecular relaxations and rearrangements that occur at differing temperatures.

Temperature-dependent viscoelastic materials for which this combination of curves is possible are called thermorheologically simple materials [134, 185]. This classification means all the material's time-dependent retardation/relaxation mechanisms have the same temperature dependence. Most amorphous polymers fulfil these criteria; however, crystalline polymers and most composite materials do not, as each phase can possess different temperature dependencies and relaxation mechanisms. Furthermore, if any phase transitions (e.g. freezing or melting) occur during the area of interest, the material is not considered thermorheologically simple.

An example where this is suitable is DMTA measurements of dynamic properties such as E' . However, this test has a significant limitation: the measured frequency range is relatively narrow due to the limitation of the instrument being used, limiting the ranges that can be investigated. Current

instruments can only provide data within a few decades of frequency or time. As a result, the instrument cannot characterise viscoelastic behaviour outside the limited frequency range and cannot capture the high-frequency plateau and the low-frequency terminal zones.

As a result of the TTS principle, the frequency response obtained is similar to measurements conducted at neighbouring temperatures, as demonstrated in Figure 6.5. These can be plotted onto dynamic moduli vs frequency graph and shifted along the frequency axis to overlap with curves at neighbouring temperatures [183, 184]. This process of shifting the data across the log frequency axis is called the Frequency-Temperature Shift Factor α_T and is defined by

$$\alpha_T = \frac{f_0}{f_T} \quad 6.1$$

where f_0 is the frequency at which the material displays the same response as the reference temperature T and f_T is the frequency at which the material reaches a particular response at temperature T . These shift factors are determined from the experimental data by shifting the curves obtained at different temperatures along the frequency axis. These data should result in either partial or complete overlap dependent on the temperature intervals tested and create a curve that displays the predicted behaviour of the polymer called a master curve.

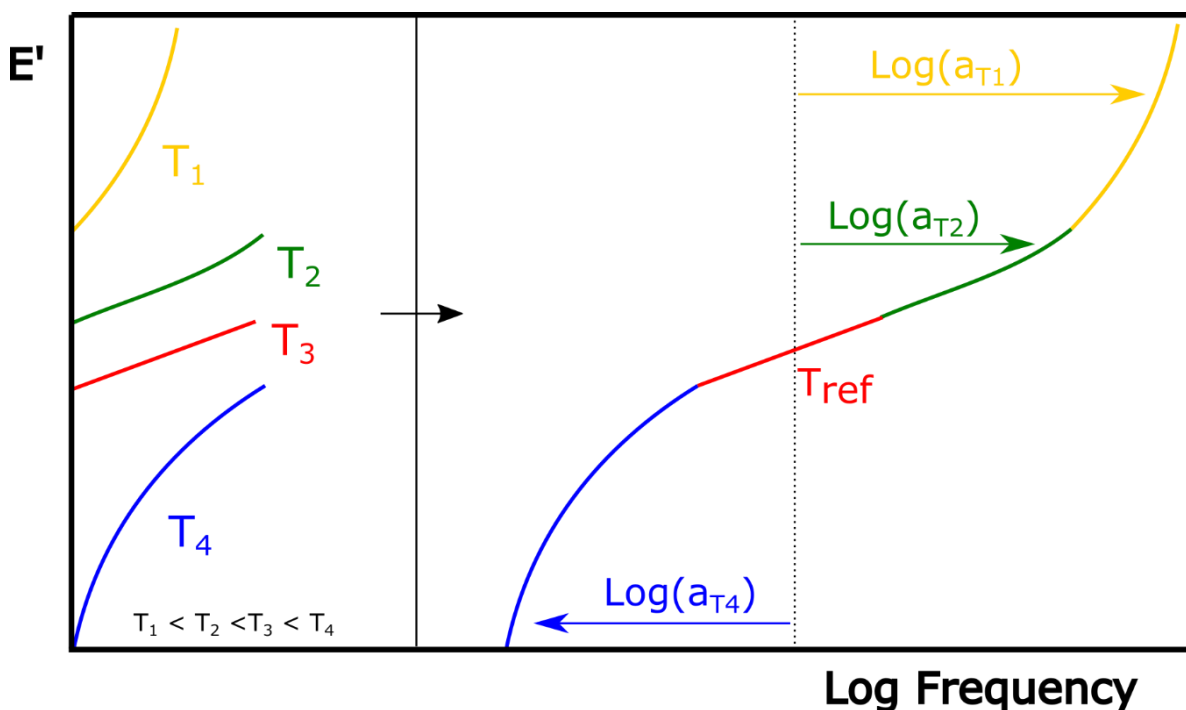


Figure 6.5 – A schematic detailing the construction of the storage modulus (E') master curve using the time-temperature superposition principle. The left part of the graph shows frequency sweep data at varying temperatures. The right shows each sweep combined around a selected reference temperature (T_{ref}). The magnitude of the shift is represented by the various shift factors (a_{Tx}). Figure adapted from the literature [186].

Temperatures above the reference temperature shift to lower frequencies, while temperatures below shift to higher frequencies. The value of the shift distance is dependent on the reference temperature selected and the material properties of the polymer being tested [183, 184]. Many formulas aim to link these shift factors to the reference temperature; however, the most common is the Williams-Landel-Ferry (WLF) equation which is calculated by

$$\log_{10} \alpha_T = \frac{-C_1 x (T - T_0)}{C_2 + (T - T_0)} \quad 6.2$$

where C_1 and C_2 are constants obtained from the fitting and, once found, should be independent of the choice of reference temperature. For amorphous polymers, the WLF equation applies to a temperature range varying from T_g to about $T_g + 100$ °C [187]. When these values are known, the constructed master curve can be shifted to any temperature within the experimental range [188]. Universal constants have been reported for rubbery amorphous polymers that convert the equation to

$$\log_{10} \alpha_T = \frac{-17.44 x (T - T_0)}{51.6 + (T - T_0)} \quad 6.3$$

Alternatively, the Arrhenius equation is used for materials below the T_g and calculated by

$$\ln \alpha_T = \frac{E_A}{R} \left(\frac{1}{T} - \frac{1}{T_0} \right) \quad 6.4$$

where E_A is the viscoelastic activation energy of the polymer being tested, and R is the universal gas constant.

For the master curves, the predicted frequency ranges vary due to the number of temperature sweeps used to create the master curve. In each case, frequency sweeps between 1 Hz and 100 Hz were conducted in 10 °C increments from -40 °C to 50 °C. Anomalous sweeps were identified from a plot of T vs $\log \alpha_T$ (discussed later in this section). These sweeps were poor quality data that resulted in considerable scatter due to being unable to maintain a sinusoidal waveform response. As a result, those sweeps identified were omitted from further testing.

In each of the master curves, the data was observed to show periodic variations attributed to the variation of data in each frequency sweep. At frequencies above 80 Hz, these results deviated from the rest of the data obtained at lower frequencies. This could have been due to several reasons such as poor material response that was not suitable for the instrument or resonance caused by the dimensions of the sample. The decision was made to keep the high-frequency data in the curve as overlaps with other data could be used to verify any trends but in any future testing lower frequencies

and a greater number of temperature would be used to improve the quality of data produced for the use in generating a master curve for the high strain rates applicable to rain droplet impacts.

6.2.3.1 Testing

The master curves of filler materials are compared in Figure 6.6. The E' of both materials increased, reaching a plateau at higher frequencies. At the lowest comparable frequency, filler A1 was found to have $\approx 160\%$ higher E' than the filler B1 material. This E' value increased and plateaued at ≈ 10 Hz, indicating an insensitivity to the applied frequency. Conversely, the filler B1 E'' increased as a function of frequency until 10^7 Hz, where it reached a similar value to filler A1. The E'' of the filler A1 material was observed to decrease upon increasing frequency until $\approx 10^7$, where E'' underwent a minimal increase. For filler B1, the E'' was observed to increase until 10 Hz and was followed by a decrease in E'' at higher frequencies. The $\tan(\delta)$ curve, which combines the influence E' and E'' , show similar max peak heights of 0.4, at 10^{-3} for filler A1 and 10^{-1} Hz for filler B1. Both of these peaks decrease to ≈ 0.2 at the highest frequency.

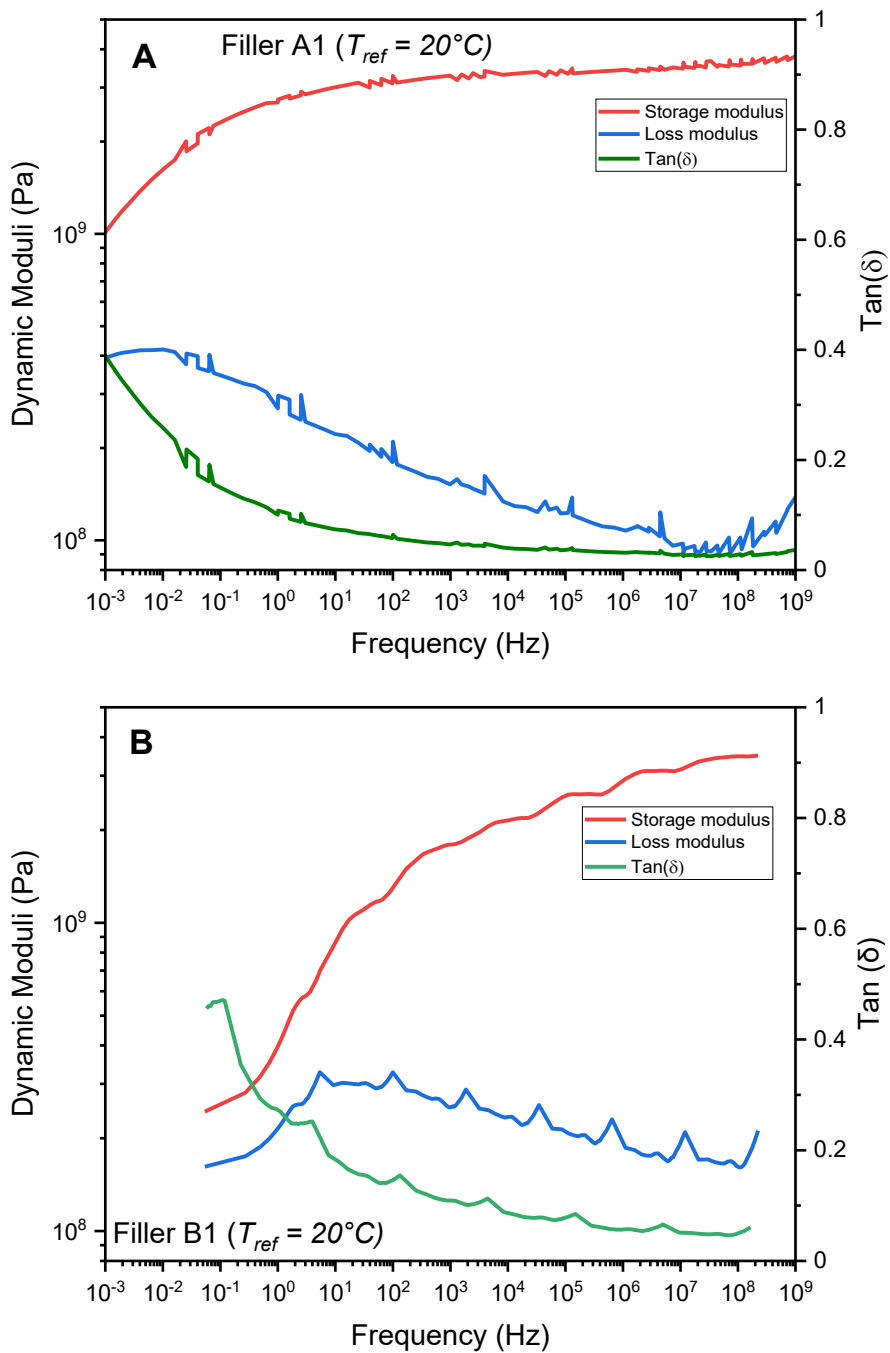


Figure 6.6 – Comparison of filler master curves generated from dual cantilever frequency sweeps. Filler A1 (A) was between -40 °C to 40 °C and 0.01% strain, and Filler B1 (B) was between -40 °C to 30 °C and 0.1% strain. Periodic variations are visible in the master curve due to the variability in the combination of multiple sweeps.

The master curves of the topcoat materials are compared in Figure 6.7. The E' of both materials were observed to be of similar magnitude and follow the increasing trend as a function of frequency. Both of the E' curves appear to begin to plateau at $\approx 10^7$ Hz at a similar magnitude. The E'' appears to follow a similar trend for both topcoat A2 and topcoat B2, where the E'' increases until 10^3 Hz before decreasing. The $\tan(\delta)$ curves of the two materials are similar in magnitude at 10^{-1} Hz. As the frequency increases, both materials' $\tan(\delta)$ increases before decreasing, appearing to begin to

plateau at a value of ≈ 0.03 at 10^6 Hz for topcoat B2 and 10^9 Hz for topcoat A2. The topcoat A2 $\tan(\delta)$ peak of ≈ 0.55 is found in the order of 10^{-1} , whereas for the topcoat B2 material, the peak value of ≈ 0.65 is found to be between 10^1 Hz and 10^2 Hz.

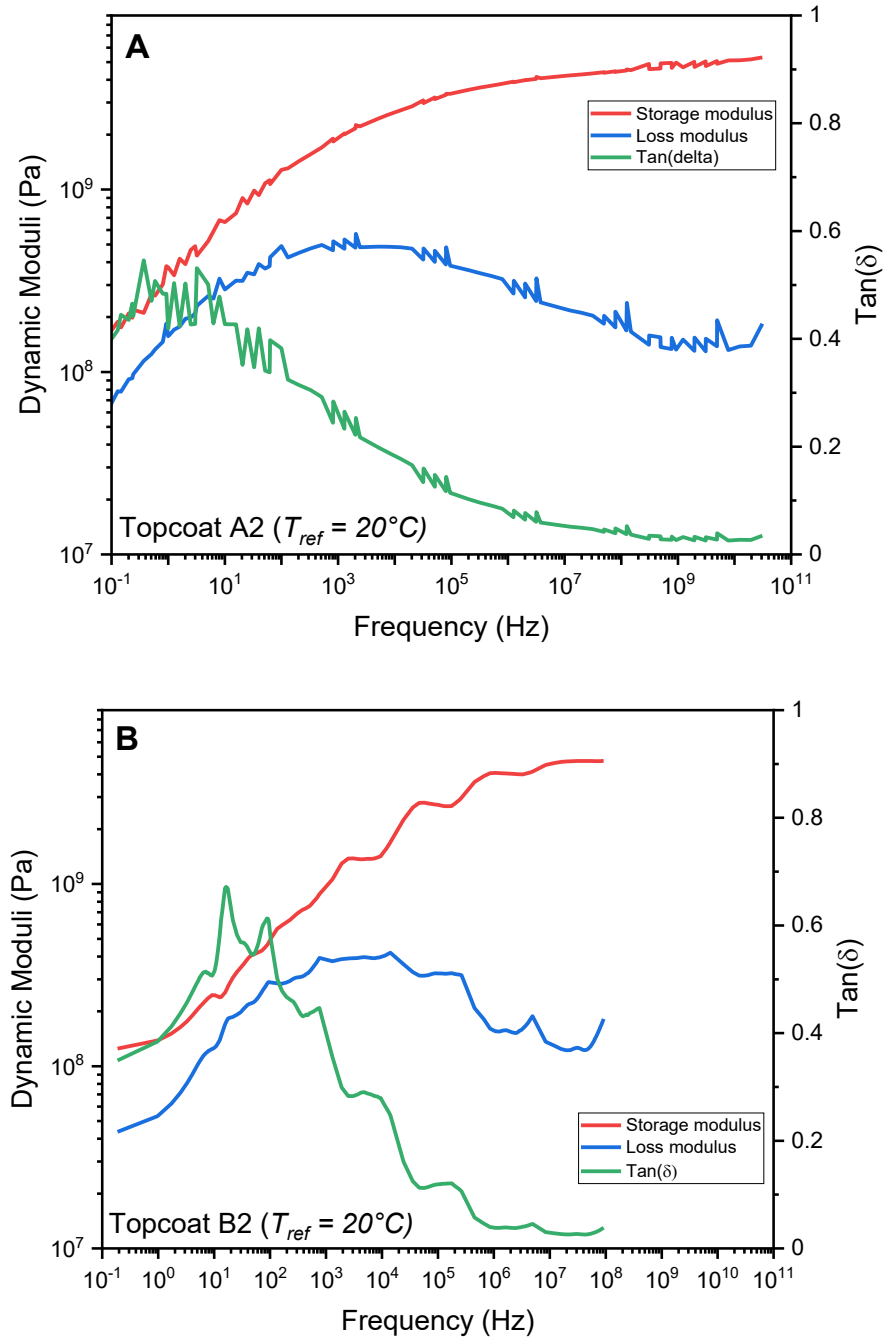


Figure 6.7 – Comparison of topcoat master curves generated from dual cantilever frequency sweeps. Topcoat A2 (A) was between -40°C to 30°C and 0.01% strain, and topcoat B2 (B) was between -30°C to 30°C and 0.1% strain. Periodic variations are visible in the master curve due to the variability in the combination of multiple sweeps.

The master curves of the LEP materials are compared in Figure 6.8. The E' of all materials was observed to increase as a function of frequency; these appeared to plateau at $\approx 10^7$ Hz for LEP B3 and LEP B4. The LEP A3 E' gradient continually increases, but no clear plateau is observed within the

frequency range. The magnitudes of the E' are observed to be in the order of LEP A3 >> LEP B3 > LEP B4, with the LEP A3 material being over 125 % greater than the LEP B3 and B4 materials at the 10 Hz and 175 % at 10^8 Hz. As with the topcoat E'' responses, the LEP E'' were observed to increase at lower frequencies and decrease at higher frequencies. For the LEP A3 material, a slight plateau was observed between 10^3 and 10^4 Hz, from which point the begins to E'' decrease. The LEP B3 and LEP B4 materials also follow this trend, but there was no clear sign of a plateau region, instead decreasing at 10^5 Hz. The magnitude of these responses was in the order of LEP A3 > LEP B3 > LEP B4. The $\tan(\delta)$ curves for the LEP A3 material were observed to decrease from a maximum of ≈ 0.7 at higher frequencies. The LEP B3 and LEP B4 peak values were 1.6 and 1.8, respectively. However, these peak values were observed at 10^2 Hz, where $\tan(\delta)$ response spiked upwards. While all $\tan(\delta)$ responses decreased, it can be observed that LEP B3 and LEP B4 had the highest $\tan(\delta)$ at frequencies below $\approx 10^5$ Hz, whereas LEP A3 had the highest $\tan(\delta)$ above this frequency.

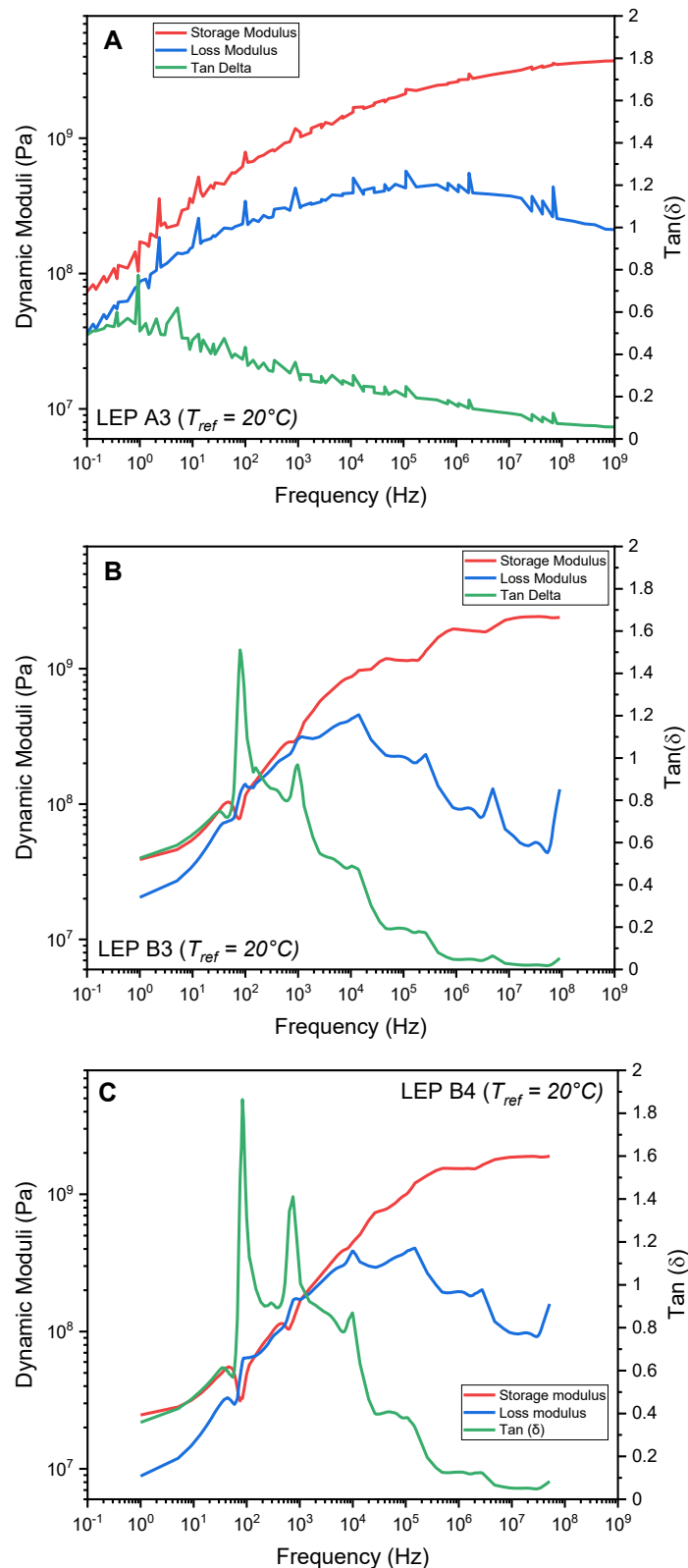


Figure 6.8 – Comparison of LEP master curves generated from dual cantilever frequency sweeps. LEP A3 (A) was at -40 °C to 30 °C and 0.01% strain, LEP B3 (B) is -30°C to 20 °C and 0.1% strain, and LEP B4 is -30°C to 20 °C and 0.1% strain. Periodic variations are visible in the master curve due to the variability in the combination of multiple sweeps.

6.2.3.2 Validation

Master curves are still only predictions of how each material can respond to deformation at frequencies above the maximum frequency of oscillation, which in this work was 100 Hz. As a result, it is essential to address the question of validity and ascertain if the resulting curves are representative of the material response at higher frequencies. This validity analysis needs to be conducted for each material being tested. While they are all based on PU/PUR chemistry, their chemical composition can vary greatly, resulting in various material properties. This discrepancy can be seen between the different material groups, as seen in the filler materials, which are considerably more brittle and possess higher T_g values when compared to topcoat and LEP materials. As a result, differences in composition and resulting properties can mean that the TTS assumption or the test parameters used may be unsuitable for acquiring a valid response; therefore, validation is needed.

Shift Factors

The first method for assessing the validity of results is by examining the shift factors (detailed in Figure 6.5). As previously mentioned, a plot of T vs $\log \alpha_T$ is used to form a curve where anomalous data points that did not follow the anticipated trend¹⁶ were omitted from analysis and used to identify working temperature ranges. The resulting curves are fitted with the WLF and the Arrhenius models, calculated by Equations 6.2 and 6.4.

The results from using the WLF model are presented in Table 6.2. Upon initial inspection, the R^2 values for all materials exceed 0.97, typically defined as an excellent correlation implying that the master curves are valid. However, upon assessment of the calculated material constants¹⁷, C_1 and C_2 suggest that certain materials may not be suitable. These values are commonly compared in two ways; by directly comparing the experimentally derived values to the universal constants ($C_1 = 17.44$ and $C_2 = 51.6$ K) or by comparing the product of the universal constants (≈ 900) to that of the experimental data [187–190]. However, certain literature states that these parameters can vary significantly between polymer types and temperatures [187, 189]. Upon examining the constants, it can be observed that the products of the fillers were in the order of 10^{32} , which is orders of magnitude over expected values. The topcoat A2 material 10^6 is also over the expected values. The remaining materials were all in the order of 10^3 , closer to the expected value, but still varied by a magnitude. The higher values can be attributed to the fact that the model is only deemed suitable above the T_g of the materials, and due to the interest in higher frequencies, lower temperatures were employed meaning that the assumption behind this model are no longer applicable.

¹⁶ Potentially due to the change in LVER at the temperature extremes used in the work.

¹⁷ A useful site to explore the effect of C_1 and C_2 constants <https://3dnex.com/tmap/dma/wlf.html>.

For temperatures below the T_g the Arrhenius model, detailed in Equation 6.4, describes the relationship between the shift factors and temperatures. Upon examining the R^2 values, it can be observed that all materials show an excellent correlation > 0.95 . Implying that the model fits the dataset and the master curve is valid. A further parameter that can be calculated from the Arrhenius equation is E_A , which is related to the activation energy of the T_g [191]. Upon evaluation, it can be observed that all values are positive and of the same magnitude as other polymeric materials [191–193]. These values can be compared to the T_g values obtained from individual temperature sweeps displayed in Figure 6.4. Topcoat B2, LEP A3, LEP B3 and LEP B4 were observed to have similar T_g ($\tan(\delta)$) values of ≈ 20 °C which also observed in the corresponding E_A in the range of ≈ 156 kJ/mol to 166 kJ/mol. Topcoat A2 was observed to have a T_g ($\tan(\delta)$) values of ≈ 25 °C which was found to be ≈ 203 kJ/mol. The filler materials that had the highest T_g ($\tan(\delta)$) values of ≈ 60 °C were observed to be an average of 185 kJ/mol. These values imply that the topcoat A2 result could be inaccurate as the other material responses appear to follow a similar trend to the measured T_g values.

Table 6.2 – Summary of the shift factors analysis using the Williams-Landel-Ferry and Arrhenius equations for dual cantilever testing.

Material	WLF			Arrhenius	
	C_1	C_2 (K)	R^2	E_a (kJ/mol)	R^2
Filler A1	8.80E+15	6.39E+16	0.9792	189.7	0.9523
Topcoat A2	8.89E+02	6.07E+03	0.9953	202.9	0.9891
LEP A3	1.82E+01	2.08E+02	0.9996	157.7	0.9980
Filler B1	6.86E+15	5.44E+16	0.9994	179.3	0.9940
Topcoat B2	2.08E+01	1.28E+02	0.9981	166.0	0.9975
LEP B3	2.29E+01	2.43E+02	0.9997	160.5	0.9995
LEP B4	2.78E+01	2.92E+02	0.9998	156.5	0.9998

Cole-Cole Plot

Cole-Cole plots, obtained from plotting E''/E' can also be used to validate master curves. This method is commonly used to verify the thermo-rheological simplicity of materials [134, 192, 194–196]. It is expected that a suitable material for TTS results in a parabolic distribution of results, with experimental points following a single line.

This parabolic shape is expected to occur at low frequencies, both E' and E'' and is relatively small. Upon increasing the frequency E' increases, but E'' increases to a greater extent reaching the peak of the parabola. At the higher frequencies, the response becomes predominately elastic, meaning that E' increases further while E'' decreases. While it is uncommon, the author has fitted quadratic equations to each curve to guide the reader and attempt to provide a mathematical way of

quantifying the shape. The Cole-Cole plots of the filler and topcoat of materials are displayed in Figure 6.9.

For the filler A1 material (Figure 6.9A), the initial evaluation shows that the fitting of a quadratic curve is excellent, with an R^2 of 0.94. While there are signs of the parabolic shape between E' values of 1000 MPa and 3000 MPa, there is a lack of data points below E' values of 1000 MPa, but this can be attributed to the test range not reaching high enough temperatures to acquire these points. At the high E' values, each sweep begins to show a ‘tail’ that deviates from the downward trend. At ≈ 3600 MPa, there is a large concentration of results implying that either E' is insensitive to change at the higher temperatures/frequencies or the assumptions of TTS begin to no longer apply.

For the filler B1 material (Figure 6.9B), an acceptable fit of the data is observed with an R^2 of 0.79. While it is possible to interpret a parabolic shape, the lack of data points at lower E' values makes this challenging to identify. Instead, the trend more closely follows a linear relationship. Interestingly, the points that group together represents frequency sweeps at various temperatures and are distributed vertically. This distribution indicates that the E' response does not vary within the frequency sweep but does change when the set temperature of the frequency sweep is increased. This observation could result in erroneous results in the master curve.

For the topcoat A2 material (Figure 6.9C), a clear parabolic shape was observed with an R^2 value of 0.83. As the value increases, periodic deviation from the curve can be seen due to the highest frequency response differing from the curve. Nevertheless, this plot implies that the data is suitable for a master curve.

For the topcoat B2 material (Figure 6.9D), a low R^2 value of 0.69 is calculated. While this is low, visual examination shows a parabolic shape that is poorly fitted due to the weighting of the results around the lower E' values. At the higher E' values, a similar phenomenon to the filler B1 material is observed where each frequency sweep appears vertical, indicating no change in E' as a result of the increase in frequency. This plot implies that the data is more suitable at lower E' values.

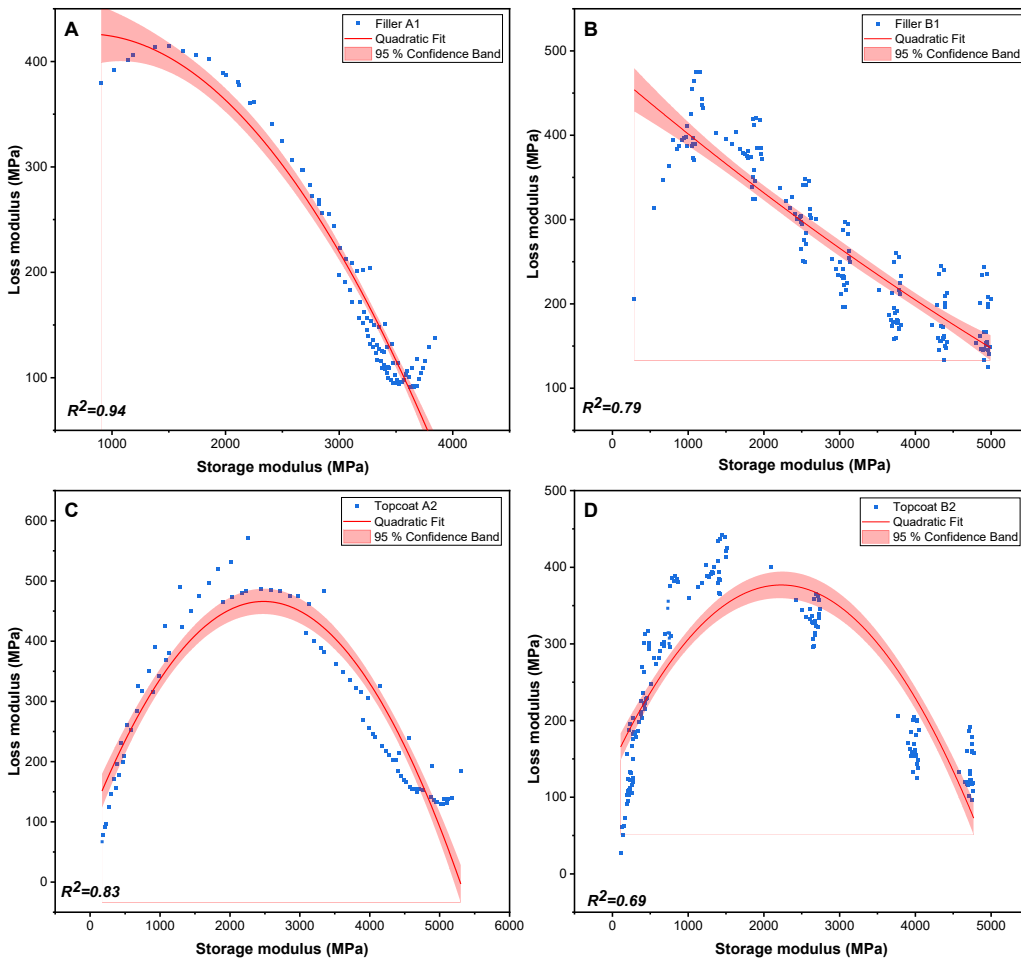


Figure 6.9 – Cole-Cole plots for validation of filler and topcoat material master curves. A: filler A1, B: filler B1, C: topcoat A2, and D: topcoat B2.

The Cole-Cole plots of the LEP of materials are displayed in Figure 6.10.

For the LEP A3 material (Figure 6.10A), a good correlation was observed with an R^2 value of 0.93. Upon visual examination, a clear parabolic shape can be observed with a greater concentration of points at the lower E' values. A periodic deviation from the curve can be observed and corresponds to a frequency value that could be a result of resonance.

For the LEP B3 material (Figure 6.10B), a poor correlation is observed with an R^2 of 0.69. Upon visual inspection, a parabolic shape could be drawn from the data. However, the responses at the lower E' points form a clear linear increase, but at higher E' values, this response does not appear to decrease smoothly. This observation could be linked to the blends of isocyanates used, resulting in two distinct responses. There is a distinct lack of points between E' values of 1000 MPa and 2200 MPa, indicating a considerable change of results between 10 °C temperature interval potentially due to overlapping with the 20 °C T_g for the material. As with the topcoat B2 and filler B1 materials, at higher E' values, the data appears to group vertically, suggesting that no change in E' is observed due to the

increase in frequency. This data implies that caution should be taken when using data from the higher frequency results.

For the LEP B4 material (Figure 6.10C), a good correlation is observed with an R^2 value of 0.82. Upon visual inspection, two distinct lines can be observed and again could be correlated to the blend of isocyanates used within the materials. As with other materials at higher E' values, a vertical grouping of the sweeps is observed. As with the LEP B3 material, caution should be taken when interpreting the results.

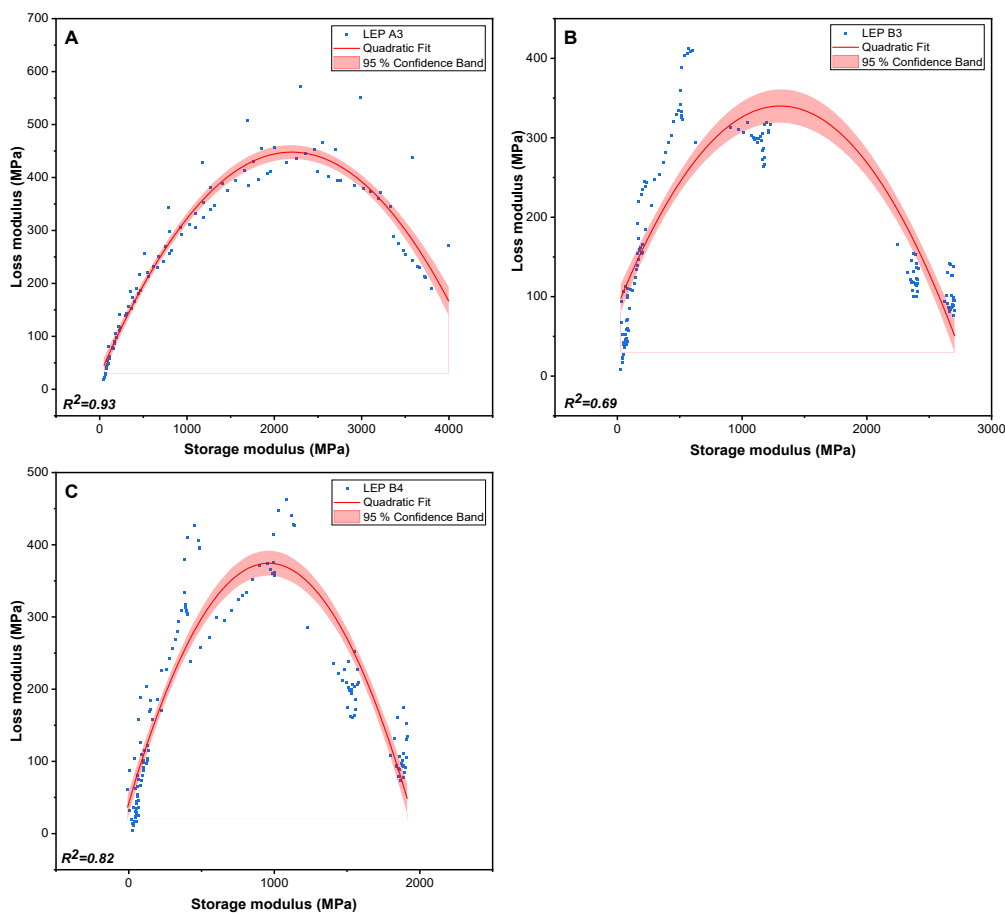


Figure 6.10 – Cole-Cole plots for validation of LEP material master curves. A: LEP A3, B: LEP B3 and C: LEP B4.

In summary, the evaluation of the shift factors identified the topcoat A2 material does not follow the expected trend in E_a . Both filler materials had distorted shapes from the Cole-Cole plots at the higher E' values. The topcoat B2, LEP B3, and LEP B4 materials resulted in parabolic curves, but all lacked overlapping data in areas and deviated from the singular curve at points in the curve, implying these are not simple materials.

6.3 Thin-Film Testing

This section details the characterisation of each coating material utilising the TF test fixture, a less commonly used fixture that measures tensile properties.

6.3.1 Determination of Linear Viscoelastic Region

As a new sample geometry and test fixture are used in this section, the ε_c and LVER values must be calculated again using the same method as in Section 6.2.1. No results for the filler A1 material are displayed in this subsection because the material was found to be unsuitable for the thin film test method. This issue was attributed to its higher tensile modulus (in Chapter 4), exceeding the instrument's force limit. While it could be possible to alter sample width and thickness, the same specimen geometry was used for all materials for consistency.

The calculated ε_c values are displayed in Figure 6.11. Higher values were observed in TF tests than in the DC tests (Figure 6.2). These differences were expected as the tests were conducted at 16 °C. The ε_c values calculated using the E' decrease were considerably higher than those obtained using other methods. This difference was as a result of minimal changes being observed in the E' values upon increasing oscillatory strain, which implies more elastic behaviour than the DC materials.

As with the DC method, an LVER limit was also chosen to be 0.1 % strain.

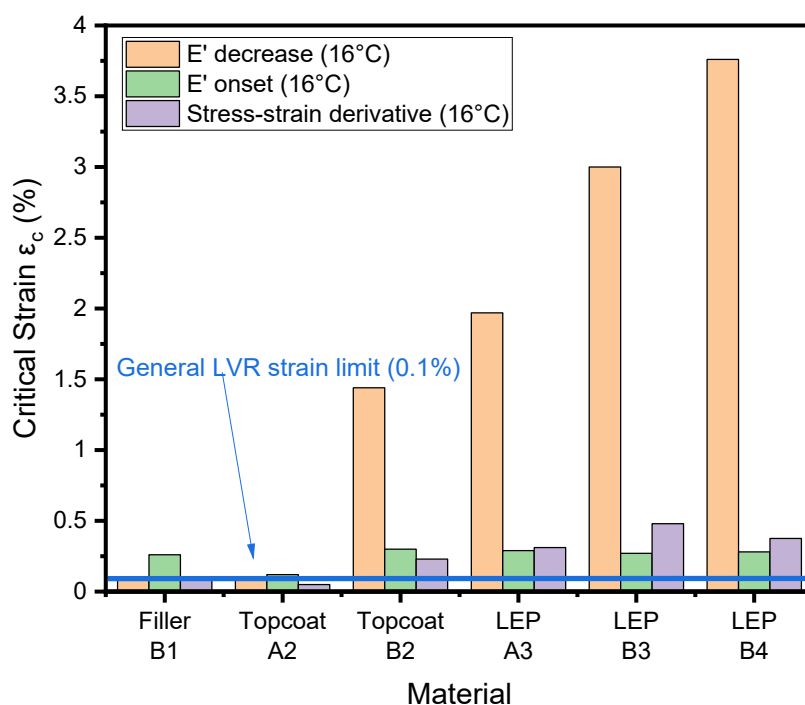


Figure 6.11 – Results from a thin film tension dynamic strain sweep where the response of a material to increasing deformation (up to 400 µm) is recorded at a constant frequency (1 Hz) and temperature (16 °C). The blue line indicates the general linear viscoelastic region strain limit used in the subsequent testing.

As previously in Figure 6.3, the σ_c values were calculated from the ε_c values presented in Figure 6.12. Average σ_c values were found to be in the order of filler B1 > topcoat A2 > topcoat B2 >> LEP B3 > LEP B4 > LEP A3. When compared to the DC tests, all the average σ_c values apart from the topcoat B2 material were found to be lower; implying that plastic deformation can occur at considerably lower stresses in tension than when compared to bending. The unexpectedly high ε_c values from the E' decrease method resulted in σ_c values similar to those obtained via the derivative method indicating they may not have been anomalous results.

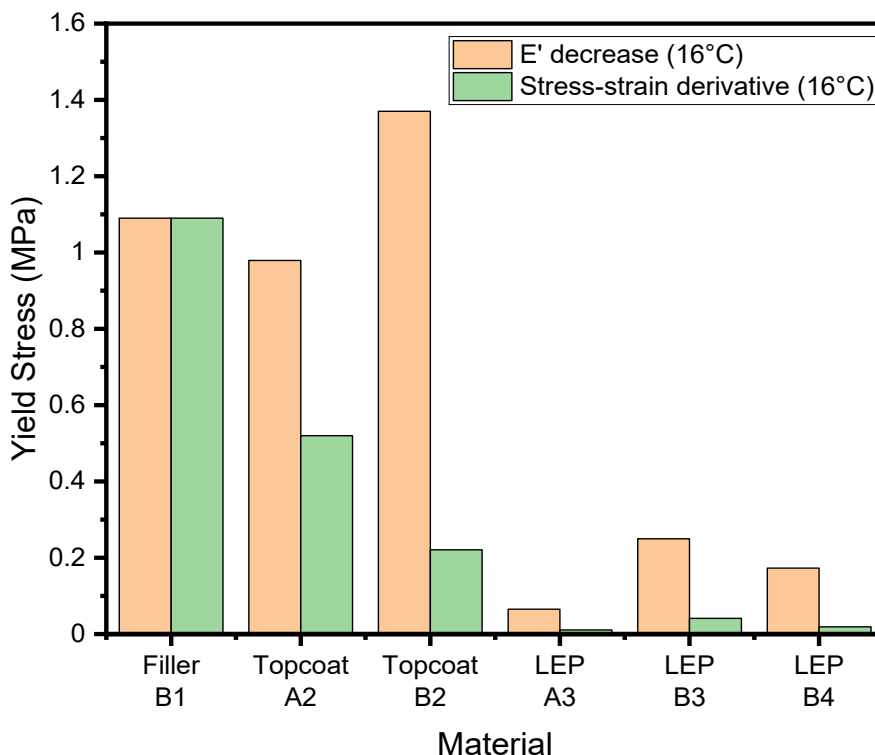


Figure 6.12 – Comparison of measured yield stresses obtained from a thin film tension dynamic strain sweep where the response of a material to increasing deformation (up to 400 μm) is recorded at a constant frequency (1 Hz) and temperature (16 °C).

6.3.2 Study of Temperature Dependence

As in Figure 6.4, the T_g values for each material were measured and reported in Figure 6.13. The trends observed in T_g values matched that seen in DC testing apart from the tan (δ) max for the topcoat B2 material, which was unexpectedly high. Generally, the TF fixture values were ≈ 15 °C lower than those using the DC fixture, with topcoat B2 being the only material to have an increase (5 °C) in T_g . It was expected that T_g values would be the same between test fixtures as the same materials and instruments were used. However, the observed difference could be attributed to the use of a bespoke heat shield in DC testing that is not used in TF testing. The shield aims to minimise the variation in temperatures to provide consistent results. In the case of this work, it may have caused temperature

change to lag due to the additional heat transfer process that the shield introduces. This additional step and the rapid temperature increase may have resulted in a higher measured T_g values in the DC tests. This issue could be overcome in future tests by using slower temperature ramp rates to allow the system to equilibrate.

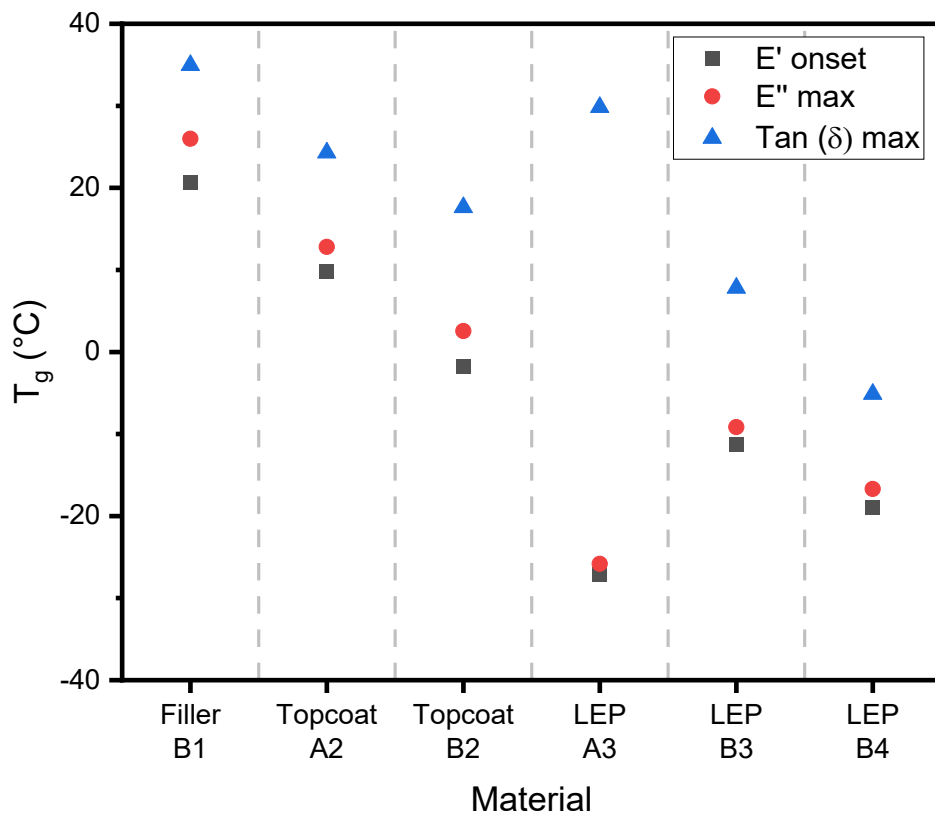


Figure 6.13 – A comparison of T_g values obtained from thin-film tensile temperature sweeps ($-40\text{ }^{\circ}\text{C}$ to $80\text{ }^{\circ}\text{C}$) at a constant frequency (1 Hz) and amplitude (0.1 %).

6.3.3 Study of Frequency Dependence

The master curve of the filler B1 is presented in Figure 6.14. The E' was observed to increase as a function of frequency, reaching a plateau at $\approx 10^6$ Hz. The E'' is observed to increase, reaching the maximum at ≈ 10 Hz before decreasing at higher frequencies. The resulting $\tan(\delta)$ curve maximum was observed at $\approx 10^{-1}$ Hz, similar to the DC test. However, the TF peak value was 0.8, considerably higher than the ≈ 0.4 maximum observed in DC testing. This observation implies that the damping behaviour is more considerable in tension than bending.

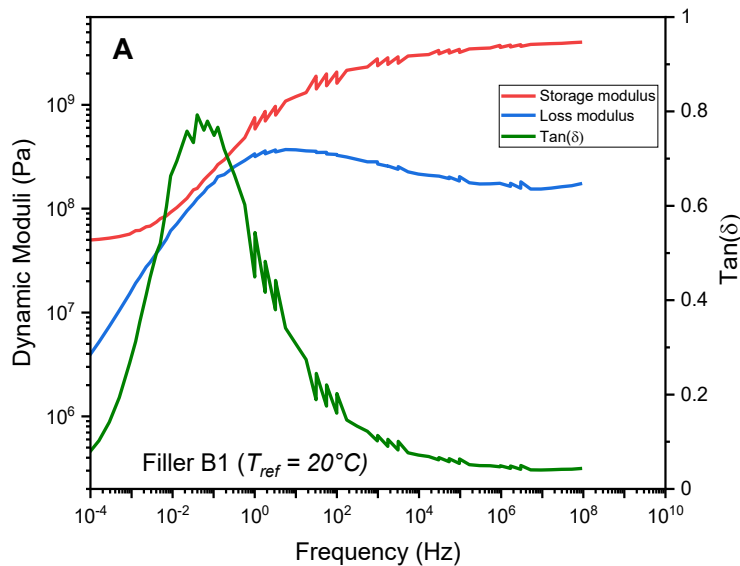


Figure 6.14 – Filler B1 master curve generated from thin-film tensile frequency sweeps at 0.1% strain and between -20 °C to 50 °C. Periodic variations are visible in the master curve due to the variability in the combination of multiple sweeps.

The master curve of the topcoat materials is presented in Figure 6.15. As with the DC results, the TF E' values of the topcoat B2 material were considerably smaller at lower frequencies. Variability in the topcoat A2 response at ≈ 1 Hz is seen, with two data points appearing not to follow the trend. These increase as a function of both plateauing at similar values at $\approx 10^7$ Hz, similar to the DC results. The E'' values of the topcoat B2 material were observed to be higher at all frequencies compared to the topcoat A2 material. The $\tan(\delta)$ peak for the topcoat A2 material was observed to be ≈ 0.6 and ≈ 0.85 for the topcoat B2 material, both higher than those observed in DC testing, again demonstrating greater damping behaviour in tension than in DC testing. The TF $\tan(\delta)$ peaks were observed at different frequencies; ≈ 10 Hz for the topcoat A2 and $\approx 10^3$ Hz for the topcoat B2 material. This difference in peak maximums implies that different materials could exhibit unique responses under identical loading conditions and must be considered when identifying which material has the most desirable properties.

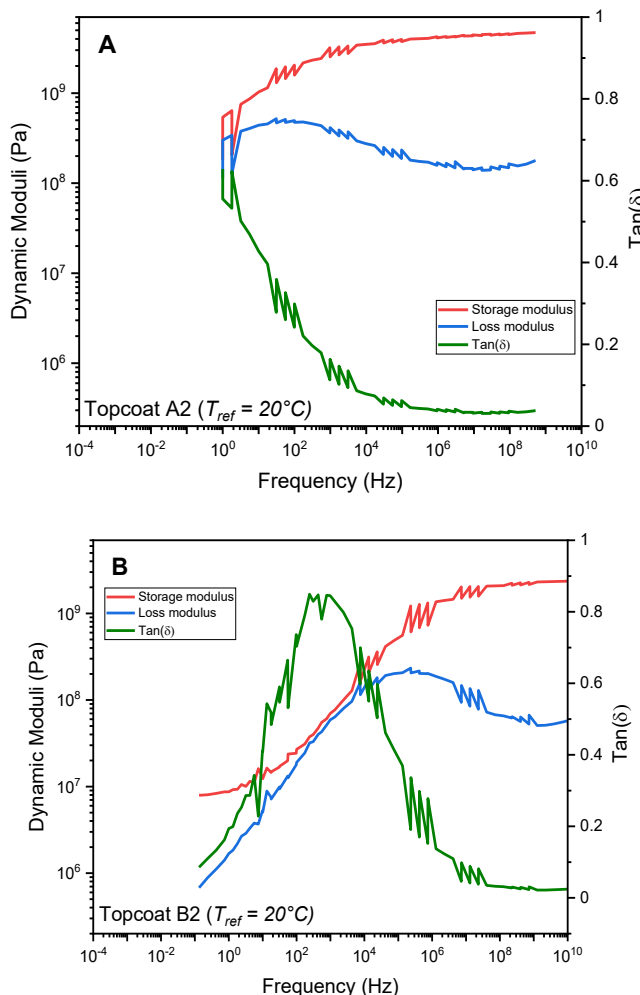


Figure 6.15 – Comparison of topcoat master curves generated from thin-film tensile frequency sweeps at 0.1% strain. Topcoat A2 (A) was between -30 °C to 30 °C, and topcoat B2 (B) was between -40°C to 30°C. Periodic variations are visible in the master curve due to the variability in the combination of multiple sweeps.

The master curve of the LEP materials is presented in Figure 6.16. The E' values of the LEP materials followed similar trends to those seen in DC testing of increasing as a function of frequency. The E'' of each material again followed similar trends of increasing as a function of the frequency. The LEP A3 material plateaus at $\approx 10^7$ Hz, with the LEP B3 and LEP B4 materials reaching a plateau at $\approx 10^5$ Hz. Above this frequency, no response for LEP A3 was captured due to the temperature range employed; however, the LEP B3 and LEP B4 material show a decrease in E'' at higher frequencies. The $\tan(\delta)$ curve of each material displays some noteworthy differences. The $\tan(\delta)$ maximum values were ≈ 0.70 for LEP A3, ≈ 0.83 for LEP B3 and ≈ 0.93 for LEP B4. These peak values were obtained by omitting sharp peaks for an average response. The frequency of these maxima was observed to be at 10^3 for both LEP A3 and LEP B3 and 10^4 for the LEP B4 material. On first observation, the LEP A3 is observed to have the worst damping properties of the LEP materials. However, upon further analysis, it can be seen that the LEP A3 material has a considerably higher $\tan(\delta)$ value at higher frequencies when compared to the other two LEP materials. This finding supports the observation that materials behave

differently at different frequencies and, as a result, may have the most desirable properties in specific frequency ranges.

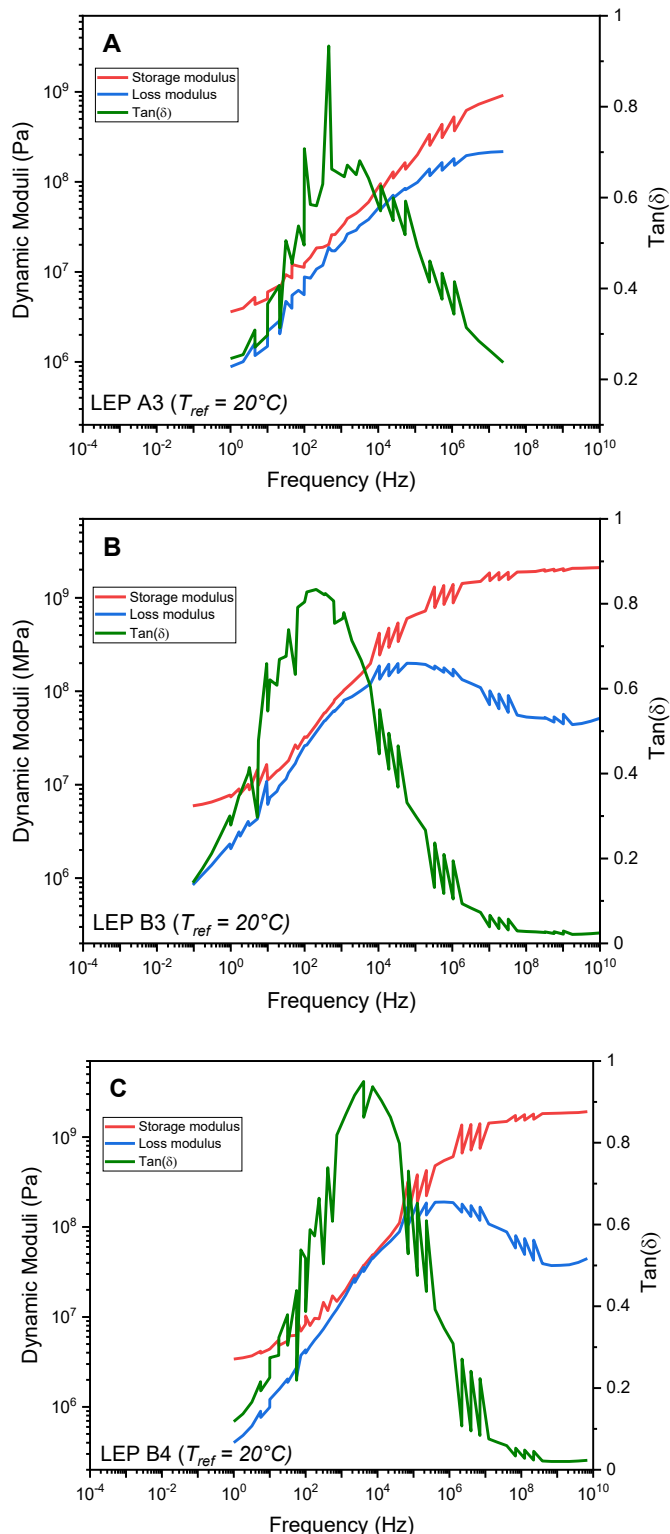


Figure 6.16 – Comparison of LEP master curves generated from thin-film tensile frequency sweeps at 0.1% strain. LEP A3 (A) was at -30 °C to 20 °C, LEP B3 (B) is -40°C to 30 °C and LEP B4 is -40°C to 20 °C. Periodic variations are visible in the master curve due to the variability in the combination of multiple sweeps.

6.3.3.1 Validation

This section repeats the validation methods that were previously discussed in depth in Section 6.3.3.1 on data generated for TF master curves.

Shift Factors

For the WLF fitting, shown in Table 6.3, excellent R^2 values of > 0.95 were observed, indicating an acceptable correlation between the temperatures and shift factors. Upon examining the constants, the resulting products for each material were considerably closer to the reference value of 900, such as LEP A3 and LEP B4. This finding can be attributed to the lower T_g values measured using the TF fixture. As a result, the criteria for the use of the WLF equation were likely to have been reached, making it a suitable equation in the cases of the identified materials.

For the Arrhenius fitting excellent R^2 values of > 0.95 were observed, indicating an acceptable correlation between the temperatures and shift factors. The trend in activation energies matched the trend in T_g values. As expected, filler B1 was the highest, LEP B3 was higher than LEP B4, matching the T_g values. LEP A3 did not match the trend and could be due to the high $\tan(\delta)$ T_g being incorrect as it was considerably different from the other values. Topcoat A2 was higher than topcoat B2, matching the T_g trend.

Table 6.3 – Summary of the shift factors analysis using the Williams-Landel-Ferry and Arrhenius equations for thin-film tensile testing.

Material	WLF			Arrhenius	
	C ₁	C ₂ (K)	R ²	E _a (kJ/mol)	R ²
Filler A1	-	-	-	-	-
Topcoat A2	5.55E+01	4.37E+02	0.95	198.36	0.95
LEP A3	9.67E+00	1.39E+02	1.00	142.30	0.99
Filler B1	1.17E+02	8.21E+02	1.00	224.36	1.00
Topcoat B2	3.49E+01	3.11E+02	1.00	184.74	1.00
LEP B3	4.82E+01	3.97E+02	1.00	190.02	1.00
LEP B4	1.94E+01	2.08E+02	1.00	170.38	0.99

Cole-Cole Plot

The Cole-Cole plots of the filler and topcoat of materials are displayed in Figure 6.17. For the filler B1 material (Figure 6.17A), the initial evaluation shows that the fitting of a quadratic curve is poor, with an R^2 of 0.71. A parabolic shape can be observed between the lowest E' values and ≈ 1700 MPa. Above this E' value grouping of data is observed, which corresponds to frequency sweeps at different temperatures. Each possesses a ‘tail’ where high-frequency measurement deviates from the expected

response. For the topcoat A2 material (Figure 6.17B), the initial evaluation shows that the fitting of a quadratic curve is good, with an R^2 of 0.83. A parabolic shape is visible up to ≈ 1900 MPa. Above this value, data points are the expected shape but do not overlap well with the curve. At the higher E' value, the sweeps start to overlap and begin to display the ‘tail’ that was described in the filler B1 material. For the topcoat B2 material (Figure 6.17C), the initial evaluation shows that the fitting of a quadratic curve is good, with an R^2 of 0.80. As with the other materials, a parabolic curve with good overlap is observed below ≈ 800 MPa. Above this value, large gaps in the curve are found with high-frequency responses again showing ‘tails’.

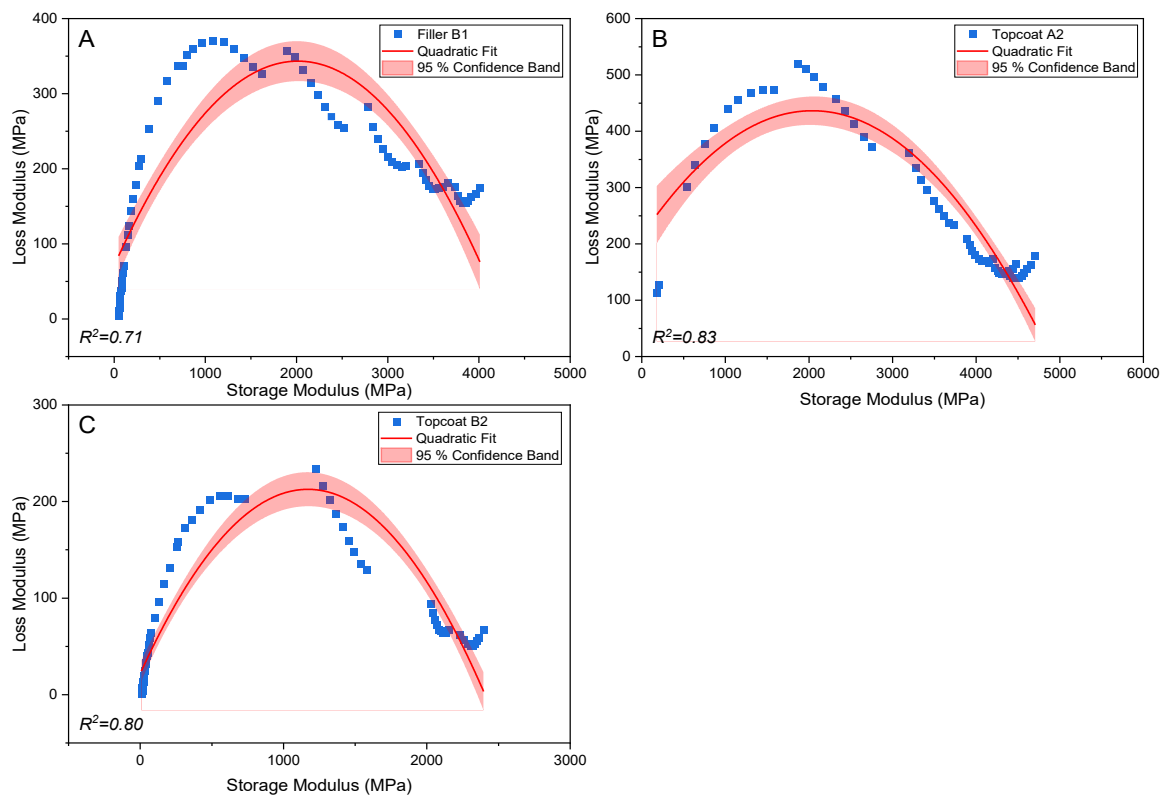


Figure 6.17 – Cole-Cole plots for validation of filler and topcoat material master curves. A: filler B1, B: topcoat A2, and C: topcoat B2.

The Cole-Cole plots of the LEP of materials are displayed in Figure 6.18. For the LEP A3 material (Figure 6.18A), the initial evaluation shows that the fitting of a quadratic curve is excellent, with an R^2 of 1.00. The measured data points are concentrated around the lower E' values. Only the peak of the parabolic curve is captured, and it can be assumed that with testing at lower temperatures, the other side of the parabola could be identified. For the LEP B3 (Figure 6.18B) and LEP B4 (Figure 6.18C), the initial evaluation shows that the fitting of quadratic curves is good, with R^2 values of 0.80 and 0.84, respectively. Similar responses were seen for both materials, with clear parabolas seen at low E' values. The higher concentration of points at the lowest E' and a lack of points above ≈ 900 MPa have detrimentally affected the quadratic fit. Above this E' value there is a lack of data points, and

unconnected curves would appear to fit if shifted differently. At the highest E' value, it can be observed that the two low sweeps do slightly overlap but include the unexpected tail shapes.

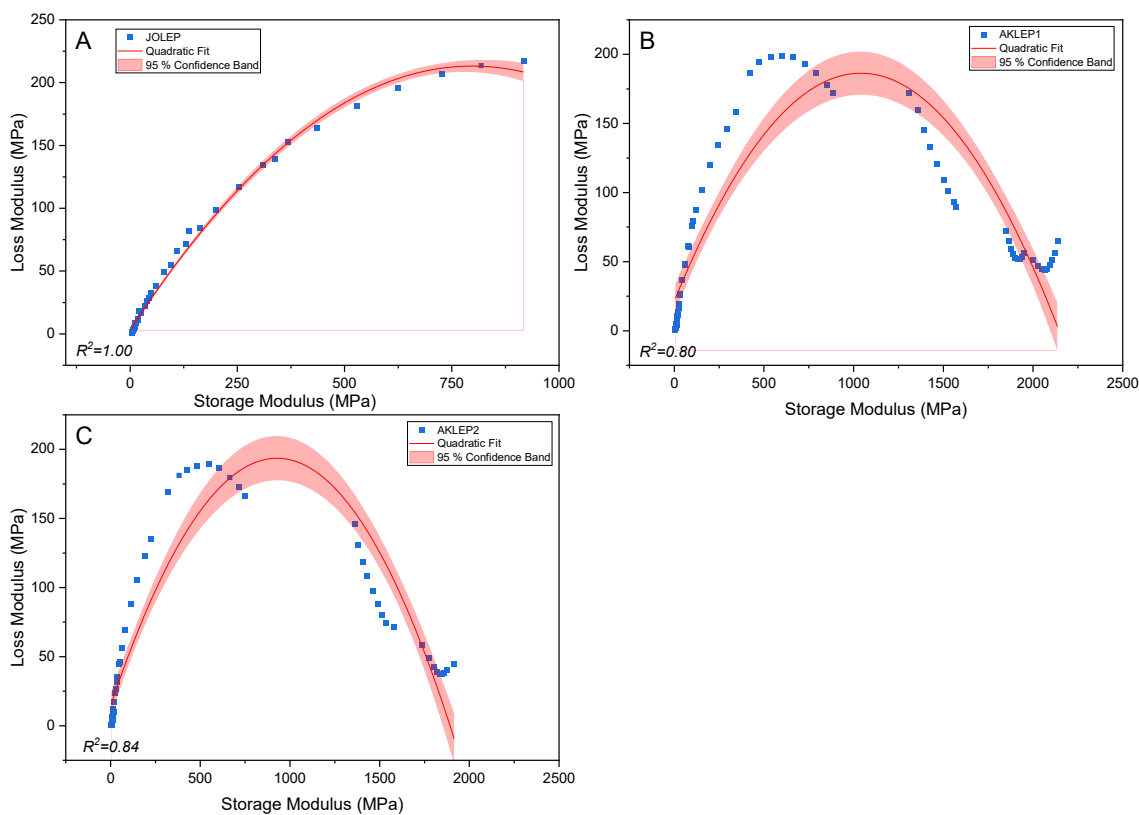


Figure 6.18 – Cole-Cole plots for validation of LEP material master curves. A: LEP A3, B: LEP B3 and C: LEP B4.

In summary, no material was observed to be entirely unsuitable for TTS use and resulted in acceptable shift factors and parabolic Cole-Cole plots. However, the LEP A3 material was identified as not following the expected relationship between T_g and E_a . The topcoat B2, LEP B3 and LEP B4 material were also observed to have a parabolic shape but had a poor overlap of data causing poor fitting at the intermediate E' values. This poor fitting of results is discussed further in Section 6.4.3.

6.4 Discussion

6.4.1 Strain Dependence

The LVER and ε_c values for each material were calculated at 0 °C for DC specimens and 16 °C for TF specimens¹⁸. However, it is known that the materials' ε_c values and LVER regions change at different temperatures. At lower temperatures, the ε_c can decrease, changing the LVER, meaning that plastic strain can occur at lower strains and stresses than at higher temperatures [197]. This relationship potentially explains why material responses in frequency sweeps (at varying temperatures) deviated

¹⁸ This difference was due to a lack of availability of the chiller system for the thin film testing, ideally testing would have been conducted at the lower 0 °C condition for both methodologies.

from expected behaviours at the highest and lowest temperatures. In future work, additional strain sweeps should be conducted at multiple temperatures to ensure each sweep is within the materials LVER. While this is possible, it requires considerably more time to characterise the materials to this detail which would come at a greater cost.

6.4.2 Temperature Dependence

The T_g of each material were obtained and compared between test methods. These values are of great importance as the T_g indicates the temperature at which the material behaviour changes considerably and has been shown in this chapter to be detrimental to the mechanical properties and influence the damping characteristics of each material. It was observed that the thin film T_g values were considerably lower than the corresponding dual cantilever results. As these material were the same, the T_g values should have been similar or (even identical in the case of $\tan \delta$ maximum peak). These differences could be explained by a thermal lag that caused the thin film samples to equilibrate at the required temperature faster than the thicker dual cantilever specimens meaning that the values were different.

The most apparent application for this is to compare the T_g values to the temperatures the material is exposed to in the offshore environment. However, the author finds that the work in the area is Eurocentric as the offshore wind sector is growing rapidly due to the abundance of lucrative offshore locations. As wind energy matures, the wind sector is expected to grow in other emerging markets, such as those found in Asia, where turbines would be exposed to a vastly different environment with potentially much greater temperatures commonly not accounted for in the current test programs. Work by Small *et al.* reports that temperatures in western Europe are (on average) lower than those seen on the eastern coast of Asia [198]. The work also reports annual temperature variations of ≈ 15 °C for western Europe and ≈ 30 °C for eastern Asia. This comparison only applies to a small region, and the difference in climate can vary considerably in neighbouring areas. The author envisages coating systems will need to be manufactured in ‘grades’ tailored for different climates worldwide, as seen in many other products like oils.

6.4.3 Frequency Dependence

Using the TTS principle, frequency sweeps at different temperatures were successfully conducted and converted into master curves. While most master curves appeared to be valid when visualised using Cole-Cole plots, many points did deviate from the expected curve. Generally, fewer deviations from the expected curve were observed in TF testing compared to DC testing. These deviations, such as those at the high frequencies, could be attributed to the changes in the LVER, as discussed before. However, it did appear that data was also clearly incorrectly located in the Y-direction. While this work

only looks at shifting the data in the X-direction, it is also possible to shift the data in the Y direction, but doing so complicates the analysis. The shifts in Y have been correlated to changes in material density, hydrological effects, and thermal expansion and/or contraction and would require a more extensive test program to identify the contributing factor [199, 200].

While using the frequency parameter is a robust approach for comparing the strain rate dependence of a material, it is often difficult to compare the results to other test methods, e.g. from finite element models. In Figure 6.19, relationships between oscillation frequency and strain rate are presented. These relationships were calculated using the sample dimensions and test parameters in a novel approach not seen before by the author in the open literature. As two different strains were used for the testing, both relationships were reported.

For comparison, tensile tests (conducted in Chapter 4) which are considered QS, used strain rates in the order of 10^{-4} s^{-1} to 10^{-3} s^{-1} . The upper strain rate limit for conventional DMTA testing is in the order of 10^{-2} s^{-1} . Alternative high strain rate testing methods such as using a Split-Hopkinson Pressure Bar are reported to reach 10^4 s^{-1} but require bespoke equipment not available outside specialist test facilities and considerable analysis to ensure valid data. The TTS approach allows for the characterisation of materials over a much wide range depending on the temperatures employed. This work made predictions between strain rates of 10^{-4} s^{-1} and 10^6 s^{-1} while using equipment more commonly available than specialist equipment.

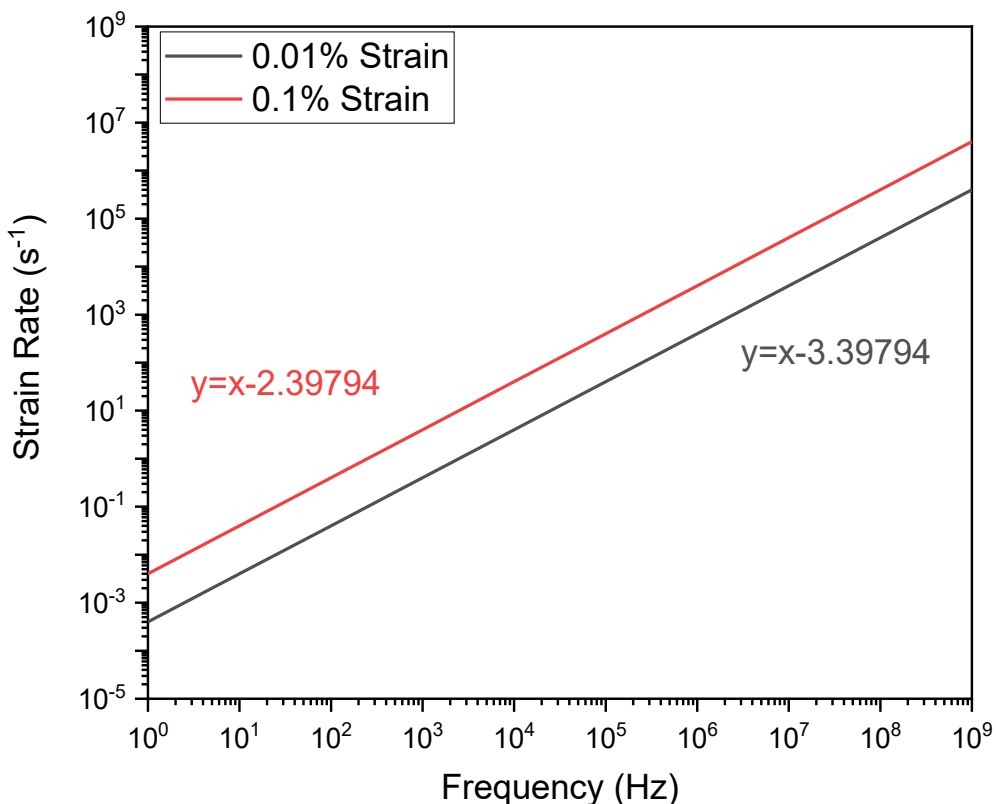


Figure 6.19 – Linear relationship between DMTA oscillation frequency (Hz) and strain rate (s) are presented. As two oscillation strains, 0.01 % (black) and 0.1% (red), were used, the graph shows each relationship and straight-line equations.

6.4.4 Comparison of Damping Characteristics

In the previous subsections, the $\tan(\delta)$ values were obtained for each material either in bending or tension. These $\tan(\delta)$ curves provide considerable amounts of information as the parameter considers the contribution of the E' and E'' , which both change as a result of factors such as changes in crosslinking density and segmental motion. Generally, it is assumed that a material with a greater $\tan(\delta)$, meaning it has an improved ability to dissipate energy, is more desirable for coatings used to protect against LEE (discussed in Chapter 2).

These values can be compared by overlaying the curves and comparing the resulting shapes. To be able to identify the influence of these changes, the values at a frequency of interest would be compared. However, in the case of this work, the intention was to capture a response over a wide range of frequencies to understand the material behaviour further, as it can be seen that the responses can vary considerably at different frequencies and temperatures. This comparison can be further complicated by the presence of (what are assumed to be) resonance peaks, where the $\tan(\delta)$ values appear disproportionately large. These points are considered not applicable as they are assumed to depend on the specimen geometry and boundary conditions, which can be different test fixtures

and are not expected to be the same in-situ. As a result, these points should be taken with caution, and instead, the general response of the material should be considered.

The value of $\tan(\delta)$ can be challenging to appreciate, but its physical meaning is associated with the ratio of energy dissipated to the energy stored under dynamic loading, which is related to the deformation caused by a droplet impact. An alternative way to visualise the data is by using the specific damping capacity (φ), which is calculated by

$$\varphi = 2\pi \tan \delta \quad 6.5$$

where (in this case) $\tan(\delta)$ is obtained from the master curves of each material [134]. This value calculates the energy ratio for a full cycle and provides a tangible value that could be applied if the impact energies are known. The benefit of using this method is that it is also usable for non-linear materials, e.g., outside of the LVER which could be beneficial if it found that rain droplet result in non-linear responses.

The φ values for the DC master curves are displayed in Figure 6.20. As the curve profiles change considerably as a function of frequency, three points at 1 Hz, 10^3 Hz and 10^7 Hz are taken as examples chosen for comparison. At 1 Hz, the materials are found to be in the order of LEP B3 > LEP A3 > topcoat A2 > topcoat B2 > LEP B4 > filler A1. This order almost follows the expected trend in material erosion performance of LEP > topcoat > filler with only LEP B4 not following the trend. At 10^3 Hz, a similar trend is observed, but the LEP B3 and LEP B4 materials show considerably greater φ values. At 10^7 Hz, all materials have similar φ values apart from LEP A3. This material appears to have the highest damping capacity at frequencies above $\approx 10^6$ Hz. These observations show that the material behaviours can vary considerably as a function of temperature, meaning a material with optimal properties at one frequency might not be the best at another and should be a consideration in material design and testing.

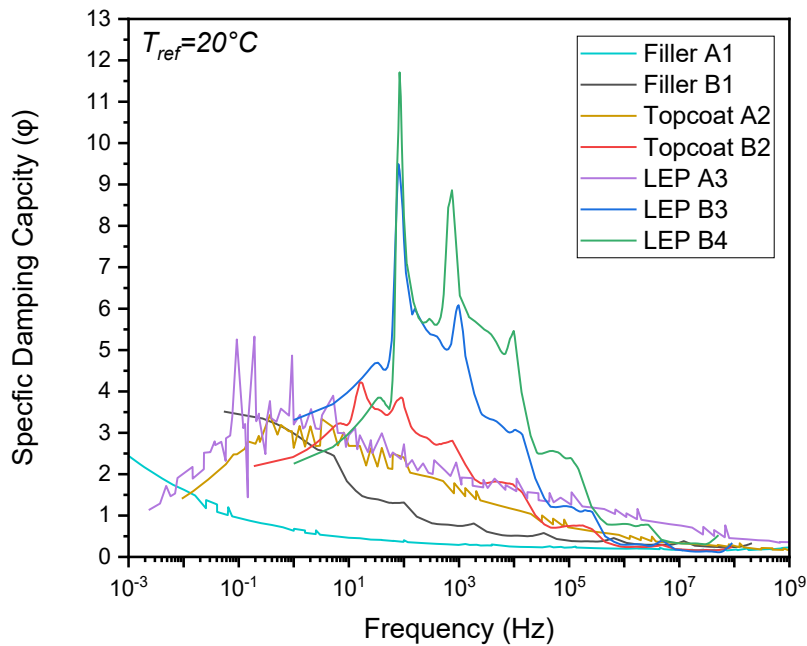


Figure 6.20 – A comparison of specific damping capacities of coating materials from dual cantilever master curves.

The φ values for the TF master curves are displayed in Figure 6.21. These curves all appear to have clear parabolic shapes and lower φ values compared to the values obtained in DC testing. As the curve profiles change considerably as a function of frequency, the same three points at 1 Hz, 10^3 Hz and 10^7 Hz are chosen as examples for comparison. At 1 Hz, the order of magnitudes is topcoat A2 > LEP B3 > filler B1 > LEP A3 \approx topcoat B2 > LEP B4. The order was not as expected at this frequency, with LEPs possessing lower than expected values. At 10^3 Hz, clear differences were observed with the filler B1 and topcoat A2 materials possessing the lowest φ values. For the other materials, this frequency corresponded to the peak maximum in the order of topcoat B2 > LEP B3 > LEP B4 \approx LEP A3, more in line with the expected performance of the materials. At 10^7 Hz, most material responses were similar, with low φ values. However, the LEP A3 response was four times higher than the other responses. This observation implies that the LEP A3 material possesses considerably more damping capacity than other materials tested at high frequencies, potentially explaining its superior performance as observed in testing described in Chapter 7.

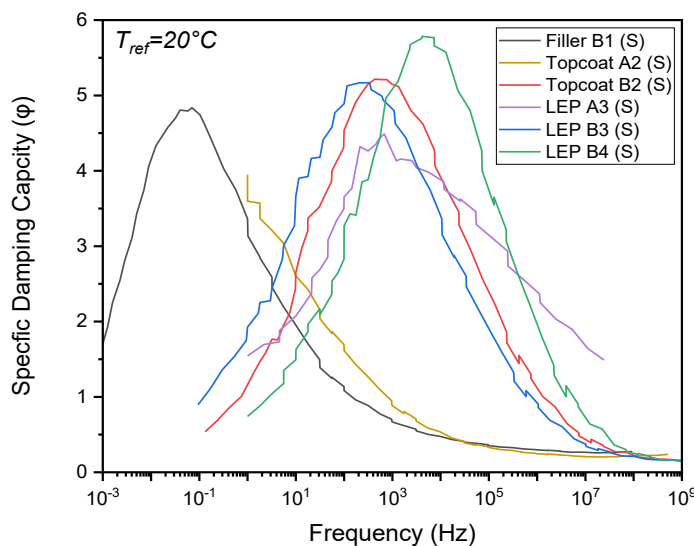


Figure 6.21 – A comparison of specific damping capacities of coating materials from thin-film tensile master curves. The data was smoothed using the adjacent averaging (25 pts) to aid visual comparison.

6.4.5 Comparison to Ultrasonic Acoustic Data

The data produced by DMTA provides a wealth of information about the behaviour of each material over a wide range of temperatures and frequencies. In literature, very few studies attempt to link measured dynamic properties and the lifetime of materials [60, 110, 136]. This work presents a novel approach that compared the predicted results from DMTA to results obtained from Ultrasonic Non-Destructive Acoustic Testing (UNDT)¹⁹.

The sound speed for each material is vital in the current understanding of lifetime prediction (further detailed in Chapter 2). This value allows for the measurement of the E of the material at higher strain rates but is also used to predict the absorption and reflection of an acoustic wave through a material. The method for obtaining the longitudinal speed of sound (C_l) for each material was obtained, as described in Section 3.8. A pitch-catch method with a single transducer was used to create an acoustic wave and capture the reflection that occurs due to a change of impedance through the material thickness. While this practice has been reported in the open literature, development of the method was still required to determine the correct sample dimensions, experimental setup and method of processing results. The main issue²⁰ that needed to be overcome was the determination of

¹⁹ This is a non-destructive approach that is commonly used to acquire the speed of sound and acoustic impedance of coating materials as seen in RP-0573 [108].

²⁰ In the interest of brevity, only the main issues surrounding the material testing are detailed, omitting equipment selection.

the correct sample thickness to be used in the tests. Initially, testing was conducted on thin-film materials ($\approx 400 \mu\text{m}$) manufactured using methods described in Section 3.2.3. However, upon testing the films, it was observed that it was challenging to differentiate reflections due to the overlap caused by the short distance the wave travels. This issue was further complicated as the more compliant materials, such as the LEPs, deformed when pressure was applied from the transducer. The resulting change in thickness causes a significant variation in thickness compared to the undeformed thickness, reducing the results' reproducibility.

Instead, samples of greater thicknesses ($\approx 2 \text{ cm}$) were manufactured to separate the reflections and improve reproducibility. At this thickness, the materials' acoustic attenuation becomes an issue when using thicker specimens as signals decrease due to the distance travelled through the medium thinner samples. This is the energy loss of acoustic waves when propagating through a material and is significant in highly damping materials such as the topcoats and LEPs. With further testing, samples of between 0.5 cm to 1 cm were suitable for all the materials tested.

Upon determining an appropriate sample thickness, a 5 MHz transducer was selected for use in further testing. This transducer was the most appropriate of the transducers available as higher ultrasound frequencies have shorter wavelengths and are absorbed/attenuated more easily.

Repeat tests were conducted for each material with data recorded on a digital oscilloscope. A script was created by the author to curate the data identifying each reflection peak and calculating the speed of sound for each material. From the speed of sound values, E was calculated using by

$$E = C_l^2 \rho \quad 6.6$$

where C_l is the longitudinal speed of sound, and ρ is the reported density from Table 6.4.

Table 6.4 – Density of each coating material used in testing.

Material	Density (kg/m ³)
LEP B3	1140
LEP B4	1140
Topcoat B2	1420
Filler B1	1600
LEP A3	1160
Topcoat A2	1300
Filler A1	1500

As expected, due to the results from previous test methods, E of the materials was in the order of filler > topcoat > LEP. These findings agree with current literature (described in Chapter 2) that states that lower E values are commonly correlated to better erosion performance.

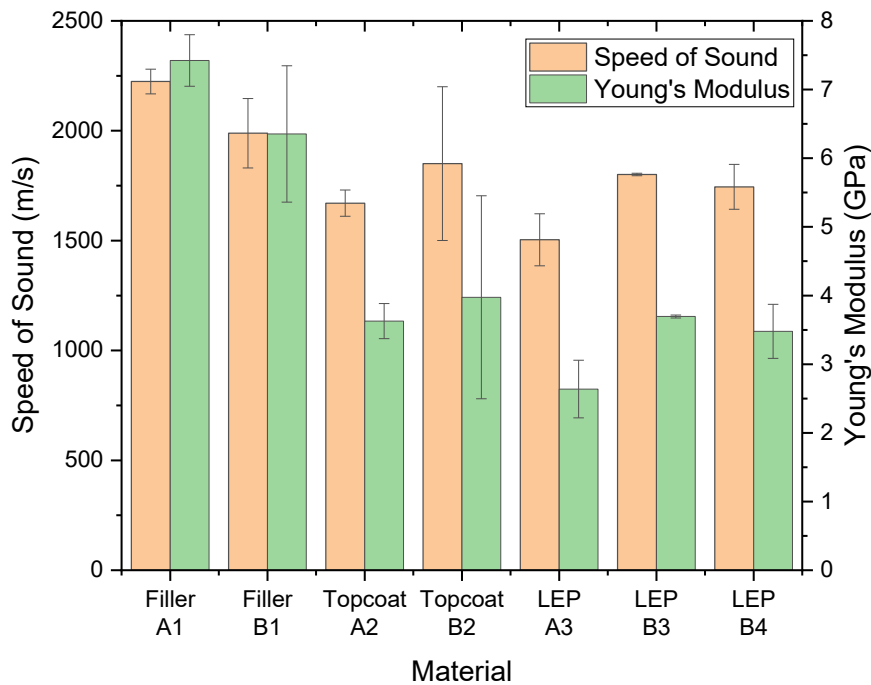


Figure 6.22 – A graph summarising the measured speed of sound values and calculated Young's modulus values obtained using a pitch-catch method and 5 MHz ultrasonic acoustic transducer ($N=4$).

As the speed of sound values calculated had been calculated, these could be compared against values obtained from DMTA data. A novel approach not used in the field of LEE was taken, calculating the speed of sound from master curves (C_{DMTA}) presented in Section 6.2.3 and Section 6.3.3. This value was calculated by

$$C_{DMTA} = \sqrt{\frac{E'(f)}{\rho}} \quad 6.7$$

where E' is the storage modulus as a function of frequency and ρ the material density. This equation presented by Lakes assumes the material to be one-dimensional, providing a simplified approach to understanding material behaviour [134]. Note this approach allows for the neglect of Poisson effects if the wavelengths of the stress waves are greater than the material diameter²¹.

The predicted C_{DMTA} values and measured C_L from DC master curves are presented in Figure 6.23. The LEP A3 and topcoat B2 C_{DMTA} values were observed to correlate to the respective C_L values at 10^6 Hz. This frequency matches the order of magnitude of the 5 MHz transducers used to measure C_L . This observation implies that for these identified materials, the method shows promise and could

²¹ From the results presented in Figure 6.22, the wavelengths were calculated to be between 300 μm to 400 μm , similar to the length of a coating film.

be interpreted as a validation of the TTS approach. While the other materials do not correlate to the measure C_L value, a clear positive correlation is observed between the frequency and C_{DMTA} values.

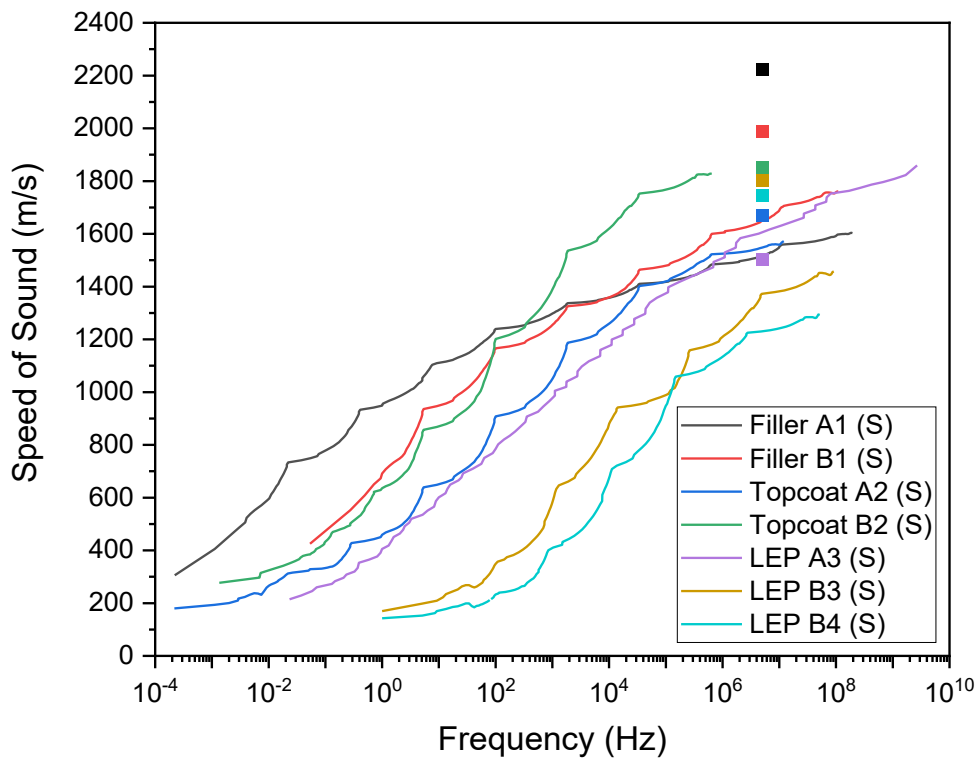


Figure 6.23 – A comparison of the measured (5 MHz) speed of sound values (squares) and predicted speed of sound values obtained from the storage modulus of dual cantilever master curves (solid lines). The data was smoothed using the adjacent averaging (10 pts) to aid visual comparison.

The predicted C_{DMTA} values and measured C_L from TF master curves are presented in Figure 6.24. Of the materials tested, only the topcoat A2 material was observed to reach the measured C_L but at a high than expected frequency of $\approx 10^8$ Hz. The majority of materials were observed to be sigmoidal in shape with a strong positive correlation. These TF C_{DMTA} were observed to be lower than the DC C_{DMTA} values as the master curve E' values were considerably lower. The considerable difference between the value indicates that the use of TF data to predict the speed of sound may not be suitable as it may not be the most influential deformation mode or could be overlooking the impact of a parameter such as the Poisson's ratio.

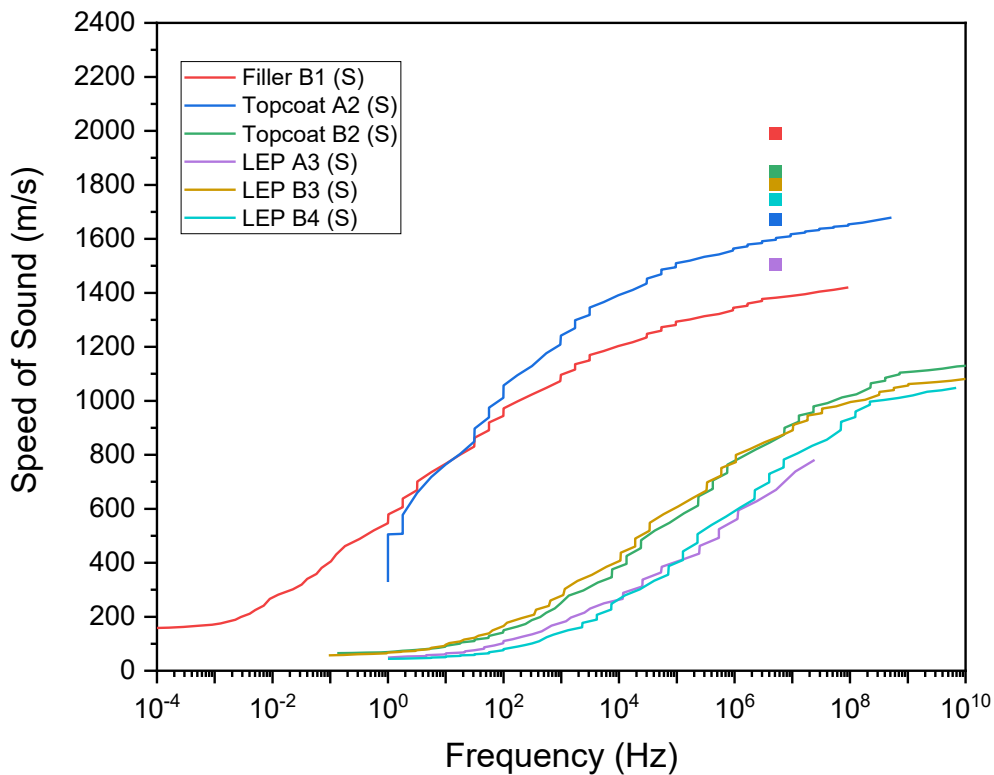


Figure 6.24 – A comparison of the measured (5 MHz) speed of sound values (squares) and predicted speed of sound values obtained from the storage modulus of thin-film tension master curves (solid lines). The data was smoothed using the adjacent averaging (10 pts) to aid visual comparison.

Out of all the materials tested, only two (which used DC data) were observed to be within a standard deviation of the value measured by acoustic testing at 10^6 Hz. While not all the values correlated, clear increasing trends were observed in all materials as a function of frequency. The DC values appeared to be considerably closer to predicted values as a result of the higher E' values obtained using this method. These differences between expected and predicted results could be attributed to the method used to acquire the E' values. These were obtained from frequency sweeps, converted into a master curve and used in a simplified equation. These steps undoubtedly contribute to error, possibly resulting in significant variations in the final results. To improve this method further, a greater understanding of the uncertainty associated with the master curve data is required and can be achieved by conducting replicate tests. Furthermore, common polymeric materials such as PET and PMMA could be used as calibration materials instead of the complex PU materials commonly composed of copolymers that can exhibit complicated behaviours.

The data presented shows clear differences in material properties as a function of both frequency and temperature. Current lifetime prediction methods commonly only use single values such as E to quantify material behaviour. However, as demonstrated in this chapter, material behaviour can vary considerably as a function of frequency/strain rate. This has direct implications on

the material used for LEPs as they are exposed to a range of impact velocities due to the rotational speeds and impact locations on the turbine. This approach presents a novel method that can be used to identify properties appropriate for the environment and impact conditions a turbine experiences. To quantify these in-situ effects, accurate measurements of the strain rates and temperatures each material experiences in the field are required (e.g. through active in-service monitoring) but are currently not commonly recorded to the authors knowledge.

6.5 Summary

This chapter successfully combined conventional DMTA approaches with the TTS approach to characterise each coating material over a wide range of strain rates applicable to LEE. The work details a methodology that can be replicated by coating manufacturers who have access to a DMTA to aid in the design of new coating solutions.

A novel comparison of coating properties under tension and bending was conducted, which resulted in considerable differences being observed between the deformation modes. Tensile responses were found to have lower dynamic moduli, resulting in greater damping magnitudes over wider frequency ranges than those found in the bending tests. These differences are important as current literature highlights tensile stresses as one of the most considerable contributors to erosion damage due to the water hammer phenomenon. These properties may be more suitable for describing material behaviour in this context. However, the values obtained using bending are still crucial as they can describe the overall response to stresses and strains experienced by the coating system, which are reported to be a combination of compressive and tensile stresses. As a result, future material characterisation campaigns should aim to capture material properties using different deformation modes to obtain a complete material response.

The damping behaviour of each material was observed to vary considerably as a function of frequency and temperature. As a result, each material response can vary under different loading and environmental conditions, a consideration not commonly accounted for in attempts to understand the erosion performance of coating systems. The work identified that each material possessed a range of frequencies where the damping behaviour was highest in both tensile and dual cantilever testing suggesting they are both suitable for analysis of materials²². However, the location of these ranges was different, indicating that each material has an optimal range where it can best dissipate energy.

²² While both testing modes showed that properties differ at different frequencies the tensile mode might be more applicable due to the current understanding of rain impacts that suggest that tensile stresses are the most important consideration due to the water hammer phenomenon.

While damping is not the only contributor to erosion performance, it does identify a previously unidentified difference that can be correlated to accelerated RET testing or in-situ performance.

The data generated in this work was also used to develop a novel approach that compared the predicted results from DMTA to measurements obtained from UNDT. While further method development is required, it was identified that the speed of sound of each material varies as a function of frequency. By obtaining the speed of sound at different temperatures and frequencies via DMTA, it is possible to directly incorporate each material's viscoelastic behaviour into current prediction models. While changes in damping properties alter the attenuation of stress waves, variations in the speed of sound result in changes to the propagation of stress waves through a coating system which has been directly linked to erosion performance.

If the strain rates of droplet impacts were known with more certainty, the methods presented in this work would identify the appropriate material properties and improve the understanding of rain droplet LEE.

However, as strain rates are mostly predicted using FEA models²³ rather than experimentally, there is still uncertainty about what strain rates are applicable. Instead, work in Chapter 7 details the results of a RET programme that quantified the erosion accelerated performance of each coating system under varying conditions to allow for correlation with the measured material properties.

²³ These droplet impacts are associated with high strain rates (10^6 - 10^9 Hz) predicted from Finite Element Analysis (FEA) models of rain droplet impacts [67].

7

Accelerated Rain Erosion Testing

This chapter presents the accelerated rain erosion testing results of each coating material using a commercial rain erosion test rig situated at the Offshore Renewable Energy Catapult. Standard and novel design of experiments approaches were utilised to quantify and compare each system's erosion performance.

7.1 Introduction

Previous Chapters 4, 5 and 6 have demonstrated considerable differences in material properties between the coatings used in the current work. Literature states that many of these parameters can directly influence rain erosion performance, but further testing was required to correlate this behaviour to erosion performance [53, 60, 72, 119]. To achieve this, composite leading edge specimens were coated²⁴ by each respective manufacturer, following their application procedures to minimise any variability caused by errors in the application. These specimens were subject to accelerated rain erosion testing using the state-of-the-art RET facilities described in Section 3.7 at the research institute in Blyth (UK) to assess the performance of each system under various test conditions and allow for comparison in Chapter 8 to measured material properties. Two approaches were taken; the first utilised conventional testing approaches, while the second used a novel research approach to increase the efficiency and data gathered from the test campaign.

7.2 Standard Approach

The first tests were designed to follow the standard approach commonly used to assess the erosion performance of coated test specimens. This method, detailed in Section 3.7, involves selecting a set of test parameters and comparing each material's erosion performance under those controlled conditions. This comparison is conducted by capturing images of each specimen following each test slice (testing interval). The time to end of incubation (observation of initial surface damage), time to break through (observation of composite substrate) and observation of the damage of the failure modes are thought to be the most important outputs and are used to compare the performance of the LEP systems being tested.

7.2.1 Method

Two groups of groups of test conditions were chosen for this initial comparison.

- A low-speed group that utilised a rotation velocity of 1000 RPM and a flow rate of 55 l/h. These were chosen as they are the OREC standard conditions which are thought to accelerate the test whilst also allowing time for typical damage mechanisms to occur. These include rotational velocities of 85 m/s to 125 m/s along the length of the specimen, a range applicable to the 100 m/s tip speeds experienced by materials seen in the offshore environment.

²⁴ The coating system for each respective system consisted of a filler layer and a LEP layer.

- A high-speed group that utilised a rotational velocity of 1200 RPM and flow rates²⁵ of 25 l/h apart from in one test where 75 l/h was used. 1200 RPM was chosen as it is required by the DNVGL-RP-0573 standard which sets the wind industry test parameters. This higher rotational velocity results in considerably harsher test conditions due to the rotational velocities exceeding the 100 m/s limit ranging between 101 m/s and 150 m/s. The use of two different flow rates can be used to observe the effects of high and low rainfall intensities

It was expected that lower velocities and flow rates would result in longer times to the end of incubation and breakthrough. The impact frequency for each test condition was calculated using the method defined in DNVGL-RP-0171 [147]. Table 7.1 presents the rain erosion tests conducted using the standard approach detailed in Section 3.7 to compare the rain erosion behaviour of each coating system. Each test was conducted in triplicate to assess the reproducibility of the results and allow for statistical analysis.

Table 7.1 – Accelerated rain erosion test plan used to compare the erosion performance of each coating system.

Test	Material	Rotational Velocity (RPM)	Flow Rate (l/h)	Needle Gauge	Droplet diameter (mm)	Impact Frequency ($s^{-1} m^{-2}$)
T1	LEP A3	1000	55	27	2.81	24304
T2	LEP A3	1200	25	27	2.77	13782
T3	LEP B3	1000	55	27	2.81	24304
T4	LEP B3	1200	25	27	2.77	13782
T5	LEP B4	1000	55	27	2.81	24304
T6	LEP B4	1200	70	27	2.82	36681

7.2.2 Results

The currently accepted damage model for LEE is based upon work by Springer (Section 2.5), which is thought to account for the effects of water hammer pressure on erosion [114]. The model can be used to estimate the number of droplets that could occur before damage is observed by using a modification of the Miner fatigue rule when the material properties and impact pressure of each droplet are known.

The erosion of leading edges is categorised into two main stages [86, 111, 114]. The first is the incubation period, where the surface shows no observable changes to surface roughness and no measurable mass loss. The second period, which occurs at the end of incubation results in irregularly

²⁵ Initially it was planned to use only one flow rate at the 1200 RPM condition however this data test was not conducted. Instead, a set of tests at a higher flow rate was included in the comparison with the difference accounted for by calculating the difference in impact frequency.

distributed pitting being observed, generally concentrated around the test specimen's high-speed tip, accompanied by a measurable mass loss. Further exposure leads to an increase in the concentration of pits, which can grow larger or form large cracks resulting in the removal of the coating layers eventually leading to damage to the underlying composite substrate. The erosion of the materials does not always occur in this order as materials are known to have sites that are more susceptible to damage [201]. These are due to factors such as manufacturing defects known to cause voids within the coating, poor adhesion between layers, or damage caused during transport and handling, such as scratches, all of which can act as initiation sites for erosion.

The observed damage is thought to be linked to the growth of cracks within the coating. The theory of crack propagation is often related to work by Griffith, who reported that crack propagation only occurs when the released strain energy is equal to or greater than the energy required to fracture a surface [202]. While this is commonly applied to brittle materials such as metals and ceramics, the concept can be applied to brittle polymeric materials commonly below the materials T_g^{26} . A polymeric material's crack resistance (often referred to as toughness) depends on a wide range of factors. These include material properties such as the chemical structure, cohesive energy and morphology, and external factors such as loading conditions, temperature and crack shape. According to the Griffith equation for homogenous isotropic materials, the applied stress is inversely proportional to the square root of the crack length. This means that the larger the crack becomes, the lower the failure stress of the material. In the case of erosion, it is thought that lower stress is required to propagate the crack as a crack grows, a concept applied using fracture toughness within the Damage Threshold Velocity equation discussed in Section 2.1. However, unlike in metals and ceramic materials where these concepts are commonly applied, polymeric materials can undergo greater elastic deformation resulting in the desirable ability to partially or completely absorb all of the fracture energy retarding crack growth.

Identification of damage sites is commonly conducted after each test slice (a period of active test time), where samples are either photographed automatically or manually inspected by the operator. As a result of this, it can be difficult to identify the end of incubation due to several factors that include:

- The selection of an unsuitable test slice duration could mean that the end of incubation or erosion progression may not be captured.

²⁶ For materials that undergo considerable plastic deformation the Griffith model has to be modified to include energy dissipation through plastic deformation through the Irwin-Orowan form of the Griffith model [202].

- The method of capturing observations can differ between operators as some only use images captured automatically, which are often of poor quality and can miss smaller damage sites that appear early in testing. Other operators remove test specimens from the rig and thoroughly photograph any damage using high resolution cameras under good lighting; this, however, adds additional time to the test process.
- Identifying appropriate damage sites is also problematic as it is commonly seen that voids at the surface appear after a short exposure period but do not act as initiation sites and remain at the same size for an extended period. Figure 7.1 shows an example of this phenomenon, which shows surface voids that appear very early during accelerated testing. These could be due to entrapped air during the mixing of the coating or through the evaporation of volatile solvents during cure. While these sites appear at the higher speed tip end, they do not undergo the expected erosion mechanism and typically do not act as first initiation sites for the erosion process. To account for this, all damage sites are recorded and photographed, allowing the analysis to retrospectively track the damage sites and identify if they progressed into active erosion.

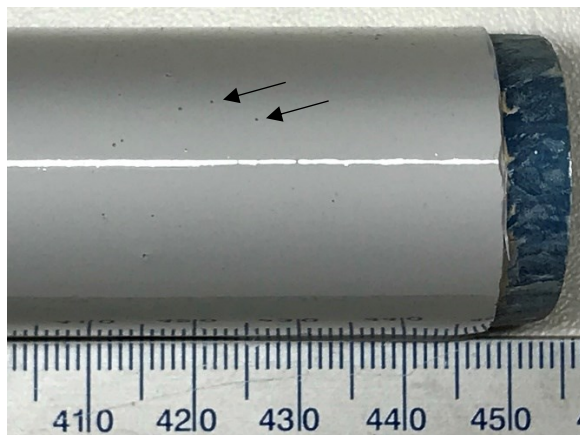


Figure 7.1 – An example of surface voids present in an accelerated leading edge erosion test specimen that did not progress into active erosion over the duration of the test. Image not to scale.

A qualitative analysis of the photographs taken during the test campaign is now presented in this section. Due to the large number of images captured, only one site for each material and test condition is included. To analyse the progression of erosion three images of the same damage sites were compared²⁷:

- After the incubation period, where damage sites are visible on the specimen.
- During the progression of the erosion at a chosen time.

²⁷ An analysis of the locations of the damage and respective times are discussed further within the quantitative analysis that follows.

- At breakthrough, where the underlying composite substrate becomes visible.

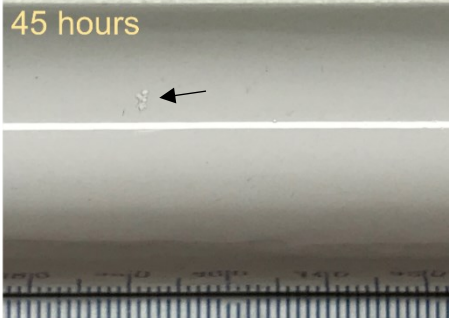
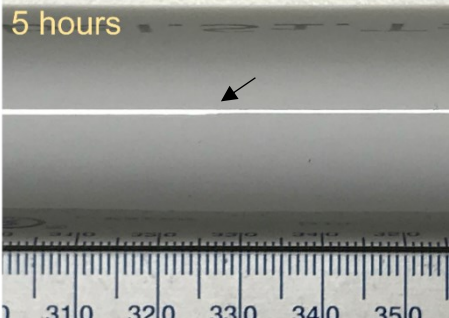
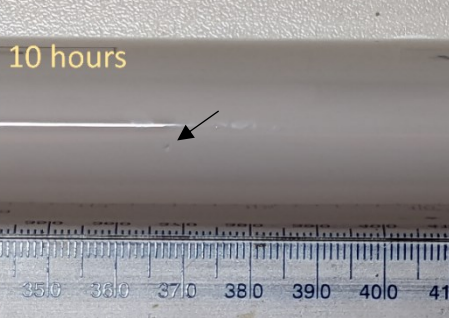
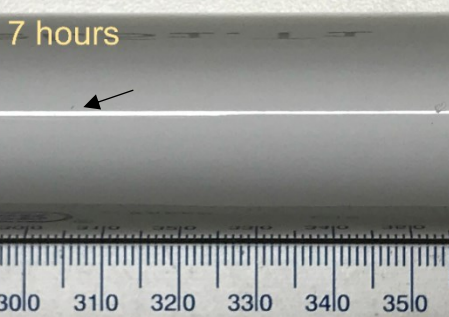
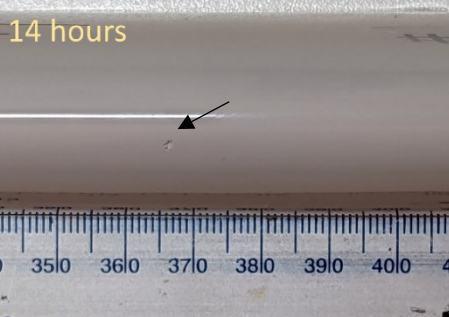
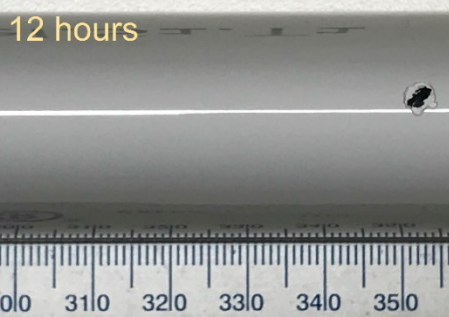
Images of the lower speed test tests (T1, T3 and T5) are presented in Table 7.2.

For the selected LEP A3 specimen, the observed damage was concentrated around a small area of the leading edge. Two damage sites can be seen, one large irregular shape and a much smaller rounded pit. The second image shows how the damage had progressed after two more hours of testing. The smaller pit had remained a similar size and shape, but the larger pit had grown considerably, with greater material removal towards the higher speed tip end. At breakthrough, the smaller pit remained unchanged. However, the larger pit had grown from losing a large amount of material, exposing the underlying composite substrate and forming a jagged damage shape. Interestingly, only a small portion of the underlying filler layer was visible, which appeared to have been eroded rapidly upon exposure.

For the LEP B3 system, the damage observed at the end of incubation was very small and difficult to capture using the available camera system. In the second photo, the damage site appeared to grow, forming a large rounded hole where the material was lost. In the final image at breakthrough, the damage to the LEP layer can be seen to have become even more rounded, exposing the underlying layers. This was a different failure mode than the LEP A3 material, which was more jagged.

For the LEP B4 material damage, a single circular damage site was initially observed. After a further four hours, the damage site was seen to grow in both width and depth. The final image at breakthrough shows that the top LEP material was removed, leaving the underlying filler layer exposed with a small break through to the composite substrate. The shape of this hole was found to have rounded edges toward the high-speed edge and sharper edges towards the lower-speed end.

Table 7.2 – A selection of images taken of rain erosion test specimens displaying the process of erosion at a chosen time. Testing was conducted at 1000 RPM and 55 l/h. Images not to scale.

Stage	Coating System		
	LEP A3 T1 (Specimen #1)	LEP B3 T3 (Specimen #2)	LEP B4 T5 (Specimen #1)
1	45 hours 	5 hours 	10 hours 
2	47 hours 	7 hours 	14 hours 
Breakthrough	49 hours 	12 hours 	18 hours 

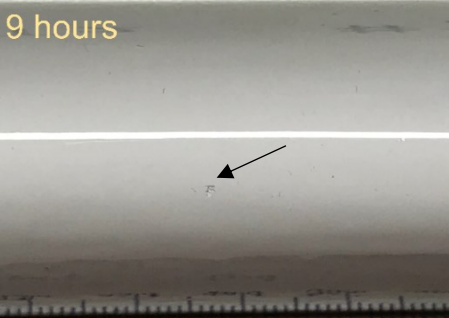
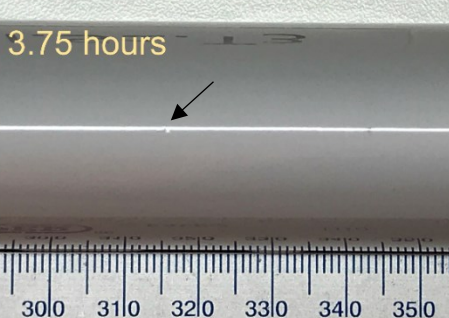
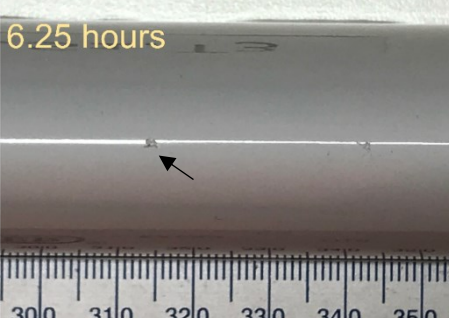
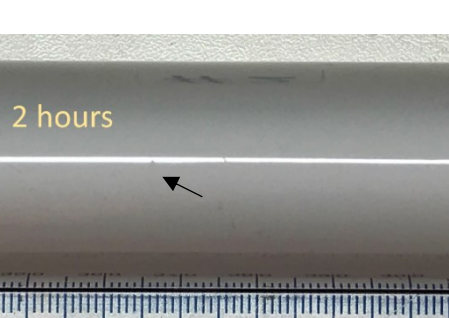
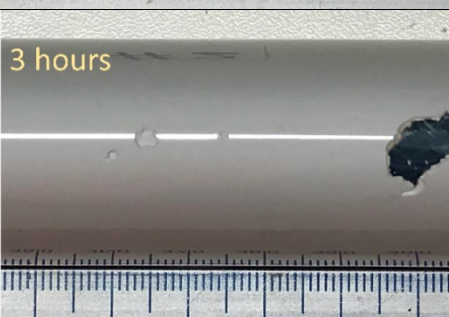
Images of the higher speed test tests (T2, T4 and T6) are presented in Table 7.3.

For the LEP A3 material, several small damage sites were observed at the end of the incubation period, with one appearing to be larger. After 2 hours, the largest damage site was observed to grow considerably, resulting in jagged shapes on the surface. At breakthrough, the large damage site grew further, showing signs of greater materials removal along the sharp damage line seen in the previous image demonstrating that these cracked areas are more susceptible to further damage.

For the LEP B3 material, several damage sites were seen in the first image, with two being considerably larger. After 2.5 hours, the two larger damage sites appear to grow due to material loss leaving behind an irregular shape on the coating surface. After a further 2.25 hours, the two damaged sites had lost further material, exposing the filler and composite substrate. The damage site showed evidence of both rounded edges and sharp cracks that would probably be the next areas where the material is lost. The damage site on the right also showed that a large piece of material was still attached to the LEP layer but not to the underlying layers. This potentially is the mechanism that causes larger pieces of LEP to be removed, leaving the rounded shapes due to the tearing of larger pieces of the material.

For the LEP B4 material, several small damage sites were observed in the first image after incubation. After 25 minutes, these grew to form circular damage sites along the leading edge. In the final image where a composite breakthrough was observed, the damage can be seen to be circular in areas that had not yet reached the underlying layers. Where it had broken through, the damage appeared to be rounded, indicating that sections of the material had been torn off. On one side of the site, the damage did extend further outside the damage site, indicating that damage would progress in that direction.

Table 7.3 – A selection of images taken of rain erosion test specimens displaying the process of erosion at a chosen incubation point. T2 and T4 testing was conducted at 1200 RPM and 25 l/h. T6 testing was conducted at 1200 RPM and 70 l/h. Images not to scale.

Stage	Coating System		
	LEP A3 T2 (Specimen #3)	LEP B3 T4 (Specimen #1)	LEP B4 T6 (Specimen #2)
1	9 hours 	3.75 hours 	1.5 hours 
2	11 hours 	6.25 hours 	2 hours 
Breakthrough	12 hours 	8.5 hours 	3 hours 

An overall observation that can be made of the images is that in the low-speed conditions (T1, T3 and T4), testing resulted in fewer damage sites that were commonly isolated from any other signs of damage. Conversely, the high-speed tests (T2, T4 and T6) resulted in a greater number of damage sites that tended to group around the high-velocity end of the specimen and progress towards the root. Figure 7.2 presents an example image allowed to run after experiencing breakthrough to the composite substrate to demonstrate the differences. Upon progression of the erosion, the low-speed tests were observed to remove the LEP material from the filler layer. The filler was often not visible in the high-speed tests as it had been eroded down to the composite during the test slice. Furthermore, at the high speeds, the edge of the active damage sites indicated that materials showed removal of rounded pieces, potentially due to tearing of the coating rather than the expected erosion mechanism.

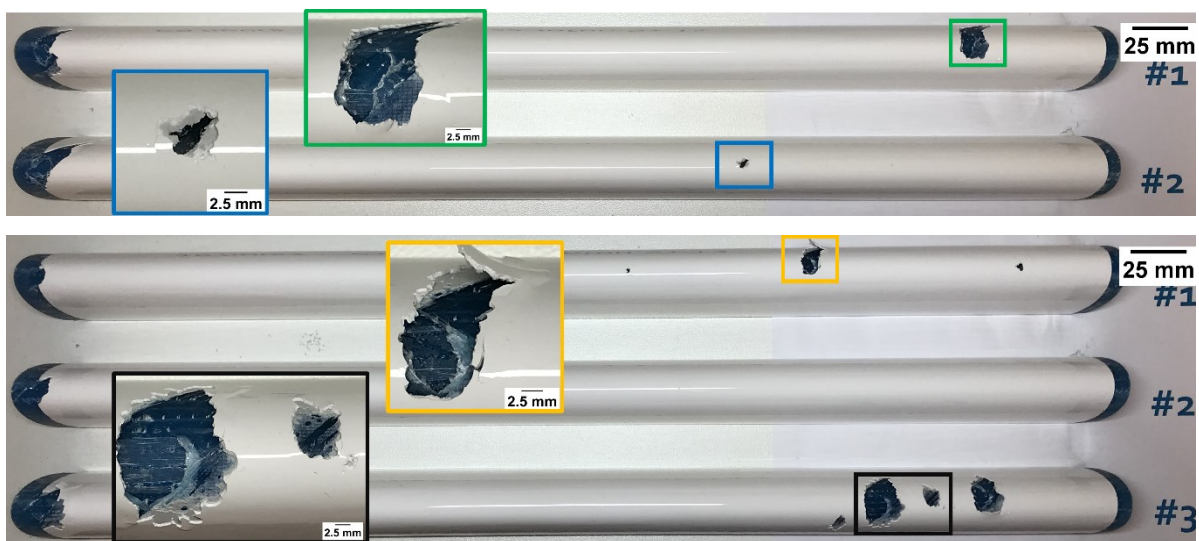


Figure 7.2 – Eroded rain erosion test specimens tested in the OREC WARET. The high-speed tip is on the right Top: LEP A3 system tested at 1000 RPM and 55 l/h (T1) at 66 hours. Only two specimens are shown as the third specimen needed to be removed due to early failure of the composite substrate. Bottom: LEP A3 system tested at 1200 RPM and 25 l/h (T2) at 16 hours.

The quantitative results from the standard test program are presented in Table 7.4 and are summarised as:

- For the low-speed group, the T1 test was observed to have the longest time to incubation with an average of \approx 33 hours, significantly greater ($P < 0.05$) than the comparable T3 and T5 tests. The latter two were found not to be significantly different ($P < 0.05$), with an average time to incubation of \approx 2.6 hours. A similar trend was observed in the times to breakthrough, with an average of \approx 45 hours for T1, significantly greater ($P < 0.05$) than T3 and T5. However, unlike the incubation times, a significant difference was observed between the breakthrough times, with T5 being significantly greater ($P < 0.05$) than T3.

- For the high-speed group, the incubation times were all considerably lower than in the low-speed group. The T2 test was observed to have the longest time to incubation, with an average of 7 hours. This result was significantly greater ($P < 0.05$) than the T4 and T6 tests, which were found to be statistically insignificant ($P < 0.05$) when compared. The average time to breakthrough for T2 and T4 was statistically insignificant ($P < 0.05$), with 14 hours and 7.8 hours, respectively. The T6 breakthrough time was 3.8 hours, significantly lower than T2 and T4.

Table 7.4 – Summaries of time to incubation and failure of each coating system under various test conditions

Test	End of incubation		Breakthrough to composite	
	Mean duration (hours)	CoV (%)	Mean duration (hours)	CoV (%)
T1	33.33 ± 23.35	23.4	45.00 ± 22.27	49.5
T2	7.00 ± 1.00	14.3	14.00 ± 3.46	24.7
T3	2.33 ± 0.58	24.7	10.33 ± 1.53	14.8
T4	0.75 ± 0.25	33.3	7.83 ± 1.84	23.5
T5	3.00 ± 0.00^{28}	0.0	17.33 ± 0.58	3.3
T6	0.83 ± 0.58	69.3	3.83 ± 0.76	19.9

For the purpose of this thesis, in which LEPs are being examined, it is the author's opinion that of the two values measured, the incubation time is a more important comparison for this work as it identifies the onset of erosion rather than including the more complex failure modes that are present when underlying coating layers are exposed²⁹. Once incubation has been reached, more complex/macro effects such as changes to material properties (e.g., through moisture uptake), peel forces, and aerodynamic effects becoming more considerable, especially during accelerated testing. As the material characterisation in previous chapters focuses on characterising pristine materials (properties that have not undergone degradation) it is thought that it more suitable to focus on incubation time where it is a less complex issue rather than focusing on when the material has displayed significant damage.

Overall, the LEP A3 material had the longest times to incubation, $\approx 160\%$ greater than those of the LEP B3 and LEP B4 materials in high and low-speed conditions. No significant differences were observed between the LEP B3 and LEP B4 times to incubation in each test group. However, the T6 test utilised a higher flow rate resulting in a $\approx 90\%$ increase in impact frequency compared with the other

²⁸ The reported standard deviation of zero is because inspection of specimens only occurs after a test slice (periods of testing) is completed. In this case all test specimens failed within a single hour slice and the times and standard deviations reflect this.

²⁹ Although data and images of failure are captured it is has not been chosen as a focus of the project.

high-speed test conditions. This difference potentially resulted in the material failing earlier, and it could be assumed that LEP B4 material could have a higher incubation time if tested at the same impact frequency.

An alternative way of comparing the result is by determining the VN curves for each material. These are determined by plotting an incubation curve that records the end of incubation periods at different impact velocities and specific numbers of impacts, as detailed in the DNVGL-RP-0171 [147]. As the RP assumes the number of impacts (N_i) is only a function of droplet impact velocity (v), the relationship can be described by

$$N_i = f(v) \quad 7.1$$

which allows for the comparison of the erosion performance of the material. As the RP assumes, the data can be described by a power-law, and each data set can be described by

$$N_i = b(v)^{-m} \quad 7.2$$

where b and m are constants. Which can be rearranged to

$$\log N_i = \log b - m \log v \quad 7.3$$

where the b and m constants are derived from a least-squares fit.

The incubation plots for each material are presented in Figure 7.3 and generally display the expected trend of lower N_i values at higher v values. However, due to the distribution of the data points, it is more beneficial to use the VN curves to compare erosion performance by combining the data for each material. Generally, the further a curve is to the right, the greater the number of impacts required to reach the end of the incubation period, meaning a superior erosion performance.

The fitting constants and R^2 values for each VN curve are presented in Table 7.5. The R^2 value for the LEP A3 material was found to be 0.79 and considered a good fit of the data. The LEP B3 and LEP B4 materials R^2 values were 0.31 and 0.18, respectively, which are considered poor fits.

For the LEP B3, the fit was reduced due to the distribution of points at ≈ 140 m/s, which do not appear to follow the same trend as the majority of the points at lower impact velocities. These anomalous points were recorded to fail at considerably lower N_i values close to the high-speed tip end of the specimen progressing toward the root. If only the high speed data set was plotted onto a VN curve the material would appear to have a much greater erosion resistance than when the two datasets are combined. While this data set could arguably be omitted, this response was consistent across the three replicate test specimens, and the removal of the data would result in the loss of half the points for the material tested. As a result, the decision was to include the results to highlight the

observation. A potential reason for this difference could be due to duration of time between tests on the same material. It was observed that over time coating material can continue to cure resulting in higher modulus materials which could alter the erosion performance of the system.

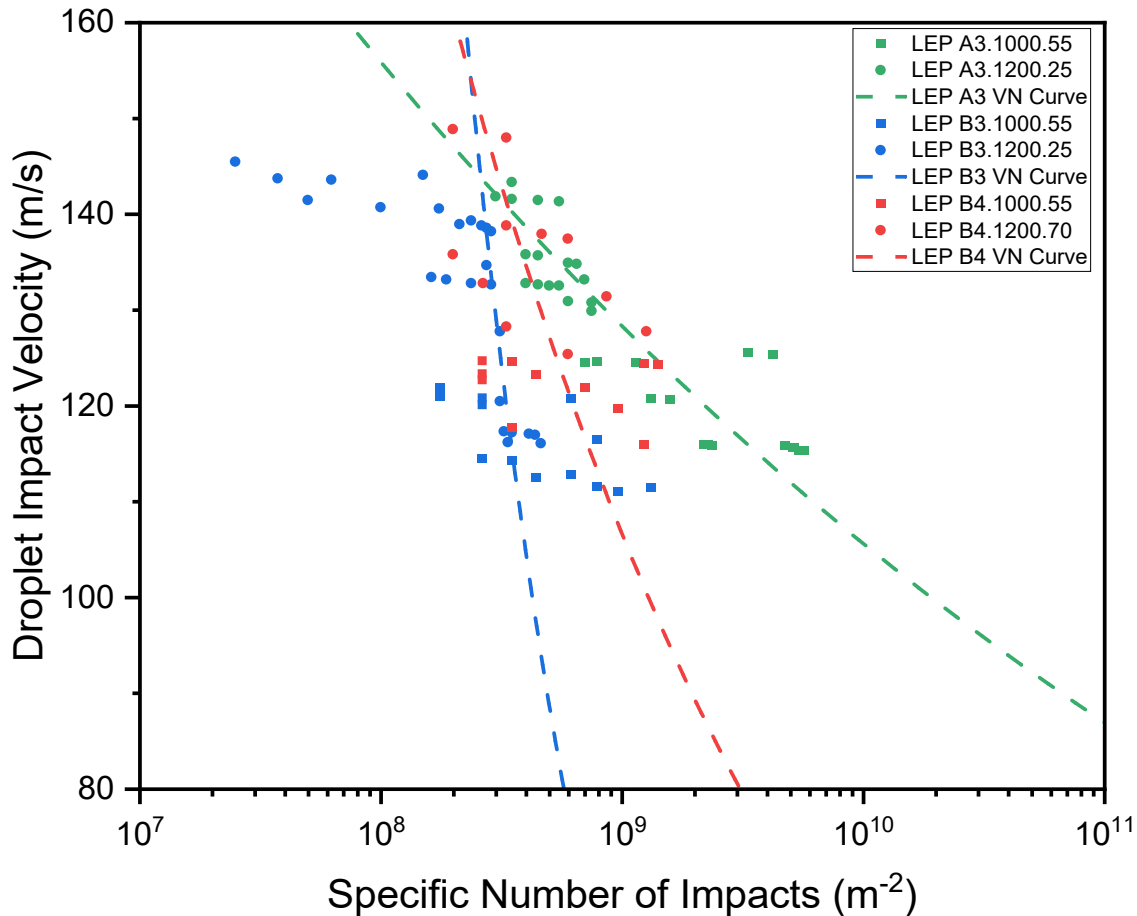


Figure 7.3 – VN graph displaying the impacts to the end of incubation at different local impact velocities. A power-law fit is presented to allow for a comparison of each test.

For the LEP B4, while a clear decreasing trend was observed, the low fit was due to a spread of data rather than anomalous results. At each velocity, a wide range of N_i values were reported resulting in the reduction of the R^2 value of the VN curve. While the material does show improved erosion performance over the LEP B3 material, the increased variability could be attributed to the changes in material composition potentially resulting in a detrimental effect on the material's ability to form defect-free coatings.

Table 7.5 – A summary of calculated VN curve constants and the respective coefficient of determination (R^2) values for each tested material.

Material	VN Curve		
	m	b	R^2
LEP A3	11.83	8.81E+33	0.79
LEP B3	1.36	2.18E+11	0.31
LEP B4	3.92	9.23E+16	0.18

Clear differences can be observed between the resulting VN curves of each material. At 80 m/s, the erosion performance follows the order LEP A3 >> LEP B4 > LEP B3 (the same order reported in the times to incubation reported in Table 7.4). Below this velocity, the difference in each material's erosion performance increases. Above 80 m/s, N_i is shown to decrease until ≈ 140 m/s, where the erosion performance for all the materials appears to be the same. Above the 140 m/s, the order of erosion performance appears to reverse to LEP B3 > LEP B4 > LEP A3, with the difference becoming more considerable at higher velocities. However, as the comparison is based upon a fitting of the data it may not accurately represent erosion performance of materials and cannot be commented upon with any confidence without further testing.

7.3 Design of Experiments Approach

Throughout this project, considerable differences in material properties and erosion performance have been identified between the commercial coating systems tested. RET test parameters are commonly selected to allow for comparison in standard testing, as seen in Section 7.2. This approach does allow for a relative comparison of erosion performance, but to fully understand each variable's contribution, a considerable test program would be required. As the results from accelerated RET testing commonly do not correlate to in-situ performance, a greater understanding of the effect of test parameters on the erosion performance is required.

It is possible to follow a traditional experimental test method changing one factor at a time to identify the contribution. However, this is inefficient and cannot determine any effects caused by multiple factors acting in combination. Instead, a design of experiments (DOE) approach can maximise the amount of information gained from the study while also reducing the number of tests required [203, 204]. It is achieved by making systematic changes to the input variables of the test and measuring the effects on a chosen final response. This approach has been used in experimental and modelling studies where an extensive testing campaign is prohibitive due to the cost of testing or the number of test parameters [205]. These issues are particularly relevant to accelerated RET testing as single specimens have been shown to last upwards of 60 hours, meaning that test campaigns can take significant amounts of time and can be prohibitive due to cost.

Factorial DOE is a method in which the effects of each factor and the combinations of factors are estimated [203]. These are geometrically constructed, commonly varying all the factors simultaneously and orthogonally³⁰. The design can be visualised as collecting data at the vertices of a cube, as shown in Figure 7.4.

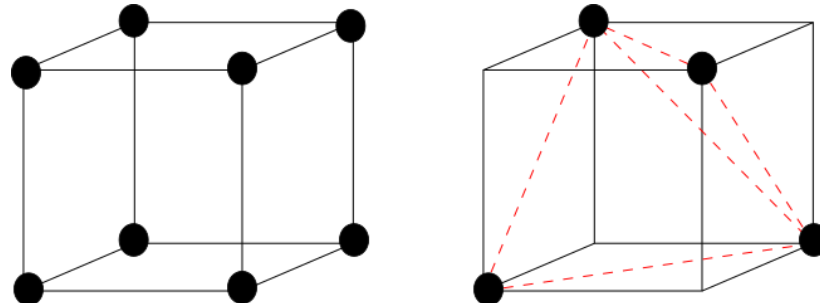


Figure 7.4 – Visualisation of full factorial (left) and $\frac{1}{2}$ factorial (right) designs utilising two levels.

A full factorial design is an approach that measures responses to all combinations of the factor levels. The number of runs necessary for a two-level full factorial design is L^k where L is the number of test levels, and k is the number of factors [203]. As the number of factors increases, the required number of tests increases exponentially due to the relationship. Fractional factorial designs are also possible as they only utilise a 'fraction' of the runs required to conduct a full factorial design. The number of tests for this approach is calculated by using L^{k-p} where p is the desired fraction size. However, due to only a subset being tested, some of the main effects and two-way interactions are confounded and cannot be separated from the effects of other higher-order interactions, which must be assumed negligible.

7.3.1 Method

A full factorial design was selected for the test program as it allowed for non-linear influences and all interactions to be evaluated. From the results gained from prior testing, such as the creation of VN curves, it is known that erosion performance is commonly not linearly correlated to any single parameter. As a result, a minimum of three levels were required to ensure that non-linear influences resulting from changing test variables were captured. The number of factors was chosen to be three, requiring a minimum of 27 tests. Increasing the factor to four would have required 81 tests, which was deemed unfeasible in one month of testing time available.

³⁰ An orthogonal experimental design refers to each factor being varied independently of one another. While this is not essential due to the computational capabilities available today, it is considered desirable as it improves the ease of explaining trends between results.

7.3.1.1 Factor Selection

The three factors selected for the DOE approach were rotational velocity, flow rate and material type.

The reasoning for the selection of these is detailed below:

- Rotational velocity: This variable directly influences the droplet impact velocity across the length of the specimen. As seen in Section 2, it is the parameter that most influences the N_i and thus the erosion performance of a coating system.
- Flow rate: This variable determines the volume of water that passes through the needles forming the rain droplet field. A higher flow rate results in a greater number of droplets produced and, as a result, varies the impact frequency.
- Material type: This variable was used to explore the effect of systematically changing the material composition. In collaboration with the manufacturer, 'hard' and 'soft' variants of the LEP A3 coating system were formulated and used in this test campaign by altering the hardener component of the system. The details are commercially sensitive and could not be disclosed.

7.3.1.2 Designed Test Plan

Table 7.6 details the designed RET test plan following the methodology described in Section 3.7. Samples were visually inspected and photographed after each slice, recording the locations and sizes of erosion sites. Slice times of 15 minutes were used for the 1200 RPM condition to ensure that the progression of erosion was captured. For the 1100 RPM and 1000 RPM conditions, slice times of one hour were used.

Table 7.6 – A summary of the rain erosion test plan following a full factorial design of experiments with three levels and three factors.

Tests Required			
Test	Rotational Velocity (RPM)	Flow Rate (l/h)	Material
1	1200	70	Hard
	1200	70	Medium
	1200	70	Soft
2	1200	50	Hard
	1200	50	Medium
	1200	50	Soft
3	1200	25	Hard
	1200	25	Medium
	1200	25	Soft
4	1100	70	Hard
	1100	70	Medium
	1100	70	Soft
5	1100	50	Hard
	1100	50	Medium
	1100	50	Soft
6	1100	25	Hard
	1100	25	Medium
	1100	25	Soft
7	1000	70	Hard
	1000	70	Medium
	1000	70	Soft
8	1000	50	Hard
	1000	50	Medium
	1000	50	Soft
9	1000	25	Hard
	1000	25	Medium
	1000	25	Soft

Several challenges were identified that needed to be considered:

- Compared to conventional testing, this approach does not conduct tests in triplicate, (only one test being conducted in each condition) as each test arm is assigned a unique specimen in all test conditions. This replication, while desirable, is not a requirement for DOE testing as information on all factors is collected in each test. This repetition means that every data point is used in the analysis multiple times and minimises the effects of any outliers.
- Due to the large number of tests required to be undertaken in a short period, careful sample management is required to ensure suitable photos and time under test were accurately recorded.

- As different materials were used in each test, it was a possibility that materials would fail at considerably different times. To overcome this, specimens that show significant breakthroughs to the composite were removed and replaced with a nickel erosion shield to prevent damage to the test rig.
- It was identified that the use of shorter slice times for the 1200 RPM test conditions could introduce another factor into the test program. Due to the additional added time, utilising the shorter slice time for all conditions would be unfeasible. Instead, it is assumed that slice time does not influence the erosion performance of the material.

7.3.2 Results

The test campaign was completed in 76 hours of active testing, with incubation periods ranging from 3.5 hours to 25 hours, dependent on the test conditions. While the manufacturers coated the specimens to minimise the risk of poor application, specimens could be observed to undergo delamination as early as 30 minutes into erosion testing. An example image is shown in Figure 7.5, which demonstrates the delamination of the LEP from the underlying layer. This type of failure is commonly associated with poor adhesion between coating layers. Manufacturers commonly overcome this by utilising adhesion promoters that improve the adhesive interactions between coating layers. The failure mechanism was observed to initiate from the specimen edge on the top or bottom face. These delaminations were not observed to initiate at the higher velocity tip; instead, these sites were randomly distributed along the length of the specimen. Testing of the specimens was still conducted as the delamination in all but one material did not reach the leading edge, meaning the onset and progression of erosion along the specimen was captured and observed to be representative of the failure modes seen in standard testing (Section 7.2). This failure mode made conducting a qualitative analysis of the progression of erosion difficult and instead the work focuses on quantitative analysis using times and locations of damage sites that occur after the incubation period as seen in Section 7.2.2.



Figure 7.5 – Images of test specimens from Test 6 that underwent 5 hours of erosion time at 1100 RPM and a flow rate of 25 l/h. This image shows the delamination issues observed in many of the test specimens used in the campaign.

7.3.2.1 Multivariate analysis

A Pareto chart of the effects to compare the relative magnitude and the statistical significance of both the main and interacting effects is presented in Figure 7.6. Values exceeding the reference line indicate effects that are considered statistically significant ($P < 0.05$).

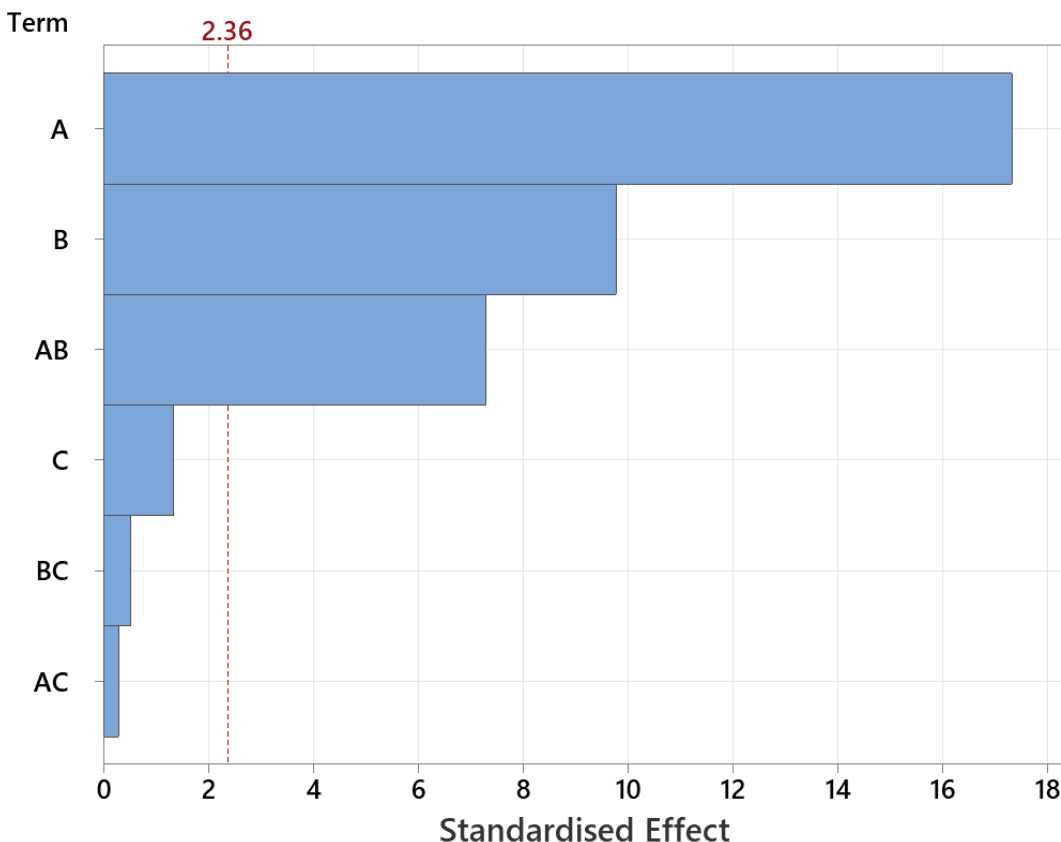


Figure 7.6 – Pareto chart comparing the standardised effects in response to time to incubation for three factors. A: Rotational velocity, B: Flow rate and C: Material. The red line indicates a threshold value, responses exceeding threshold are considered statistically significant ($P < 0.05$).

For the time to the end of incubation response, three significant ($P < 0.05$) effects were identified. These include (A) rotational velocity, (B) flow rate and (AB) the interaction between the rotation velocity and flow rate. Surprisingly, the choice of material; in this case, the effect of the material was considered insignificant ($P > 0.05$). From the data, it can also be observed that the largest effect is (A) rotational velocity which has $\approx 50\%$ greater effect when compared to (B) the flow rate and $\approx 75\%$ greater than the effects of them combined (AB).

The main effects plot for the time to the end of incubation is shown in Figure 7.7. The plot compares the mean times to end of incubation for each value of a variable used in the model, in this case, the chosen factors. By comparing the slope of these curves, the relative magnitude of these effects can be determined. It can be observed that increased rotational velocity results in the most considerable reduction in the incubation time. The increase in flow rate also decreases the incubation

time but to a lesser extent. The choice of material shows that a softer material increases time to the end of incubation; however, this was shown to be insignificant in the earlier Pareto chart.

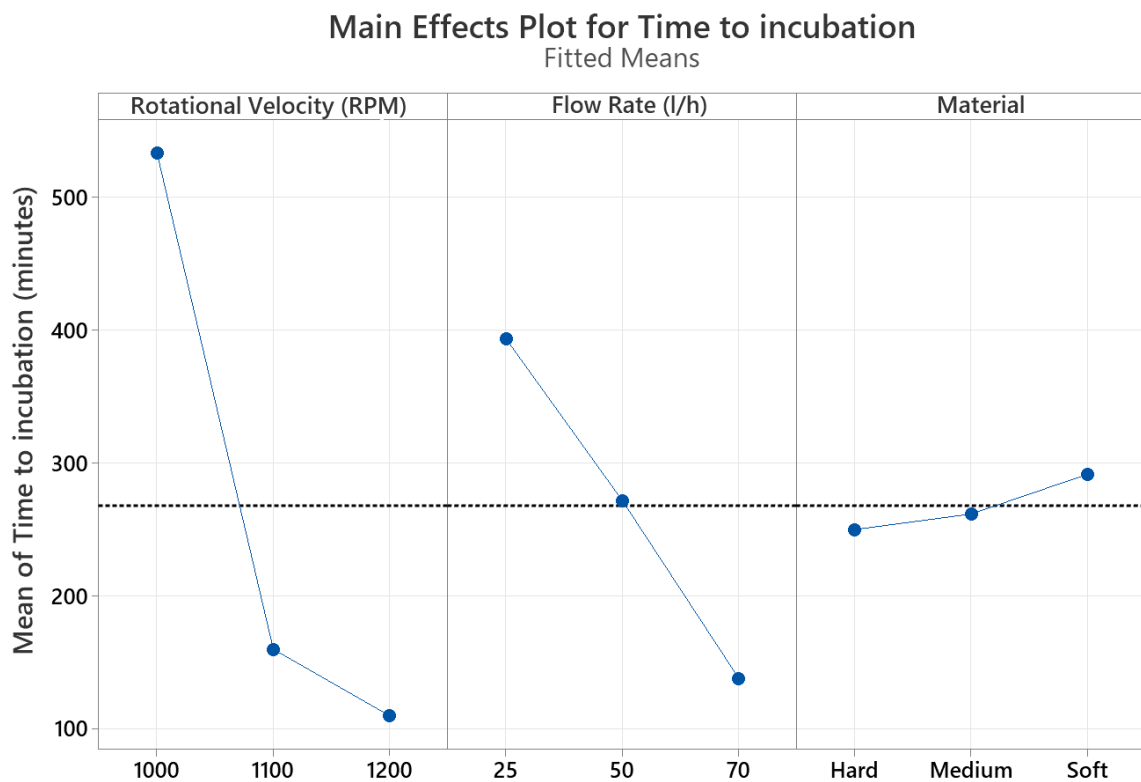


Figure 7.7 – A main effects plot for the time to incubation. The dashed line indicates the average time to the end of incubation.

While the Pareto plot shows the significance and absolute magnitude of interactions, the interaction plots shown in Figure 7.8 assess how any two-way interactions affect the response, e.g. positively or negatively. If lines in each plot are parallel, it can be stated that no interactions are observed. The greater the difference in the gradient of each line, the greater the effect of interaction. It can be noted that the soft material deviates from the observed trend performing better at 70 l/h flow rate and 1000 RPM. However, this is not considered significant ($P > 0.05$), as demonstrated in the Pareto chart. The combined interaction of rotation velocity and flow rate reduces the incubation time, with the effect being more prominent at lower rotation speeds. At the highest rotational speed, the increase in flow rate unexpectedly shows an increase in time to the end of incubation.

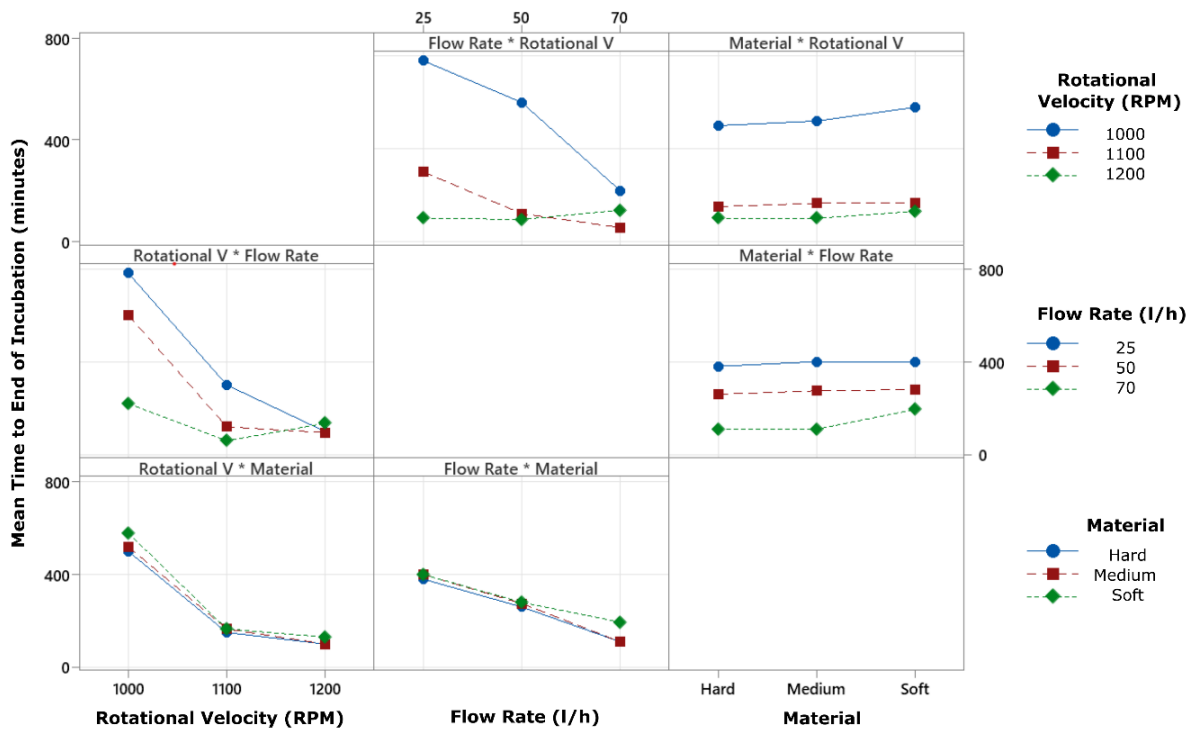


Figure 7.8 – Interaction plots displaying the relationship between each chosen factor A: rotational velocity, B: Flow rate and C: Material.

As the rotational velocity and flow rate were the only significant main interactions, a contour plot can aid in visualising the relationship between the two factors. The contour plot in Figure 7.9 shows how the incubation time relates to the two identified factors based on a model equation. The model is found to explain 99.20 % of the variation in data. The $R^2_{\text{predicted}}$ is 87.63 %, indicating that the model explains 87.63 % of the variation when used for prediction, indicating that the plot is a good prediction when applied to the dataset acquired from testing. The plot clearly demonstrates that rotational velocity has a greater influence on incubation time than flow rate. By referring to this plot, the erosion performance of all three materials can be compared as the material factor was shown to be insignificant ($P > 0.05$).

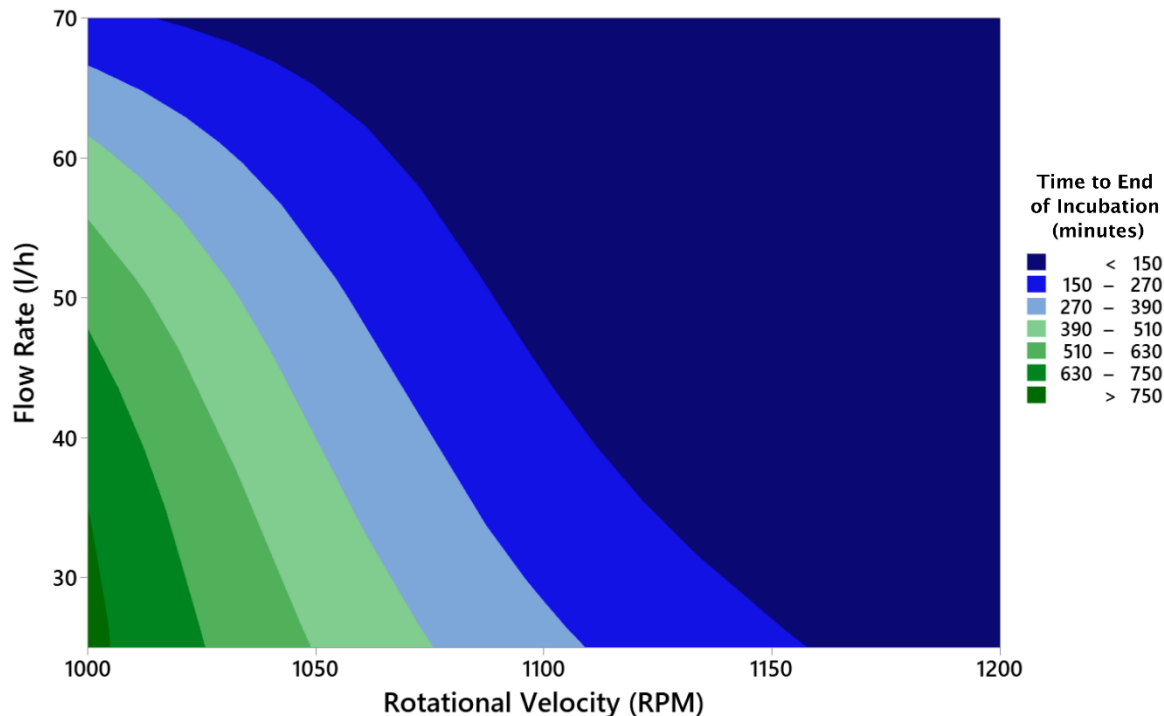


Figure 7.9 – A contour plot of time to end of incubation against flow rate and rotational velocity is presented. The model has a $R^2_{predicted}$ value of 87.63 %, indicating a good fit of the experimental data.

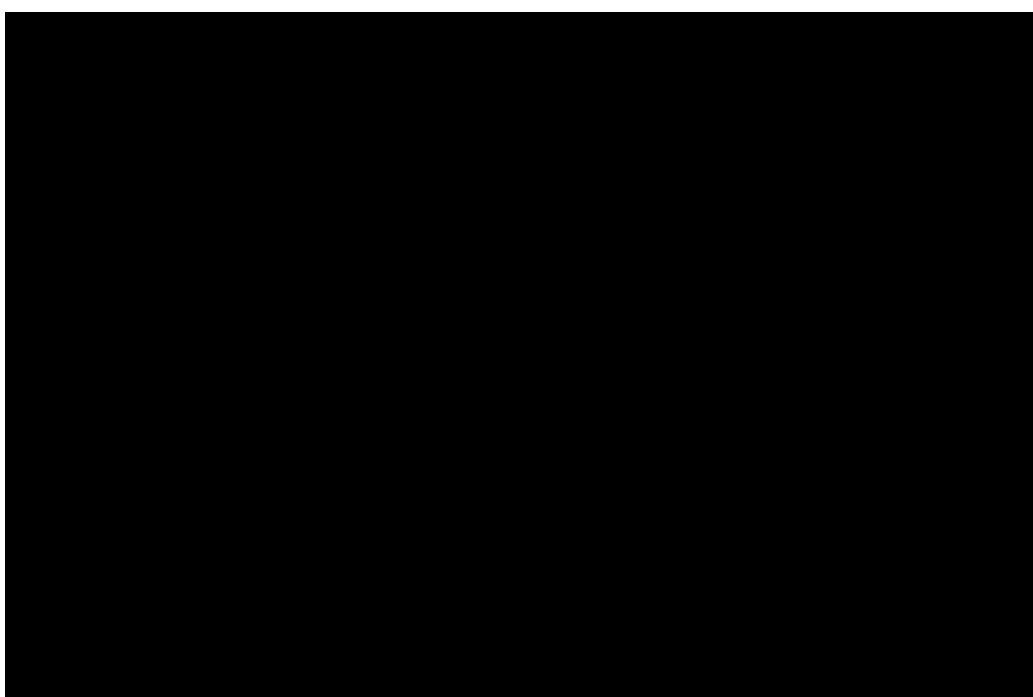
As the rotational velocity is specific to the test rig being used, Table 7.7 is presented displaying a conversion to a more general value of impact velocity that can be more easily compared with other studies. As erosion always started from closer to the high speed tip end in this set of tests it can be generalised that it occurred closer to the reported maximum impact velocity rather than the lower velocities that occur at the lower speed end.

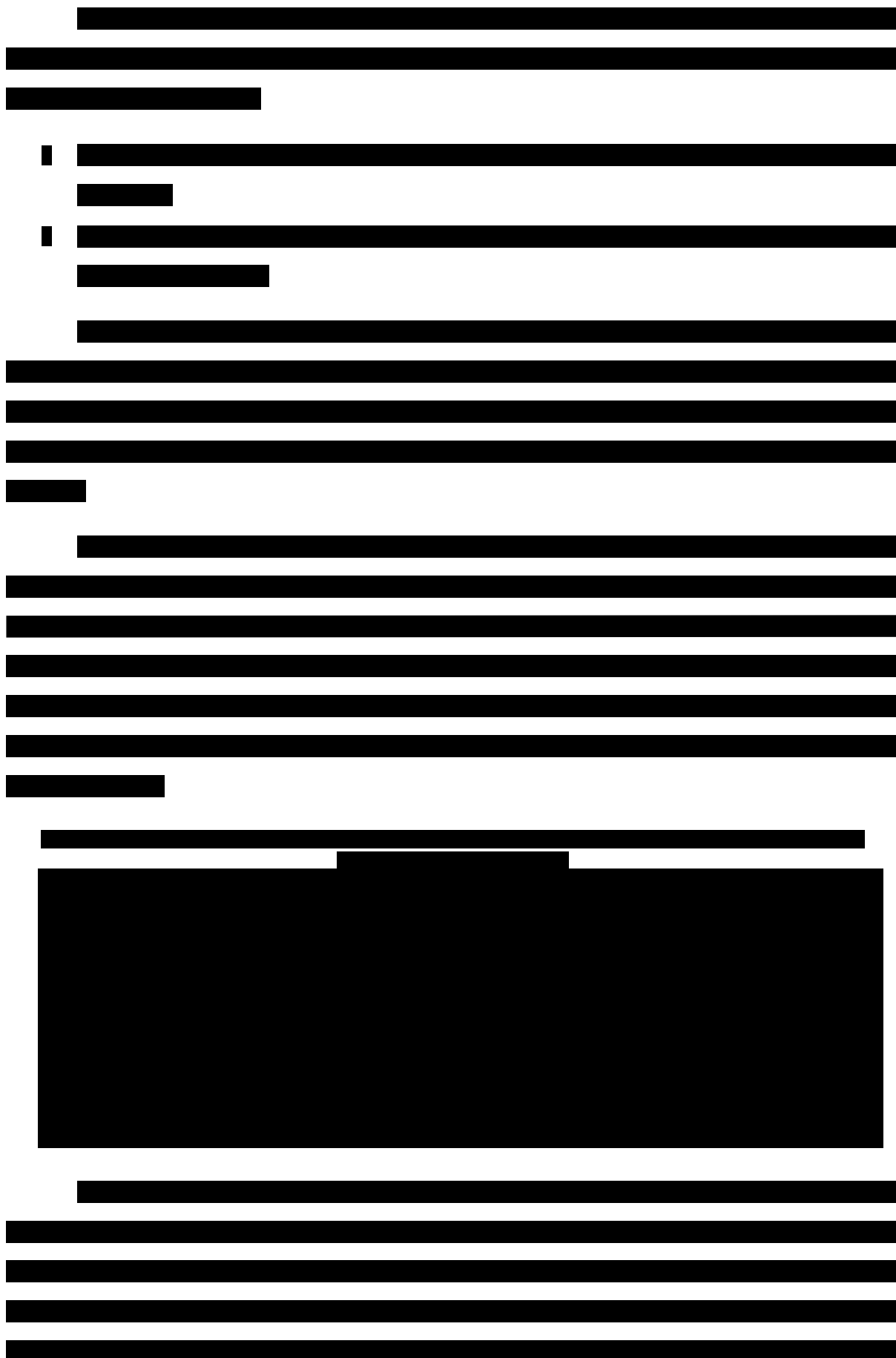
Table 7.7 – Conversion of the rotational velocities used in the design of experiments test to rain droplet impact velocities.

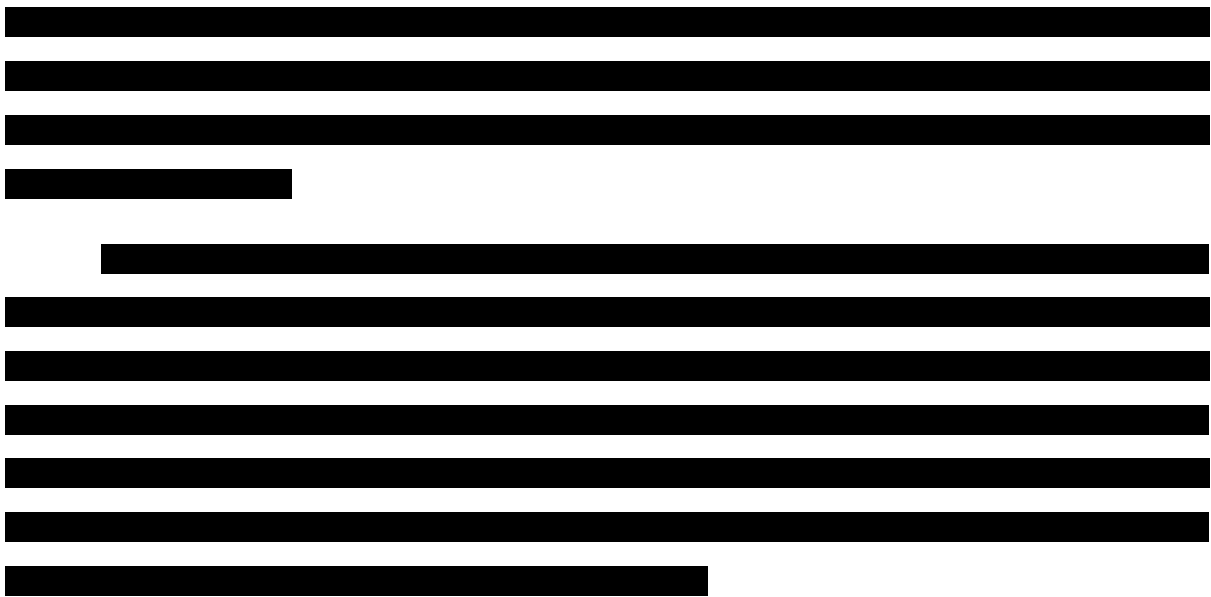
RPM	Impact Velocity (m/s)	
	Minimum	Maximum
1000	85	125
1050	89	131
1100	93	138
1150	97	144
1200	101	150

7.4 Thin Film Testing









7.5 Discussion

The standard RET approach was successfully used to determine the erosion performance of the three systems under the chosen conditions. This allows for a relative comparison of the materials by initially comparing the times to the end of incubation and breakthrough to the composite. The test results showed differing amounts of variability with certain tests resulting in average coefficients of variation of $\approx 28\%$ for the end of incubation and $\approx 22\%$ for breakthrough, both of which could be argued to be higher than standard test methods using simple materials. However, some variability is commonly expected during accelerated testing due to how the material undergoes degradation, with more complex materials highlighting this. LEE is considered a fatigue problem, with test specimens appearing visually unaffected until a level of fatigue degradation is reached at a certain location and the incubation period is reported to end. The author's view is that this approach is very sensitive to the manufacturing defects present in the test specimens³². This was observed in several tests where initial damage sites would occur at locations far from the high-speed end and could be attributed to a visible or underlying defect. To mitigate this, tests are conducted in triplicate to validate observed results through statistical analysis and thorough records of the progression of the erosion throughout the test.

³²There are numerous potential causes of the manufacturing defects, but the most apparent to the author was the repeated use of the material from the same paint tin. Upon repeated opening and closing of each container, the material consistency appeared to change, resulting in an inferior finish than if using an unopened tin. This could be attributed to partial curing during storage that could have occurred due to poor resealing of the single-use tins. This variability is also a significant issue for the coating of turbines in offshore environments where the coating of a blade can be conducted over several days (depending on weather delays).

The standard testing approach is still a relative comparison between materials under a set of specific test conditions. While there are test conditions considered more suitable due to the resulting impact velocities, correlation to in-situ performance still proves challenging [108, 121]. Instead, using VN curves allows for numerous data sets, including multiple test conditions to be combined to create a curve that can be used to compare material behaviour over a wide range of impact velocities. While in this work, a clear difference was observed between coating materials, it has been observed to be less straightforward in other cases. This can be attributed to the assumption that the number of impacts to failure is only a function of the droplet impact velocity. Therefore, this curve fitting approach does not capture information regarding the failure mode that the material undergoes or the effect of increased impact frequencies. The latter is particularly important as it has been identified that not only do viscoelastic materials require a period of time to recover any deformation (Chapter 5) but also that higher strain rates result in variable material properties (Chapter 6), both of which could be amplified by constructive interference of droplets. The influence of material properties on erosion performance is discussed further in Chapter 8.

A DOE approach was implemented in this work to maximise the amount of data gathered from these tests and minimise the number of tests required. This alternative approach uses a more systematic approach to conducting a test campaign allowing for the influence of each factor of interest and their interactions to be quantified. Furthermore, the need for repeat experiments can be eliminated as the experiments obtain information on all factors from each test, allowing for identifying any outliers and statistical comparisons to be conducted. This approach can be easily implemented into the current test programs and should, in the author's view, be conducted on all commercial materials to allow for an improved understanding of material behaviour over a wider range than the standard approach currently allows.

As previously highlighted, the specimens tested did show clear signs of delamination failure during testing, which may have influenced the results. These failures could have affected the coating of the interface or exacerbated the damage due to the moisture ingress into the underlying layers. However, it was observed that in all but one of the tests, the delamination did not appear to affect the leading edge and allowed for the end of incubation and progression of erosion to be captured.

The first factor to be discussed is the difference in coating material used within the test. As previously mentioned, materials of similar composition but with varying material properties were requested and supplied. However, the manufacturer could not disclose the exact difference in material composition, and, as a result, direct links to be made to material structure could not be

made³³. Through qualitative analysis, it was found that clear differences were seen between the materials compared to the LEP A3 material used in previous chapters. As the name suggests, the hard material appeared to be stiffer (upon bending) and harder (more resistant to indentation). Conversely, the soft material appeared to be the most compliant and the softest of the three materials. For DOE testing, numerical values are preferred as inputs for the levels within a factor, allowing for functions to be created relating the data to the measured parameter. This function would allow for the extrapolation of data and aid in interpreting the impact of the factor. However, this is not possible due to the categoric material types; instead, only basic trends can be observed for this factor rather than functions explaining the material response. In future work, this should be linked to a measured numerical variable which opens up the possibility of linking it to either material properties or the chemical composition, e.g. chain length allowing for links to be drawn from the molecular level to the system level.

Tensile test data for the two variant materials was provided by the manufacturers and is presented in Table 7.9. These results were obtained using larger specimens and at a considerably higher strain rate than used in Chapter 4 and as a result the measured values may not be comparable as there could be strain rate dependency at these high strain rates as observed with other materials in Chapter 6. Nevertheless, the results show that the soft variant possessed considerably greater *STB* and *UTS* values with significantly lower *E* values.

Table 7.9 – Tensile test data provided by coating manufacturer for comparison. Tests were conducted at a displacement rate of 100 mm/min, under a pretension of 0.1 N using cast samples of 36 mm x 6 mm x 2 mm (N=2).

	Ultimate Tensile Stress (MPa)	Strain To Break	Youngs Modulus (MPa)
LEP A4 (Soft)	28.59 ± 0.93	5.25 ± 0.22	5.2 ± 0.04
LEP A5 (Hard)	18.86 ± 0.96	3.01 ± 0.05	65.75 ± 3.35

³³ The choice to use these materials was to ensure that the work used industrially relevant materials to produce data relevant to modern coating materials used in the field. However, taking this approach comes at the cost of not knowing the exact compositions of the materials used. This issue is not unlike what occurs during commercial RET studies, where samples are submitted with minimal information meaning the operator cannot use prior knowledge to inform their observations and conclusions from each test.

DMTA was also used to analyse the material behaviour following methodologies detailed in Chapter 6 to identify the difference between them. Figure 7.11 displays the E' and E'' values obtained using the TTS principle. As expected, the E' of the Soft material was consistently lower at all frequencies, especially below 10^3 Hz, where the difference was considerable, correlating with the observed compliant behaviour. The Medium and Hard material E' values followed appear similar with Hard > Medium below 10 Hz. Above this frequency, the medium material E' appears to be marginally higher. The E'' moduli followed a similar trend following a similar order of Medium > Hard > Soft.

Figure 7.12 displays the $\tan \delta$ values for each material over a range of frequencies. This value is a ratio of the E'' to E' and is linked to the ability of a material to dissipate energy, commonly considered to be a desirable property. It can be seen that $\tan \delta$ values for each material decreased as a function of frequency in the order of Medium > Soft > Hard, apart from above 10^5 Hz, where the order becomes Medium > Hard > Soft.

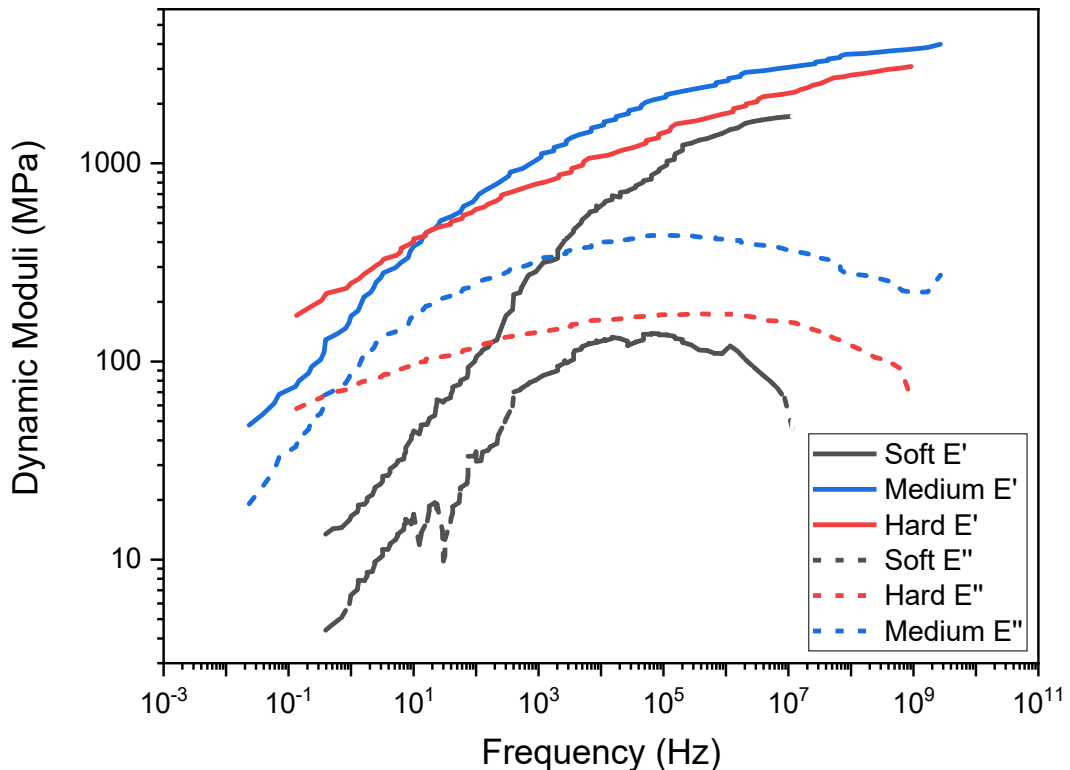


Figure 7.11 – Comparison of storage and loss moduli from dual cantilever master curves generated frequency sweeps calculated for a reference temperature of 20 °C using an amplitude of 0.1% strain. Medium was at -40 °C to 30 °C, Hard (B) is -40°C to 30 °C and strain, and Soft is -40°C to 30 °C. Each curve is smoothed using a 25 point adjacent averaging method.

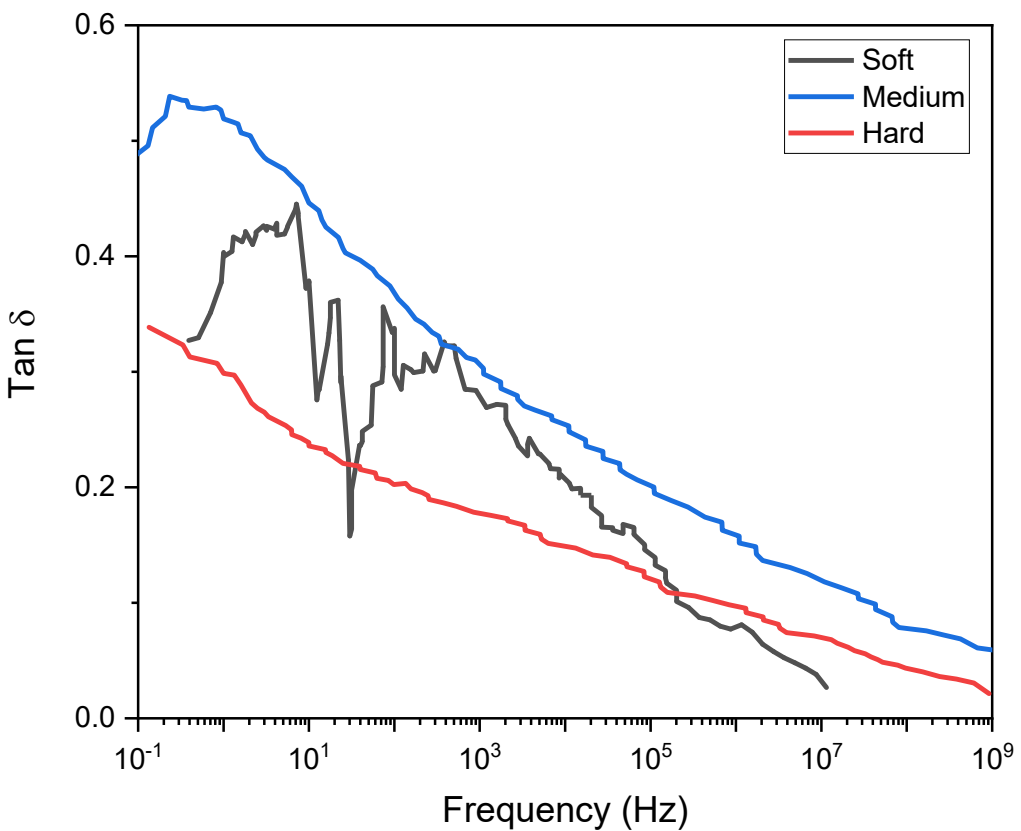


Figure 7.12 – Comparison of $\tan(\delta)$ from dual cantilever master curves generated frequency sweeps calculated for a reference temperature of 20 °C using an amplitude of 0.1% strain. Medium was at -40 °C to 30 °C, Hard (B) is -40°C to 30 °C and strain, and Soft is -40°C to 30 °C. Each curve is smoothed using a 25 point adjacent averaging method.

The change in material did show slight variations in the time to the end of incubation, with the softer materials appearing to have improved erosion performance. However, upon further analysis, these were determined to be statistically insignificant ($P > 0.05$), making it difficult to correlate any changes in performance to results obtained from the DMTA. Instead, it is only possible to speculate that the materials were not dissimilar enough to discern a significant difference between each material's performance³⁴.

The second factor tested was the rotational velocity, which is commonly reported as the most influential parameter in measuring the erosion performance of a coating system. This observation is reflected in VN curves which assume that the number of impacts to the end of incubation is only a function of the impact velocity. This explains why erosion begins close to the high-speed tip in many tests rather than in areas closer to the root. As a result, tip speeds of in-situ turbines are commonly limited to extend the lifetime of current coating solutions. The findings from the DOE campaign were shown to correlate with these observations showing that the effect of rotational velocity on the end

³⁴ The author does appreciate that there are limitations to how much a coating system can be varied as it must maintain adequate mechanical performance, be suitable for processing, and form a coating with minimal defects to be useable as a coating.

of incubation time was $\approx 50\%$ greater than the next important parameter flow rate. The author identifies this as the first quantifiable observation of how much more of an influence this factor is over other test parameters such as flow rate.

The third factor is the flow rate, which adjusts the speed at which droplets are produced at open needles. A greater flow rate increases the number of droplets produced, increasing the droplet impact frequency. This factor was the second most influential parameter in the erosion performance of the tested coatings and could be linked to the varying rainfall intensities observed offshore. This finding is important as while current methods such as VN curves take the changes in impact velocity into account, they do not capture the effects of greater impact frequencies which appear to be a significant factor ($P < 0.05$). As the LEP materials tested have shown considerable viscoelastic behaviour changes to flow rate and subsequent impact frequency could provide an explanation for the reduction in erosion performance. Viscoelastic materials are known to recover elastic deformation upon the removal of stress with the time taken for this to occur dependent on the chemical composition and the temperature of the material [134]. Further studies around the recovery times of each material under varying conditions is required to understand to what extent this behaviour can influence erosion performance.

A further benefit of utilising the DOE approach is that any combined effects can be identified and quantified. From this test, it was found that the combined effects of rotational velocity and flow rate were almost as influential as the single flow rate factor. This observation implies that increases in the impact velocity and impact frequency have synergistic effects that can further reduce the time to the end of incubation. The reason for this behaviour could be attributed to the viscoelastic behaviours that include strain rate dependence and deformation recovery, which, as seen in Chapters 4, 5 and 6, varies considerably between materials and under different loading conditions.

7.6 Summary

This chapter utilised accelerated rain erosion testing to quantify the erosion performance of the coating systems used in the thesis. A conventional test approach was initially utilised, allowing for relative comparisons of each coating system under different test conditions. Clear differences in erosion performance were observed from the observed failures and trends extrapolated using VN curves. As expected, all materials showed worse erosion performance under the test conditions with higher rotational velocities. This approach, however, only allowed for relative comparison of materials, and from the small data set, influences of individual parameters could not be discerned. To achieve this using the conventional methods, ‘a one factor at a time’ approach would be required, which would require a considerably greater amount of test time.

A further development of the method was also presented using a novel thin film test approach to examine the changes in material behaviour as a result of exposure to accelerated RET testing. This trial suggested considerable decreases in both the quasi-static and dynamic material properties as a result of accelerated rain erosion testing.

To maximise the amount of information gained from RET testing, a novel DOE approach was designed and employed to reduce the number of tests required and allow for the influence of individual and combinations of test parameters to be quantified. The test campaign successfully quantified the individual and combined influences of the rotational velocity and the flow rate, two of the commonly varied parameters used in accelerated RET testing. The findings highlighted a shortfall of the VN curve approach, which only takes into account change in rotational velocity and neglects other contributions which were shown to be significant in this work. The use of the novel DOE approach demonstrates that it is possible to design a more efficient test program that can provide information about the materials over a wider range of test conditions. This approach can be implemented with no changes to the current test setup and used within further academic research or offered as part of commercial test campaigns to provide customers with considerably more data than in conventional test approaches.

With the erosion performance of the coating materials determined, Chapter 8 aims to discuss the trends seen throughout the characterisation of the materials correlating these to the measured erosion performance.

8

Discussion

This chapter provides a comparison of the measured material properties from Chapters 4, 5 and 6 to the accelerated rain erosion testing results from Chapter 7. Trends were observed between individual parameters, and the implications on the multilayer system level are discussed.

8.1 Single Parameter Correlations To Erosion Performance

Chapters 4, 5 and 6 presented the results and a thorough discussion of several test methods used to characterise each coating material to find quantifiable differences. This current chapter aims to identify if any measured/calculated material properties correlate with the relative erosion performance detailed in Chapter 7 and if the findings agree with the current literature. While it is not feasible to compare every parameter within this thesis, key findings are highlighted, and their potential importance is discussed.

The work detailed in Chapter 7 allowed for the relative erosion performance of the coating systems to be determined from accelerated rain erosion testing. Using the VN curve approach³⁵, shown in Figure 7.3, it was calculated that at impact velocities below 140 m/s, the material performance was LEP A3 > LEP B4 > LEP3. The specific number of impacts to incubation (N_i) between these materials was calculated to increase as the impact velocities decreased.

Initially, a qualitative approach of comparing observed trends was used to speculate which material properties correlated with improved erosion performance. A quantitative approach was then used to fit the data confirming the sign of the correlation (positive or negative) and determining the linear correlation coefficient (R^2) for each observed trend. Due to the nature of the data, correlations were drawn from three points, resulting in somewhat poor resolution making it challenging to identify with any certainty which type of trend was being observed *e.g.* linear or quadratic. This reduced number of points also made the R^2 values very sensitive to changes in the midpoint between the two extreme values. Therefore, the comparison presented in this section should be considered qualitative.

The author acknowledges that correlating single parameters is a simplified approach. It is undoubtedly a complex problem that needs to be addressed at the system level accounting for the interaction between each material³⁶. Nevertheless, this comparison is an acceptable starting point and allows for speculative trends to be identified.

8.1.1 Tensile Testing

The thin film tensile testing campaign results are detailed in Chapter 4. The test method is commonly used as a relatively simple and quick quasi-static characterisation method to capture basic material

³⁵ While this approach aims to provide an indication of in-situ performance, currently there is no thoroughly validated method to relate test results to in-field erosion performance during its complete lifetime.

³⁶ GFRP composite test specimens were used for all tests as a standardised substrate. However underlying coating layers were not standardised, with each system using its respective complete system to coat the specimen. While it would have been beneficial to standardise everything but the LEP layers to minimise the number of variables, it would also have increased the risk of incompatibilities between materials due to poor adhesion and made the results less commercially applicable.

properties. While the complete datasets and interpretation of the results are available in the relevant chapters, a summary of the key parameters and their relative order are presented below³⁷:

Strain to Break (*STB*) – LEP A3 > LEP B4 \approx LEP B3

Ultimate Tensile Strength (*UTS*) – LEP B3 > LEP B4 > LEP A3

Toughness – LEP B3 > LEP B4 > LEP A3

Modulus (*E*) – LEP B3 > LEP B4 > LEP A3

Clear repeating trends that match the order of relative erosion performance can be seen for all but the *STB* parameter, in which the LEP B4 and LEP B3 were not found to be significantly different ($P > 0.05$).

The results indicate that the materials with a higher *STB* have improved erosion performance ($R^2 = 1.00$). Higher values indicate that a material is more deformable, whereas low values indicate that a brittle material is less able to elongate before failing. This finding agrees with current literature that reports that more compliant materials possess improved rain erosion performance due to their ability to undergo different failure modes [34, 129, 130, 138].

The UTS values indicate that a lower value is beneficial for erosion performance ($R^2 = 0.87$). This finding was unexpected as this is a key material input in the most accepted erosion model presented by Springer [72, 86]. The model suggests that higher *UTS* values result in greater material strengths, calculated from Equation 2.5, improving erosion performance. Instead, the increase in *UTS* in this work correlates with a reduction in relative erosion performance, implying that it is not suitable to solely use *UTS* values to predict performance.

Materials with higher toughness values were found to have worse erosion performance ($R^2 = 0.81$). This parameter is generally considered desirable as higher values imply that a material can absorb more energy before rupturing. This unexpected trend can be explained as high toughness materials require materials to withstand high stresses and strains. During a rain droplet impact, it is reported that a material undergoes low strains and high stresses (due to the water hammer phenomenon) [72, 86]. The LEP A3 material has the highest *STB* values and the lowest *UTS* values, resulting in lower toughness but the best erosion performance. This finding indicates that toughness measured through tensile testing cannot solely be used to predict erosion performance directly; however, it can be used as a metric to compare the suitability of the material as an engineering material for the desired application.

³⁷ While the use of tensile testing provides interesting correlations under these conditions these result may vary significantly we tested at high strain rates.

The E values indicate that a lower value is beneficial for erosion performance ($R^2 = 0.91$ for E_{tan} method and $R^2 = 0.84$ for the E_{sec} method), agreeing with the reported literature [114]. These values are also used within the Springer lifetime prediction model, with lower values typically improving erosion performance as they are reported to reduce the impact pressures, as detailed in Section 2.4 [72, 86, 136].

8.1.2 Nanoindentation

The nanoindentation test campaign results are detailed in Chapter 5. The method utilises a specialist method to apply a low strain rate deformation to each coating material while recording the material response. Three key measured parameters for comparison to the measured erosion performance are summarised below:

Reduced modulus (E_r) – LEP A3 > LEP B4 > LEP B3

Short term recovery (STR) – LEP B4 > LEP B3 > LEP A3

Plastic work ($W_{plastic}$) – LEP A3 >> LEP B3 > LEP B4³⁸

Contrary to the tensile testing data, the nanoindentation results indicate that an increased E_r is beneficial for rain erosion performance ($R^2 = 0.84$)³⁹. This value is related to the indentation modulus through Equation 3.4; however, as the Poisson's ratio (ν) for the materials was unknown, the actual E value could not be determined. Instead E_r values should be considered to have wider error ranges to account for the potential differences arising from differing ν values⁴⁰.

The STR results indicate that a higher value correlates to lower erosion performance, contrary to current literature ($R^2 = 0.86$)³⁹ [60, 128]. However, it should be noted that the measurement of STR is dependent on the test parameters and environmental conditions. As the material being tested in this work are considered viscoelastic their behaviours are both time and temperature-dependent. It is possible that by conducting the tests at different temperatures and over longer periods, the STR values can differ, and as a result, comparisons should mainly be conducted between data testing using the same methodology and under the same conditions. It is also important to consider that these results were correlated to accelerated testing which is known to be different from the conditions in situ where rain is more variable in size, speed and frequency.

³⁸ The trend shown is from the test 1 (Section 5.3.1) where the LEP B4 value is considerably higher than measured in test 3 (Section 5.3.3). The difference demonstrates how different test parameters can affect the measured response. Nevertheless in both tests the LEP A3 material $W_{plastic}$ values were the highest correlating with superior erosion performance.

³⁹ R^2 value calculated from data in test 1 (Section 5.3.1).

⁴⁰ The difference between E values using ν values of 0.3 and 0.5 was found to be approximately 20 %.

The measurement of the work distribution of the LEP materials response was a novel approach to characterisation. The two best-performing coatings, the LEP A3 and the LEP B4, were found to be similar displaying high $W_{plastic}$ values indicating a predominately plastic response. The LEP B3 response was considerably different, displaying a predominantly elastic response. From these data, it is possible to speculate that materials with predominately plastic work are correlated to increased erosion performance ($R^2 = 0.93$)³⁹. This was an interesting result as it is commonly thought that plastic deformation was detrimental to the erosion performance of a coating system. Instead the ability of a material to undergo plastic deformation may provide an alternative mechanism to delaying the failure of the material. As this is a novel approach to testing LEP materials, no direct comparisons are available in the literature, but with the data and methodology presented in this thesis, comparisons can be made in the future to confirm these correlations.

8.1.3 Dynamic Thermal Mechanical Analysis

The DMTA testing campaign results are detailed in Chapter 6. The test method is thought to be commonly used to characterise the dynamic and thermal properties of a wide range of materials, including coatings. However, it is challenging to directly compare the erosion performance and the results from testing due to the wealth of data produced as a result of three main reasons:

- The DMTA method itself has many different types of tests that can be conducted, each of which has a wide range of variable parameters. As a result, appropriate test methodologies must be selected to ensure that results are valid for the selected approach (e.g. staying within the LVER), applicable to the issue of LEE, and produce data comparable to other materials.
- Due to the viscoelastic character of the coating material being tested, results are not only single values. A response of coating material can vary as a function of temperature or strain rate and, as a result, gives a range of results that need to be captured to understand the material behaviour.
- The final point is that, unlike other test methods that produce values commonly used in engineering applications, e.g. E , those reported in DMTA are more complex and require further data processing and interpretation.

The first two parameters to be compared are summarised below⁴¹:

$$\text{Critical strain } (\varepsilon_c) - \text{LEP B4} \approx \text{LEP B3} >> \text{LEP A3}$$

$$\text{Yield stress } (\sigma_c) - \text{LEP B3} >> \text{LEP A3} \approx \text{LEP B4}$$

⁴¹ The values used are from the dual cantilever testing (Section 6.2) but general tends also apply to the results obtained using thin film tensile testing.

It is the authors opinion that the σ_c value is the more important value of the two. This is because it is currently thought that a rain droplet impact only causes small strains to the coating. An example of this is presented by Keegan who defines 0.379 as the maximum strain that occurs during a rain droplet impact (60° impact angle, 100 m/s and 3 mm droplet diameter) [67]. Conversely due to the water hammer phenomenon considerable tensile stresses are experienced by the coating that are thought to lead to damage meaning that σ_c could be considered more important [86].

The ε_c for the LEP A3 material was considerably lower than for the LEP B3 and LEP B4 materials. This finding correlates to the *STB* values measured through tensile testing and implies that materials that can withstand high strains with minimal plastic deformation are beneficial to erosion performance agreeing with the reported literature ($R^2 = 0.99$)⁴¹ [34, 129, 130, 138].

The σ_c showed an unexpected trend, with the materials with the best erosion performance displaying the lowest values⁴¹ ($R^2 = 0.22$). However, the trend had a low R^2 value implying a lower level of confidence in this result than the others identified trends. This finding implies that plastic deformation at high stresses, like those caused by the water phenomena, may provide a beneficial alternative mechanism that improves rain erosion performance. This mechanism can mitigate excess energy by undergoing irreversible changes to the microstructure of the system [126].

A key finding from the DMTA campaign was identifying and quantifying each material change in behaviour as a function of temperature and frequency/strain rate. These changes are commonly not considered when designing and testing LEP systems. The author's opinion is that it is an essential area that needs to be developed to understand LEE further.

The strain rate dependent behaviour of the coating material was characterised; however, it is challenging to provide a simple comparison as it varies depending on the strain rate of interest. A metric that allows for straightforward visual comparison is the specific damping capacity (φ), calculated using Equation 6.5, which compares the ability of each material to dissipate energy. The results from the dual cantilever testing are summarised below:

Below 10^6 Hz (10^3 s⁻¹) – LEP B4 > LEP B3 >> LEP A3

Above 10^6 Hz (10^3 s⁻¹) – LEP A3 > LEP B4 > LEP B3

The results present an interesting change in behaviour around the 10^6 Hz value. Below this value, the order of erosion performance does not correlate with measured ψ values. However, above the 10^6 Hz value, the order of φ values matches the measured erosion performance of the materials. This behaviour was also observed in the thin film DMTA tests, with the LEP A3 material possessing the highest φ values above 10^6 Hz. This indicates that materials' damping properties vary as a function of

strain rate and may directly affect the erosion performance of each material at higher strain rates ($R^2 = 0.88$), agreeing with reported literature [60, 72, 110, 134–136, 138, 141]. The 10^6 Hz value is calculated to be a strain rate in the order of $\approx 10^3 \text{ s}^{-1}$, which is considerably lower than some of the predicted strain rates caused by droplet impacts in the literature [67]. This threshold value can also be related to a phenomenon observed during accelerated rain erosion testing (Chapter 7), where more brittle failure modes are seen at greater rotational velocities, resulting in higher impact velocities. However, these observations all utilised a reference temperature of 20°C , which was comparable to the accelerated RET testing setup. Conducting these tests at different temperatures would change the material behaviour at each strain rate by shifting the responses relative to the chosen reference temperature while maintaining the same overall behaviours.

8.2 System-Level Correlations to Erosion Performance

Chapters 5, 6, and 7 demonstrated that material behaviours such as UTS , E and the speed of sound (C_L) can vary as a function of both temperature and applied strain rate. In order to explore the potential effect of varying C_L through conducting a parametric analysis using the equations presented by Springer [111, 114]. It considers the interactions between each LEP when coated on a substrate. In this case, GFRP substrates are used, which are assumed to have identical material properties to allow for comparison.

The performance of a material is commonly calculated by using the Corrected Number of Impacts to Failure (N_{IC}) which accounts for the droplet pressure waves interacting with a coating on a substrate [111]. This value is calculated by

$$N_{IC} = \frac{8.9}{d^2} \left(\frac{S_{ec}}{\bar{\sigma}^o} \right)^{5.7} \quad 8.1$$

where d is the droplet diameter, S_{ec} is the effective material strength (Equation 8.3) and $\bar{\sigma}^o$ is the average impact pressure (Equation 8.2). From this equation, it is clear that materials that possess high S_{ec} values and result in lower $\bar{\sigma}^o$ values are more favourable for increasing erosion performance according to the current understanding. The following sections explore the impact of C_L on the input parameters and the resulting N_{IC} .

8.2.1 Average Impact Pressure

The first parameter to be evaluated is the average impact pressure ($\bar{\sigma}^o$) caused by a droplet impact which is calculated by

$$\bar{\sigma}^o = \frac{1+\varphi_{sc}}{1-\varphi_{sc}\varphi_{Lc}} \left[1 - \varphi_{sc} \frac{1+\varphi_{Lc}1-e^{-\gamma}}{1\varphi_{sc}\gamma} \right] P \quad 8.2$$

where P is the water hammer pressure (calculated from Equation 2.2), \bar{k} is the number of wave reflections, γ is the ‘linking’ equation and φ_{xy} are relative impedances between different mediums⁴².

The $\bar{\sigma}^0$ values presented in Figure 8.1 were calculated using a range of C_L values and using the input values for each material and droplet impact conditions which are detailed in Table 8.1 and Table 8.2, respectively. This approach is considered as first order as it uses individual material properties of only the substrate and LEP omitting the effect of other layers that can be present such as fillers, topcoats or adhesion promoters.

Table 8.1 – Material input parameters used in average impact pressure and effective material strength calculations.

Material Inputs						
	Measured Speed of Sound (m/s)	Density (kg/m ³)	Thickness (mm)	Ultimate Tensile Strength (MPa)	Fatigue Constant	Poisson’s Ratio
LEP A3	1503	1160	1	0.5	20.9	0.3
LEP B3	1801	1140	1	2.4	20.9	0.3
LEP B4	1744	1140	1	1.7	20.9	0.3
Substrate	2392	1930	-	-	-	-
Droplet	1463	1000	-	-	-	-

Table 8.2 – Droplet impact input parameters used in average impact pressure and effective material strength calculations.

Droplet Impact Inputs	
Velocity (m/s)	115
Droplet Diameter (mm)	2.4

The current approach for predicting $\bar{\sigma}^0$ values commonly utilise constant parameters for values such as C_L . The values calculated using this approach are displayed as coloured squares in Figure 8.1. It can be observed that under the same impact conditions, the values follow the order of LEP B3 > LEP B4 > LEP A3, in agreement with the earlier ranking of erosion performance. This finding supports the current understanding that lower impact pressures are beneficial as they result in greater N_{IC} values (Equation 8.1) and therefore greater predicted erosion performance.

⁴² Further details available in literature [86, 111].

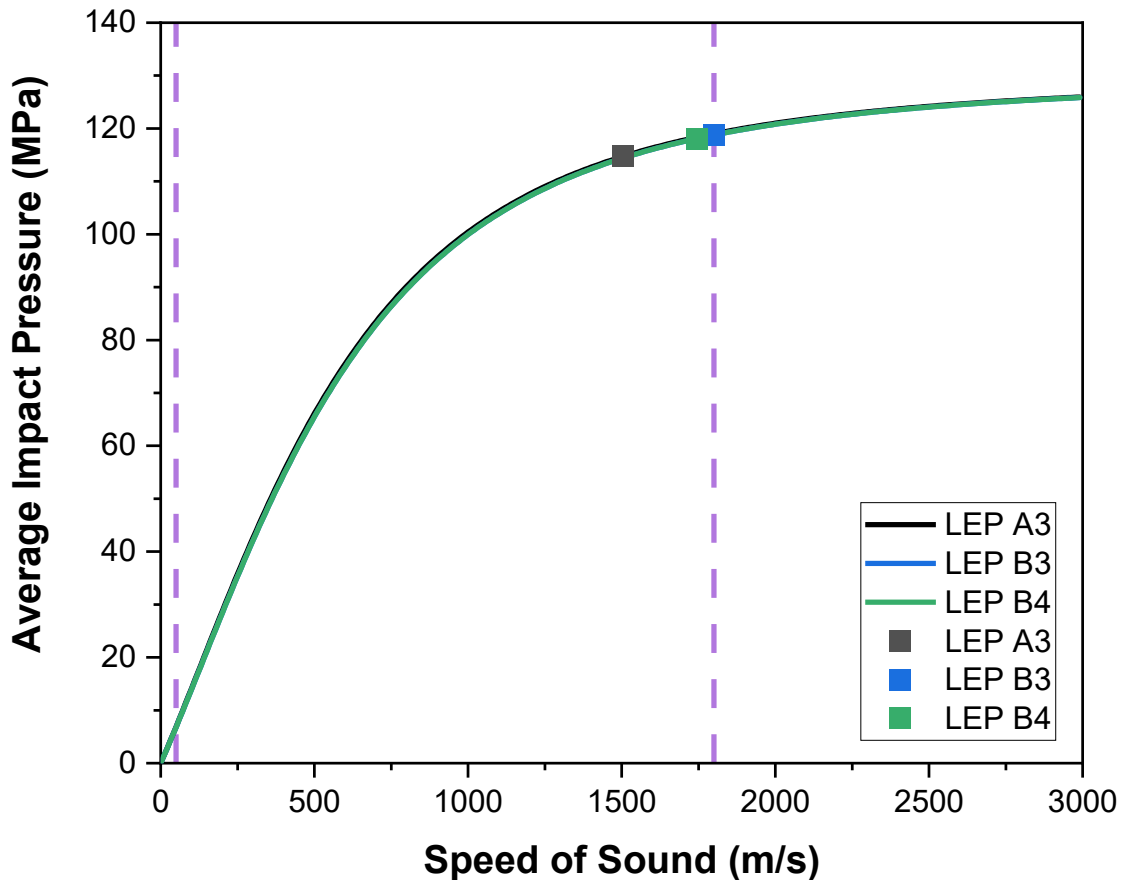


Figure 8.1 – A parametric analysis of the effect of varying the speed of sound on the predicted average impact pressure using the Springer approach [111, 114]. The solid lines that overlap indicate the predicted values for LEP A3 (black), LEP B3 (blue) and LEP B4 (green). The coloured squares indicate the calculated value using each respective speed of sound measurement obtained using ultrasonic acoustic testing (Chapter 6). The purple dashed lines indicate the range of speed of sound values predicted from DMTA (Chapter 6).

The response for all the parametric analyses (solid lines) show that $\bar{\sigma}^o$ values are lower at decreased C_L values. A positive linear relationship is observed between 1 m/s and 500 m/s, at which the response plateaus. Interestingly due to the small difference in material properties, no considerable differences were observed between the materials when using the same substrate and impact parameters. This observation is important as in Chapter 6, the predicted C_L of each material was calculated to vary as a function of strain rate and temperature. The measured values were found to range between ≈ 50 m/s to ≈ 1800 m/s, corresponding to $\bar{\sigma}^o$ values of 7 MPa and 119 MPa. At the extreme values, this could result in a 177 % variation in the resulting impact pressure and would significantly affect the performance of the coating material or the accuracy of any predictions.

8.2.2 Effective Strength

The second parameter to be evaluated is the Effective Strength (S_{ec}), which accounts for both the measured material parameters and the difference in acoustic properties between materials. The S_{ec} values for each coating material are calculated by

$$S_{ec} = \frac{1}{1 + 2\bar{k}|\varphi_{sc}|} S \quad 8.3$$

where S is the material strength (Equation 2.5), \bar{k} is the number of wave reflections and φ_{sc} is the relative impedance between the substrate and the coating⁴³.

The resulting S_{ec} values were calculated using a constant C_L parameter (measured using acoustic testing) and are presented as coloured squares in Figure 8.2. Unlike the $\bar{\sigma}^0$ values clear differences are observed in S_{ec} values for each material. The order of values was LEP B3 > LEP B4 > LEP A3, correlating with the increase in UTS values required as an input in Equation 8.2.

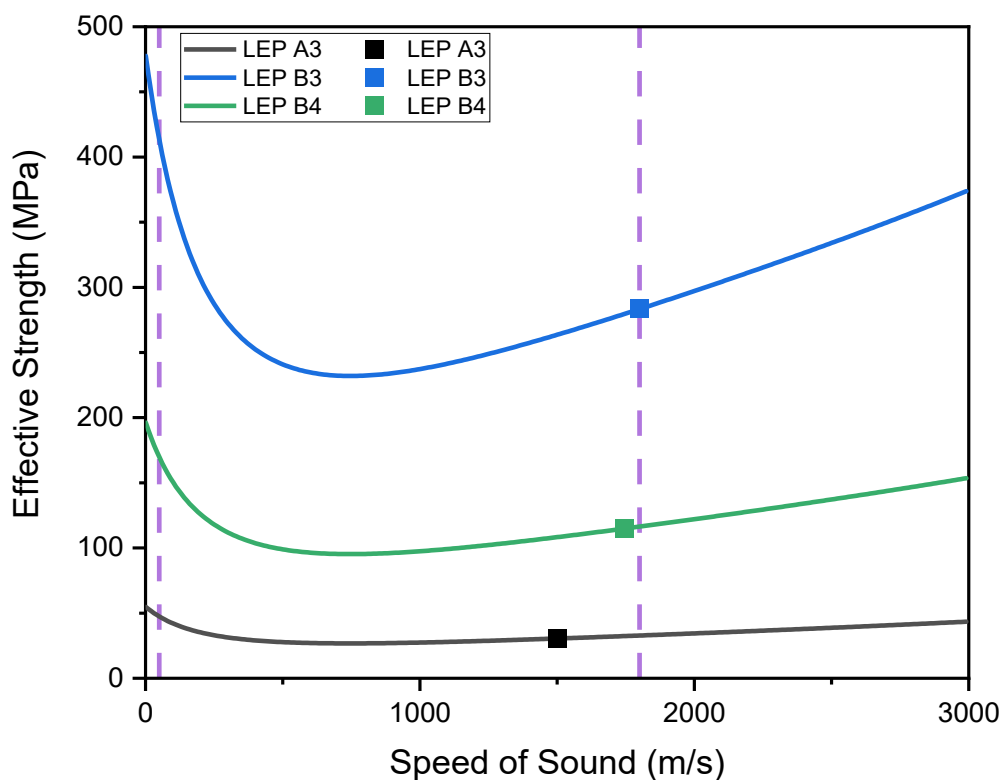


Figure 8.2 – A parametric analysis of the effect of varying the speed of sound on the predicted effective material strength using the Springer approach [111, 114]. The solid lines indicate the predicted values for LEP A3 (black), LEP B3 (blue) and LEP B4 (green). The coloured squares indicate the calculated value using each respective single speed of sound measurement obtained using ultrasonic acoustic testing. The purple dashed lines indicate the range of speed of sound values predicted from DMTA (Chapter 6).

⁴³ Further details available in literature [86, 111].

As with the $\bar{\sigma}^0$, it can be seen the S_{ec} also varies as a function of C_L . The response for all the parametric analyses in Figure 8.2 (solid lines) shows that S_{ec} values follow a negative parabolic curve with the higher S_{ec} values around the lower and upper C_L values. This shape is a result of the changes in the relative acoustic impedances that occur as the C_L values are varied and would be different if an alternative substrate was used. Within the ≈ 50 m/s to ≈ 1800 m/s values predicted from Chapter 7 considerable difference in S_{ec} values were observed. The most apparent difference was observed in the LEP B3 material, with the calculated values ranging from 412 MPa and 232 MPa. The LEP B4 material was found to have values ranging from 169 MPa to 95 MPa. The LEP A3 material which possessed the lowest S_{ec} values was found to have values ranging from 47 MPa to 27 MPa. As the S_{ec} values are key in determining the N_{IC} values, these variations would considerably vary the predicted erosion performance.

8.3 Summary

This chapter correlated results from accelerated rain erosion testing to those of measured material parameters, identifying several speculative trends which are summarised in Table 8.3. These are indicative of desirable behaviour that can be used to guide and inform the improvement and design of new coating materials.

Table 8.3 – A summary of the material parameters and their individual correlation to measured erosion performance. Reliability is reported from calculated R² values where values > 0.95 are considered excellent, values below 0.95 and above 0.85 are considered good, and values below 0.85 are considered poor.

Test Method	Material Parameter	Correlation to Erosion	Reliability
Tensile Testing	Strain to Break (STB)	Direct	Excellent
	Ultimate Tensile Strength (UTS)	Direct	Good
	Toughness	Inverse	Good
	Tensile Modulus ($E_{Tensile}$)	Inverse	Good
Nanoindentation	Indentation Modulus ($E_{Indentation}$)	Direct	Good
	Short Term Recovery (STR)	Inverse	Good
	Plastic Work Percentage ($W_{Plastic}$)	Direct	Good
DMTA	Critical Strain (ε_c)	Inverse	Excellent
	Yield Stress (σ_c)	Inverse	Poor
	Specific Damping (φ)	Direct	Good

A system-level approach was also undertaken to evaluate each LEP material coated onto a composite substrate to explore the effects of multilayer interactions. A correlation was found between lower $\bar{\sigma}^0$ and measured erosion performance. Conversely calculated S_{ec} values were inversely correlated with erosion performance. This finding demonstrates how calculating the S_{ec} from material

properties can give unexpected results. Instead, it is common for the S_{ec} value to be determined semi-empirically from erosion test data, avoiding the use of multiple test methods.

While this work provides a thorough characterisation of commercial test materials, a glaring issue in LEE research is the lack of understanding and agreement on the definition of relevant *in-situ* environmental conditions and how they translate into the resulting strain rates. As demonstrated in previous chapters, each coating material was observed to be viscoelastic, resulting in significantly different behaviours as a function of temperature and loading rate. To explore this effect on the predicted erosion performance, the effect of variable C_L values were evaluated. The work demonstrated that material parameters are not constant and vary due to the environmental and impact conditions, a factor not currently accounted for in the understanding of LEE. However, these findings assume that the C_L can vary independently of other material parameters, which is not the case as altering a parameter can change other behaviours. Changes in the C_L values are related to changes in either the E or the ρ values of each material. These two parameters can influence other key parameters, such as mechanical properties (*e.g.* *UTS* and *STB*) or dynamic behaviour (*e.g.* damping performance), both of which have been identified to influence erosion performance in Chapter 2.

It is commonly accepted that while accelerated rain erosion is useful in providing a relative comparison between materials under specific conditions, it is not yet possible to use this data to predict the lifetime *in-situ* accurately. As a result, these observed correlations may not be directly applicable to the offshore environment. However, with accurate knowledge of the offshore conditions, the framework developed within this thesis could be used to bridge the gap. The novel methodologies detailed can be used to capture both the quasi-static and dynamic properties giving a more extensive understanding of material behaviour over a range of conditions, which is particularly important for modern viscoelastic LEP materials. As a result, the influence of changes in material composition material properties can be rapidly obtained, potentially minimising the need for expensive component-level testing.

9

Conclusions and Future Work

This Chapter details the key findings from this thesis and relates them proposed research question defined in Chapter 1. The research contributions to academia and industry are highlighted and key areas of future work that the author suggests should be conducted to close final research gaps and further advance the understanding of LEE.

9.1 Research Question

The research question this thesis seeks to answer is:

What are the key physicochemical properties of modern viscoelastic materials that are affecting their performance as leading edge protection systems, and how can their characterisation be improved?

The research question was found to be valid and relevant to the current issue of LEE that occurs during accelerated testing and on offshore turbines. However, this hypothesis was broad and required a considerable literature review and downselection to find the most suitable approaches to capture the desired behaviour. The question was answered as the work presented in this thesis successfully characterised commercial viscoelastic LEP materials capturing the changes in material parameters using an array of test methods and correlating them to erosion performance.

The research question was answered using a set of aims and objectives, which are reviewed below:

Aim 1 – Detailing the state of the art in the understanding of LEE

- Objective 1.1 – Conduct a review of academic literature surrounding material characterisation.
- Objective 1.2 – Conduct a review of the industrial literature surrounding modern coatings.
- Objective 1.3 – Summarise the literature and identify gaps and directions for further research.

Aim 1 was met as an extensive review of the literature was presented in Chapter 2, which summarises state of the art literature and the current industrial solutions utilised offshore. Several gaps in the literature were identified relating to the characterisation of viscoelastic materials providing direction for the research conducted in this work.

Aim 2 – Material and Method Development

- Objective 2.1 – Determine the relevant commercial materials for use in the project.
- Objective 2.2 – Understand current testing methods used for modern viscoelastic coatings.
- Objective 2.3 – Development of a multi-method/step characterisation methodology.

Aim 2 was met as commercially available materials were selected for testing to allow for data gathered and correlations to be applicable to modern coating solutions used *in-situ*. The BLEER project facilitated collaboration with two coating manufacturers that offered the required material and expertise. Conventional (Tensile testing, Chapter 4) and complex methods (Nanoindentation, Chapter

5 and DMTA, Chapter 6) were modified to capture coating material properties and viscoelastic behaviours.

Aim 3 – Coupon Level Testing

- Objective 3.1 – Individually characterise the different materials used in coating solutions.
- Objective 3.2 – Capture the strain-rate dependent behaviour of each coating material.
- Objective 3.3 – Capture the temperature-dependent behaviour of each coating material.
- Objective 3.4 – Utilise non-destructive ultrasonic testing to characterise each coating material.
- Objective 3.5 – Determine the implications for the coupon level testing on erosion performance.

Aim 3 was met as the strain rate and temperature-dependent behaviours of individual materials used in the chosen coating systems were characterised using several methods, including ultrasonic non-destructive testing to determine the speed of sound of each material. The results from coupon level testing were compared to literature and correlated to the erosion performance of each coating system.

Aim 4 – Component Level Understanding

- Objective 4.1 – Characterise the coating systems under larger-scale test conditions.
- Objective 4.2 – Optimise rain erosion test methodology to improve the amount of data gathered for testing.
- Objective 4.3 – Determine coupon level testing effects on VE and rain erosion performance.

Aim 4 was met as each coating system was subjected to conventional and novel thin film accelerated rain erosion testing in Chapter 7 to determine the relative erosion performance of each system. A novel DOE approach was designed and employed with the RET testing to reduce the number of tests required and allowed for the influence of individual and combinations of test parameters to be quantified. Measured material properties were correlated with erosion performance highlighting key material parameters.

Aim 5 – Modelling and New Design Understanding

- Objective 5.1 - Use knowledge gained from component level studies to comment on full structure in-service erosion performance.
- Objective 5.2 – Identify and discuss how knowledge gained from this work can be applied to in-service conditions.

Aim 5 was partially met as effects of environmental and loading conditions on current prediction models were discussed. However, these were only speculative comments requiring a greater amount of site-specific data to predict the variability in material properties.

Through addressing these aims and objectives, the author believes that significant contributions to the field of LEE have been made through advancements in understanding and improving current test capabilities. The thesis details methods academia and industry can use to characterise materials and compare results to those presented.

9.2 Key Findings

Tensile testing of thin films was successfully used to characterise individual materials used within the chosen coating systems. Results generally agreed with the literature and the Springer prediction model with the materials designed for use as LEPs possessing a high *STB*, High *UTS* and low *E*. This commonly used approach identified the presence of strain rate dependent behaviour in several materials highlighting the limitations of solely using tensile testing to characterise coating materials as these behaviours are not commonly captured.

Nanoindentation of coated specimens was used to characterise individual materials used in selected coating systems exploring the effects of varying loading rate, maximum load, and repeated indentation, each of which can be compared to the varying conditions caused by rain droplet impacts. As with the tensile testing, strain rate dependent behaviour was observed in several materials. The use of different maximum loads resulted in significant differences in the properties of all the materials tested. Clear differences were observed when materials underwent repeated indentation with LEP materials demonstrating the greatest amount of recovery between indents but did show different elastic/plastic work distributions. An alternate method not seen in current LEP characterisation literature of extracting additional information from an indentation load-depth curve was presented and compared with the current *STR* approach. Unlike *STR*, which considers two data points, the new method includes information from all parts of the load-hold-unload curve, making it more sensitive to material differences.

DMTA was successfully combined with the TTS approach to characterise the viscoelastic properties of each coating material over a wide range of strain rates, and temperatures thought to be applicable to LEE. The work details a methodology that can be replicated by coating manufacturers or academics who have access to a suitable DMTA to aid in the design of new coating solutions. A novel comparison of coating properties under tension and bending was conducted, which resulted in considerable differences between the deformation modes, highlighting the importance of using the

correct test to acquire relevant material properties. The damping behaviour of each material was observed to vary considerably as a function of frequency and temperature. As a result, each material response can vary under different loading and environmental conditions, a consideration not commonly accounted for in attempts to understand the erosion performance of coating systems. The data generated in this work was also used to develop a novel approach that compared the predicted results from DMTA to measurements obtained from UNDT. While further method development is required, it was identified that the speed of sound of each material varies as a function of frequency. By obtaining the speed of sound at different temperatures and frequencies via DMTA, it was shown that it is possible to directly incorporate each material's viscoelastic behaviour into current prediction models.

Accelerated rain erosion testing was utilised to quantify the erosion performance of the coating systems used in the thesis. A conventional test approach was initially utilised, allowing for relative comparisons of each coating system under different test conditions. Clear differences in erosion performance between coating systems were identified from the observed failures and trends extrapolated using VN curves. All materials showed worse erosion performance under the test conditions with higher rotational velocities, with LEP A3 consistently demonstrating the best erosion performance. Preliminary testing was conducted using a novel thin film approach that was used to determine changes in material parameters as result of exposure to rain droplet impacts. To maximise the amount of information gained from rain erosion testing, a novel DOE approach was designed and employed to reduce the number of tests required and allow for the influence of individual and combinations of test parameters to be quantified. The test campaign successfully quantified the individual and combined influences of the rotational velocity and the flow rate, two of the commonly varied parameters used in accelerated RET testing.

Several measured properties were found to correlate with the relative erosion performance and are summarised in Table 8.3. System-level correlations to erosion were also made by conducting a parametric study on the effect of varying C_L and combining them with the current Springer methodology. The results highlighted how S_{ec} and $\bar{\sigma}^o$ could vary due to the strain rate and temperature dependencies present in modern viscoelastic materials.

9.3 Research Impact

The collaboration with two industrial partners through BLEER facilitated the use of commercial materials and allowed for the information from this work to be disseminated directly to manufacturers throughout the project. This relationship also allowed manufacturers to comment on the feasibility and relevance of the approaches presented within this thesis. Currently, coating manufacturers must

undertake expensive testing campaigns to identify which materials are best for erosion performance. This approach can be inefficient as current methods utilise iterations of current systems making small improvements that can be costly and generate considerable amounts of chemical waste. More information about each coating material can be gathered by incorporating the approaches detailed within this thesis, allowing for a more rapid and cost-effective development process. The developed methods were disseminated through the thesis, presentations (internally to the WBRH and externally at international conferences), and articles so that academic or industrial readers of the thesis could implement the approaches and compare their results with those presented.

The socio-economic impact of this project, while small, contributes to the advancement of the wind energy sector. Improvements in coating lifetimes reduce the overall levelised cost of energy through reductions in O&M costs estimated to be £1.3 million over a turbine lifetime and could contribute to removing the current limitations on tip speeds imposed by LEE. Overcoming these issues in the fastest-growing renewable technology industry would be a step toward phasing out fossil fuels, replacing them with sustainable sources such as wind and providing a secure energy source, minimising the effects caused by the volatility of the modern energy market.

9.4 Future Work

To improve any future experimental work based upon this thesis the author presents several recommendation that should be considered:

- Further work is required in identifying and quantifying manufacturing defects using basic methods such as density measurements or more expensive X-ray computed tomography to identify quality of samples and correlate to failure locations and modes.
- Tensile testing at a wider range of strain rates should be conducted to assess if materials possess strain rate dependence. This could be conducted using larger universal test machines and suitably sized specimens.
- Determination of the changes in material properties around defects and interfaces.
- The assessment of critical strains and yield stresses should be conducted at the lowest temperature used in testing to ensure DMTA analysis remains within the LVER.
- When performing TTS experiments smaller frequency ranges should be used and instead utilise a greater number of temperature increments to create the master curves.
- As materials are known to recovery over time accelerated erosion testing should either use equal slice and recovery times or conduct a campaign to confirm that these parameters have no significant impact on performance.

To further the understanding of LEE, three research gaps have been identified as key areas for future work:

1. Environmental effects

The material properties utilised within current lifetime prediction models are derived from pristine materials and are assumed constant throughout the service life of a coating. However, preliminary testing in Chapter 7 using the novel thin-film approach identified considerable changes in the material properties as a result of accelerated rain erosion testing which is also thought to occur offshore. A further consideration is that while accelerated testing controls many variables, it does not consider many of the environmental conditions that a coatings system would experience offshore such as rain droplet impacts and extended weathering. The effects of environmental weathering of these materials were not studied, which is important as it overlooks the influence of UV radiation, variations in heat, salinity, and humidity on coating properties during both long term storage and operation. These can affect materials on the molecular level, causing changes such as bond breakages resulting in reductions in macro-level mechanical properties, potentially accelerating the erosion process. While it is possible to explore the effects of rain erosion and extended weather separately, the author hypothesises that they are synergistic and result in more rapid and severe erosion. These findings could explain the lack of correlation in erosion performance between accelerated rain erosion tests and coatings in an offshore environment.

2. Strain Rate Validation

As demonstrated in Chapters 5, 6 and 7, modern LEP materials are viscoelastic, and the material behaviours change as a function of both temperature and strain rate. As a result, an accurate measurement of the strain rates caused by droplet impacts is required to inform and validate the predictions made in this thesis. This would require further understanding of how droplet impact velocity and droplet diameters influence the resulting strain rate. To achieve this, specialist high strain rate measurement techniques are required. Examples of methods that could be employed include coupon level testing using a Split-Hopkinson Pressure Bar (SHPB), ultra-high-speed cameras in combination with Digital Image Correlation, or the inclusion of strain gauges⁴⁴ within the coating system to capture impacts during accelerated testing or in the offshore environment.

⁴⁴ Preliminary work toward the inclusion of strain gauges with the LEP coating layer has been reported by *Herring* in parallel work as part of the BLEER project [121].

3. Multiscale Approach

In this thesis, Chapters 4, 5, and 6 utilised coupon-level testing and correlated behaviours with component-level testing in Chapter 7. If the chemical composition of a coating system was known, Molecular Dynamics (MD) could be used to model the three-dimensional network structure and evaluate its dynamic properties⁴⁵. The additional level could create a rapid prototyping approach that could allow for coating manufacturers to more efficiently investigate the effects of changing composition using a systematic approach. The use of MD also allows for the prediction of macro-scale properties over a wide range of test conditions as it does not face the same limitation as experimental testing. This approach would allow optimal material properties to be determined and correlated to the coupon and component levels.

⁴⁵ Early stage development of this approach was conducted in alongside this project with promising results but was not reported within the thesis.

References

- [1] Rayner NA. Global analyses of sea surface temperature, sea ice, and night marine air temperature since the late nineteenth century. *J Geophys Res* 2003; 108: 4407–4431.
- [2] Walther G-R, Post E, Convey P, Menezels A, Parmesan C, Beebee TJC, Fromentin J-M, Hoegh-Guldberg O, Bairlein F. Ecological responses to recent climate change. *Nature* 2002; 416: 389–395.
- [3] Parmesan C, Yohe G. A globally coherent fingerprint of climate change impacts across natural systems. *Nature* 2003; 421: 37–42.
- [4] Hurrell JW. Decadal trends in the north atlantic oscillation: Regional temperatures and precipitation. *Science (80-)* 1995; 269: 676–679.
- [5] Mann ME, Zhang Z, Hughes MK, Bradley RS, Miller SK, Rutherford S, Ni F. Proxy-based reconstructions of hemispheric and global surface temperature variations over the past two millennia. *Proc Natl Acad Sci* 2008; 105: 13252–13257.
- [6] Reay D, Sabine C, Smith P, Hymus G. Climate change 2007: Spring-time for sinks. *Nature* 2007; 446: 727–728.
- [7] Church JA, White NJ. A 20th century acceleration in global sea-level rise. *Geophys Res Lett* 2006; 33: 1–4.
- [8] Gleason KL, Lawrimore JH, Levinson DH, Karl TR, Karoly DJ. A revised U.S. Climate Extremes Index. *J Clim* 2008; 21: 2124–2137.
- [9] Alley RB, Brigham-Grette J, Miller GH, White JWC. *Past Climate Variability and Change in the Arctic and at High Latitudes*. Washington, USA: U.S. Climate Change Science Program. Epub ahead of print 2009. DOI: 20103085720.
- [10] Statement by the President on the Paris Climate Agreement | whitehouse.gov, <https://obamawhitehouse.archives.gov/the-press-office/2015/12/12/statement-president-paris-climate-agreement> (accessed 24 November 2021).
- [11] IEA. *Carbon Dioxide Emissions From Fuel Combustion Highlights*. Paris: Organization for Economic Co-operation and Development (OECD), 2016.
- [12] NOAA. Carbon Dioxide | Vital Signs – Climate Change: Vital Signs of the Planet. NASA, <https://climate.nasa.gov/vital-signs/carbon-dioxide/> (2019, accessed 7 December 2021).
- [13] European Parliament, Council of the European Union. Regulation (EU) No 333/2014. *Off J Eur Union* 2014; 15–21.
- [14] Committe on Climate Change. Net Zero: The UK's contribution to stopping global warming. *Committe Clim Chang* 2019; 275.
- [15] Climate Change Act 2008. Statute Law Database.
- [16] UK net zero target | The Institute for Government, <https://www.instituteforgovernment.org.uk/explainers/net-zero-target> (accessed 29 April 2021).
- [17] UK Government. The Climate Change Act 2008 (2050 Target Amendment) Order 2019. 2019; 2008: 1–2.

- [18] Letcher TM. *Wind Energy Engineering*. London: Elsevier, 2017.
- [19] The Heathrow judgment is not “undemocratic judicial activism” | The Institute for Government, <https://www.instituteforgovernment.org.uk/blog/court-appeal-heathrow-unlawful> (accessed 29 April 2021).
- [20] Mathews JA. How carbon credits could drive the emergence of renewable energies. *Energy Policy* 2008; 36: 3633–3639.
- [21] How does carbon offsetting work? | Deloitte UK, <https://www2.deloitte.com/uk/en/focus/climate-change/zero-in-on-carbon-offsetting.html> (accessed 14 December 2021).
- [22] A Guide to Carbon Offsets: a dose of hope and skepticism – Broader Impacts Group, <https://web.whoi.edu/big/a-guide-to-carbon-offsets-a-dose-of-hope-and-skepticism/> (accessed 14 December 2021).
- [23] 2030 Energy Strategy - European Commission, <https://ec.europa.eu/energy/en/topics/energy-strategy-and-energy-union/2030-energy-strategy> (accessed 16 July 2018).
- [24] European Council agrees climate and energy goals for 2030 - European Commission, <https://ec.europa.eu/energy/en/news/european-council-agrees-climate-and-energy-goals-2030> (accessed 16 July 2018).
- [25] Schiermeier Q. European Union moves to strengthen renewable-energy goals. *Nature*, 2018. Epub ahead of print 17 January 2018. DOI: 10.1038/d41586-018-00879-9.
- [26] EU. Directive (EU) 2018/2001 of the European Parliament and of the Council on the promotion of the use of energy from renewable sources. *Off J Eur Union* 2018; 2018: 82–209.
- [27] EU legislation and UK law, <https://www.legislation.gov.uk/eu-legislation-and-uk-law> (accessed 14 December 2021).
- [28] Palen R, Diaz Alonso F. *Share of Renewable Energy in the EU up to 17.5% in 2017*, <https://ec.europa.eu/eurostat/documents/2995521/9571695/8-12022019-AP-EN.pdf/b7d237c1-ccea-4adc-a0ba-45e13602b428> (2019, accessed 29 July 2019).
- [29] House of Parliament. Developments in Wind Power. *Parliam Off Sci Technol* 2019; 2015–2020.
- [30] National Grid. *Future Energy Scenarios*, <https://www.nationalgrid.com/NR/rdonlyres/C7B6B544-3E76-4773-AE79-9124DDBE5CBB/56766/UKFutureEnergyScenarios2012.pdf> (2014, accessed 30 April 2021).
- [31] BEIS. *Implementing The End of Unabated Coal by 2025*, www.nationalarchives.gov.uk/doc/open-government-licence/ (2018, accessed 30 April 2021).
- [32] Infrastructure Commission N. *National Infrastructure Commission report*. 2016.
- [33] BP Statistical Review of World Energy 2021. *Statistical Review of World Energy – 2021 The global energy market in 2020*, <https://www.bp.com/en/global/corporate/energy-economics/statistical-review-of-world-energy.html> (2021).
- [34] Herring R, Dyer K, Martin F, Ward C. The increasing importance of leading edge erosion and a review of existing protection solutions. *Renew Sustain Energy Rev* 2019; 115: 109382.
- [35] Cohen J. The First Oil Shock? Nixon, Congress, and the 1973 Petroleum Crisis. <https://doi.org/101080/2152084420211886501> 2021; 12: 49–68.
- [36] Hamilton JD. Causes and Consequences of the Oil Shock of 2007-08. 2009; 2007–2015.

- [37] Kuramochi T. Review of energy and climate policy developments in Japan before and after Fukushima. *Renew Sustain Energy Rev* 2015; 43: 1320–1332.
- [38] Wind Europe. *Offshore wind in Europe : Key trends and statistics 2020*. 2020. Epub ahead of print 2020. DOI: 10.1016/S1471-0846(02)80021-X.
- [39] *Offshore Wind in Europe - Key trends and statistics 2019*. 2018.
- [40] Building the world's largest offshore wind farm in the UK | REVE News of the wind sector in Spain and in the world, <https://www.evwind.es/2021/03/24/building-the-worlds-largest-offshore-wind-farm-in-the-uk/79994> (accessed 6 May 2021).
- [41] *Wind Turbine Control Methods - National Instruments*, <http://www.ni.com/white-paper/8189/en/> (accessed 27 July 2018).
- [42] Department of Business Energy and Industrial Strategy. Contracts for difference. *Policy Paper*, <https://www.gov.uk/government/publications/contracts-for-difference/contract-for-difference> (2022, accessed 8 March 2022).
- [43] BEIS. Electricity Generation Cost Report 2020. *BEIS Electr Gener Cost Rep* 2020; 69.
- [44] Sen S, Ganguly S. Opportunities, barriers and issues with renewable energy development – A discussion. *Renew Sustain Energy Rev* 2017; 69: 1170–1181.
- [45] Kaldellis JK, Zafirakis D. The wind energy (r)evolution: A short review of a long history. *Renew Energy* 2011; 36: 1887–1901.
- [46] Hau E, von Renouard H. *Wind Turbines*. Berlin, Heidelberg: Springer Berlin Heidelberg. Epub ahead of print 2006. DOI: 10.1007/3-540-29284-5.
- [47] Kinney JR. Reinventing the Propeller : Aeronautical Specialty and the Triumph of the Modern Airplane. 2017; 392.
- [48] Markard J, Petersen R. The offshore trend: Structural changes in the wind power sector. *Energy Policy* 2009; 37: 3545–3556.
- [49] Kyle Spearman D. *Floating Wind Joint Industry Project*. 2020.
- [50] Ancona D, Mcveigh J. *Wind Turbine-Materials and Manufacturing Fact Sheet*, <http://citeseerx.ist.psu.edu/viewdoc/download?doi=10.1.1.464.5842&rep=rep1&type=pdf> (2001, accessed 24 July 2018).
- [51] Carrasco JM, Galván E, Portillo R. Wind turbine applications. *Altern Energy Power Electron* 2011; 177–230.
- [52] Offshore wind: How big will blades get?: CompositesWorld, <https://www.compositesworld.com/articles/offshore-wind-how-big-will-blades-get> (accessed 30 July 2018).
- [53] Ouachan I, Dyer K, Hamerton I, Ward C. Engineering viscoelastic properties in polyurethane coatings to reduce erosion risks in wind turbine blades. *SAMPE J* 2021; 57: 16–24.
- [54] General Electric. World's Largest Offshore Wind Turbine | Haliade-X | GE Renewable Energy, <https://www.ge.com/renewableenergy/wind-energy/offshore-wind/haliade-x-offshore-turbine> (accessed 29 July 2019).
- [55] Shohag MAS, Hammel EC, Olawale DO, Okoli OI. Damage mitigation techniques in wind turbine blades: A review. *Wind Eng* 2017; 41: 185–210.

- [56] Twidell J. Book Review: Wind Energy — The Facts Wind Energy – The Facts : a guide to the technology, economics and future of wind power, 2009', European Wind Energy Association, published by Earthscan, London. *Wind Eng* 2009; 33: 305–307.
- [57] EPRI. *A White Paper on Wind Turbine Blade Defect and Damage Categorization: Current State of the Industry*. 2020.
- [58] Pinar Pérez JM, García Márquez FP, Tobias A, Papaelias M. Wind turbine reliability analysis. *Renew Sustain Energy Rev* 2013; 23: 463–472.
- [59] Jensen JP. Evaluating the environmental impacts of recycling wind turbines. *Wind Energy* 2019; 22: 316–326.
- [60] Mishnaevsky L. Toolbox for optimizing anti-erosion protective coatings of wind turbine blades: overview of mechanisms and technical solutions. *Wind Energy* 2019; 22: 1636–1653.
- [61] Ouachan I, Kuball M, Liu D, Dyer K, Ward C, Hamerton I. Understanding of leading-edge protection performance using nano-silicates for modification. *J Phys Conf Ser* 2019; 1222: 012016.
- [62] Kay A. *Blade Leading Edge Erosion Programme (BLEEP): Reducing the Cost Impacts of Wind Turbine Blade Erosion*. Glasgow, <https://ore.catapult.org.uk/app/uploads/2017/12/TLI-SP-00005-Bleep-v2.pdf> (2016, accessed 18 December 2018).
- [63] Ilsted Bech J, Bay Hasager C, Bak C, Bech JI, Hasager CB, Bak C. Extending the life of wind turbine blade leading edges by reducing the tip speed during extreme precipitation events. *Wind Energy Sci* 2018; 3: 729–748.
- [64] Greaves P. Design of offshore wind turbine blades. In: *Offshore Wind Farms: Technologies, Design and Operation*. Woodhead Publishing, 2016, pp. 105–135.
- [65] Mishnaevsky L, Hasager CB, Bak C, Tilg A-MM, Bech JI, Doagou Rad S, Fæster S, Rad D, Faester S, Doagou Rad S, Fæster S. Leading edge erosion of wind turbine blades: understanding, prevention and protection. *Renew Energy* 2021; 169: 953–969.
- [66] Dyer K, Greaves P. Futureproofing the Next Generation of Wind Turbine Blades. *Ingenia*, 2017, pp. 30–35.
- [67] Keegan MH. *Wind Turbine Blade Leading Edge Erosion: An investigation of rain droplet and hailstone impact induced damage mechanisms*. 2014.
- [68] Pugh K, Nash JW, Reaburn G, Stack MM. On analytical tools for assessing the raindrop erosion of wind turbine blades. *Renewable and Sustainable Energy Reviews* 2021; 137: 110611.
- [69] Gohardani O. Impact of erosion testing aspects on current and future flight conditions. *Progress in Aerospace Sciences* 2011; 47: 280–303.
- [70] Katsaprakakis D Al, Papadakis N, Ntintakis I. A comprehensive analysis of wind turbine blade damage. *Energies* 2021; 14: 5974.
- [71] Mishnaevsky L, Thomsen K. Costs of repair of wind turbine blades: Influence of technology aspects. *Wind Energy* 2020; 23: 2247–2255.
- [72] Cortés E, Sánchez F, O'Carroll A, Madramany B, Hardiman M, Young TM, O'Carroll A, Madramany B, Hardiman M, Young TM. On the material characterisation of wind turbine blade coatings: the effect of interphase coating-laminate adhesion on rain erosion performance. *Mater (Basel, Switzerland)* 2017; 10: 1146–1168.

- [73] Schmitt GF, Tatnall GJ, Foulke KW. Joint Air Force-Navy Supersonic Rain Erosion Evaluations of Materials. 1972; 160.
- [74] Nash D, Leishman G, Mackie C, Dyer K, Yang L. A staged approach to erosion analysis of wind turbine blade coatings. *Coatings* 2021; 11: 681.
- [75] Bartolomé L, Teuwen J. Prospective challenges in the experimentation of the rain erosion on the leading edge of wind turbine blades. *Wind Energy* 2019; 22: 140–151.
- [76] Yang R, He Y, Zhang H. Progress and trends in nondestructive testing and evaluation for wind turbine composite blade. *Renew Sustain Energy Rev* 2016; 60: 1225–1250.
- [77] Carroll J, McDonald A, McMillan D. Failure rate, repair time and unscheduled O&M cost analysis of offshore wind turbines. *Wind Energy* 2016; 19: 1107–1119.
- [78] Dong og Siemens giver Horns Rev 2 storstilet vinge-makeover | Ingeniøren, <https://ing.dk/artikel/dong-og-siemens-giver-horns-rev-2-storstilet-vinge-makeover-173761> (accessed 23 July 2018).
- [79] Bech JI, Hasager CB, Bak C. Extending the life of wind turbine blade leading edges by reducing the tip speed during extreme precipitation events. *Wind Energy Sci Discuss* 2018; 1–35.
- [80] London Array braced for blade fix - Offshore Wind | reNEWS - Renewable Energy News, <http://renews.biz/110465/london-array-braced-for-blade-fix/> (accessed 23 July 2018).
- [81] Anholt grapples with blade fix - Offshore Wind | reNEWS - Renewable Energy News, <http://renews.biz/110279/anholt-grapples-with-blade-fix/> (accessed 23 July 2018).
- [82] Wind Europe. Scotland awards seabed rights for massive amounts of offshore wind, most of it floating | WindEurope, <https://windeurope.org/newsroom/press-releases/scotland-awards-seabed-rights-for-massive-amounts-of-offshore-wind-most-of-it-floating/> (accessed 25 January 2022).
- [83] Mishnaevsky L. Repair of wind turbine blades: Review of methods and related computational mechanics problems. *Renew Energy* 2019; 140: 828–839.
- [84] Leading B, Protection E, Johansen NF. Test Methods for Evaluating Rain Erosion Performance of Wind Turbine Blade Leading Edge Protection Systems Nicolai Frost-Jensen Johansen PhD Thesis Test Methods for Evaluating Rain.
- [85] Cortés E, Sánchez F, Domenech L, Olivares A, Young TM, O'Carroll A, Chinesta F, O'carroll A, Chinesta F. Manufacturing issues which affect coating erosion performance in wind turbine blades. *AIP Conf Proc*; 1896. Epub ahead of print 2017. DOI: 10.1063/1.5008010.
- [86] Springer GS, Yang CI, Larsen PS. Analysis of rain erosion of coated materials. *J Compos Mater* 1974; 8: 229–252.
- [87] Gaudern N. A practical study of the aerodynamic impact of wind turbine blade leading edge erosion. *J Phys Conf Ser*; 524. Epub ahead of print 2014. DOI: 10.1088/1742-6596/524/1/012031.
- [88] Sareen A, Sapre CA, Selig MS. Effects of leading edge erosion on wind turbine blade performance. *Wind Energy* 2014; 17: 1531–1542.
- [89] Sapre CA. *Turbine blade erosion and the use of wind protection tape*. University of Illinois, 2012.
- [90] Langel CM, Chow R, Dam CP Van, Maniaci DC. RANS based methodology for predicting the influence of leading edge erosion on airfoil performance. 2017; 1–170.

- [91] Ehrmann RS, White EB, Maniaci DC, Chow R, Langel CM, Van Dam CP. Realistic Leading-Edge Roughness Effects on Airfoil Performance. *Epub ahead of print* 2013. DOI: 10.2514/6.2013-2800.
- [92] Zidane IF, Saqr KM, Swadener G, Ma X, Shehadeh MF. On the role of surface roughness in the aerodynamic performance and energy conversion of horizontal wind turbine blades: a review. *Int J Energy Res* 2016; 40: 2054–2077.
- [93] Schramm M, Rahimi H, Stoevesandt B, Tangager K. The influence of eroded blades on wind turbine performance using numerical simulations. *Energies* 2017; 10: 1–15.
- [94] Han W, Kim J, Kim B. Effects of contamination and erosion at the leading edge of blade tip airfoils on the annual energy production of wind turbines. *Renew Energy* 2018; 115: 817–823.
- [95] Herring R. Integration of Thermoplastic/Metallic Erosion Shields into Wind Turbine Blades to Combat Leading Edge Erosion. In: *Fraunhofer Offshore Wind R&D 2018*. Bremerhaven, Germany, 2018.
- [96] Wind | Protective Coatings | PPG Protective & Marine Coatings, <https://www.ppgpmc.com/protective/power/wind/products> (accessed 18 March 2022).
- [97] Mankiewicz: Coating Systems Wind Power, <https://www.mankiewicz.com/en/markets/wind-power> (accessed 18 March 2022).
- [98] Paints & Coatings for Wind Energy application areas - Hempel, <https://www.hempel.com/markets/wind> (accessed 18 March 2022).
- [99] TEKNOS. TEKNOBLADE REPAIR 9000-10 - Teknos, <https://www.teknos.com/products/teknoblade-repair-9000-10/> (accessed 31 January 2022).
- [100] RELEST Wind HS Topcoat, <https://www.international-pc.com/products/relest-wind-hs-topcoat> (accessed 18 November 2021).
- [101] Painting the wind | Jotun, <https://www.jotun.com/ww/en/corporate/about-jotun/jotun-stories/wind-energy.aspx> (accessed 18 November 2021).
- [102] Reghunadhan A, Thomas S. Polyurethanes: Structure, properties, synthesis, characterization, and applications. In: *Polyurethane Polymers: Blends and Interpenetrating Polymer Networks*. Elsevier, 2017, pp. 1–16.
- [103] Shelke NB, Nagarale RK, Kumbar SG. Polyurethanes. In: *Natural and Synthetic Biomedical Polymers*. Elsevier, 2014, pp. 123–144.
- [104] 3MTM Polyurethane Protective Tape 8671 | 3M United States, https://www.3m.com/3M/en_US/company-us/all-3m-products/~/3M-Polyurethane-Protective-Tape-8671/?N=5002385+3292668437&rt=rud (accessed 17 November 2018).
- [105] Li DJP. Polyurea Elastomer Technology: History, Chemistry & Basic Formulating Techniques.
- [106] Sharmin E, Zafar F. Polyurethane: An introduction. In: Zafar F (ed) *Polyurethane*. London: IntechOpen. *Epub ahead of print* 2012. DOI: 10.5772/51663.
- [107] Prisacariu C. *Polyurethane Elastomers*. Vienna: Springer Vienna. *Epub ahead of print* 2011. DOI: 10.1007/978-3-7091-0514-6.
- [108] DNV-GL, DNV GL. DNVGL-RP-0573: Evaluation of erosion and delamination for leading edge protection systems of rotor blades.
- [109] Slot HMM, Gelinck ERM RM, Rentrop C, Van der Heide E. Leading edge erosion of coated wind

- turbine blades: Review of coating life models. *Renew Energy* 2015; 80: 837–848.
- [110] Mishnaevsky L, Sütterlin J. Micromechanical model of surface erosion of polyurethane coatings on wind turbine blades. *Polym Degrad Stab* 2019; 166: 283–289.
- [111] Eisenberg D, Laustsen S, Stege J. Wind turbine blade coating leading edge rain erosion model : development and validation. *Wind Energy* 2018; 21: 1–10.
- [112] ASTM. Standard Test Method for Tensile Properties of Thin Plastic Sheeting. *ASTM Int* 2004; 12: 1–8.
- [113] Standard Test Method for Tensile Properties of Plastics 1. DOI: 10.1520/D0638-14.
- [114] Springer GS. Erosion by liquid impact. John Wiley & Sons Inc, 1976, p. 264.
- [115] Tatekura Y, Watanabe M, Kobayashi K, Sanada T. Pressure generated at the instant of impact between a liquid droplet and solid surface. *R Soc Open Sci* 2018; 5: 181101.
- [116] Engel OG. Waterdrop collisions with solid surfaces. *J Res Natl Bur Stand (1934)* 1955; 54: 281.
- [117] Zahavi J, Nadin S, Schmitt GF. Indirect damage in composite materials due to raindrop impact. *Wear* 1981; 72: 305–313.
- [118] Cook SS. Erosion by water-hammer. *Proc R Soc A Math Phys Eng Sci* 1928; 119: 481–488.
- [119] Herring R, Domenech L, Renau J, Šakalytė A, Ward C, Dyer K, Sánchez F. Assessment of a wind turbine blade erosion lifetime prediction model with industrial protection materials and testing methods. *Coatings* 2021; 11: 767.
- [120] DNV. Wind turbine blade erosion to be tackled in new Joint Industry Project. *Online Article* 2019; 2019–2020.
- [121] Herring R. *Leading edge erosion of wind turbine blades: an assessment and improvement of the translation between test results and in-situ performance*. University of Bristol, 2022.
- [122] Keegan MH, Nash DH, Stack MM. On erosion issues associated with the leading edge of wind turbine blades. *J Phys D Appl Phys*; 46. Epub ahead of print 2013. DOI: 10.1088/0022-3727/46/38/383001.
- [123] Granta Design Limited. Granta EduPack software. *Granta Design*.
- [124] Johansen NF-J. *Test Methods for Evaluating Rain Erosion Performance of Wind Turbine Blade Leading Edge Protection Systems*. APA, 2020.
- [125] Ferraiuolo M, Scigiano R, Riccio A, Bottone E, Rennella M. Thermo-structural design of a ceramic matrix composite wing leading edge for a re-entry vehicle. *Compos Struct* 2019; 207: 264–272.
- [126] Ashby M, Johnson K. *Materials and Design*. 2010. Epub ahead of print 2010. DOI: 10.1016/C2009-0-26530-5.
- [127] O'Carroll A. *Correlation of Mechanical Properties to Rain Erosion Resistance of Polymeric Materials*. University of Limerick, 2018. Epub ahead of print 2018. DOI: 10.13140/RG.2.2.33222.93769.
- [128] O'Carroll A, Hardiman M, Tobin EFF, Young TMM. Correlation of the rain erosion performance of polymers to mechanical and surface properties measured using nanoindentation. *Wear* 2018; 412–413: 38–48.
- [129] Mishnaevsky Jr. L, Fæster S, Mikkelsen L, Kusano Y, Bech JI. Micromechanisms of leading edge

- erosion of wind turbine blades: X-Ray tomography analysis and computational studies. *Renew Energy* 2019; Submitted: 1–21.
- [130] Sigamani NS. Characterization of Polyurethane At Multiple Scales for Erosion Mechanisms Under Sand Particle Impact. 2010; 92.
- [131] Barkoula NM, Karger-Kocsis J. Processes and influencing parameters of the solid particle erosion of polymers and their composites. *Journal of Materials Science* 2002; 37: 3807–3820.
- [132] ELLE™ - Prevents leading edge erosion on wind turbine blades, <https://www.polytech.com/wtg-manufacturers/elle-leading-edge-protection/> (accessed 22 February 2022).
- [133] Doagou-Rad S, Mishnaevsky L. Rain erosion of wind turbine blades: computational analysis of parameters controlling the surface degradation. *Meccanica* 2020; 55: 725–743.
- [134] Lakes RS. *Viscoelastic Solids* (1998). CRC Press. Epub ahead of print 22 November 2017. DOI: 10.1201/9781315121369.
- [135] Karger-Kocsis J, Kuleznev VN. Dynamic mechanical and impact properties of polypropylene/EPDM blends. *Polymer (Guildf)* 1982; 23: 699–705.
- [136] Arena G, Friedrich K, Acierno D, Padenko E, Russo P, Filippone G, Wagner J. Solid particle erosion and viscoelastic properties of thermoplastic polyurethanes. *Express Polym Lett* 2015; 9: 166–176.
- [137] Slikkerveer PJ, Touwslager FJ. Erosion of elastomeric protective coatings. *Wear* 1999; 236: 189–198.
- [138] Owden FPB, Brunton JH. The deformation of solids by liquid impact at supersonic speeds. *Proc R Soc London Ser A Math Phys Sci* 1961; 263: 433–450.
- [139] Hutchings IM, Deuchar DWT, Muhr AH. Erosion of unfilled elastomers by solid particle impact. *J Mater Sci* 1987 2211 1987; 22: 4071–4076.
- [140] Godfrey M, Siederer O, Zekonyte J, Barbaros I, Wood R. The effect of temperature on the erosion of polyurethane coatings for wind turbine leading edge protection. *Wear* 2021; 476: 203720.
- [141] Domenech L, Renau J, Šakalyte A, Sánchez F. Top coating anti-erosion performance analysis in wind turbine blades depending on relative acoustic impedance. Part 1: Modelling approach. *Coatings* 2020; 10: 685.
- [142] Domenech L, García-Peñas V, Šakalyte A, Francis DP, Skoglund E, Sánchez F. Top coating anti-erosion performance analysis in wind turbine blades depending on relative acoustic impedance. Part 2: Material characterization and rain erosion testing evaluation. *Coatings* 2020; 10: 1–20.
- [143] Tcharkhtchi A, Farzaneh S, Abdallah-Elhirtsi S, Esmaeilou B, Nony F, Baron A. Thermal aging effect on mechanical properties of polyurethane. *Int J Polym Anal Charact* 2014; 19: 571–584.
- [144] Wypych G. Handbook of UV degradation and stabilization.
- [145] Shokrieh MM, Bayat A. Effects of ultraviolet radiation on mechanical properties of glass/polyester composites. *J Compos Mater* 2007; 41: 2443–2455.
- [146] Berketis K, Tzetzis D, Hogg PJ. The influence of long term water immersion ageing on impact damage behaviour and residual compression strength of glass fibre reinforced polymer (GFRP).

- Mater Des* 2008; 29: 1300–1310.
- [147] DNV. DNVGL-RP-0171: Testing of rotor blade erosion protection systems.
- [148] ISO - ISO/TS 19392-1:2018 - Paints and varnishes — Coating systems for wind-turbine rotor blades — Part 1: Minimum requirements and weathering, <https://www.iso.org/standard/72928.html> (accessed 24 February 2022).
- [149] As DG. CLASS PROGRAMME Type approval Coatings for protection of FRP structures with heavy rain erosion loads.
- [150] Sward G (ed). *Paint Testing Manual*. 100 Barr Harbor Drive, PO Box C700, West Conshohocken, PA 19428-2959: ASTM International. Epub ahead of print 1 January 1972. DOI: 10.1520/STP500-EB.
- [151] Elcometer. Elcometer 3520 Baker Film Applicator, <https://www.elcometer.com/en/coatings-inspection/all-coatings-inspection/film-application-test-charts/elcometer-3520-baker-film-applicator.html> (accessed 4 March 2022).
- [152] Menard KP, Menard NR. *Dynamic Mechanical Analysis in the Analysis of Polymers and Rubbers*. Epub ahead of print 2015. DOI: 10.1002/0471440264.pst102.pub2.
- [153] Fischer-Cripps AC. Review of analysis methods for sub-micron indentation testing. *Vacuum* 2000; 58: 569–585.
- [154] Johnson KL. *Contact Mechanics*. Cambridge University Press. Epub ahead of print 16 May 1985. DOI: 10.1017/CBO9781139171731.
- [155] Hainsworth SV., Chandler HW, Page TF. Analysis of nanoindentation load-displacement loading curves. *J Mater Res* 1996; 11: 1987–1995.
- [156] Pharr GM. An improved technique for determining hardness and elastic modulus using load and displacement sensing indentation experiments. *J Mater Res* 1992; 7: 1564–1583.
- [157] Ghanbari S, Bahr DF. An energy-based nanoindentation method to assess localized residual stresses and mechanical properties on shot-peened materials. *J Mater Res* 2019; 34: 1121–1129.
- [158] Pöhl F, Hardes C, Theisen W. Scratch behavior of soft metallic materials. *AIMS Mater Sci* 2016; 3: 390–403.
- [159] Kanari K. *Toughening composite laminates using hierarchical electrospun fibrous veils*. 2021.
- [160] What is Ultrasonic Testing - Pulse-Echo Method - Definition | Material Properties, <https://material-properties.org/what-is-ultrasonic-testing-pulse-echo-method-definition/> (accessed 9 February 2022).
- [161] MathWorks. Bandpass-filter signals - MATLAB bandpass. *MathWorks Documentation*, <https://www.mathworks.com/help/signal/ref/bandpass.html> (2019, accessed 9 February 2022).
- [162] MathWorks. Discrete-time analytic signal using Hilbert transform - MATLAB hilbert - MathWorks United Kingdom, https://www.mathworks.com/help/signal/ref/hilbert.html?s_tid=srchtitle_hilbert_1 (2019, accessed 9 February 2022).
- [163] Fan JT, Weerheim J, Sluys LJ. High-strain-rate tensile mechanical response of a polyurethane elastomeric material. *Polymer (Guildf)* 2015; 65: 72–80.

- [164] Deuschle J. Mechanics of Soft Polymer Indentation. 2008; 189.
- [165] Doktor G. Nanoindentation testing of soft polymers :
- [166] Li Z, Brokken-Zijp JCM, De With G. Determination of the elastic moduli of silicone rubber coatings and films using depth-sensing indentation. *Polymer (Guildf)* 2004; 45: 5403–5406.
- [167] Loubet JL, Oliver WC, Lucas BN. Measurement of the loss tangent of low-density polyethylene with a nanoindentation technique. *J Mater Res* 2000; 15: 1195–1198.
- [168] Odegard GM, . BT, Herring HM, Gates TS, Herring HM. Characterization of viscoelastic properties of polymeric materials through nanoindentation. *Exp Mech* 2003; 45: 130–136.
- [169] Ebenstein D. Nanoindentation of soft tissues and other biological materials. In: *Handbook of Nanoindentation*. Pan Stanford Publishing, pp. 279–324.
- [170] Hardiman M, Vaughan TJ, McCarthy CT. The effects of pile-up, viscoelasticity and hydrostatic stress on polymer matrix nanoindentation. *Polym Test* 2016; 52: 157–166.
- [171] Bruker Nano Surfaces Division. Hysitron TI Premier | Nanoindenter Overview | Bruker. 2017; 4.
- [172] Selby AP. Nanoindentation of soft contact lens materials.
- [173] Oliver WC, Pharr GM. Measurement of hardness and elastic modulus by instrumented indentation: Advances in understanding and refinements to methodology. *J Mater Res* 2004; 19: 3–20.
- [174] Hardiman M, Vaughan TJ, McCarthy CT. The effects of pile-up, viscoelasticity and hydrostatic stress on polymer matrix nanoindentation. *Polym Test* 2016; 52: 157–166.
- [175] Tang B, Ngan AHW. *Accurate measurement of tip-sample contact size during nanoindentation of viscoelastic materials*. 2003.
- [176] Cao Y, Yang D, Soboyejo W. Nanoindentation method for determining the initial contact and adhesion characteristics of soft polydimethylsiloxane. *Epub ahead of print* 2005. DOI: 10.1557/JMR.2005.0256.
- [177] Cheng YT, Cheng CM. Relationships between initial unloading slope, contact depth, and mechanical properties for conical indentation in linear viscoelastic solids. *J Mater Res* 2005; 20: 1046–1053.
- [178] Ngan AHW, Tang B. Viscoelastic effects during unloading in depth-sensing indentation. *J Mater Res* 2002; 17: 2604–2610.
- [179] Zhao P-C, Li W, Huang W, Li C-H, Hsu S-H, Hager MD. molecules A Self-Healing Polymer with Fast Elastic Recovery upon Stretching. DOI: 10.3390/molecules25030597.
- [180] Cheng YT, Cheng CM. Relationships between hardness, elastic modulus, and the work of indentation. *Appl Phys Lett* 1998; 73: 614.
- [181] TA Instruments. *Determining the Linear Viscoelastic Region in Oscillatory Measurements*, <https://www.tainstruments.com/pdf/literature/RH107.pdf> (2021, accessed 19 March 2022).
- [182] TA. DMA basic theory and applications, http://people.clarkson.edu/~skrishna/DMA_Basic_Theory_Applications.pdf.
- [183] Li R. Time-temperature superposition method for glass transition temperature of plastic materials. *Mater Sci Eng A* 2000; 278: 36–45.

- [184] Hernández WP, Castello DA, Roitman N, Magluta C. Thermorheologically simple materials: A bayesian framework for model calibration and validation. *J Sound Vib* 2017; 402: 14–30.
- [185] Plazek D. Time-temperature superposition-a users guide.
- [186] Cho KS. Time-temperature superposition. In: *Springer Series in Materials Science*. Springer Verlag, 2016, pp. 437–457.
- [187] Ashter SA. Mechanics of Materials. *Thermoforming of Single and Multilayer Laminates* 2014; 123–145.
- [188] Mours M, Winter HH. Mechanical Spectroscopy of Polymers. *Exp Methods Polym Sci Mod Methods Polym Res Technol* 2012; 495–546.
- [189] Wang B, Chang G, Lin X, Guo W. Analysis on Parameters of WLF Equation for Viscoelastic Damping Materials. 2016, pp. 4–6.
- [190] Shangguan Y, Chen F, Jia E, Lin Y, Hu J, Zheng Q. New insight into Time-Temperature correlation for polymer relaxations ranging from secondary relaxation to terminal flow: Application of a Universal and developed WLF equation. *Polymers (Basel)*; 9. Epub ahead of print 2017. DOI: 10.3390/polym9110567.
- [191] Grandgirard J, Poinsot D, Krespi L, Nénon JP, Cortesero AM. Costs of secondary parasitism in the facultative hyperparasitoid Pachycrepoideus dubius: Does host size matter? *Entomol Exp Appl* 2002; 103: 239–248.
- [192] Butaud P, Placet V, Klesa J, Ouisse M, Foltête E, Gabrion X. Investigations on the frequency and temperature effects on mechanical properties of a shape memory polymer (Veriflex). *Mech Mater* 2015; 87: 50–60.
- [193] Lai G, Li Y, Li G. Effect of concentration and temperature on the rheological behavior of collagen solution. *Int J Biol Macromol* 2008; 42: 285–291.
- [194] Marashdeh WF, Iroh JO. Viscoelastic behavior and construction of master curve for graphene/polyimide nanocomposites. *High Perform Polym* 2017; 29: 943–950.
- [195] Szabo JP, Keough IA. Method for analysis of dynamic mechanical thermal analysis data using the Havriliak-Negami model. In: *Thermochimica Acta*. Elsevier, pp. 1–12.
- [196] Mark J. *Physical properties of polymers handbook*. Berlin, Heidelberg: Springer Berlin Heidelberg. Epub ahead of print 2014. DOI: 10.1007/978-3-642-41714-6_31317.
- [197] Liao T, Jiang Z, Li R, Gao Y, Men Y. Stretching temperature dependence of the critical strain in the tensile deformation of polyethylene copolymer. *Eur Polym J* 2017; 97: 188–197.
- [198] Small C, Cohen JE. Continental physiography, climate, and the global distribution of human population. *Curr Anthropol* 2004; 45: 269–277.
- [199] Ferry JD. *Viscoelastic properties of polymers*. 1980. Epub ahead of print 1980. DOI: 10.1149/1.2428174.
- [200] Tobolsky A V., Andrews RD. Systems manifesting superposed elastic and viscous behavior. *J Chem Phys* 1945; 13: 3–27.
- [201] Bartolomé L, Teuwen J. Prospective challenges in the experimentation of the rain erosion on the leading edge of wind turbine blades. *Wind Energy* 2019; 22: 140–151.
- [202] Griffith AA. The phenomena of rupture and flow in solids. *Masinovedenie* 1995; 4: 9–14.

- [203] Telford JK. A brief introduction to design of experiments. *Johns Hopkins APL Tech Dig (Applied Phys Lab)* 2007; 27: 224–232.
- [204] Cavazzuti M. Design of Experiments. In: *Optimization Methods*. Berlin, Heidelberg: Springer Berlin Heidelberg, pp. 13–42.
- [205] Ilzarbe L, Álvarez MJ, Viles E, Tanco M. Practical applications of design of experiments in the field of engineering: a bibliographical review. *Qual Reliab Eng Int* 2008; 24: 417–428.
- [206] Haines PJ (Peter J. *Principles of Thermal Analysis and Calorimetry*. Cambridge: Royal Society of Chemistry. Epub ahead of print 2002. DOI: 10.1039/9781847551764.
- [207] ASTM. G73 – 10 (Reapproved 2017) Standard Test Method for Liquid Impingement Erosion Using Rotating Apparatus1. Epub ahead of print 2017. DOI: 10.1520/G0073-10R17.